NONLINEAR OPTICAL PROPERTIES OF SEMICONDUCTOR AND OXIDE NANOSTRUCTURES

by

Yanjun Ma

B.S. in Physics, Univ. of Sci. and Tech. of China, 2005

Submitted to the Graduate Faculty of

the Dietrich School of Arts and Sciences in partial fulfillment

of the requirements for the degree of

Doctor of Philosophy in Physics

University of Pittsburgh

2013

UNIVERSITY OF PITTSBURGH

DEPARTMENT OF PHYSICS AND ASTRONOMY

This dissertation was presented

by

Yanjun Ma

It was defended on

March 28th 2013

and approved by

Jeremy Levy, Professor, Department of Physics and Astronomy

Robert P. Devaty, Associate Professor, Department of Physics and Astronomy

W. Vincent Liu, Associate Professor, Department of Physics and Astronomy

Gurudev Dutt, Assistant Professor, Department of Physics and Astronomy

Robert Griffiths, Otto Stern University Professor, Department of Physics

Dissertation Director: Jeremy Levy, Professor, Department of Physics and Astronomy

NONLINEAR OPTICAL PROPERTIES OF SEMICONDUCTOR AND OXIDE NANOSTRUCTURES

Yanjun Ma, PhD

University of Pittsburgh, 2013

Light-matter interaction is a historically ancient topic, yet it is still under intense research, owing to the invention of novel optical techniques and the growth of unprecedented materials. The first goal of the work presented in this thesis is to understand the fundamental origin of various nonlinear optical phenomena. Susceptibilities are physical quantities describing the way that a material system responds to an optical field. We present in Chapter 3 the derivations of susceptibilities based on quantum mechanical statistics, revealing the electronic origin of optical nonlinearities.

Different theoretical tools have been applied to the interaction between light and a material system. Among them, the Jaynes-Cumming model is of importance in that it describes the interplay between a quantized light field and a two-level system. In Chapter 4, we will theoretically discuss the application of the Jaynes-Cumming model to the Faraday/Kerr rotation experiments on a single electron spin. As a magneto-optic effect, Faraday/Kerr rotation is one example of various nonlinear optical processes that are studied in detail in Chapter 3.

The second part of this thesis is dedicated to experimental demonstration of applications by exploiting different nonlinear mechanisms. One example is the mode-locked ultrafast laser discussed in Chapter 5. Another is the generation and detection of THz radiation in oxide nanostrucutures, which is covered in both Chapter 6 and Chapter 7.

TABLE OF CONTENTS

LIST OF TABLES

LIST OF FIGURES

PREFACE

This thesis is a summary of the past seven years of my life, which is a journey consisting of pain and joy, trivial results and exciting achievements. The work presented here is a result based on the efforts of many people. First of all, Jeremy Levy, as a hard-working and brilliant advisor, inspires me in every way. He is always there when I need help, guidance and encouragement. I could not make it so far without his support. He sets the example of a successful scientist to me. I also would like to express my gratitude to my committee, Robert P. Devaty, Gurudev Dutt, W. Vincent Liu, Robert Griffiths. Their commitment and guidance has helped me to improve this dissertation.

Patrick Irvin, who is the most senior member in our group, helped me tremendously when I joined the group. Most of the lab skills I know I learned from him. Without his training, I could not survive in the lab in the first place. My dear wife, Cheng Cen, was a graduate student of Jeremy as well. It is she who experimentally demonstrated the conductive AFM lithography method that defines the playground of my research. The support given by her to me, however, is not only the scientific background but also personal care and love. She always believes in me even when I doubt myself.

A special acknowledgement is due to my parents. I did not realize how important their love is to me until I am more than 5000 miles away from them. This thesis is written for my father especially, for he could not be there to see my graduation. I only wish I could have realized it earlier that he is not just a father to me, but my best friend forever and ever.

Our research is not possible without samples. Therefore, I want to thank our collaborator, Prof. Chang-Beom Eom and his group memebers from the University of Wisconsin for providing us high quality samples.

This thesis is organized as the following: Chapter 1 provides a general background infor-

mation regarding the materials studied in this thesis. Chapter 2 establishes the formalism for studying the light-matter interaction. Chapter 3 shows the theoretical derivation for different orders of nonlinear optical susceptibilities and different nonlinear optical phenomena are discussed as well. Chapter 4 discusses the theoretical exploration about the interaction between photons and a single electron spin. This work is done by Jeremy and I. Chapter 5 shows the effort to build an ultrafast solid state laser. This work is done by Jeremy Levy and Yanjun Ma. Chapter 6 discusses the measurements for the nanoscale photoconductivity in oxide heterostructures. The optical measurements are carried out by Patrick Irvin and Yanjun Ma. Sample processing is done by Daniela Bogorin, who was a postdoc of our group then. Numerical simulations are performed by Cheng Cen. Samples are provided by our collaborators at University of Wisconsin. Chapter 7 shows the experiments demonstrating the generation and detection of THz field at nanoscale. The optical measurements and data analysis are conducted by Yanjun Ma. Sample processing is finished by Mengcheng Huang. Samples, again, come from the same group at University of Wisconsin. Chapter 8 summarizes several possible directions for future research.

1.0 INTRODUCTION

Nonlinear optics is the study of phenomena that occur as a consequence of the modification of the optical properties of a material system by the presence of light. Nonlinear optical phenomena are *nonlinear* in the sense that they occur when the response of a material to an applied optical field depends in a nonlinear manner on the strength of the optical field. For example, in the two-photon absorption process (See Chapter 3), the absorbed optical energy is converted to electric current that scales quadratically with the strength of the applied light field.

1.1 NONLINEAR SUSCEPTIBILITY

In order to describe an optical nonlinearity more precisely, let us consider how the dipole moment per unit volume, or polarization[1] $\vec{P}(\omega)$ of a material system depends on the strength $\vec{E}(\omega)$ of an applied optical field. In the case of linear optics, the induced polarization depends linearly on the electric field

$$\vec{P}(\omega) = \varepsilon_0 \chi^{(1)} \vec{E}(\omega), \tag{1.1}$$

where the coefficient $\chi^{(1)}$ is known as the linear susceptibility and ε_0 is the permittivity of vacuum. In Chapter 2 and Chapter 3, we will see the derivation of the linear susceptibility. In nonlinear optics, the optical response of a material system can often be described by gen-

[1]Since in the time domain, generally, the polarization is given by the convolution between the susceptibility and the electric field, to simplify the expression, we work in the frequency domain.

eralizing Eq.(1.1) by expressing the polarization $\vec{P}(\omega)$ as a power series in the field strength $\vec{E}(\omega)$ as

$$\vec{P}(\omega) = \epsilon_0(\chi^{(1)}\vec{E}(\omega) + \chi^{(2)}\vec{E}^2(\omega) + \chi^{(3)}\vec{E}^3(\omega) + \ldots). \tag{1.2}$$

The quantities $\chi^{(2)}$ and $\chi^{(3)}$ are known as the second and third order nonlinear optical susceptibilities, respectively. The quantities $\vec{P}^{(2)}(\omega) = \chi^{(2)}\vec{E}^2(\omega)$ and $\vec{P}^{(3)}(\omega) = \chi^{(3)}\vec{E}^3(\omega)$ are second and third order of nonlinear polarizations, respectively. For now, we write down susceptibilities as scalar quantities. In Chapter 3, we will study the derivation of nonlinear susceptibilities based on density matrix formulism. We will also show the tensorial nature of the susceptibilities.

Typically, only laser light is sufficiently intense to modify the optical properties of a material system. This is because generally the nonlinear susceptibilities are by far smaller than the linear susceptibility $\chi^{(1)}$. From linear optics, we see the refractive index is

$$n = \sqrt{\varepsilon_r} = \sqrt{1 + \chi^{(1)}}, \tag{1.3}$$

where the quantity ε_r is the relative permittivity of a material system, which is assumed to be nonmagnetic. From Eq.(1.3), it can be seen that the linear susceptibility $\chi^{(1)}$ is on the order of unity.

We can make a simple order-of-magnitude estimate of the size of these nonlinear susceptibilities. One can expect that the lowest-order nonlinear polarization $\vec{P}^{(2)}(\omega)$ is comparable to the linear response when the amplitude of the applied field $\vec{E}(\omega)$ is on the order of the characteristic atomic electric field E_{atom}

$$E_{atom} = e^2/(4\pi\varepsilon_0 a_0^2), \tag{1.4}$$

where e is the charge of the electron and a_0 is the Bohr radius of the hydrogen atom. Numerically, we find $E_{atom} = 5.14 \times 10^9$ V/cm. The second order susceptibility $\chi^{(2)}$ will be on the order of $\chi^{(1)}/E_{atom} \approx 1/E_{atom}$. We therefore find that $\chi^{(2)} \approx 1.94 \times 10^{-10}$ cm/V. Similarly, we expect $\chi^{(3)}$ to be on the order of $1/E_{atom}^2$, which gives $\chi^{(3)} \approx 3.78 \times 10^{-20}$ cm^2/V^2.

The reason that the polarization plays a key role in the description of nonlinear optics is that a time-varying polarization can act as the source of new components of the electromagnetic field. To see that, we need to derive the wave equation.

Typically, in nonlinear optical media, neither free charge nor free current exists. Inside a material, we have

$$\vec{D} = \varepsilon \vec{E} = \varepsilon_0 \vec{E} + \vec{P},$$

and

$$\vec{B} = \mu \vec{H}.$$

The Maxwell equations are

$$\begin{aligned} \nabla \cdot \vec{D} &= 0 \\ \nabla \cdot \vec{B} &= 0 \\ \nabla \times \vec{E} &= -\frac{\partial \vec{B}}{\partial t} \\ \nabla \times \vec{H} &= \frac{\partial \vec{D}}{\partial t}. \end{aligned} \tag{1.5}$$

The equation for the divergence of $\vec{D}$ and the equation for the curl of $\vec{H}$ can be rewritten as

$$\nabla \cdot \vec{E} = 0 \tag{1.6}$$

$$\nabla \times \vec{B} = \mu \frac{\partial}{\partial t}(\varepsilon_0 \vec{E} + \vec{P}). \tag{1.7}$$

If the material is nonmagnetic ($\mu_r \approx 1$), then $\mu = \mu_0 = \frac{1}{\varepsilon_0 c^2}$. The wave equation is then

$$(\nabla^2 - \frac{1}{c^2}\frac{\partial^2}{\partial t^2})\vec{E} = \frac{1}{\varepsilon_0 c^2}\frac{\partial^2}{\partial t^2}\vec{P}. \tag{1.8}$$

The right-hand side of Eq.(1.8) is indeed the polarization term. Therefore if we know the polarization, we can derive the light field by solving the differential equation Eq.(1.8).

1.2 MATERIALS

1.2.1 Semiconductor Quantum Dot

A quantum dot structure confines electrons in all directions, which means that their states are quantized in all directions. Because of the strong localization of the electrons inside a quantum dot, the quantum dot is sometimes referred to an artificial atom[1].

There are different ways to produce quantum dot semiconductor structures. The synthesis of colloidal quantum dots is realized by controllably heating and cooling a solution of crystals so that semiconductor nanocrystals of desired size nucleate out of the solution[2].

A second type of quantum dot is formed from a high quality GaAs/AlGaAs quantum well[3, 4]. A 2D electron gas is formed by doping the AlGaAs layer with Si. Lateral confinement is then accomplished by etching a mesa structure[5] or by forming lateral electrodes using electron beam lithography. By applying a bias to the lateral contacts, the electrons in the 2DEG are depleted, thus forming a region with a potential minimum defined by the electrodes. These types of quantum dots allow extraordinary control over the carriers and have been used to measure single spins electrically[6].

A third type of quantum dot is formed during growth and provides confinement based on the material structure, either by interface roughness in a quantum well structure or by the epitaxial layer forming islands on the substrate. The first type is known as interface fluctuation quantum dots. These are made by pausing the growth of the quantum well material, during which time the atoms migrate to form large monolayer islands. The second type are self-assembled quantum dots, which form because of strain between the substrate and epitaxial layer. The different growth modes of self-assembled quantum dots are classified as Stranski-Krastanow (SK) or Volmer-Weber (VW). SK growth is characterized by the initial formation of a few monolayers of the epitaxial material on the substrate, which is known as the wetting layer. At some point layer growth becomes unfavorable because of strain and islands begin to form. This is considered the normal growth mode for heteroepitaxial growth and is what occurs for growth of Ge on Si and InAs on GaAs. VW growth is the direct formation of islands of the epitaxial material on the substrate. This occurs

because the epitaxial molecules bond more strongly to each other than the substrate. SK growth of Ge on Si will produce $\approx$ 20 nm dots, however if a nucleation layer of C is first deposited, Ge will grow in the VW growth mode and form dots with size $<$ 10 nm.

Quantum dots can be applied to various applications such as LEDs[7], lasers[8] and single-photon sources[9]. Electron spins in quantum dots have also been suggested as implementations of qubits for quantum computation[10]. One way to experimentally detect the electron spins in quantum dots is through magneto-optical effects such as Kerr rotation. In Chapter 4, we will discuss our theoretical study of Faraday rotation of a single electron spin in a single quantum dot.

1.2.2 Oxide Nanostructure

$SrTiO_3$, which was studied extensively in the 1950s and 60s, shows diverse properties[11]. Its cubic structure and high dispersion once made synthetic strontium titanate a prime candidate for simulating diamond[2]. At room temperature, it is a centrosymmetric paraelectric material with a perovskite structure (Figure 1.1). At low temperatures it approaches a ferroelectric phase transition with a very large dielectric constant $\sim 10^4$ but remains paraelectric down to the lowest temperatures measured as a result of quantum fluctuations, making it a quantum paraelectric[12].

$SrTiO_3$, a non-polar oxide, can itself be used as a substrate for growth of $LaAlO_3$, a polar oxide. In 2004, by using pulsed laser deposition (PLD) to grow thin layer of $LaAlO_3$ on top of $SrTiO_3$ substrate, Ohtomo and Hwang discovered the existence of a two-dimensional electron gas (2DEG) at the interface of these two insulators[13]. Since then scientists are exploring the mechanism resulting in the formation of the 2DEG experimentally and theoretically. Oxygen vacancies are believed to be responsible for materials grown at low oxygen pressure. Electron reconstruction due to the polar catastrophe is believed to be responsible for crystals grown at high oxygen pressure[14]. Since $LaAlO_3$ is a polar material, when its thickness exceeds a critical value that is found to be 3 unit cells (u.c.)[15], there is polar-

[2]A simulant is a material that imitates another one. A diamond simulant, in general, means the material looks close to the original in terms of color, refraction and dispersion of light and hardness. See dimondreview for detailed information.

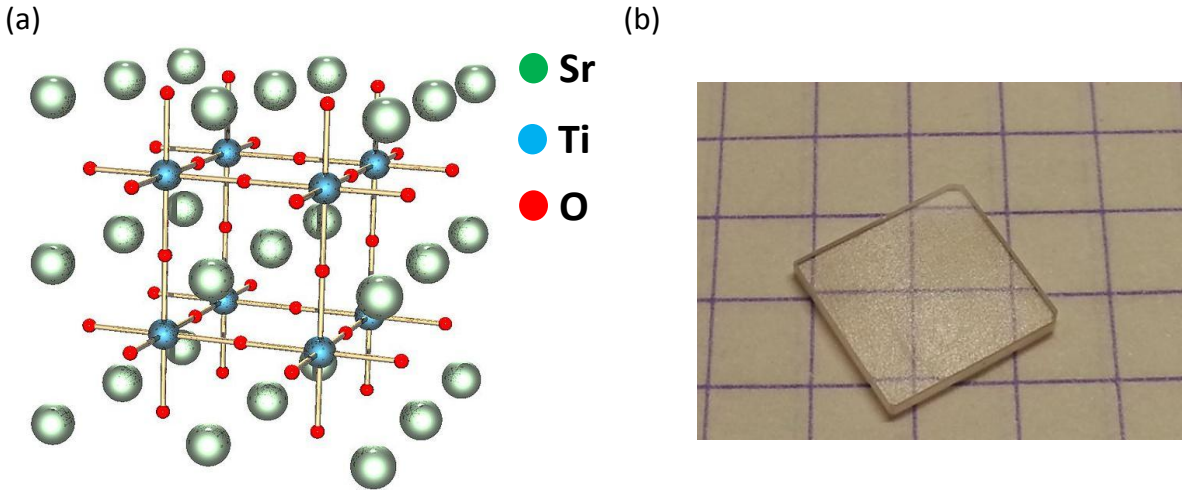

Figure 1.1: (a)The atomic structure of $SrTiO_3$. (b) A piece of 5mm x 5mm $SrTiO_3$ crystal.

ization catastrophe in which an electronic reconstruction occurs, transferring e/2 charge per unit cell to the interface, resulting in the 2DEG formation. The sheet carrier density is theoretically calculated to be 3.2×10^{14} cm^{-2}. However, the experimentally measured value is on the order of 10^{13} cm^{-2}[13, 16, 15, 17]. Further study shows that one possibility for solving this discrepancy between theory and experiment is that part of electrons are doped to the interface are in localized states[16].

Both LAO and STO are materials with wide bandgaps. For LAO, the indirect bandgap between the valence band and conduction band is $E_g \approx 5.6$ eV [13, 18], which is about $\lambda_g \approx 220$ nm. For STO, its direct bandgap is about $E_g \approx 3.75$ eV ($\lambda_g \approx 330$ nm) while its indirect bandgap is about $E_g \approx 3.25$ eV ($\lambda_g \approx 380$ nm)[19]. In terms of the optical properties, both materials show inversion symmetry in the bulk (Table 1.1). Because of that, the $\chi^{(2)}$ tensor vanishes. At the interface, however, since the inversion symmetry is broken, a finite $\chi^{(2)}$ term will emerge, which can be confirmed from second harmonic generation[20].

Thiel et al. [15] have demonstrated that an electric field can be used to reversibly induce the 2DEG. Dr. Cheng Cen in our group has used a conducting AFM probe to pattern nanoscale devices in the interface [21, 22]. Wires with width as small as 2.1 nm have been

	$LaAlO_3$	$SrTiO_3$
Crystal System	Trigonal	Cubic
Crystal Class	$\bar{3}m(D_{3d})$	$m\bar{3}m(O_h)$
$\chi^{(2)}$ elements	All vanish	All vanish

Table 1.1: Table for $LaAlO_3$ and $SrTiO_3$

drawn by applying a positive bias to an AFM tip in contact with the sample. By varying the magnitude of the tip bias the potential profile can be modulated. Experiments performed in vacuum demonstrate that the switching performance of a transistor is not degraded after nine days. These wires are used as building blocks for more complicated structures like diodes [23], single-electron transistors [24] and photoconductive nanostructures [25] that will be discussed in Chapter 6 and nanoscale broadband THz generator and detector which will be discussed in Chapter 7.

As a summary, $LaAlO_3/SrTiO_3$ shows various interesting properties: when two insulating materials are put together, the interface becomes conducting [13, 15]. At the low temperature it can be superconducting [26, 27]; when two transparent materials are grown together, the photoconductivity from visible to near-infrared wavelength, is discoverd at the interface [25]; when two nonmagnetic materials are stacked together, magnetic ordering can show up at the interface[28, 29]. There is also discussion of the coexistence of superconductivity and ferromagnetism [30, 31].

2.0 LIGHT-MATTER INTERACTION

The focus of this thesis is the interaction between light and electrons in solids. This chapter serves as an extended introduction about light-matter interaction. First of all, the quantization of the electromagnetic field is reviewed. The motion of electrons under the influence of external electric field $\vec{E}_{ex}$ and magnetic field $\vec{B}_{ex}$ in solids is theoretically described by the Drude-Lorentz model. The simplest case for a solid state system is a bipartite system which contains only two energetic states. The interaction between the light field and a bipartite system is described by the Jaynes-Cumming model, which will be briefly covered in this chapter. The discussion in this chapter forms the basis for Chapter 4 that presents the study of Faraday rotation due to a single electron spin in quantum dots.

2.1 QUANTUM MECHANICAL MODEL OF LIGHT

In this section, the light field is assumed to be in an empty space, which means that the charge density is zero $\rho = 0$ and the current density is vanishing $j = 0$. Important results such as the quantization of electromagnetic field, Fock states and coherent states are summarized in this section.

2.1.1 Quantization of Electromagnetic Field

We start with the classical description of the electromagnetic field given by the Maxwell equations[32]

$$\nabla \cdot \vec{E} = 0, \tag{2.1}$$
$$\nabla \times \vec{E} = -\frac{\partial \vec{B}}{\partial t}, \tag{2.2}$$
$$\nabla \cdot \vec{B} = 0, \tag{2.3}$$
$$\nabla \times \vec{B} = \frac{1}{c^2}\frac{\partial \vec{E}}{\partial t}. \tag{2.4}$$

A scalar potential function ϕ and a vector potential function $\vec{A}$ are introduced so that both the electric field and magnetic field can be written in the following forms:

$$\vec{E} = -\nabla\phi - \frac{\partial \vec{A}}{\partial t}, \tag{2.5}$$
$$\vec{B} = \nabla \times \vec{A}. \tag{2.6}$$

Under Coulomb gauge,

$$\nabla \cdot \vec{A} = 0, \tag{2.7}$$

according to Eq.(2.1), one can have

$$\nabla^2\phi = 0. \tag{2.8}$$

The electric and magnetic field will then be

$$\vec{E} = -\frac{\partial \vec{A}}{\partial t}, \tag{2.9}$$
$$\vec{B} = \nabla \times \vec{A}. \tag{2.10}$$

Note that both the electric field $\vec{E}$ and the magnetic field $\vec{B}$ are real physical quantities, which indicates that the vector potential $\vec{A}$ should be real as well. By replacing the $\vec{E}$ and $\vec{B}$

in Eq.(2.4) with the above results, one can obtain the wave equation for the vector potential $\vec{A}$.

$$\nabla^2\vec{A} - \frac{1}{c^2}\frac{\partial^2\vec{A}}{\partial^2 t} = 0. \tag{2.11}$$

The fact that the vector potential $\vec{A}$ satisfies the wave equation suggests that $\vec{A} = \vec{A}(\vec{r}, t)$ can be decomposed on the basis of plane waves[33].

$$\vec{A}(\vec{r}, t) = \frac{1}{\varepsilon_0^{1/2} L^{3/2}} \sum_{\vec{k}} \sum_{s} [c_{\vec{k}s}\hat{\varepsilon}_{\vec{k}s} e^{i(\vec{k}\cdot\vec{r} - \omega_{\vec{k}}t)} + c^*_{\vec{k}s}\hat{\varepsilon}^*_{\vec{k}s} e^{-i(\vec{k}\cdot\vec{r} - \omega_{\vec{k}}t)}], \tag{2.12}$$

where the coefficient before summation is introduced to simply the Hamiltonian, which will be shown later on. The second term on the right side of Eq.(2.12) is the complex conjugate of the first term, which is there to ensure $\vec{A}$ is real. $\hat{\varepsilon}_{\vec{k}s}$ and its complex conjugate are unit vectors defining the polarization directions for a plane wave propagating in the direction of $\vec{k}$ with frequency $\omega_{\vec{k}}$. The subscript s indicates the two mutually perpendicular transverse directions that are normal to wave vector $\vec{k}$. This can be seen from the Coulomb gauge condition by taking the following identity into account:

$$\nabla e^{i\vec{k}\cdot\vec{r}} = \partial_m e^{ik_n r_n}\hat{m} = ik_n\delta_{nm}e^{ik_n r_n}\hat{m} = i\vec{k}e^{i\vec{k}\cdot\vec{r}}.$$

One can then have $\vec{k}\cdot\hat{\varepsilon} = \vec{k}\cdot\hat{\varepsilon}^* = 0$. The electric and magnetic field can be found from Eq.(2.12), Eq.(2.9) and Eq.(2.10)

$$\vec{E}(\vec{r}, t) = \frac{i}{\varepsilon_0^{1/2} L^{3/2}} \sum_{\vec{k}} \sum_{s} \omega_{\vec{k}} [c_{\vec{k}s}\hat{\varepsilon}_{\vec{k}s} e^{i(\vec{k}\cdot\vec{r} - \omega_{\vec{k}}t)} - c.c.], \tag{2.13}$$

$$\vec{B}(\vec{r}, t) = \frac{i}{\varepsilon_0^{1/2} L^{3/2}} \sum_{\vec{k}} \sum_{s} [c_{\vec{k}s}\hat{(\vec{k}} \times \varepsilon_{\vec{k}s}) e^{i(\vec{k}\cdot\vec{r} - \omega_{\vec{k}}t)} - c.c.]. \tag{2.14}$$

By introducing the following functions[33]

$$q_{\vec{k}s}(t) = [c_{\vec{k}s}e^{-i\omega_{\vec{k}}t} + c.c.], \tag{2.15}$$

$$p_{\vec{k}s}(t) = -i\omega_{\vec{k}}[c_{\vec{k}s}e^{-i\omega_{\vec{k}}t} - c.c.], \tag{2.16}$$

the electric and magnetic field can also be expressed in terms of $q_{\vec{k}s}$ and $p_{\vec{k}s}$

$$\vec{E}(\vec{r},t) = \frac{i}{2\varepsilon_0^{1/2}L^{3/2}}\sum_{\vec{k}}\sum_{s}\{[\omega_{\vec{k}}q_{\vec{k}s}(t)+ip_{\vec{k}s}(t)]\hat{\varepsilon}_{\vec{k}s}e^{i\vec{k}\cdot\vec{r}}-c.c.\}, \tag{2.17}$$

$$\vec{B}(\vec{r},t) = \frac{i}{2\varepsilon_0^{1/2}L^{3/2}}\sum_{\vec{k}}\sum_{s}\{[q_{\vec{k}s}(t)+\frac{i}{\omega_{\vec{k}}}p_{\vec{k}s}(t)]\vec{k}\times\hat{\varepsilon}_{\vec{k}s}e^{i\vec{k}\cdot\vec{r}}-c.c.\}. \tag{2.18}$$

The energy of the electromagnetic field can be calculated as

$$H(t)=\frac{1}{2}\int_{L^3}[\varepsilon_0\vec{E}^2(\vec{r},t)+\mu_0\vec{B}^2(\vec{r},t)]d^3r=\frac{1}{2}\sum_{\vec{k}}\sum_{s}[p_{\vec{k}s}^2(t)+\omega_{\vec{k}}^2q_{\vec{k}s}^2(t)]. \tag{2.19}$$

Note that $q_{\vec{k}s}(t)$ and $p_{\vec{k}s}(t)$ form a pair of canonical coordinates. From Eq.(2.15) and Eq.(2.16), one can see both functions oscillate sinusoidally in time, and $p_{\vec{k}s}(t)$ shows a $\frac{\pi}{2}$ phase shift relative to $q_{\vec{k}s}(t)$. Therefore, based on Fourier analysis, one can think of $q_{\vec{k}s}(t)$ and $p_{\vec{k}s}(t)$ as two independent variables. Namely, partial derivatives like $\frac{\partial q_{\vec{k}s}}{\partial p_{\vec{k}s}}$ and $\frac{\partial p_{\vec{k}s}}{\partial q_{\vec{k}s}}$ should vanish. Since different $\vec{k}$ represents different plane waves and s represent different polarization directions, one can expect $\frac{\partial p_{\vec{k}s}}{\partial p_{\vec{i}j}}=\delta_{\vec{k}\vec{i}}\delta_{sj}$ and $\frac{\partial q_{\vec{k}s}}{\partial q_{\vec{i}j}}=\delta_{\vec{k}\vec{i}}\delta_{sj}$. The Poisson bracket for $q_{\vec{k}s}(t)$ then can be calculated as the following:

$$\{q_{\vec{k}s},q_{\vec{u}v}\}=\sum_{\vec{i}j}[\frac{\partial q_{\vec{k}s}}{\partial q_{\vec{i}j}}\frac{\partial q_{\vec{u}v}}{\partial p_{\vec{i}j}}-\frac{\partial q_{\vec{k}s}}{\partial p_{\vec{i}j}}\frac{\partial q_{\vec{u}v}}{\partial q_{\vec{i}j}}]=0. \tag{2.20}$$

The Poisson bracket for $p_{\vec{k}s}(t)$ is

$$\{p_{\vec{k}s},p_{\vec{u}v}\}=\sum_{\vec{i}j}[\frac{\partial p_{\vec{k}s}}{\partial q_{\vec{i}j}}\frac{\partial p_{\vec{u}v}}{\partial p_{\vec{i}j}}-\frac{\partial p_{\vec{k}s}}{\partial p_{\vec{i}j}}\frac{\partial p_{\vec{u}v}}{\partial q_{\vec{i}j}}]=0. \tag{2.21}$$

The Poisson bracket between $q_{\vec{k}s}(t)$ and $p_{\vec{k}s}(t)$ is

$$\{q_{\vec{k}s},p_{\vec{u}v}\}=\sum_{\vec{i}j}[\frac{\partial q_{\vec{k}s}}{\partial q_{\vec{i}j}}\frac{\partial p_{\vec{u}v}}{\partial p_{\vec{i}j}}-\frac{\partial q_{\vec{k}s}}{\partial p_{\vec{i}j}}\frac{\partial p_{\vec{u}v}}{\partial q_{\vec{i}j}}]=\sum_{\vec{i}j}\frac{\partial q_{\vec{k}s}}{\partial q_{\vec{i}j}}\frac{\partial p_{\vec{u}v}}{\partial p_{\vec{i}j}}. \tag{2.22}$$

The above summation is nonzero only when $\vec{k}=\vec{u}$ and $s=v$. Therefore

$$\{q_{\vec{k}s},p_{\vec{u}v}\}=\delta_{\vec{k}\vec{u}}\delta_{sv}. \tag{2.23}$$

From Eq.(2.19), Hamiltonian equation can be derived as

$$\frac{dq_{\vec{k}s}(t)}{dt} = \frac{\partial H(t)}{\partial p_{\vec{k}s}(t)}, \tag{2.24}$$

$$\frac{dp_{\vec{k}s}(t)}{dt} = -\frac{\partial H(t)}{\partial q_{\vec{k}s}(t)}. \tag{2.25}$$

Now we are finally ready to describe the electromagnetic field in quantum mechanics. The canonical pair $q_{\vec{k}s}(t)$ and $p_{\vec{k}s}(t)$ can be replaced with operators $\hat{q}_{\vec{k}s}(t)$ and $\hat{p}_{\vec{k}s}(t)$ in Hilbert space. It should be mentioned here that since classically both $q_{\vec{k}s}(t)$ and $p_{\vec{k}s}(t)$ are real, in Hilbert space, operators $\hat{q}_{\vec{k}s}(t)$ and $\hat{p}_{\vec{k}s}(t)$ should be Hermitian. Based on the postulates of quantum mechanics, each pair of canonically conjugate operators has the nonzero commutator $i\hbar$. The Poisson brackets Eq.(2.20), Eq.(2.21) and Eq.(2.23) can be extended to Hilbert space as the following commutators:

$$[\hat{q}_{\vec{k}s}(t), \hat{q}_{\vec{u}v}(t)] = 0 \tag{2.26}$$

$$[\hat{p}_{\vec{k}s}(t), \hat{p}_{\vec{u}v}(t)] = 0 \tag{2.27}$$

$$[\hat{q}_{\vec{k}s}(t), \hat{p}_{\vec{u}v}(t)] = i\hbar\delta_{\vec{k}\vec{u}}\delta_{sv} \tag{2.28}$$

In Hilbert space, the electric field, magnetic field and Hamiltonian are

$$\hat{\vec{E}}(\vec{r},t) = \frac{i}{2\varepsilon_0^{1/2}L^{3/2}}\sum_{\vec{k}}\sum_{s}\{[\omega_{\vec{k}}\hat{q}_{\vec{k}s}(t) + i\hat{p}_{\vec{k}s}(t)]\hat{\varepsilon}_{\vec{k}s}e^{i\vec{k}\cdot\vec{r}} - h.c.\}, \tag{2.29}$$

$$\hat{\vec{B}}(\vec{r},t) = \frac{i}{2\varepsilon_0^{1/2}L^{3/2}}\sum_{\vec{k}}\sum_{s}\{[\hat{q}_{\vec{k}s}(t) + \frac{i}{\omega_{\vec{k}}}\hat{p}_{\vec{k}s}(t)]\vec{k}\times\hat{\varepsilon}_{\vec{k}s}e^{i\vec{k}\cdot\vec{r}} - h.c.\}, \tag{2.30}$$

$$\hat{H}(t) = \frac{1}{2}\sum_{\vec{k}}\sum_{s}[\hat{p}^2_{\vec{k}s}(t) + \omega^2_{\vec{k}}\hat{q}^2_{\vec{k}s}(t)], \tag{2.31}$$

where h.c. stands for Hermitian conjugate, and $\hat{\varepsilon}_{\vec{k}s}$ should be understood as unit vectors for polarization directions, not quantum mechanical operators.

The following operators can be defined[33]

$$\hat{a}_{\vec{k}s}(t) = \frac{1}{\sqrt{2\hbar\omega_{\vec{k}}}}[\omega_{\vec{k}}\hat{q}_{\vec{k}s}(t) + i\hat{p}_{\vec{k}s}(t)], \tag{2.32}$$

$$\hat{a}^{\dagger}_{\vec{k}s}(t) = \frac{1}{\sqrt{2\hbar\omega_{\vec{k}}}}[\omega_{\vec{k}}\hat{q}_{\vec{k}s}(t) - i\hat{p}_{\vec{k}s}(t)]. \tag{2.33}$$

The commutation relations for $\hat{a}_{\vec{k}s}(t)$ and $\hat{a}^{\dagger}_{\vec{k}s}(t)$ are straightforward to compute

$$[\hat{a}_{\vec{k}s}(t), \hat{a}_{\vec{u}v}(t)] = 0 \tag{2.34}$$

$$[\hat{a}^{\dagger}_{\vec{k}s}(t), \hat{a}^{\dagger}_{\vec{u}v}(t)] = 0 \tag{2.35}$$

$$[\hat{a}_{\vec{k}s}(t), \hat{a}^{\dagger}_{\vec{u}v}(t)] = \delta_{\vec{k}\vec{u}}\delta_{sv} \tag{2.36}$$

By comparing Eq.(2.15) and Eq.(2.16) with Eq.(2.32) and Eq.(2.33), one realizes that the classical counterpart of $\hat{a}_{\vec{k}s}(t)$ and $\hat{a}^{\dagger}_{\vec{k}s}(t)$ are $c_{\vec{k}s}e^{-i\omega_{\vec{k}}t}$ and $c^{*}_{\vec{k}s}e^{i\omega_{\vec{k}}t}$, respectively. The time dependence of both operators is harmonic:

$$\hat{a}_{\vec{k}s}(t) = \hat{a}_{\vec{k}s}(0)e^{-i\omega_{\vec{k}s}t}, \tag{2.37}$$

$$\hat{a}^{\dagger}_{\vec{k}s}(t) = \hat{a}^{\dagger}_{\vec{k}s}(0)e^{i\omega_{\vec{k}s}t}. \tag{2.38}$$

The Hermitian operators $\hat{q}_{\vec{k}s}(t)$ and $\hat{q}_{\vec{k}s}(t)$ can be solved from Eq.(2.32) and Eq.(2.33) in terms of $\hat{a}_{\vec{k}s}(t)$ and $\hat{a}^{\dagger}_{\vec{k}s}(t)$:

$$\hat{q}_{\vec{k}s}(t) = \sqrt{\frac{\hbar}{2\omega_{\vec{k}}}}(\hat{a}_{\vec{k}s}(t) + \hat{a}^{\dagger}_{\vec{k}s}(t)), \tag{2.39}$$

$$\hat{p}_{\vec{k}s}(t) = -i\sqrt{\frac{\hbar\omega_{\vec{k}}}{2}}(\hat{a}_{\vec{k}s}(t) - \hat{a}^{\dagger}_{\vec{k}s}(t)). \tag{2.40}$$

The relations above can be used to replace the $\hat{q}_{\vec{k}s}(t)$ and $\hat{p}_{\vec{k}s}(t)$ in Eq.(2.29), Eq.(2.30) and Eq.(2.31).

$$\hat{\vec{E}}(\vec{r},t) = \sqrt{\frac{\hbar\omega_{\vec{k}}}{2\varepsilon_0 L^3}}\sum_{\vec{k}s}[\hat{a}_{\vec{k}s}(t)e^{i\vec{k}\cdot\vec{r}}\hat{\varepsilon}_{\vec{k}s} - \hat{a}^{\dagger}_{\vec{k}s}(t)e^{-i\vec{k}\cdot\vec{r}}\hat{\varepsilon}^{*}_{\vec{k}s}], \tag{2.41}$$

$$\hat{\vec{B}}(\vec{r},t) = i\sqrt{\frac{\hbar}{2\varepsilon_0 L^3}\omega_{\vec{k}}}\sum_{\vec{k}s}[\hat{a}_{\vec{k}s}(t)e^{i\vec{k}\cdot\vec{r}}\vec{k}\times\hat{\varepsilon}_{\vec{k}s} - \hat{a}^{\dagger}_{\vec{k}s}(t)e^{-i\vec{k}\cdot\vec{r}}\vec{k}\times\hat{\varepsilon}^{*}_{\vec{k}s}], \tag{2.42}$$

$$\hat{H}(t) = \sum_{\vec{k}s}\hbar\omega_{\vec{k}s}[\hat{a}^{\dagger}_{\vec{k}s}(t)\hat{a}_{\vec{k}s}(t) + \frac{1}{2}]. \tag{2.43}$$

2.1.2 Coherent State of Light

In quantum mechanics, the electromagnetic field is quantized as we briefly discussed in the previous section. The state of light can be described by different quantum states such as coherent states and squeezed states. Since a laser is widely exploited to study of light-matter interaction in laboratories, we will focus on the coherent state which is used for coherent light source such as lasers and parametric oscillators. It is convenient to represent a coherent state on the basis of Fock states $|n_{\vec{k}s}>$, which is the eigenstate of number operator $\hat{n}_{\vec{k}s} \equiv \hat{a}^{\dagger}_{\vec{k}s}(t)\hat{a}_{\vec{k}s}(t)$

$$\hat{n}_{\vec{k}s}|n_{\vec{k}s}> = n_{\vec{k}s}|n_{\vec{k}s}>, \tag{2.44}$$

where $n_{\vec{k}s}$ means the number of photons in the mode specified by the indices $\vec{k}$ and s and $< n_{\vec{k}s}|n_{\vec{u}v} >= \delta_{\vec{k}\vec{u}}\delta_{sv}$. By using the commutation relation Eq.(2.36) the effect of $\hat{a}_{\vec{k}s}(t)$ and $\hat{a}^{\dagger}_{\vec{k}s}(t)$ on Fock states can be derived. For simplicity, the subscripts $\vec{k}$ and s will be omitted from now on. Each operator, however, is still understood to be associated with a specific mode of the electromagnetic field. The time dependence is also ignored because it is simply harmonic oscillation (See Eq.(2.37) and Eq.(2.38)). For $\hat{a}$, one can have

$$\hat{a}\hat{n}|n> = n\hat{a}|n>, \tag{2.45}$$

$$\hat{a}\hat{n}|n> = (1+\hat{n})\hat{a}|n>, \tag{2.46}$$

which gives immediately

$$\hat{n}\hat{a}|n>=(n-1)\hat{a}|n>, \tag{2.47}$$

which means that $\hat{a}|n>=g|n-1>$. Without losing the generality, the coefficient g can be assumed to be real (Complex coefficient only provides a global phase factor to the state, which is not important in quantum mechanics.).

$$g^2=<n-1|g^2|n-1>=<n|\hat{a}^\dagger\hat{a}|n>=n. \tag{2.48}$$

Therefore $g=\sqrt{n}$. For $\hat{a}^\dagger$, one can start with

$$\hat{n}\hat{a}^\dagger|n>=\hat{a}^\dagger(1+\hat{n})|n>=(n+1)\hat{a}^\dagger|n>, \tag{2.49}$$

which indicates that $\hat{a}^\dagger|n>=f|n+1>$. Again the coefficient f is assumed to be real. Its value is

$$f^2=<n+1|f^2|n+1>=<n|\hat{a}\hat{a}^\dagger|n>=<n|(1+\hat{n})|n>=n+1. \tag{2.50}$$

Therefore $f=\sqrt{n+1}$. As a summary, one can have the following relations

$$\hat{a}|n> = \sqrt{n}|n-1>, \tag{2.51}$$

$$\hat{a}^\dagger|n> = \sqrt{n+1}|n+1>. \tag{2.52}$$

Based on the above results, the operators $\hat{a}_{\vec{k}s}(t)$ and $\hat{a}^\dagger_{\vec{k}s}(t)$ are called annihilation and creation operators respectively.

The coherent state is defined as the eigenstate of annihilation operators:

$$\hat{a}|\alpha>=\alpha|\alpha>. \tag{2.53}$$

In the presentation of Fock states, the coherent state is

$$|\alpha>=e^{-\frac{|\alpha|^2}{2}}\sum_{n=0}^{\infty}\frac{\alpha^n}{\sqrt{n!}}|n>. \tag{2.54}$$

The probability to be in the state $|n>$ is

$$p(n) = |<n|\alpha>|^2 = e^{|\alpha|^2}\frac{|\alpha|^{2n}}{n!}. \tag{2.55}$$

The eigenvalue of a coherent state $|\alpha>$ physically means the average number of photons

$$<\alpha|\hat{a}^\dagger\hat{a}|\alpha> = |\alpha|^2 = \sum_{n=0}^{\infty} np(n). \tag{2.56}$$

2.2 DRUDE-LORENTZ MODEL

The motion of electrons under the influence of an external electric field $\vec{E}_{ex}$ and magnetic field $\vec{B}_{ex}$ in solids is theoretically described by the Drude-Lorentz model.

$$m\ddot{\vec{r}}(t) = -m\omega_0^2\vec{r}(t) - m\gamma\dot{\vec{r}}(t) - e\vec{E}_{ex} - e\frac{\vec{v}}{c}\times\vec{B}_{ex}, \tag{2.57}$$

where r is the distance between electrons and positive nuclei, m is the mass of the carrier, ω_0 is the resonant frequency due to the bounding force and the term $m\gamma\dot{\vec{r}}(t)$ describes the damping effect. When the speed of the carrier $\vec{v}$ is much lower than the speed of light c, the last term in Eq.(2.57) vanishes[1].

By doing Fourier transformation on both sides of Eq.(2.57), one has

$$m(\omega^2 - \omega_0^2 - i\omega\gamma)\vec{r}(\omega) = e\vec{E}_{ex}(\omega). \tag{2.58}$$

The solution is found easily to be

$$\vec{r}(\omega) = \frac{e\vec{E}_{ex}(\omega)}{m}\frac{1}{\omega^2 - \omega_0^2 - i\omega\gamma} \tag{2.59}$$

The polarization is defined as the average of the electric dipole moment over the volume

$$\vec{P}(\omega) = Ne\vec{r}(\omega), \tag{2.60}$$

[1]This can be confirmed by noticing that the Fermi speed v_F is typically order of 10^6 m/s, which is two orders of magnitude smaller than the speed of light

Metal	ω_p (10^{15} Hz)	λ_p (nm)	E_p (eV)
Au	2.183	137.43	~ 9
Pt	1.244	241.16	~ 5.13
Ag	2.18	137.62	~ 8.98
Al	3.57	84.03	~ 14.71
Cu	1.914	156.74	~ 7.389
K	0.8896	337.23	~ 3.72
Na	1.381	217.23	~ 5.71

Table 2.1: Table for plasmon frequency, wavelength and energy in metals

where N is the number of carriers per unit volume. The polarization can also be related to the external electric field through the susceptibility χ

$$\vec{P}(\omega) = \varepsilon_0 \chi \vec{E}_{ex}. \tag{2.61}$$

Therefore the susceptibility can be solved as

$$\chi = \frac{Ne^2}{\varepsilon_0 m} \frac{1}{(\omega^2 - \omega_0^2 - i\omega\gamma)}. \tag{2.62}$$

In Chapter 3, we will see the Eq.(2.62) is actually the first order of susceptibility. Higher orders of nonlinear susceptibilities can be derived in the formalism of the quantum density matrix. The term

$$\omega_p = \sqrt{\frac{Ne^2}{\varepsilon_0 m}} \tag{2.63}$$

is defined as the plasmon frequency. This is the bulk plasmon frequency. Typically, for metals, the plasmon frequency is in the UV light frequency range (Table 2.1)[2].

For metals, the plasmon frequency plays an important role in terms of optical properties. When the light frequency is lower than the plasmon frequency, the electrons can respond fast

[2]The information for this table is from www.wave-scattering.com.

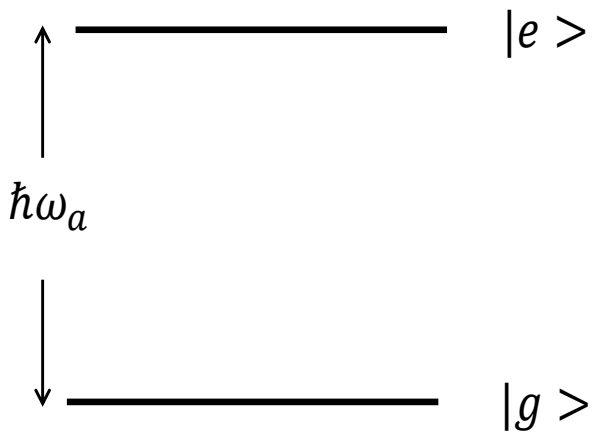

Figure 2.1: The eigenstates of a bipartite system.

enough to screen the light field. Therefore, the light is reflected. When the light frequency is higher than the plasmon frequency, the electrons cannot screen the field, and the light is transmitted. In Chapter 8, we will discuss another important plasmonic effect happening at the interface between metals and dielectrics, which is said to be the surface plasmon polariton (SPP). SPP has different characteristics than the bulk plasmons.

Let's consider a bipartite system that has only only two energy levels (Figure 2.1), ground state $|g>$ and one excited state $|e>$. They form a complete basis

$$< g|g >=< e|e >= 1, \tag{2.64}$$

$$< g|e >=< e|g >= 0, \tag{2.65}$$

$$|g >< g| + |e >< e| = I, \tag{2.66}$$

where I is the identical operator. We also assume that they both have definite parities (either symmetry or antisymmetry). The Hamiltonian for two-level system is defined in such a way that

$$\hat{H}_A|g> = -\frac{1}{2}\hbar\omega_a|g>, \tag{2.67}$$

$$\hat{H}_A|e> = \frac{1}{2}\hbar\omega_a|e>, \tag{2.68}$$

where ω_a is the resonant frequency and $\hbar\omega_a$ is the energy gap. The Hamiltonian is then

$$\hat{H}_A = \frac{1}{2}\hbar\omega_a(|e><e| - |g><g|). \tag{2.69}$$

Similar to the case of the electromagnetic field in which $\hat{a}$ or $\hat{a}^\dagger$ annihilates or creates a photon, here we can introduce operators, in the Schrödinger picture, to lower or raise the energy level [33]:

$$\hat{b}|g> = 0, \tag{2.70}$$

$$\hat{b}|e> = |g>, \tag{2.71}$$

$$\hat{b}^\dagger|g> = |e>, \tag{2.72}$$

$$\hat{b}^\dagger|e> = 0. \tag{2.73}$$

Based on the definition, we can find

$$\hat{b}^\dagger\hat{b}|g> = 0, \tag{2.74}$$

$$\hat{b}^\dagger\hat{b}|e> = |e>, \tag{2.75}$$

$$\hat{b}\hat{b}^\dagger|g> = |g>, \tag{2.76}$$

$$\hat{b}\hat{b}^\dagger|e> = 0. \tag{2.77}$$

Therefore we obtain the relations

$$\hat{b} = |g><e|, \tag{2.78}$$

$$\hat{b}^\dagger = |e><g|, \tag{2.79}$$

$$\hat{b}^\dagger\hat{b} = |e><e|, \tag{2.80}$$

$$\hat{b}\hat{b}^\dagger = |g><g|. \tag{2.81}$$

Eq.(2.69) becomes

$$\hat{H}_A = \frac{1}{2}\hbar\omega_a(\hat{b}^\dagger\hat{b} - \hat{b}\hat{b}^\dagger) \equiv \hbar\omega_a\sigma_z. \tag{2.82}$$

The commutation relations can be found

$$[\hat{\sigma}_z, \hat{b}] = \frac{1}{2}[(|e><e| - |g><g|), |g><e|] = -|g><e| = -\hat{b}. \tag{2.83}$$

and

$$[\hat{\sigma}_z, \hat{b}^\dagger] = \frac{1}{2}[(|e><e| - |g><g|), |e><g|] = |e><g| = \hat{b}^\dagger. \tag{2.84}$$

In the Heisenberg picture, $\hat{b}$ and $\hat{b}^\dagger$ will be

$$\hat{b}(t) = e^{i\omega_a\sigma_z t}\hat{b}e^{-i\omega_a\sigma_z t} = \hat{b}e^{-i\omega_a t}, \tag{2.85}$$

$$\hat{b}^\dagger(t) = e^{i\omega_a\sigma_z t}\hat{b}^\dagger e^{-i\omega_a\sigma_z t} = \hat{b}^\dagger e^{i\omega_a t}. \tag{2.86}$$

2.3 LIGHT-MATTER INTERACTION

Now we consider the interaction between light and solid state systems. For simplicity, we assume the material is nonmagnetic, which means the relative permeability $\mu_r \approx 1$. We focus on the interaction between the electric field and electrons. The total charge is $q = \int d^3r\rho(\vec{r})$.

In [32], it is shown that when a charge distribution is in an external potential $\Phi(\vec{r})$, the total energy is

$$E = q\Phi(0) - \vec{d}\cdot\vec{E} - \frac{1}{6}\sum_{ij} Q_{ij}\frac{\partial E_j}{\partial r_i}(0) + \dots. \tag{2.87}$$

If the charge is distributed over a space with dimensions much smaller than the wavelength of the electromagnetic field, then the electric field can be treated as a spatially uniform field. The field gradient approaches to zero, which results in the vanishing of the quadruple and even higher order terms. If the total charge is neutral, such as in the case of atoms, then the first term in Eq.(2.87) is zero, leaving only the dipole term present. To illustrate the dipole interaction, we can study a simple example of a two-level system that has only one electron interacting with light. Since only one electron is included, the second term in Eq.(2.87) becomes

$$V = -e\vec{r}\cdot\vec{E}. \tag{2.88}$$

The unperturbed Hamiltonian is

$$\hat{H}_A = \hbar\omega_a\sigma_z, \tag{2.89}$$

$$\hat{H}_L = \hbar\omega_k(\hat{a}^\dagger\hat{a} + \frac{1}{2}), \tag{2.90}$$

where ω_a is the resonant frequency and ω_k is the frequency of light. It is assumed that the states of the bipartite system have definite parities. The quantum mechanical operator of the electric dipole is

$$\begin{aligned}\hat{d} &= -e\hat{\vec{r}} = -e(|g><g| + |e><e|)\hat{\vec{r}}(|g><g| + |e><e|)\\ &= -e(\vec{r}_{ge}|g><e| + \vec{r}_{eg}|e><g|)\\ &= \vec{d}_{ge}\hat{b} + \vec{d}^*_{ge}\hat{b}^\dagger.\end{aligned} \tag{2.91}$$

Because we assume that the dimensions of the bipartite system is by far less than the wavelength, we have the following approximation:

$$e^{i\vec{k}\cdot\vec{r}} \approx 1 - i\vec{k}\cdot\vec{r} \approx 1.$$

The electric field operator then is

$$\hat{\vec{E}} = \sqrt{\frac{\hbar\omega}{2\varepsilon_0 L^3}}(\hat{a}\hat{\varepsilon} - \hat{a}^\dagger\hat{\varepsilon}^*). \tag{2.92}$$

The interaction operator becomes

$$\hat{V} = \sqrt{\frac{\hbar\omega}{2\varepsilon_0 L^3}}(\vec{d}_{ge}\hat{b} + \vec{d}^*_{ge}\hat{b}^\dagger)(\hat{a}\hat{\varepsilon} - \hat{a}^\dagger\hat{\varepsilon}^*). \tag{2.93}$$

By introducing the rotating wave approximation, $\hat{V}$ can be simplified as

$$\hat{V} = \sqrt{\frac{\hbar\omega}{2\varepsilon_0 L^3}}(\vec{d}^*_{ge}\hat{b}^\dagger\hat{a}\hat{\varepsilon} - \vec{d}_{ge}\hat{b}\hat{a}^\dagger\hat{\varepsilon}^*). \tag{2.94}$$

The physical picture of the $\hat{b}^\dagger\hat{a}$ term is that by absorbing one photon the bipartite system is promoted to excited state. On the contrary, the term $\hat{b}\hat{a}^\dagger$ means that the bipartite system decays from its excited state to ground state by emitting a photon.

By combining all the above results, one can obtain the full Hamiltonian

$$\begin{aligned}\hat{H} &= \hat{H}_L + \hat{H}_A + \hat{V} \\ &= \hbar\omega_k(\hat{a}^\dagger\hat{a} + \frac{1}{2}) + \hbar\omega_a\sigma_z \\ &+ \sqrt{\frac{\hbar\omega}{2\varepsilon_0 L^3}}(\vec{d}^*_{ge}\hat{b}^\dagger\hat{a}\hat{\varepsilon} - \vec{d}_{ge}\hat{b}\hat{a}^\dagger\hat{\varepsilon}^*).\end{aligned} \tag{2.95}$$

This Hamiltonian $\hat{H}$ is Jaynes-Cumming model[34]. Jaynes-Cumming model is of great interest in atomic physics and quantum optics, both experimentally and theoretically.

3.0 NONLINEAR OPTICAL RESPONSE

Nonlinear optical effects, resulting from the interaction between light and solid state systems, is the focus of the study of this thesis. As pointed out in Chapter 1, nonlinear responses can be described by the polarization

$$\vec{P} = \varepsilon_0(\chi^{(1)}\vec{E} + \chi^{(2)}\vec{E}\vec{E} + \chi^{(2)}\vec{E}\vec{E}\vec{E} + ...). \tag{3.1}$$

In this chapter we will review the derivation of nonlinear susceptibilities $\chi^{(n)}$. This is usually done with density matrix formulism, which describes the dynamics of an ensemble of electrons[35]. Before we begin the calculation for $\chi^{(n)}$, let's briefly review the properties of density matrix formulism.

3.1 DENSITY MATRIX

The Hamiltonian H is used for the solid state system. Its eigenstates are give by

$$\hat{H}|n>= E_n|n> . \tag{3.2}$$

Any general state can be decomposed on the basis

$$|\Phi(t)>= \sum_n C_n(t)|n> . \tag{3.3}$$

According to the theory of quantum mechanics, the probability for the system to be found in the state $|k>$ is

$$
\begin{aligned}
p_k(t) &= |< k|\Phi(t)>|^2 \\
&= \sum_{mn} C_m(t)C_n^*(t) < k|m >< n|k > \\
&=< k|\hat{\rho}|k >,
\end{aligned} \tag{3.4}
$$

where the operator

$$
\hat{\rho}(t) = \sum_{mn} C_m(t)C_n^*(t)|m >< n| \equiv \sum_{mn} \rho_{mn}(t)|m >< n| \tag{3.5}
$$

is defined as the density matrix operator. The off-diagonal elements have to do with the coupling between different states, while the diagonal coefficients $\rho_{nn}(t) = C_n(t)C_n^*(t)$ represent the probability for the system to be in the eigenstate $|n>$. Therefore the trace of the density matrix is

$$
Tr(\hat{\rho}(t)) = \sum_n \rho_{nn} = 1. \tag{3.6}
$$

The expectation value of an operator $\hat{A}$ can be found as

$$
\begin{aligned}
< \hat{A} > &=< \Phi(t)|\hat{A}|\Phi(t) > \\
&= \sum_{mn} C_m(t)C_n^*(t) < n|\hat{A}|m > \\
&= \sum_{mnl} C_m(t)C_n^*(t) < n|l >< l|\hat{A}|m > \\
&= \sum_{mnl} C_m(t)C_n^*(t) < l|\hat{A}|m >< n|l > \\
&= Tr(\hat{A}\hat{\rho}(t)).
\end{aligned} \tag{3.7}
$$

From the Schrödinger equation and Eq.(3.3), we can have

$$
\dot{C}_n(t) = -\frac{i}{\hbar} E_n C_n(t). \tag{3.8}
$$

The time evolution of $\hat{\rho}(t)$ is described by the Liouville equation

$$
\begin{aligned}
\frac{d}{dt}\hat{\rho}(t) &= \sum_{mn} \dot{C}_m(t)C_n^*(t)|m><n| + \sum_{mn} C_m(t)\dot{C}_n^*(t)|m><n| \\
&= -\sum_{mn} \frac{i}{\hbar} E_m C_m(t)C_n^*(t)|m><n| + \sum_{mn} C_m(t)\frac{i}{\hbar}E_n C_n^*(t)|m><n| \\
&= -\frac{i}{\hbar}(\sum_{mn} C_m(t)C_n^*(t)\hat{H}|m><n| - \sum_{mn} C_m(t)C_n^*(t)|m><n|\hat{H} \\
&= -\frac{i}{\hbar}(\hat{H}\hat{\rho}(t) - \hat{\rho}(t)\hat{H}) \\
&= -\frac{i}{\hbar}[\hat{H}, \hat{\rho}(t)]. \qquad (3.9)
\end{aligned}
$$

More generally, the equation of motion can have a phenomelogical term describing the damping effect [35, 36]

$$
\dot{\rho}_{mn}(t) = -\frac{i}{\hbar}[\hat{H}, \hat{\rho}(t)]_{mn} - \gamma_{mn}(\rho_{mn}(t) - \rho_{mn}^{eq}), \qquad (3.10)
$$

In Chapter 2, we see that the light field with a large number of photons can be treated as a classical field. The interaction between such a field and a solid state system can be described by the following potential energy

$$
\hat{V} = -e\hat{\vec{r}} \cdot \vec{E} = \sum_k \hat{\vec{d}} \cdot \vec{E}(\omega_k)e^{-i\omega_k t}. \qquad (3.11)
$$

3.2 NONLINEAR SUSCEPTIBILITY

In this section, we will describe how to derive the susceptibilities. The idea is that by using the density matrix, the polarization induced by an optical field in a material can be deduced. The nth order of polarization $P^{(n)}$ is related to the susceptibility $\chi^{(n)}$ by the equation

$$
P^{(n)} = \varepsilon_0 \chi^{(n)} E^n. \qquad (3.12)
$$

In the following discussion, Eq.(3.12) will be modified because of the tensorial nature of the susceptibilities.

3.2.1 First Order of Susceptibility

In order to calculate susceptibilities, we need to get an expression for the electric dipole moment $\vec{p} =< \hat{d} >$. The polarization is defined as

$$\vec{P} = N\vec{p}, \tag{3.13}$$

where N is the electron density. From the previous discussion, we know $< \hat{d} >= Tr(\hat{d}\hat{\rho}(t))$. Therefore we need to know the functional form of $\hat{\rho}(t)$. Let's assume that the initial condition is $\hat{\rho}(0) = \hat{\rho}^{eq}$, where

$$\rho_{nn}(0) = \rho_{nn}^{eq}, \tag{3.14}$$

$$\rho_{mn}(0) = 0(m \neq n). \tag{3.15}$$

The full Hamiltonian is $\hat{H} = \hat{H}_0 + \hat{V}$ so that the commutation relation becomes

$$\begin{aligned}
[\hat{H}, \hat{\rho}(t)]_{mn} &= [\hat{H}_0, \hat{\rho}(t)]_{mn} + [\hat{V}, \hat{\rho}(t)]_{mn} \\
&= (\hat{H}_0\rho_{mn}(t) - \rho_{mn}(t)|m >< n|\hat{H}_0) + [\hat{V}, \hat{\rho}(t)]_{mn} \\
&= (E_m - E_n)\rho_{mn}(t) + [\hat{V}, \hat{\rho}(t)]_{mn}.
\end{aligned} \tag{3.16}$$

We can define $\hbar\omega_{mn} = E_m - E_n$. Eq.(3.10) then becomes

$$\dot{\rho}_{mn}(t) = -i\omega_{mn}\rho_{mn}(t) - \frac{i}{\hbar}[\hat{V}, \hat{\rho}(t)]_{mn} - \gamma_{mn}(\rho_{mn}(t) - \rho_{mn}^{eq}). \tag{3.17}$$

In the frame of the perturbation theory, we have

$$V_{mk} \to \lambda V_{mk}, \tag{3.18}$$

$$\rho_{mn}(t) = \rho_{mn}^{(0)}(t) + \lambda\rho_{mn}^{(1)}(t) + \lambda^2\rho_{mn}^{(2)}(t) + ..., \tag{3.19}$$

where λ is the perturbation parameter which can vary from 0, meaning no perturbation, to 1, which implies full perturbation. From Eq.(3.17), Eq.(3.18) and Eq.(3.19), we can equate the terms for the same order of λ to obtain

$$\dot{\rho}^{(0)}_{mn}(t) = -i\omega_{mn}\rho^{(0)}_{mn}(t) - \gamma_{mn}(\rho^{(0)}_{mn}(t) - \rho^{eq}_{mn}), \tag{3.20}$$

$$\dot{\rho}^{(1)}_{mn}(t) = -(i\omega_{mn} + \gamma_{mn})\rho^{(1)}_{mn}(t) - \frac{i}{\hbar}[\hat{V}, \hat{\rho}^{(0)}(t)]_{mn}, \tag{3.21}$$

$$\dot{\rho}^{(2)}_{mn}(t) = -(i\omega_{mn} + \gamma_{mn})\rho^{(2)}_{mn}(t) - \frac{i}{\hbar}[\hat{V}, \hat{\rho}^{(1)}(t)]_{mn}. \tag{3.22}$$

We can assume the following steady state solution for $\rho^{(0)}_{mn}(t)$ as the initial conditions:

$$\rho^{(0)}_{nn}(t) = \rho^{(0)}_{nn}(0) = \rho^{(eq)}_{nn}, \tag{3.23}$$

$$\rho^{(0)}_{mn}(t) = 0 (m \neq n). \tag{3.24}$$

As we discussed before, all the states $|n>$ have definite parity by assumption. The expectation value of electric dipole moment induced by $\hat{\rho}^{(0)}$ is

$$\begin{aligned} Tr(\hat{\vec{d}}\hat{\rho}^{(0)}) &= \sum_{mnl} \rho^{(eq)}_{mn} < l|\vec{d}|m >< n|l > \\ &= \sum_{mn} \rho^{(eq)}_{mn} < n|\vec{d}|m > \\ &= \sum_{n} \rho^{(eq)}_{nn} < n|\vec{d}|n > \\ &= 0. \end{aligned} \tag{3.25}$$

This result is not surprising because in the equilibrium state, the electric dipole should be randomly oriented and the ensemble average goes to zero.

The solution for a higher order $\rho^{(n)}_{mn}(t)$ is given by [35]

$$\rho^{(n)}_{mn}(t) = \int_{-\infty}^{t} -\frac{i}{\hbar}[\hat{V}, \hat{\rho}^{(n-1)}(t')]_{mn} e^{-(i\omega_{mn}+\gamma_{mn})(t-t')} dt'. \tag{3.26}$$

For the first order $\rho^{(1)}_{mn}(t)$, we have

$$\begin{aligned}
\rho^{(1)}_{mn}(t) &= -\int_{-\infty}^{t} \frac{i}{\hbar}[\hat{V}, \hat{\rho}^{(0)}(t')]_{mn} e^{-(i\omega_{mn}+\gamma_{mn})(t-t')} dt' \\
&= -\frac{i}{\hbar} e^{-(i\omega_{mn}+\gamma_{mn})t} \int_{-\infty}^{t} \sum_{l} (\hat{V}_{ml}\rho^{(eq)}_{ln} - \rho^{(eq)}_{ml}\hat{V}_{ln}) e^{(i\omega_{mn}+\gamma_{mn})t'} dt' \\
&= -\frac{i}{\hbar} e^{-(i\omega_{mn}+\gamma_{mn})t} (\rho^{(eq)}_{nn} - \rho^{(eq)}_{mm}) \int_{-\infty}^{t} \hat{V}_{mn} e^{(i\omega_{mn}+\gamma_{mn})t'} dt' \\
&= -\frac{i}{\hbar} e^{-(i\omega_{mn}+\gamma_{mn})t} (\rho^{(eq)}_{nn} - \rho^{(eq)}_{mm}) \sum_{k} \hat{\vec{d}}_{mn} \cdot \vec{E}(\omega_k) \int_{-\infty}^{t} e^{(i(\omega_{mn}-\omega_k)+\gamma_{mn})t'} dt' \\
&= \frac{1}{\hbar} (\rho^{(eq)}_{mm} - \rho^{(eq)}_{nn}) \sum_{k} \frac{\hat{\vec{d}}_{mn} \cdot \vec{E}(\omega_k)}{(\omega_{mn} - \omega_k) - i\gamma_{mn}} e^{-i\omega_k t}.
\end{aligned} \tag{3.27}$$

The electric dipole moment caused by $\hat{\rho}^{(1)}$ is

$$\begin{aligned}
Tr(\hat{\vec{d}}\hat{\rho}^{(1)}) &= \sum_{mnl} \rho^{(1)}_{mn} < l|\vec{d}|m >< n|l > \\
&= \sum_{mn} \rho^{(1)}_{mn} \vec{d}_{nm} \\
&= \sum_{mn} \frac{1}{\hbar} (\rho^{(eq)}_{mm} - \rho^{(eq)}_{nn}) \sum_{k} \frac{\vec{d}_{nm}\vec{d}_{mn} \cdot \vec{E}(\omega_k)}{(\omega_{mn} - \omega_k) - i\gamma_{mn}} e^{-i\omega_k t}.
\end{aligned} \tag{3.28}$$

According to Eq.(3.13), the polarization caused by $\hat{\rho}^{(1)}$ is

$$P^{(1)} = N \sum_{mn} \frac{1}{\hbar} (\rho^{(eq)}_{mm} - \rho^{(eq)}_{nn}) \sum_{k} \frac{\hat{\vec{d}}_{nm}\hat{\vec{d}}_{mn} \cdot \vec{E}(\omega_k)}{(\omega_{mn} - \omega_k) - i\gamma_{mn}} e^{-i\omega_k t}. \tag{3.29}$$

From Eq.(3.1), we also have

$$P^{(1)} = \varepsilon_0 \chi^1 \sum_{k} \vec{E}(\omega_k) e^{-i\omega_k t}. \tag{3.30}$$

Hence the first order susceptibility $\chi^{(1)}$ is

$$\chi^{(1)}(\omega_k) = \frac{N}{\varepsilon_0 \hbar} \sum_{mn} (\rho^{(eq)}_{mm} - \rho^{(eq)}_{nn}) \frac{\hat{\vec{d}}_{nm}\hat{\vec{d}}_{mn}}{(\omega_{mn} - \omega_k) - i\gamma_{mn}}. \tag{3.31}$$

It is not difficult to see the tensorial nature of the susceptibility. It is conventional to express the susceptibility tensor in terms of its components

$$\chi^{(1)}_{ij}(\omega_k) = \frac{N}{\varepsilon_0 \hbar} \sum_{mn} (\rho^{(eq)}_{mm} - \rho^{(eq)}_{nn}) \frac{\hat{d^i}_{nm} \hat{d^j}_{mn}}{(\omega_{mn} - \omega_k) - i\gamma_{mn}}. \tag{3.32}$$

3.2.2 Second Order of Susceptibility

Once we have the first order susceptibility Eq.(3.32), we can calculate the second order susceptibility $\chi^{(2)}$. From Eq.(3.26), we have

$$\begin{aligned}
\rho^{(2)}_{mn}(t) &= \int_{\infty}^{t} -\frac{i}{\hbar} [\hat{V}, \hat{\rho}^{(1)}(t')]_{mn} e^{-(i\omega_{mn} + \gamma_{mn})(t-t')} dt' \\
&= e^{-(i\omega_{mn} + \gamma_{mn})t} \int_{\infty}^{t} -\frac{i}{\hbar} \sum_{l} (\hat{V}_{ml} \rho^{(1)}_{ln}(t') - \rho^{(1)}_{ml}(t') \hat{V}_{ln}) e^{(i\omega_{mn} + \gamma_{mn})t'} dt' \\
&= e^{-(i\omega_{mn} + \gamma_{mn})t} \\
&\int_{\infty}^{t} -\frac{i}{\hbar} \sum_{lp} (\hat{\vec{d}}_{ml} \rho^{(1)}_{ln}(t') - \rho^{(1)}_{ml}(t') \hat{\vec{d}}_{ln}) \cdot \vec{E}(\omega_p) e^{(i(\omega_{mn} - \omega_p) + \gamma_{mn})t'} dt'.
\end{aligned} \tag{3.33}$$

From Eq.(3.27), the commutation relation is

$$\hat{\vec{d}}_{ml} \rho^{(1)}_{ln}(t') = \frac{1}{\hbar} (\rho^{(eq)}_{ll} - \rho^{(eq)}_{nn}) \sum_{k} \frac{\hat{\vec{d}}_{ml} \hat{\vec{d}}_{ln} \cdot \vec{E}(\omega_k)}{(\omega_{ln} - \omega_k) - i\gamma_{ln}} e^{-i\omega_k t'}, \tag{3.34}$$

$$\rho^{(1)}_{ml}(t') \hat{\vec{d}}_{ln} = \frac{1}{\hbar} (\rho^{(eq)}_{mm} - \rho^{(eq)}_{ll}) \sum_{k} \frac{\hat{\vec{d}}_{ml} \cdot \vec{E}(\omega_k) \hat{\vec{d}}_{ln}}{(\omega_{ml} - \omega_k) - i\gamma_{ml}} e^{-i\omega_k t'}. \tag{3.35}$$

The integral can be calculated to obtain

$$\begin{aligned}
\rho^{(2)}_{mn}(t) = &\sum_{lpk} e^{-i(\omega_p + \omega_k)t} \\
&\{ \frac{\rho^{(eq)}_{nn} - \rho^{(eq)}_{ll}}{\hbar^2} \frac{[\hat{\vec{d}}_{ml} \cdot \vec{E}(\omega_p)][\hat{\vec{d}}_{ln} \cdot \vec{E}(\omega_k)]}{[(\omega_{mn} - \omega_p - \omega_k) - i\gamma_{ln}][(\omega_{ln} - \omega_k) - i\gamma_{ln}]} \\
&- \frac{\rho^{(eq)}_{ll} - \rho^{(eq)}_{mm}}{\hbar^2} \frac{[\hat{\vec{d}}_{ml} \cdot \vec{E}(\omega_k)][\hat{\vec{d}}_{ln} \cdot \vec{E}(\omega_p)]}{[(\omega_{mn} - \omega_p - \omega_k) - i\gamma_{ml}][(\omega_{ml} - \omega_k) - i\gamma_{ml}]} \}
\end{aligned} \tag{3.36}$$

The electric dipole moment caused by $\rho^{(2)}_{mn}(t)$ is

$$
\begin{aligned}
Tr(\hat{\vec{d}}\hat{\rho}^{(2)}) &= \sum_{mnl} \rho^{(2)}_{mn} < l|\vec{d}|m >< n|l > \\
&= \sum_{mn} \rho^{(2)}_{mn} \vec{d}_{nm} \\
&= \sum_{mn} \sum_{lpk} e^{-i(\omega_p+\omega_k)t} \\
&\{\frac{\rho^{(eq)}_{nn} - \rho^{(eq)}_{ll}}{\hbar^2} \frac{\vec{d}_{nm}[\hat{\vec{d}}_{ml} \cdot \vec{E}(\omega_p)][\hat{\vec{d}}_{ln} \cdot \vec{E}(\omega_k)]}{[(\omega_{mn} - \omega_p - \omega_k) - i\gamma_{ln}][(\omega_{ln} - \omega_k) - i\gamma_{ln}]} \\
&- \frac{\rho^{(eq)}_{ll} - \rho^{(eq)}_{mm}}{\hbar^2} \frac{\vec{d}_{nm}[\hat{\vec{d}}_{ml} \cdot \vec{E}(\omega_k)][\hat{\vec{d}}_{ln} \cdot \vec{E}(\omega_p)]}{[(\omega_{mn} - \omega_p - \omega_k) - i\gamma_{ml}][(\omega_{ml} - \omega_k) - i\gamma_{ml}]}\}. \qquad (3.37)
\end{aligned}
$$

The spectrum of the dipole moments is

$$
< \hat{\vec{d}} >= \sum_r < \hat{\vec{d}}(\omega_r) > e^{-i\omega_r t}, \qquad (3.38)
$$

Where $\omega_r = \omega_p + \omega_k$. The tensor $\chi^{(2)}(\omega_p + \omega_k, \omega_p, \omega_k)$ is

$$
\begin{aligned}
&\chi^{(2)}_{ijk}(\omega_p + \omega_k, \omega_p, \omega_k) = \frac{N}{\varepsilon_0 \hbar^2} \sum_{mnl} \\
&\{(\rho^{(eq)}_{nn} - \rho^{(eq)}_{ll}) \frac{\hat{d^i}_{nm} \hat{d^j}_{ml} \hat{d^k}_{ln}}{[(\omega_{mn} - \omega_p - \omega_k) - i\gamma_{ln}][(\omega_{ln} - \omega_k) - i\gamma_{ln}]} \\
&- (\rho^{(eq)}_{ll} - \rho^{(eq)}_{mm}) \frac{\hat{d^i}_{nm} \hat{d^j}_{ml} \hat{d^k}_{ln}}{[(\omega_{mn} - \omega_p - \omega_k) - i\gamma_{ml}][(\omega_{ml} - \omega_k) - i\gamma_{ml}]}\}. \qquad (3.39)
\end{aligned}
$$

3.2.3 Third Order of Susceptibility

The third order susceptibility $\chi^{(3)}$ can be derived in a similar way. In order to simplify the tedious derivation, we rewrite the $\rho^{(2)}_{mn}(t)$ as

$$
\rho^{(2)}_{mn}(t) \equiv \sum_{lpk} A_{mnl}(\omega_p, \omega_k) e^{-i(\omega_p+\omega_k)t}, \qquad (3.40)
$$

where the coefficient $A_{mnl}(\omega_p, \omega_k)$ is

$$A_{mnl}(\omega_p,\omega_k)=\frac{\rho_{nn}^{(eq)}-\rho_{ll}^{(eq)}}{\hbar^2}\frac{[\hat{\vec{d}}_{ml}\cdot\vec{E}(\omega_p)][\hat{\vec{d}}_{ln}\cdot\vec{E}(\omega_k)]}{[(\omega_{mn}-\omega_p-\omega_k)-i\gamma_{ln}][(\omega_{ln}-\omega_k)-i\gamma_{ln}]}$$
$$-\frac{\rho_{ll}^{(eq)}-\rho_{mm}^{(eq)}}{\hbar^2}\frac{[\hat{\vec{d}}_{ml}\cdot\vec{E}(\omega_k)][\hat{\vec{d}}_{ln}\cdot\vec{E}(\omega_p)]}{[(\omega_{mn}-\omega_p-\omega_k)-i\gamma_{ml}][(\omega_{ml}-\omega_k)-i\gamma_{ml}]}. \tag{3.41}$$

The $\rho_{mn}^{(3)}(t)$ is

$$\begin{aligned}
\rho_{mn}^{(3)}(t)&=\int_{-\infty}^{t}-\frac{i}{\hbar}[\hat{V},\hat{\rho}^{(2)}(t')]_{mn}e^{-(i\omega_{mn}+\gamma_{mn})(t-t')}dt'\\
&=e^{-(i\omega_{mn}+\gamma_{mn})t}\int_{-\infty}^{t}-\frac{i}{\hbar}\sum_a(\hat{V}_{ma}\rho_{an}^{(2)}(t')-\rho_{ma}^{(2)}(t')\hat{V}_{an})e^{(i\omega_{mn}+\gamma_{mn})t'}dt'\\
&=e^{-(i\omega_{mn}+\gamma_{mn})t}\\
&\int_{-\infty}^{t}-\frac{i}{\hbar}\sum_{aq}(\hat{\vec{d}}_{ma}\rho_{an}^{(2)}(t')-\rho_{ma}^{(2)}(t')\hat{\vec{d}}_{an})\cdot\vec{E}(\omega_q)e^{(i(\omega_{mn}-\omega_q)+\gamma_{mn})t'}dt'\\
&=e^{-(i\omega_{mn}+\gamma_{mn})t}\\
&\int_{-\infty}^{t}-\frac{i}{\hbar}\sum_{aq}(\hat{\vec{d}}_{ma}\sum_{lpk}A_{anl}(\omega_p,\omega_k)-\sum_{lpk}A_{mal}(\omega_p,\omega_k)\hat{\vec{d}}_{an})\cdot\\
&\vec{E}(\omega_q)e^{(i(\omega_{mn}-\omega_q-\omega_p-\omega_k)+\gamma_{mn})t'}dt'\\
&=-\frac{i}{\hbar}e^{-(i\omega_{mn}+\gamma_{mn})t}\\
&\int_{-\infty}^{t}\sum_{aq}\sum_{lpk}(\hat{\vec{d}}_{ma}A_{anl}(\omega_p,\omega_k)-A_{mal}(\omega_p,\omega_k)\hat{\vec{d}}_{an})\cdot\\
&\vec{E}(\omega_q)e^{(i(\omega_{mn}-\omega_q-\omega_p-\omega_k)+\gamma_{mn})t'}dt'\\
&=\frac{1}{\hbar}\sum_{aq}\sum_{lpk}\frac{[A_{mal}(\omega_p,\omega_k)\hat{\vec{d}}_{an}-\hat{\vec{d}}_{ma}A_{anl}(\omega_p,\omega_k)]\cdot\vec{E}(\omega_q)}{(\omega_{mn}-\omega_q-\omega_p-\omega_k)-i\gamma_{mn}}e^{-i(\omega_q+\omega_p+\omega_k)t}.
\end{aligned}\tag{3.42}$$

The electric dipole moment induced by $\rho_{mn}^{(3)}(t)$ is

$$
\begin{aligned}
Tr(\hat{\vec{d}}\hat{\rho}^{(3)}) &= \sum_{mn} \rho^{(3)}_{mn}\vec{d}_{nm} \\
&= \frac{1}{\hbar}\sum_{aq}\sum_{lpk}\frac{\vec{d}_{nm}[A_{mal}(\omega_p,\omega_k)\hat{\vec{d}}_{an} - \hat{\vec{d}}_{ma}A_{anl}(\omega_p,\omega_k)]\cdot\vec{E}(\omega_q)}{(\omega_{mn}-\omega_q-\omega_p-\omega_k)-i\gamma_{mn}}e^{-i(\omega_q+\omega_p+\omega_k)t} \\
&= \frac{1}{\hbar}\sum_{aq}\sum_{lpk}[\frac{\vec{d}_{nm}A_{mal}(\omega_p,\omega_k)\hat{\vec{d}}_{an}\cdot\vec{E}(\omega_q)}{(\omega_{mn}-\omega_q-\omega_p-\omega_k)-i\gamma_{mn}} \\
&- \frac{\vec{d}_{nm}\hat{\vec{d}}_{ma}\cdot\vec{E}(\omega_q)A_{anl}(\omega_p,\omega_k)}{(\omega_{mn}-\omega_q-\omega_p-\omega_k)-i\gamma_{mn}}]e^{-i(\omega_q+\omega_p+\omega_k)t} \\
&= \frac{1}{\hbar^3}\sum_{aq}\sum_{lpk}e^{-i(\omega_q+\omega_p+\omega_k)t} \\
&[\frac{(\rho^{(eq)}_{aa}-\rho^{(eq)}_{ll})\vec{d}_{nm}[\hat{\vec{d}}_{ml}\cdot\vec{E}(\omega_p)][\hat{\vec{d}}_{la}\cdot\vec{E}(\omega_k)][\hat{\vec{d}}_{an}\cdot\vec{E}(\omega_q)]}{[(\omega_{mn}-\omega_q-\omega_p-\omega_k)-i\gamma_{mn}][(\omega_{ma}-\omega_p-\omega_k)-i\gamma_{la}][(\omega_{la}-\omega_k)-i\gamma_{la}]} \\
&- \frac{(\rho^{(eq)}_{ll}-\rho^{(eq)}_{mm})\vec{d}_{nm}[\hat{\vec{d}}_{ml}\cdot\vec{E}(\omega_p)][\hat{\vec{d}}_{la}\cdot\vec{E}(\omega_k)][\hat{\vec{d}}_{an}\cdot\vec{E}(\omega_q)]}{[(\omega_{mn}-\omega_q-\omega_p-\omega_k)-i\gamma_{mn}][(\omega_{ma}-\omega_p-\omega_k)-i\gamma_{ml}][(\omega_{ml}-\omega_k)-i\gamma_{ml}]} \\
&- \frac{(\rho^{(eq)}_{nn}-\rho^{(eq)}_{ll})\vec{d}_{nm}[\hat{\vec{d}}_{al}\cdot\vec{E}(\omega_p)][\hat{\vec{d}}_{ln}\cdot\vec{E}(\omega_k)][\hat{\vec{d}}_{ma}\cdot\vec{E}(\omega_q)]}{[(\omega_{mn}-\omega_q-\omega_p-\omega_k)-i\gamma_{mn}][(\omega_{an}-\omega_p-\omega_k)-i\gamma_{ln}][(\omega_{la}-\omega_k)-i\gamma_{ln}]} \\
&+ \frac{(\rho^{(eq)}_{ll}-\rho^{(eq)}_{aa})\vec{d}_{nm}[\hat{\vec{d}}_{al}\cdot\vec{E}(\omega_p)][\hat{\vec{d}}_{ln}\cdot\vec{E}(\omega_k)][\hat{\vec{d}}_{ma}\cdot\vec{E}(\omega_q)]}{[(\omega_{mn}-\omega_q-\omega_p-\omega_k)-i\gamma_{mn}][(\omega_{an}-\omega_p-\omega_k)-i\gamma_{an}][(\omega_{al}-\omega_k)-i\gamma_{an}]}]
\end{aligned}
$$

. (3.43)

From Eq.(3.38), where $\omega_r = \omega_q + \omega_p + \omega_k$, the tensor $\chi^{(3)}(\omega_q+\omega_p+\omega_k,\omega_q,\omega_p,\omega_k)$ is

$$\chi^{(3)}_{ijkl}(\omega_q+\omega_p+\omega_k,\omega_q,\omega_p,\omega_k)=\frac{N}{\varepsilon_0\hbar^3}\sum_{aq}\sum_{lpk}$$
$$\Big[\frac{(\rho^{(eq)}_{aa}-\rho^{(eq)}_{ll})\hat{d}^i{}_{nm}\hat{d}^j{}_{ml}\hat{d}^k{}_{la}\hat{d}^l{}_{an}}{[(\omega_{mn}-\omega_q-\omega_p-\omega_k)-i\gamma_{mn}][(\omega_{ma}-\omega_p-\omega_k)-i\gamma_{la}][(\omega_{la}-\omega_k)-i\gamma_{la}]}$$
$$-\frac{(\rho^{(eq)}_{ll}-\rho^{(eq)}_{mm})\hat{d}^i{}_{nm}\hat{d}^j{}_{ml}\hat{d}^k{}_{la}\hat{d}^l{}_{an}}{[(\omega_{mn}-\omega_q-\omega_p-\omega_k)-i\gamma_{mn}][(\omega_{ma}-\omega_p-\omega_k)-i\gamma_{ml}][(\omega_{ml}-\omega_k)-i\gamma_{ml}]}$$
$$-\frac{(\rho^{(eq)}_{nn}-\rho^{(eq)}_{ll})\hat{d}^i{}_{nm}\hat{d}^j{}_{al}\hat{d}^k{}_{la}\hat{d}^l{}_{an}}{[(\omega_{mn}-\omega_q-\omega_p-\omega_k)-i\gamma_{mn}][(\omega_{an}-\omega_p-\omega_k)-i\gamma_{ln}][(\omega_{la}-\omega_k)-i\gamma_{ln}]}$$
$$+\frac{(\rho^{(eq)}_{ll}-\rho^{(eq)}_{aa})\hat{d}^i{}_{nm}\hat{d}^j{}_{al}\hat{d}^k{}_{la}\hat{d}^l{}_{an}}{[(\omega_{mn}-\omega_q-\omega_p-\omega_k)-i\gamma_{mn}][(\omega_{an}-\omega_p-\omega_k)-i\gamma_{an}][(\omega_{al}-\omega_k)-i\gamma_{an}]}\Big]$$
. (3.44)

Even higher order susceptibilities can be derived by repeating this procedure until the nth order. However, the algebra will become more and more complicated, and since we are mainly interested in the second and third order nonlinearities, we will only present the formula up to $n=3$ in this thesis.

3.2.4 Origin of Nonlinear Response

The optical nonlinearities we have discussed so far have electronic origin. The motion of electrons is described by various dipole moments $\hat{d}_{nm}$ which are included in the susceptibilities. The unperturbed dipole moment, given by Eq.(3.28), has the same spectrum as the input electromagnetic field. This describes the coherent response of electrons. If the optical field is harmonic, the trajectories of the coherently driven electrons can be classically thought as perfect circles like in Figure 3.1(a). When the perturbation is included, higher order dipole moments, for example the ones given by Eq.(3.37) and (Eq.(3.43)), show spectral contents that are absent in the spectra of the incident fields. This describes the incoherent response of electrons, which can be thought as jitters occurring on top of the harmonic motion(Figure 3.1(b)). Since the trajectories now are generally an anharmonic function of time, their spectra can contain frequencies that are not present in the incident electromagnetic field.

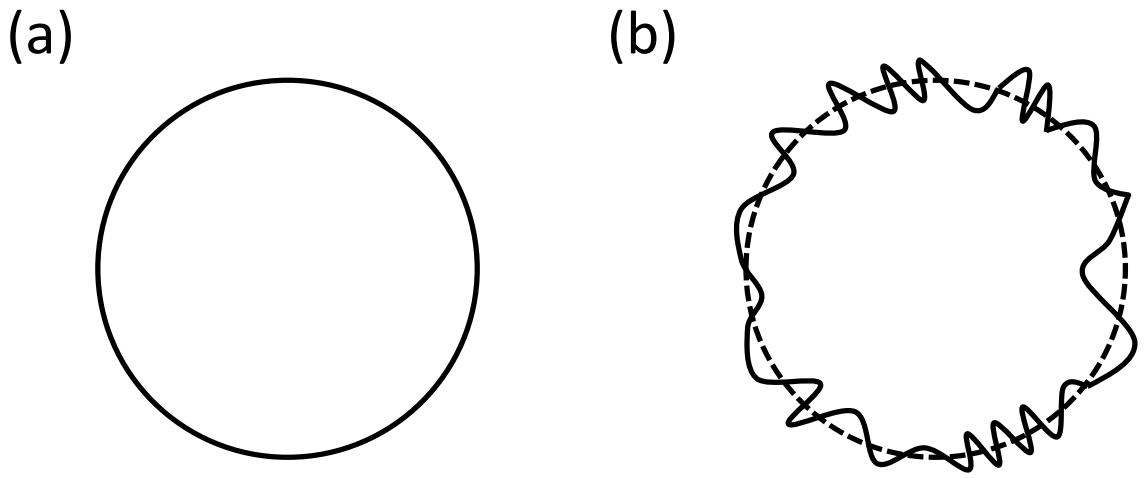

Figure 3.1: (a), The trajectory of the harmonic motion of electrons without perturbation in real space. (b), The trajectory of the motion of electrons under perturbation.

Now we see that the motion of electrons can have a variety of frequencies that are not necessary to be the same as the ones in the input optical field. It is usually true that not every frequency can be emitted. For a certain frequency to be emitted as a field, the oscillations of electric dipoles at that frequency have to be in-phase so that constructive interference can occur. This is said to be the phase matching condition.

3.3 PROPERTIES OF SUSCEPTIBILITIES

To complete the study, here we summarize the properties that the nonlinear susceptibilities have.

3.3.1 Complex Conjugation

Recall that the energy difference $\hbar\omega_{mn} = E_m - E_n$. If the two indices are exchanged, then $\omega_{nm} = -\omega_{mn}$. For the electric dipole operator, there is

$$\hat{\vec{d}}_{mn} =< m|\hat{\vec{d}}|n >= (< n|\hat{\vec{d}}|m >)^* = \hat{\vec{d}}^*_{nm}$$

Because γ_{mn} is the damping rate, describing the decoherence between states $|m>$ and $|n>$, it is usually assumed to be real and symmetric about the indices $\gamma_{mn} = \gamma_{nm}$[36, 35]. Now if we take the complex conjugate of $\chi^{(1)}$, it will be

$$\begin{aligned}
\chi^{(1)}_{ij}(\omega_k)^* &= \frac{N}{\varepsilon_0\hbar}\sum_{mn}(\rho^{(eq)}_{mm} - \rho^{(eq)}_{nn})\frac{\hat{d^i}^*_{nm}\hat{d^j}^*_{mn}}{(\omega_{mn} - \omega_k) + i\gamma_{mn}} \\
&= \frac{N}{\varepsilon_0\hbar}\sum_{mn}(\rho^{(eq)}_{mm} - \rho^{(eq)}_{nn})\frac{\hat{d^i}_{mn}\hat{d^j}_{nm}}{(-\omega_{nm} - \omega_k) + i\gamma_{mn}} \\
&= \frac{N}{\varepsilon_0\hbar}\sum_{mn}(\rho^{(eq)}_{nn} - \rho^{(eq)}_{mm})\frac{\hat{d^i}_{mn}\hat{d^j}_{nm}}{(\omega_{nm} + \omega_k) - i\gamma_{nm}} \\
&= \chi^{(1)}(-\omega_k).
\end{aligned} \tag{3.45}$$

According to Eq.(3.39) and Eq.(3.44), we have similar results for $\chi^{(2)}$ and $\chi^{(3)}$:

$$\begin{aligned}
\chi^{(2)}(\omega_p + \omega_k, \omega_p, \omega_k)^* &= \chi^{(2)}(-\omega_p - \omega_k, -\omega_p, -\omega_k) \\
\chi^{(3)}(\omega_q + \omega_p + \omega_k, \omega_q, \omega_p, \omega_k)^* &= \chi^{(3)}(-\omega_q - \omega_p - \omega_k, -\omega_q, -\omega_p, -\omega_k).
\end{aligned} \tag{3.46}$$

3.3.2 Intrinsic Symmetry

The nonlinear polarization due to the tensor $\chi^{(2)}_{ijk}$ is

$$P_i(\omega_p + \omega_k) = \chi^{(2)}_{ijk}(\omega_p + \omega_k, \omega_p, \omega_k)E_j(\omega_p)E_k(\omega_k). \tag{3.47}$$

During the nonlinear process, physically it should not matter which of the fields, $\vec{E}(\omega_p)$ and $\vec{E}(\omega_k)$, comes in first. There is no reason for the medium to favor one field over the other. Mathematically this physical picture means that if two frequency components ω_p and ω_k are interchanged, the value of $\chi^{(2)}$ does not change as long as, when the frequencies are interchanged, the corresponding indices for electric field are interchanged accordingly.

$$\chi^{(2)}_{ijk}(\omega_p + \omega_k, \omega_p, \omega_k) = \chi^{(2)}_{ikj}(\omega_p + \omega_k, \omega_k, \omega_p). \tag{3.48}$$

The valid of this identity has been rigorously proved and generalized for high orders of susceptibilities in Ref. [35].

3.3.3 Lossless Medium and Kleinman Symmetry

As we pointed out in the Introduction chapter, if the medium has certain loss, the refractive index will be a complex function, of which the imaginary part describes the absorption. In density matrix formulsim, the dissipation is given by the γ term in Eq.(3.10). If the dissipation in the medium can be ignored somehow (for example, the frequency of incident photons are far away from the lowest resonant frequency), then the coefficient γ approaches to zero [35]. It is obvious that from Eq.(3.32), the tensor $\chi^{(1)}$ is real. This is true for $\chi^{(2)}$ and $\chi^{(3)}$ too by examining Eq.(3.39) and Eq.(3.44).

If all frequencies are far away from resonance, then the mix of frequencies by susceptibility tensors should be reversible, which means all the frequency components can be freely interchanged as long as the indices are interchanged accordingly. Let's take $\chi^{(2)}_{ijk}(\omega_p + \omega_k, \omega_p, \omega_k)$ as an example. Conventionally, the first argument in the tensor always is the sum of all the remaining arguments. When the frequencies are exchanged, we should keep track of the sign in front of each frequency:

$$\chi^{(2)}_{ijk}(\omega_p + \omega_k, \omega_p, \omega_k) = \chi^{(2)}_{kij}(-\omega_k, -\omega_p - \omega_k, \omega_p). \tag{3.49}$$

However, we already know $\chi^{(2)}_{kij}(-\omega_k, -\omega_p - \omega_k, \omega_p) = \chi^{(2)*}_{kij}(\omega_k, \omega_p + \omega_k, -\omega_p)$. But since the medium is lossless, the tensor should be real. We can have

$$\chi^{(2)}_{ijk}(\omega_p + \omega_k, \omega_p, \omega_k) = \chi^{(2)}_{kij}(\omega_k, \omega_p + \omega_k, -\omega_p). \tag{3.50}$$

When the frequency of incident photons is far away from resonance in the medium, the medium is dissipationless and the tensor is independent of the frequency, meaning we can interchange the indices freely without interchanging the order of frequencies in the argument list.

3.3.4 Spatial Symmetry

The spatial symmetry that the materials have can put constraints on the susceptibility tensors. In terms of crystals, there are seven crystal classes. The spatial symmetries for the crystal classes and for isotropic materials are summarized in Table 3.1

The isotropic materials and cubic crystals have the highest symmetry: The $\chi^{(1)}$ tensor is diagonal and all nonzero elements are the same. They do not exhibit the property of birefringence. All other crystal classes are anisotropic and consequently display the property of birefringence. Tetragonal, trigonal, and hexagonal crystals are said to be uniaxial crystals since there is only one particular direction (the z axis) for which the linear optical properties show rotational symmetry. Crystals of the triclinic, monoclinic, and orthorhombic systems are biaxial. Because of their complex structures, the $\chi^{(2)}$ and $\chi^{(3)}$ tensor for different crystal systems will not be included in this thesis, but can be found in Ref.[35]. Note that one important difference between $\chi^{(2)}$ and $\chi^{(3)}$ process is that every kind of crystal has nonvanishing $\chi^{(3)}$ tensor, but only the materials that is non-centrosymmetric have nonzero $\chi^{(2)}$ coefficient. Materials that have inversion symmetry has no $\chi^{(2)}$ term.

3.4 EXAMPLES OF NONLINEAR PROCESSES

3.4.1 Second Order Nonlinear Process

Second order nonlinear process results from $\chi^{(2)}$ term. Two electric fields are involved in this process.

3.4.1.1 Pockels Effect The Pockels effect is an electro-optical effect, which includes one static field and one optical field:

$$P_i(\omega) = \varepsilon_0 \chi^{(2)}_{ijk}(\omega, 0, \omega) E_j(0) E_k(\omega), \tag{3.51}$$

where $E_j(0)$ is the static field which, for example, can be an external DC voltage applied to the material. The generated polarization has the same frequency as the optical field. When

Crystal System	$\chi^{(1)}$
Cubic, Isotropic	$\begin{pmatrix} xx & 0 & 0 \\ 0 & xx & 0 \\ 0 & 0 & xx \end{pmatrix}$
Tetragonal, Trigonal, Hexagonal	$\begin{pmatrix} xx & 0 & 0 \\ 0 & xx & 0 \\ 0 & 0 & zz \end{pmatrix}$
Orthorhombic	$\begin{pmatrix} xx & 0 & 0 \\ 0 & yy & 0 \\ 0 & 0 & zz \end{pmatrix}$
Monoclinic	$\begin{pmatrix} xx & 0 & xz \\ 0 & yy & 0 \\ zx & 0 & zz \end{pmatrix}$
Triclinic	$\begin{pmatrix} xx & xy & xz \\ yx & yy & yz \\ zx & zy & zz \end{pmatrix}$

Table 3.1: Form of the linear susceptibility tensor $\chi^{(1)}$ as determined by the symmetry properties of the optical medium, for each of the seven crystal classes and for isotropic materials. The nonvanishing elements are denoted by their cartesian indices [35].

the Pockels effect is included, the polarization is

$$\begin{aligned} P_i &= \varepsilon_0(\chi_{ik}^{(1)} + \chi_{ijk}^{(2)} E_j(0))E_k \\ &= \varepsilon_0 \chi_{eff} E_k, \end{aligned} \tag{3.52}$$

where the effective susceptibility is

$$\chi_{eff} = \chi^{(1)} + \chi^{(2)} E(0).$$

We can make use of the Pockels effect to construct an electro-optical modulator which is also called a Pockels cell. The polarization is dependent on the electric field

$$\vec{P} = \varepsilon_0 \chi_{eff} \vec{E}$$

The wave equation Eq.(1.8) can be

$$\nabla^2 \vec{E} = \varepsilon_r \frac{1}{c^2} \frac{\partial^2}{\partial t^2} \vec{E}, \tag{3.53}$$

where $\varepsilon_r = 1 + \chi_{eff}$. Due to the tensor nature of χ_{eff}, the relative permittivity is generally a tensor. By assuming that the optical field is a plane wave, one has

$$\vec{k} \times \vec{k} \times \vec{E} + \varepsilon_r \frac{\omega^2}{c^2} \vec{E} = 0. \tag{3.54}$$

or

$$\sum_{ij} ((k_i k_j - k^2 \delta_{ij}) + (\varepsilon_r)_{ij} \frac{\omega^2}{c^2}) E_j = 0. \tag{3.55}$$

In its principle coordinate system, the permittivity tensor is [35]

$$\begin{pmatrix} \varepsilon_{r1} & 0 & 0 \\ 0 & \varepsilon_{r2} & 0 \\ 0 & 0 & \varepsilon_{r3} \end{pmatrix} \tag{3.56}$$

For an uniaxial material, the permittivity tensor results in a tensor for refractive indices

$$\begin{pmatrix} n_1^2 & 0 & 0 \\ 0 & n_2^2 & 0 \\ 0 & 0 & n_3^2 \end{pmatrix} \tag{3.57}$$

where $n_1 = n_2 \neq n_3$. The special axis (n_3) is called the c-axis. One can define

$$n_1 = n_2 \equiv n_o,$$

$$n_3 \equiv n_e.$$

The quantity n_0 is said to be the ordinary refractive index while n_e is referred as the extraordinary refractive index. The appearance of two different indices of refraction is the birefringence. The Eq.(3.55) becomes

$$\begin{pmatrix} n_o^2\frac{\omega^2}{c^2} - k_2^2 - k_3^2 & k_1k_2 & k_1k_3 \\ k_2k_1 & n_o^2\frac{\omega^2}{c^2} - k_1^2 - k_3^2 & k_2k_3 \\ k_3k_1 & k_3k_2 & n_e^2\frac{\omega^2}{c^2} - k_1^2 - k_2^2 \end{pmatrix} \begin{pmatrix} E_1 \\ E_2 \\ E_3 \end{pmatrix} = 0. \tag{3.58}$$

In order to have a nonzero solution, the determinant of the matrix must be zero, which gives rise to two solutions for the wave vector

$$k^2 = n_o^2\frac{\omega^2}{c^2} \tag{3.59}$$

and

$$\frac{k_1^2}{n_0^2} + \frac{k_2^2}{n_0^2} + \frac{k_3^2}{n_e^2} = \frac{\omega^2}{c^2} \tag{3.60}$$

Because the group velocity is $v_g = \nabla_k\omega$, for the first solution, the group velocity is parallel to the wave vector $\vec{k}$. For the second solution, however, generally the group velocity is not parallel to the wave vector.

Another way to describe the birefringence is the index ellipsoid matrix, which is the inverse of the permittivity matrix, $\eta_{ij} = (\varepsilon_r)^{-1}_{ij}$.

$$d = \begin{pmatrix} \frac{1}{n_1^2} & 0 & 0 \\ 0 & \frac{1}{n_2^2} & 0 \\ 0 & 0 & \frac{1}{n_3^2} \end{pmatrix} \tag{3.61}$$

Therefore we can write

$$\vec{E} = \frac{1}{\varepsilon_0}\eta\vec{D}$$

The wave equation Eq.(3.55) becomes

$$\vec{k} \times \vec{k} \times \eta\vec{D} + \frac{\omega^2}{c^2}\vec{D} = 0. \tag{3.62}$$

The unit vector in the direction of $\vec{k}$ is defined as $\hat{k}$. Then the wave equation becomes

$$(\hat{k} \times \hat{k} \times \eta)\vec{D} = -\frac{\omega^2}{k^2c^2}\vec{D} = -\frac{1}{n^2}\vec{D}. \tag{3.63}$$

The matrix $\hat{k}\times\hat{k}\times\eta$ has its eigenvalues the inverse of refractive indices and its eigenvectors as the displacement fields. In the principle coordinates system the matrix η can be expressed by a surface

$$\frac{x_1^2}{n_0^2} + \frac{x_2^2}{n_0^2} + \frac{x_3^2}{n_e^2} = 1 \tag{3.64}$$

This surface is called index ellipsoid. However, if an external field is applied, then the refractive index will be modulated.

$$\eta_{ij} = \eta_{ij}^{(0)} + \sum_k r_{ijk}E_k + \sum_{mn} s_{ijmn}E_mE_n + \cdots \tag{3.65}$$

When the medium is lossless, the matrix η_{ij} is real and symmetric. Since the first two indices are symmetric, a reduced notation is used for r_{ijk}.

Let's consider the medium that has symmetry $\bar{4}2m(\mathrm{D}_{2d})$ for example (the material that has the symmetry of D_{2d} belongs to the tetragonal crystal system, which is uniaxial.). We

also assume that the electric field is in Z direction (Figure 3.2(a) and (b)). In this case the index ellipsoid surface is

$$\frac{x_1^2}{n_0^2} + \frac{x_2^2}{n_0^2} + \frac{x_3^2}{n_e^2} + 2r_{63}E_3x_1x_2 = 1 \tag{3.66}$$

By transforming to a new coordinate system

$$x = \frac{x_1 - x_2}{\sqrt{2}} \tag{3.67}$$

$$y = \frac{x_1 + x_2}{\sqrt{2}} \tag{3.68}$$

$$z = x_3 \tag{3.69}$$

the equation will become

$$x^2(\frac{1}{n_0^2} + r_{63}E_3) + y^2(\frac{1}{n_0^2} - r_{63}E_3) + \frac{z^2}{n_e^2} = 1 \tag{3.70}$$

where (Figure 3.2(c))

$$n_x = n_0^2 - \frac{1}{2}n_0^3r_{63}E_3 \tag{3.71}$$

$$n_y = n_0^2 + \frac{1}{2}n_0^3r_{63}E_3 \tag{3.72}$$

$$n_z = n_e. \tag{3.73}$$

In this new principle coordinate system (Figure 3.2(b)), when the optical field propagates a distance of L, the phase difference between its x and y component will be

$$\begin{aligned}\delta\phi &= \frac{2\pi}{\lambda}(n_y - n_x)L \\ &= \frac{2\pi n_0^3 r_{63}E_3L}{\lambda}\end{aligned} \tag{3.74}$$

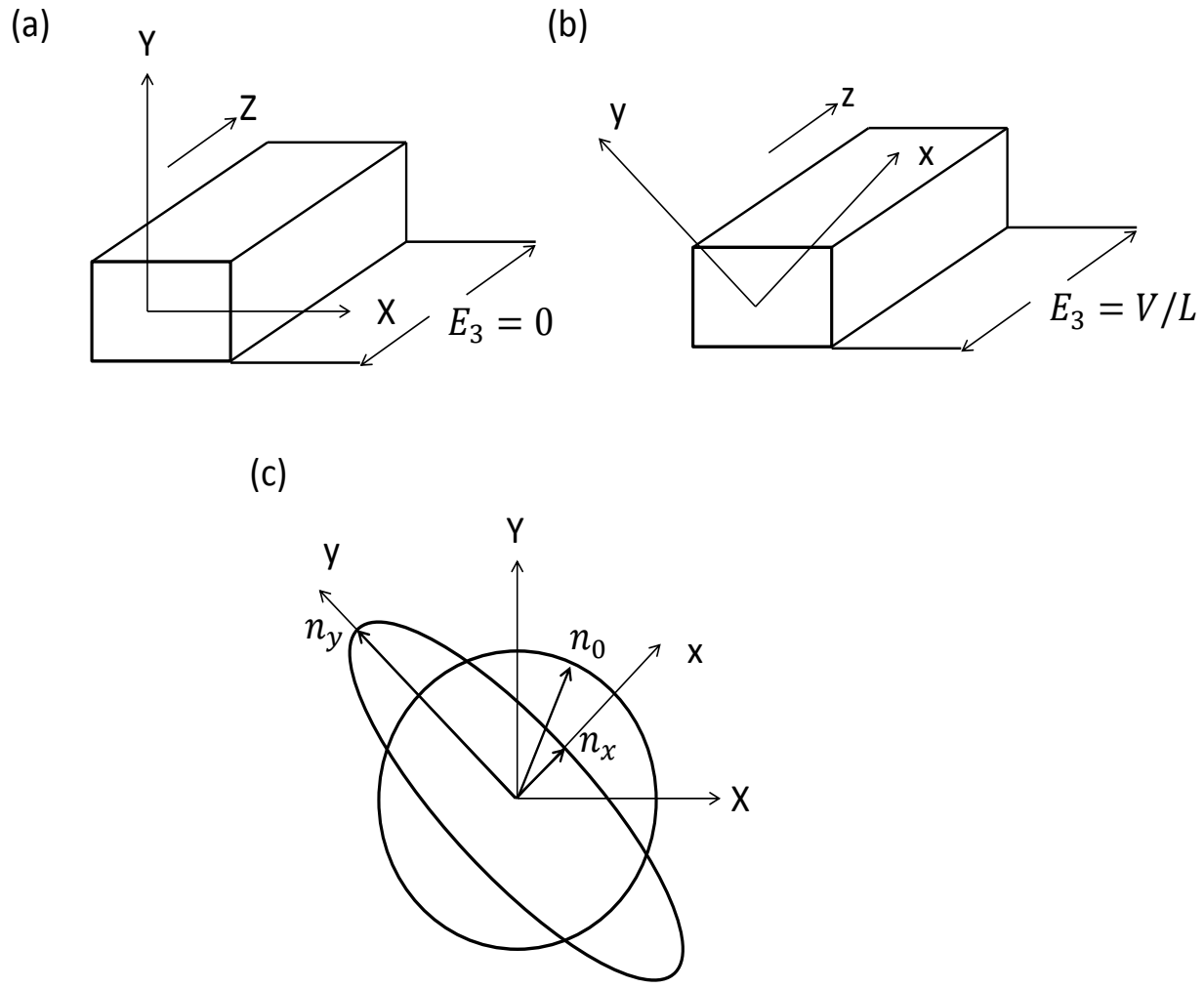

Figure 3.2: The electro-optical effect. (a) Principle axes in the absence of an applied field. (b) Principle axes in the presence of an applied field. (c) The intersection of the index ellipsoid with the plane z = Z = 0.

We also have $V = E_3 L$, which is the voltage cross the medium. Therefore the phase difference will be

$$\delta\phi = \frac{2\pi n_0^3 r_{63} V}{\lambda}. \tag{3.75}$$

It is clear that by controlling the voltage in the experiment, one can make use of the Pockels effect to realize different phases.

3.4.1.2 Second Harmonic Generation Second harmonic generation (SHG) is a nonlinear process during which two identical optical fields $E(\omega)$ are mixed by the $\chi^{(2)}$ tensor to result in a field with doubled frequency $E(2\omega)$

$$P_i(2\omega) = \varepsilon_0 \chi^{(2)}_{ijk}(2\omega, \omega, \omega) E_j(\omega) E_k(\omega), \tag{3.76}$$

During the second harmonic generation, both the energy and the momentum must be conserved. The energy is naturally conserved since $2\omega = \omega + \omega$. This condition for the conservation of momentum is usually known as phase matching. Phase matching condition can be seen from the wave equation Eq.(1.8). The polarization term on the right hand side of the equation can be separated into linear and nonlinear part, P_1 and P_{NL} respectively. The linear part is $P_1 = \varepsilon_0 \chi^{(1)} E$. The wave equation can then be rewritten as the following form:

$$(\nabla^2 - \frac{\varepsilon_r^{(1)}}{c^2}\frac{\partial^2}{\partial t^2})\vec{E}(\vec{r}, t) = \frac{1}{\varepsilon_0 c^2}\frac{\partial^2}{\partial t^2}\vec{P_{NL}}(\vec{r}, t), \tag{3.77}$$

where $\varepsilon_r^{(1)} = 1 + \chi^{(1)}$. The result of the Fourier transform of the wave equation is.

$$(\nabla^2 - \frac{\varepsilon_r^{(1)}\omega^2}{c^2})\vec{E}(\vec{r}, \omega) = -\frac{\omega^2}{\varepsilon_0 c^2}\vec{P}_{NL}(\vec{r}, \omega). \tag{3.78}$$

As usual we can represent the electric field as a plane wave

$$E_i = \tilde{E}_i(z) e^{-i\omega_i t} = A_i e^{i(k_i z - \omega_i t)},$$

where E_1 and E_2 represent the two input fields while E_3 represents the output field. The nonlinear polarization caused by the second order nonlinear process is

$$P_{NL}(\vec{r},\omega) = \tilde{P}_{NL}(\vec{r})e^{-i\omega_3 t}$$

The spatial dependence part given by

$$\tilde{P}_{NL}(\vec{r}) = \varepsilon_0\chi^{(1)}\tilde{E}_1(z)\tilde{E}_2(z) = \varepsilon_0\chi^{(1)}A_1A_2e^{i(k_1+k_2)z}$$

By plugging these quantities into the wave equation Eq.(3.78) one has

$$\frac{d^2A_3}{dz^2} + 2ik_3\frac{dA_3}{dz} = -\frac{\omega_3^2}{c^2}\chi^2A_1A_2e^{i(k_1+k_2-k_3)z}. \tag{3.79}$$

The solution to this equation has its maximum [35] when the momentum mismatching $\Delta k = k_1 + k_2 - k_3$ vanishes, which is referred to as the phase matching condition

$$k_1 + k_2 = k_3. \tag{3.80}$$

Second harmonic generation is a special case of a more general process called sum frequency generation, in which the input frequencies are ω_1 and ω_2 while the output field has frequency $\omega_3 = \omega_1 + \omega_2$. This process is given by a nonlinear polarization

$$P_i(\omega_1 + \omega_2) = \varepsilon_0\chi^{(2)}_{ijk}(\omega_1 + \omega_2, \omega_1, \omega_2)E_j(\omega_1)E_k(\omega_2). \tag{3.81}$$

Similarly we can have difference frequency generation during which a difference frequency $\omega_3 = \omega_1 - \omega_2$ is generated by a polarization

$$P_i(\omega_1 - \omega_2) = \varepsilon_0\chi^{(2)}_{ijk}(\omega_1 - \omega_2, \omega_1, \omega_2)E_j(\omega_1)E_k(\omega_2). \tag{3.82}$$

Second harmonic generation can be achieved with many nonlinear crystals such as Barium Borate BaB_2O_4 (BBO) and Potassium Titanyl Phosphate (KTP). From the phase matching condition and the definition $n_i = \varepsilon_r(\omega_i)$, we can have

$$n_1\omega_1 + n_2\omega_2 = n_3\omega_3. \tag{3.83}$$

We can assume that $\omega_1 < \omega_2 < \omega_3$. For normal dispersion, which means the refractive index increases monotonically as a function of frequency, this condition cannot be fulfilled for

	Positive Uniaxial ($n_e > n_o$)	Negative Uniaxial ($n_e < n_o$)
Type I	$n_3^o\omega_3 = n_1^e\omega_1 + n_2^e\omega_2$	$n_3^e\omega_3 = n_1^o\omega_1 + n_2^o\omega_2$
Type II	$n_3^o\omega_3 = n_1^o\omega_1 + n_2^e\omega_2$	$n_3^e\omega_3 = n_1^e\omega_1 + n_2^o\omega_2$

Table 3.2: Phase matching methods for uniaxial crystals.

certain nonlinear processes. For example, for second harmonic generation, $\omega_3 = 2\omega_1 = 2\omega_2$, then we end up with

$$n(\omega) = n(2\omega).$$

This is generally not satisfied because of the dispersion of the materials. For sum frequency generation, $\omega_3 = \omega_1 + \omega_2$, we can have

$$(n_1 - n_3)\omega_1 = (n_3 - n_2)\omega_2. \tag{3.84}$$

If the material has normal dispersion, then the left side is negative while the right side is positive.

To overcome the difficulty of matching the phase in the presence of dispersion, birefringence is usually exploited. In type I phase matching, the polarization of two input electric fields are parallel, namely they experience the same index. In type II phase matching, the polarization of two input electric fields are perpendicular, namely one of them experiences the normal index while the other experiences the extraordinary index (See Table 3.2).

3.4.1.3 Optical Parametric Amplifier Another $\chi^{(2)}$ process is the optical parametric process. The difference between a parametric and nonparametric process is that the state of the optically active medium does not change during a parametric process while it does change during a nonparametric process. Optical parametric amplification is related to the difference frequency generation: The pumping frequency ω_p is divided into two smaller frequencies ω_1

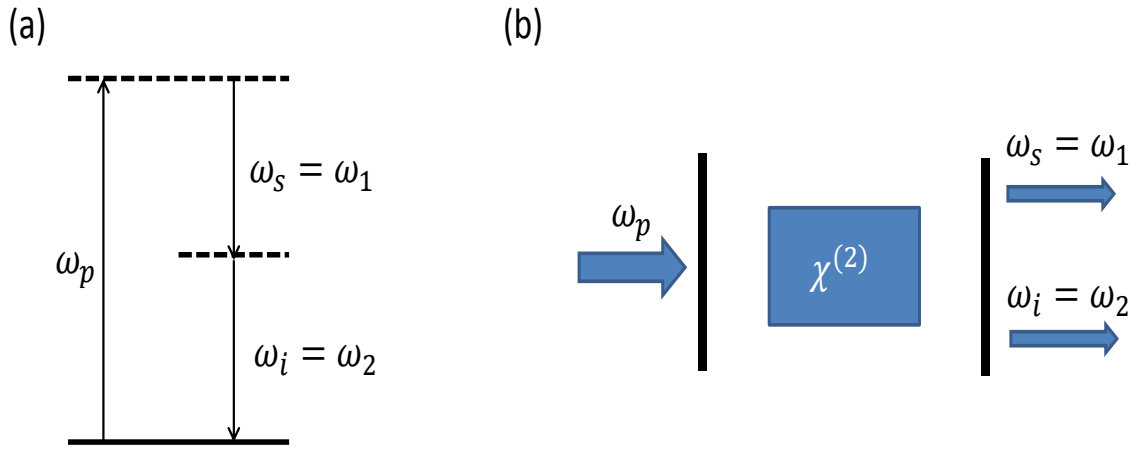

Figure 3.3: Optical parametric oscillator. (a), Band diagram for the optical parametric process. (b), The structure of the optical parametric amplifier.

(the signal frequency) and ω_2 (the idle frequency) (Figure 3.3(a)).

The cavity may be tuned to amplify one of the two frequencies, either ω_2 or ω_3, or both of them. One application example of the optical parametric amplifier is the Opal laser system in the lab, which is pumped by the output laser pulse from a Ti:sapphire laser (Tsunami) and generates two infrared photons.

3.4.2 Third Order Nonlinear Process

A third order nonlinear process results from the $\chi^{(3)}$ tensor.

3.4.2.1 Kerr Effect The Kerr effect is an electro-optical effect in which one static electric field and two optical fields are involved. Since it is proportional to the square of the optical field, it is referred as a quadratic electro-optical effect. The refractive index, including the Kerr effect, is

$$n = n_0 + n_2 I, \tag{3.85}$$

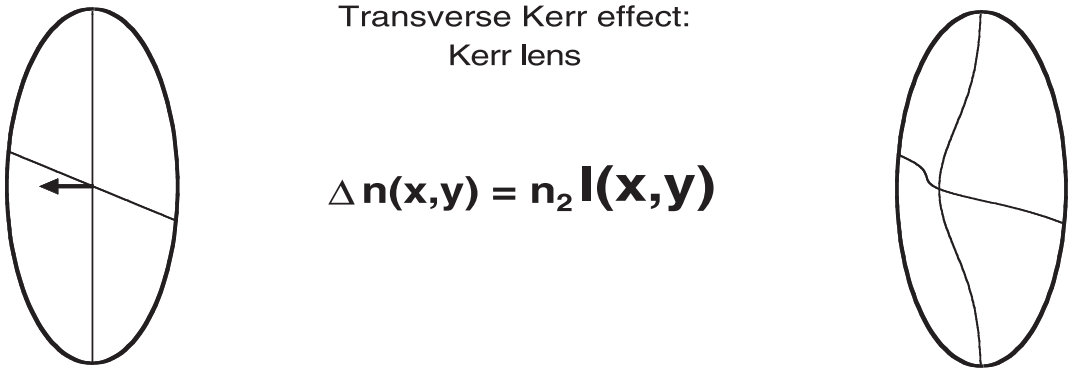

Figure 3.4: Kerr lensing effect induced by the third order nonlinearity.[38]

where I is the light intensity and the nonlinear refractive index n_2 is related to the real part of the third order susceptibility $\chi_R^{(3)}$ [37]

$$n_2 = \frac{\chi_R^{(3)}}{n_0^2 \varepsilon_0 c}. \tag{3.86}$$

If an intense beam passes through a material that has large a $\chi^{(3)}$ coefficient, and the beam intensity has a Gaussian spatial distribution, then the refractive index will be the largest at the center of the beam. The medium will effectively acts as a positive lens, which focuses the beam (Figure 3.4). This is the effect of Kerr lensing[1].

In Chapter 7, we will discuss the quadratic electro-optical effect experimentally characterized in the oxide heterostructure $LaAlO_3/SrTiO_3$.

3.4.2.2 Self Phase Modulation Self phase modulation (SPM) is a third order process that usually occurs during the interaction with intense light field such as the one induced by ultrashort laser pulses. We can use Eq.(3.85) to study the self phase modulation. Suppose the laser pulse has a Gaussian time dependence, then the intensity will be

[1]The effect described by Eq. (3.85) is also said to be the transverse Kerr effect. The self-phase modulation discussed in the following section is sometimes said to be the longitudinal Kerr effect.

$$I(t) = I_0 e^{-\frac{t^2}{\tau^2}}.$$

Then the refractive index, according to Eq.(3.85), will also be a function of time

$$n(t) = n_0 + n_2 I_0 e^{-\frac{t^2}{\tau^2}}. \tag{3.87}$$

After the beam passes through a distance L inside the medium, the phase factor becomes

$$\phi(t) = \omega_c t - \frac{2\pi}{\lambda_c} n(t) L. \tag{3.88}$$

The instantaneous frequency is

$$\begin{aligned} \dot{\phi}(t) &= \omega_c - \frac{2\pi}{\lambda_c}\dot{n}(t)L \\ &= \omega_c + (\frac{4\pi n_2 I_0 L}{\lambda_c \tau^2} e^{-\frac{t^2}{\tau^2}})t \\ &\equiv \omega_c + \alpha t, \end{aligned} \tag{3.89}$$

where the coefficient

$$\alpha = \frac{4\pi n_2 I_0 L}{\lambda_c \tau^2} e^{-\frac{t^2}{\tau^2}} \tag{3.90}$$

is called the chirp parameter.

Figure 3.5 shows that a pulse propagating through a $\chi^{(3)}$ medium undergoes a self frequency shift (the red curve in Figure 3.5) because of self-phase modulation. The front of the pulse is shifted to lower frequencies (red shift), the back to higher frequencies (blue shift). Since the frequencies in such a pulse increases in time, it is said to be the up-chirp (Figure 3.6), which corresponds to a positive chirp parameter α. When the chirp parameter is negative, it results in the case of down-chirp (Figure 3.7). By introducing new frequencies, self-phase modulation can spectrally broaden the original pulse. In Chapter 5 we will discuss how the interplay between self-phase modulation and negative group velocity dispersion (GVD) can result in the formation of an ultrashort laser pulse. In Chapter 6, supercontinuum white light source [39] used for characterizing the spectral response of the oxide nanoscale photodetector is realized by SPM.

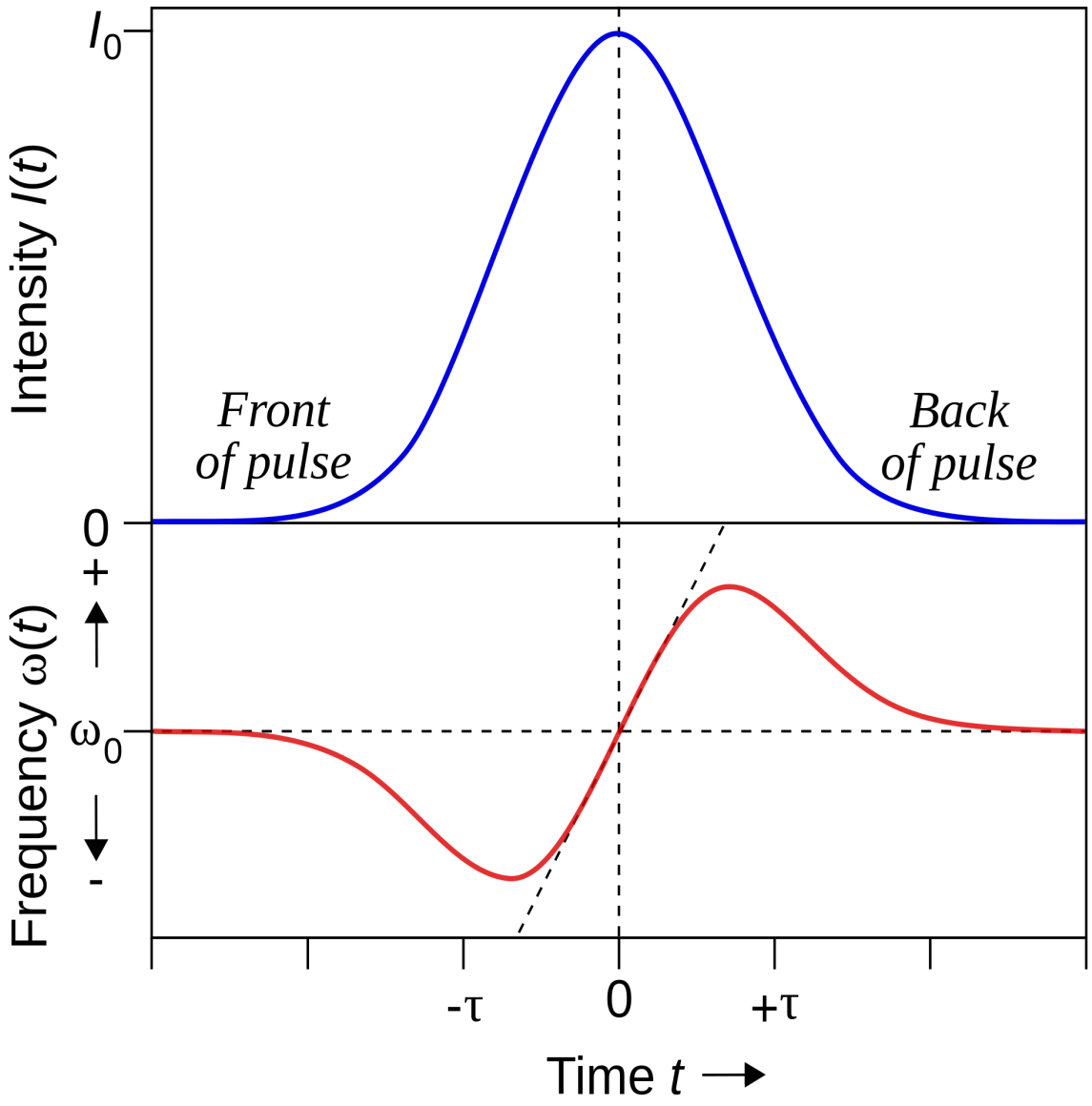

Figure 3.5: Self phase modulation. The blue curve is the intensity profile in the time domain. The red curve shows the instantaneous frequency $\dot{\phi}(t)$. (*This figure is crafted by Emmanuel Boutet and released on Wikipedia website.)*

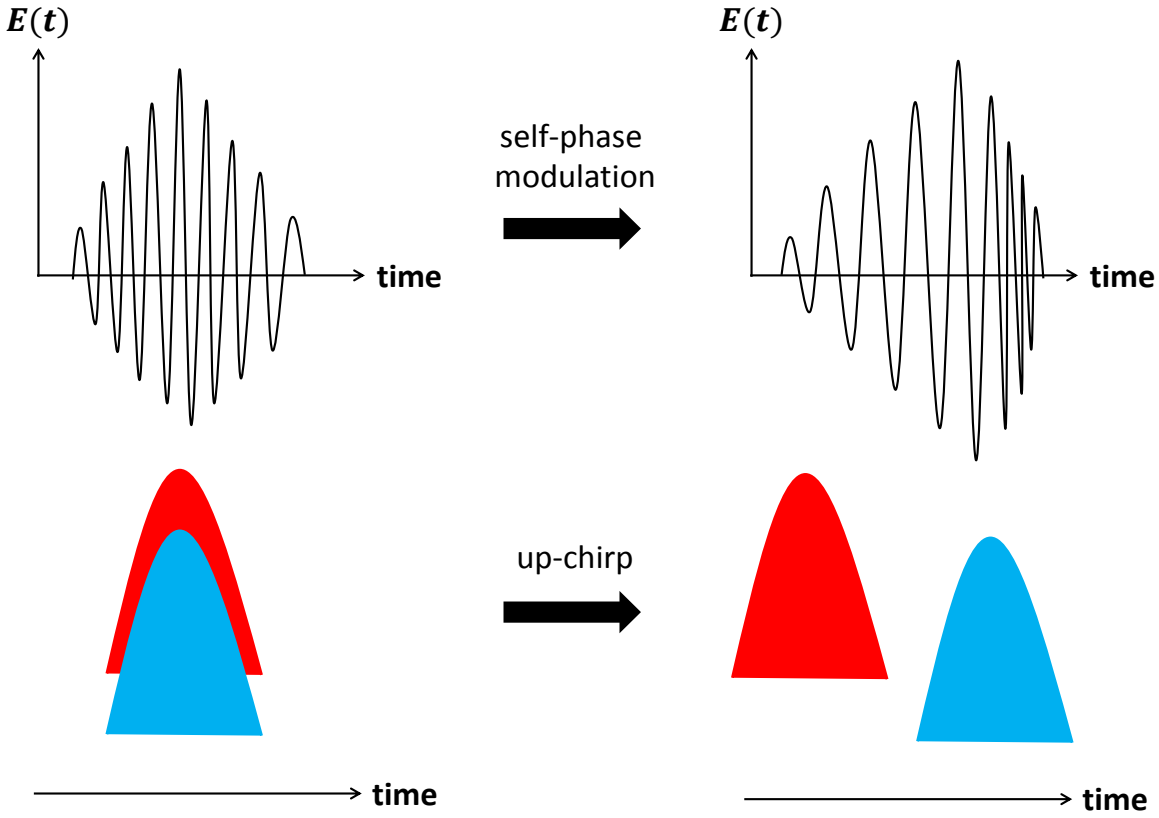

Figure 3.6: Up-chirp induced by self-phase modulation.Blue and Red represent the wave package in blue and red wavelength range, respectively.

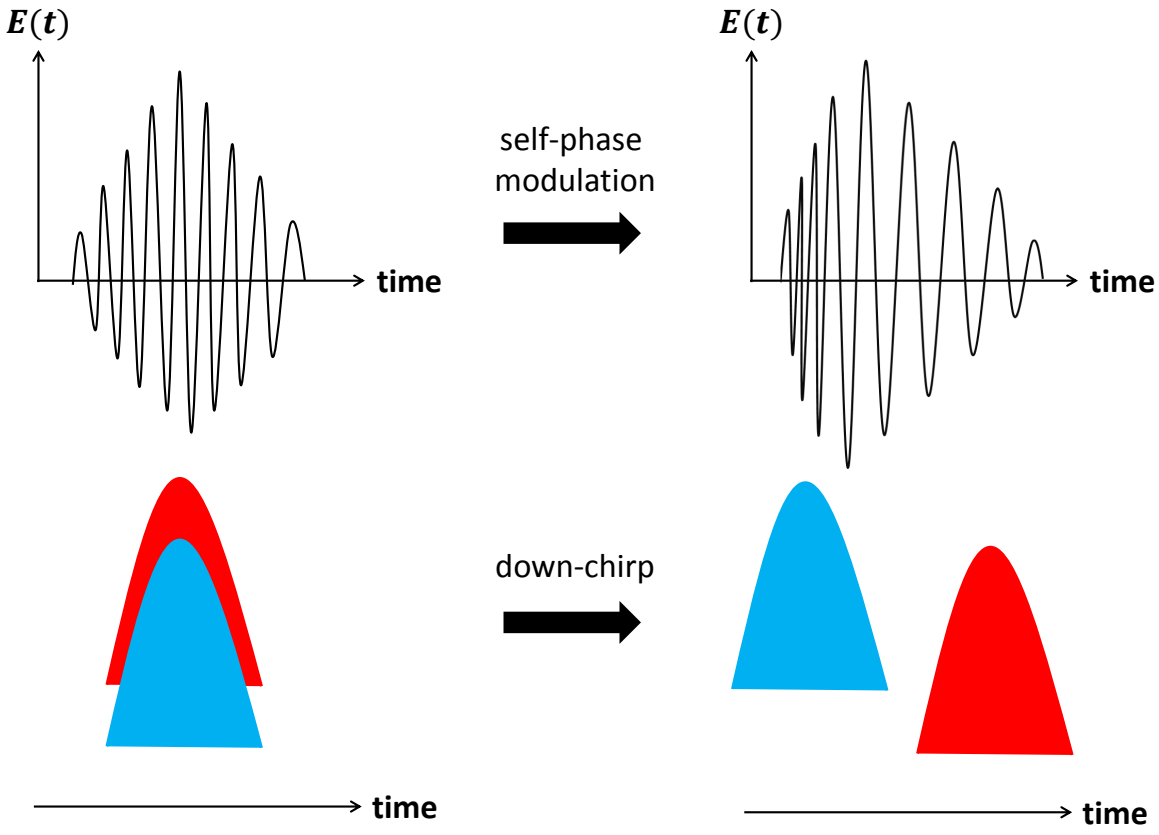

Figure 3.7: Down-chirp induced by self-phase modulation.

3.4.2.3 Two Photon Absorption Two photon absorption (TPA) is related to the imaginary part of the $\chi^{(3)}$ coefficient. The absorption coefficient is defined by

$$a = \alpha + \beta I, \tag{3.91}$$

where the α is the linear absorption coefficient while β is the two-photon absorption coefficient, which is related to the imaginary part of $\chi^{(3)}$[37]

$$\beta = \chi_I^{(3)} \frac{2\omega}{n_0^2 \varepsilon_0 c^2}.$$

As a nonlinear process, two-photon absorption can be used to realize the interferometric autocorrelation measurement. One example is the semiconductor material[2]GaAsP [42]. In the experiments discussed in Chapter 7, we also use a GaAsP detector. Because of TPA, when exposed to the mode-locked laser, the measured photocurrent from the GaAsP detector shows a quadratic dependence on the incident light power (Figure 3.8).

3.5 ACOUSTO-OPTIC EFFECT

Acousto-optics is a branch of physics that studies the interactions between sound waves and light waves, especially the diffraction of laser light by ultrasound or sound in general. The acousto-optic effect is extensively used in the measurement and study of ultrasonic waves. However, the growing principal area of interest is in acousto-optical devices for the deflection, modulation, signal processing and frequency shifting of light beams. This is due to the increasing availability and performance of lasers, which have made the acousto-optic effect easier to observe and measure. Technical progresses in both crystal growth and high frequency piezoelectric transducers have brought valuable benefits to acousto-optic components' improvements.

The acousto-optic effect is a specific case of photoelasticity, where there is a change of a material's permittivity ε due to a mechanical strain, meaning the susceptibility depends on

[2] $GaAs_{1-x}P_x$ is a semiconductor. Its direct and indirect bandgap depend on the mole fraction of phosphorus [40, 41].

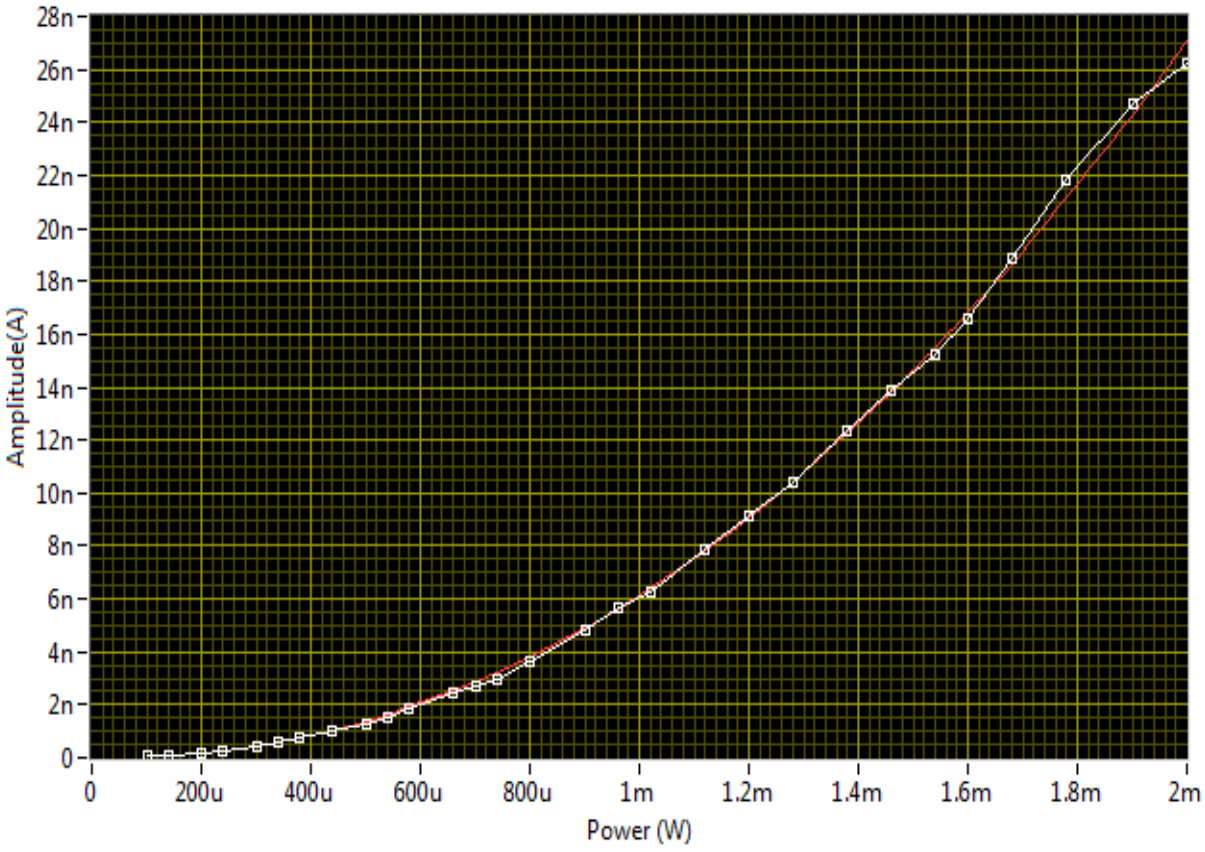

Figure 3.8: GaAsP detector based on two-photon absorption. The white dots show the measured results. The red curve is a fit to the function of $I = aP^2$, where I is the measured photocurrent and P is the incident power.

not only the electric field but also the local atomic displacement.

Acousto-optic modulators (AOM) and photoelastic modulators (PEM) are two examples of acousto-optical devices. In an acousto-optic modulator, different parameters of the acoustic wave, including the amplitude and frequency, can be varied so that the properties of the optical wave can be modulated through Bragg diffraction. A simple method of modulating the optical beam propagating through the acousto-optic device is done by switching the acoustic field on and off (Figure 3.9). When it is off, the beam is undiverted, the intensity of light directed at the Bragg diffraction angle is zero. When switched on and Bragg diffraction occurs, the intensity at the Bragg angle increases. So the acousto-optic device is modulating the output along the Bragg diffraction angle, switching it on and off. The device is operated as a modulator by keeping the acoustic wavelength (frequency) fixed and varying the drive power to vary the amount of light in the deflected beam.

A PEM is an optical device used to modulate the polarization of a light source. The photoelastic effect is used to change the birefringence of the optical element in the photoelastic modulator. The principle of operation of photoelastic modulators is based on the photoelastic effect, in which a mechanically stressed sample exhibits birefringence proportional to the resulting strain. Photoelastic modulators are resonant devices at which the precise oscillation frequency is determined by the properties of the optical element/transducer assembly (An example of photoelastic modulator is shown in Figure 3.10).

The transducer is tuned to the resonance frequency of the optical element along its long dimension, determined by its length and the speed of sound in the material. A current is then sent through the transducer to vibrate the optical element through stretching and compressing which changes the birefringence of the transparent material. A certain amount of retardation can be introduced in the transmitted light beam so that the polarization of the transmitted light is varied coherently (Figure 3.11).

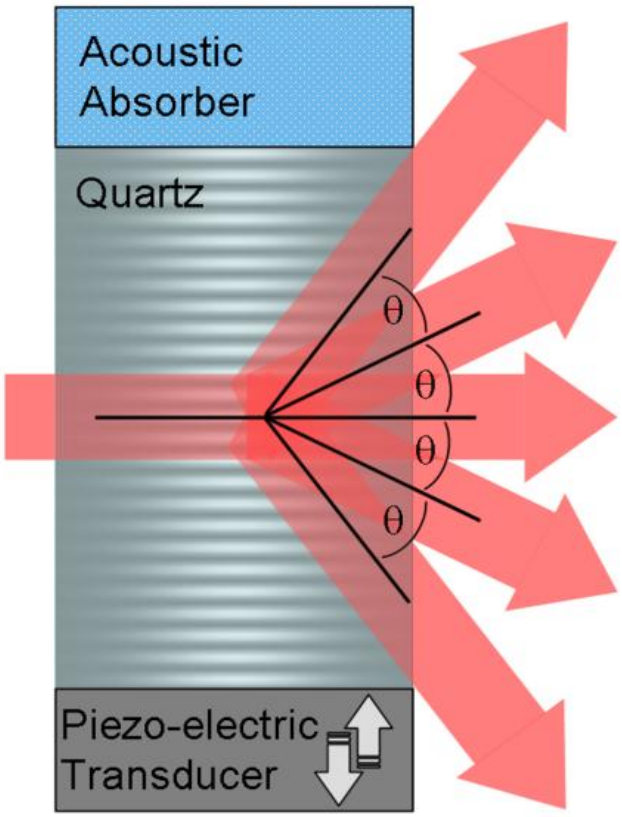

Figure 3.9: An acousto-optic modulator. (*This figure is made by J S Lundeen and released on the website of Wikipedia.*)

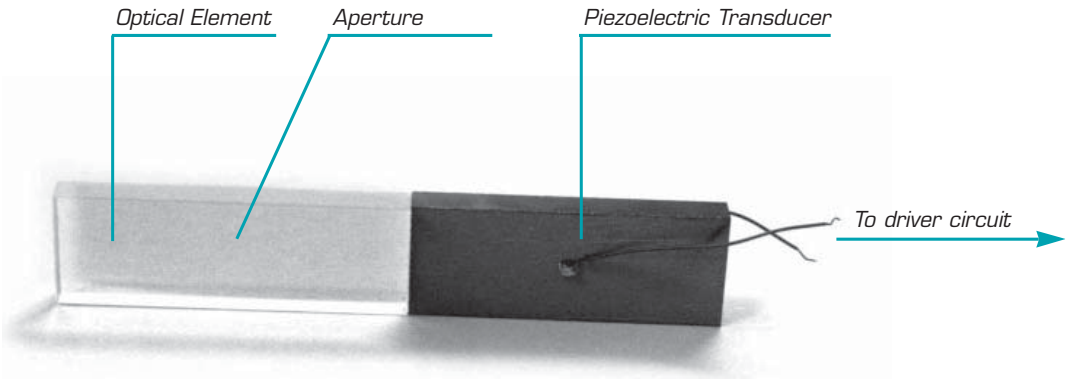

Figure 3.10: A photoelastic modulator. (*This figure is from the website of Hinds Instrument.*)

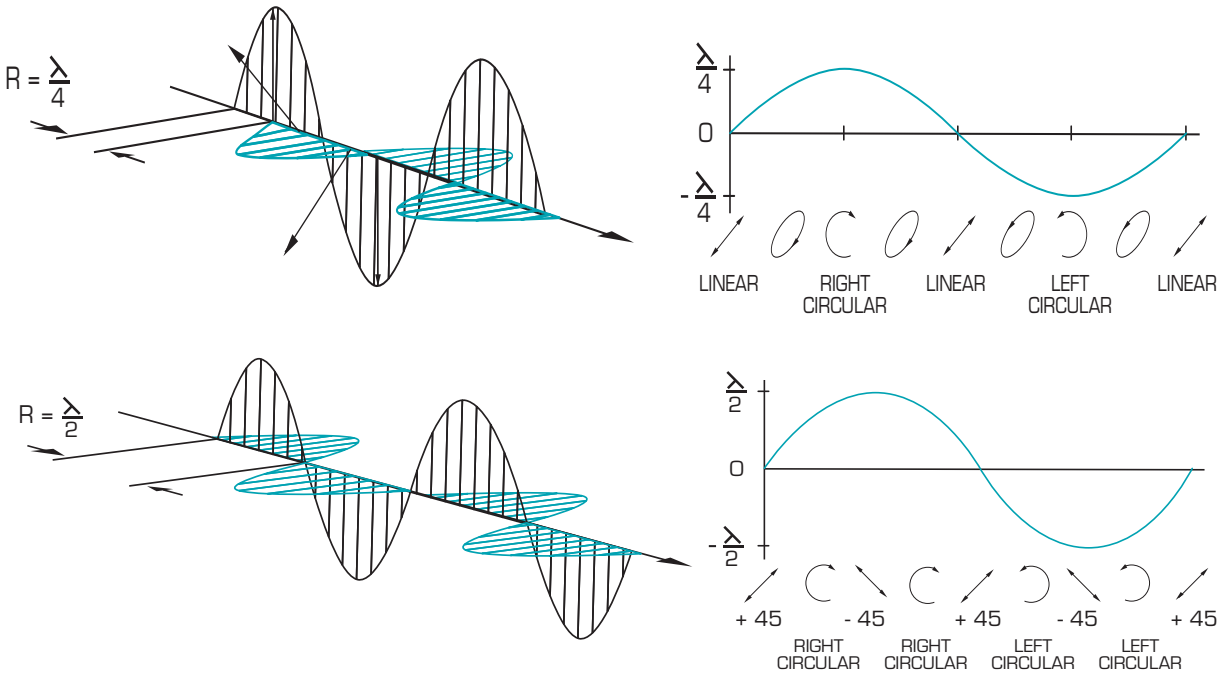

Figure 3.11: The quarter-wave and half-wave retardation induced by a PEM. (*This figure is from the website of Hinds Instrument.*)

3.6 MAGNETO-OPTIC EFFECT

A magneto-optic effect is any one of a number of phenomena in which an electromagnetic wave propagates through a medium that has been altered by the presence of a quasistatic magnetic field [43]. In such a material, left- and right-circularly polarized light can propagate at different speeds, resulting in a number of important phenomena such as Faraday/Kerr rotation. The Faraday effect causes a rotation of the plane of polarization which is linearly proportional to the component of the magnetic field in the direction of propagation(Figure 3.12). One application of this effect is the Faraday isolators [44, 45]. The difference between the Faraday effect and Kerr effect is that the transmitted light is measured for the Faraday effect while the reflected light is measured for the Kerr effect (Figure 3.13)(See, for example, the Chpater 5 in Ref.[46]).

In particular, in a magneto-optic material the presence of a magnetic field (either externally applied or because the material itself is ferromagnetic) can cause a change in the permittivity tensor of the material. Classically, we can consider the motion of electrons under the influence of a magnetic field $\vec{B} = \mu_0 \chi_{(m)} \vec{H}$, which is given by Eq.(2.57) in Chapter 2:

$$m\ddot{\vec{r}}(t) = -m\omega_0^2 \vec{r}(t) - m\gamma \dot{\vec{r}}(t) - e\vec{E} - e\mu_0 \chi_{(m)} \frac{\vec{v}}{c} \times \vec{H}, \tag{3.92}$$

where μ_0 is the permeability of free space and $\chi_{(m)}$ is the magnetic susceptibility. By performing the Fourier transform on both sides, Eq.(3.92) becomes

$$-m\omega^2 \vec{r}(\omega) = -m\omega_0^2 \vec{r}(\omega) - im\gamma\omega \vec{r}(\omega) - e\vec{E}(\omega) + i\mu_0 \chi_{(m)} \frac{\omega e}{c} (\vec{r}(\omega) \times \vec{H}(\omega)). \tag{3.93}$$

We treat the magnetic field as a perturbation by introducing a dimensionless parameter λ. Therefore we have

$$\vec{H} \to \lambda \vec{H}, \tag{3.94}$$

$$\vec{r}(\omega) = \vec{r}^{(0)}(\omega) + \lambda \vec{r}^{(1)}(\omega) + \lambda^2 \vec{r}^{(2)}(\omega) + \cdot. \tag{3.95}$$

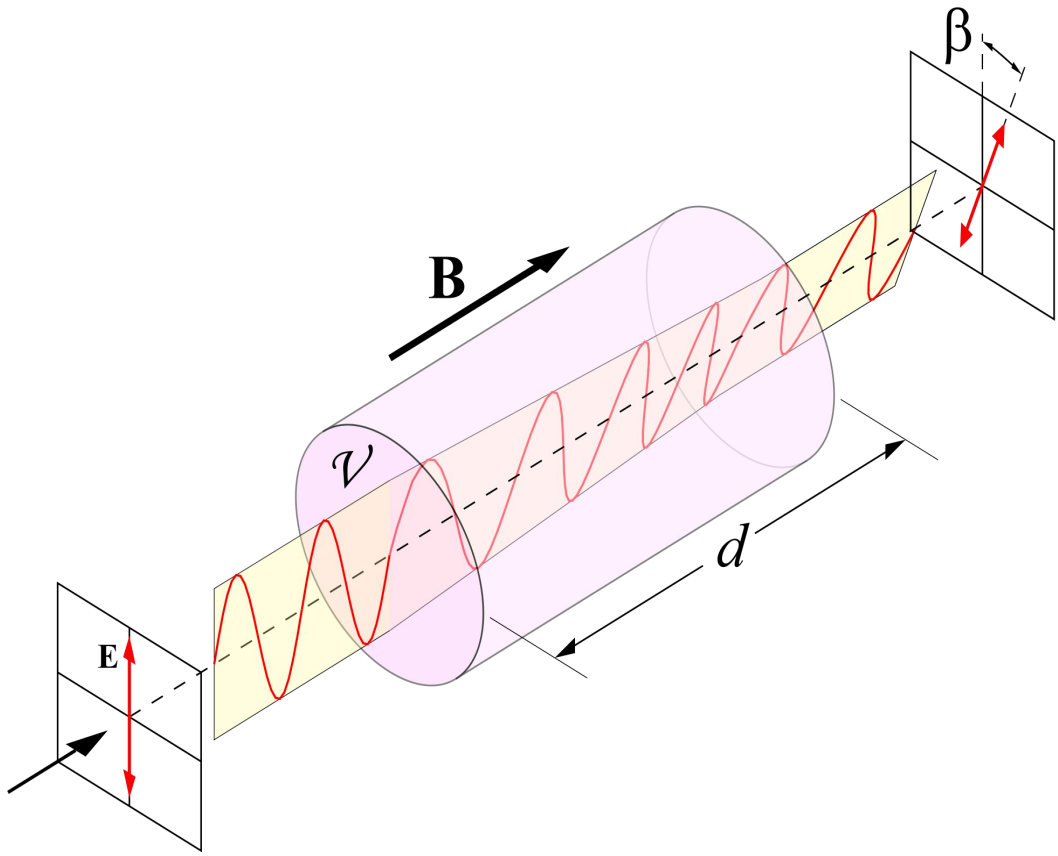

Figure 3.12: Faraday rotation. The presence of a magnetic field can alter the polarization of the light. (*This figure is crafted by DrBob and released on the website of Wikipedia.*)

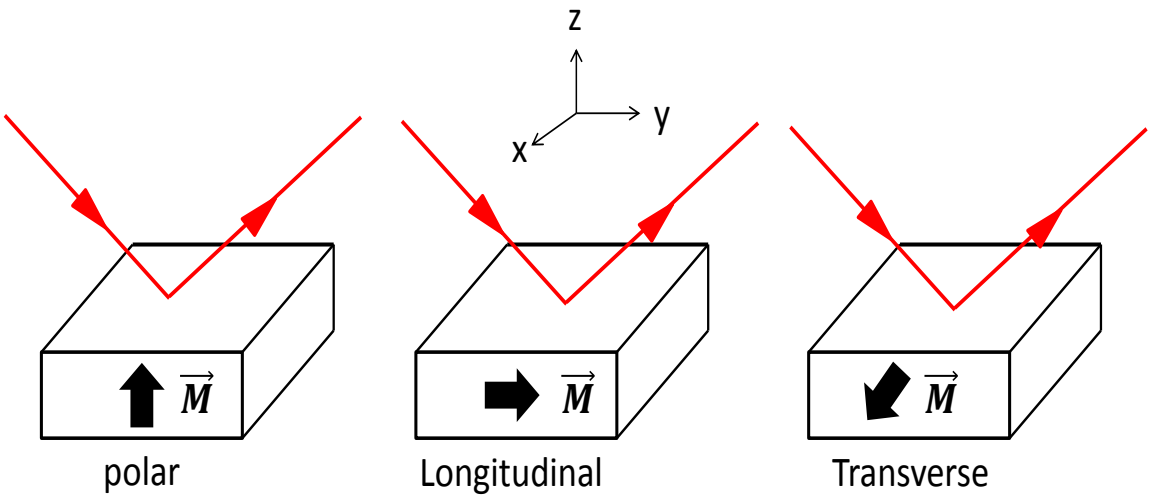

Figure 3.13: Different geometries for magneto-optical Kerr effect.

The unperturbed term $\vec{r}^{(0)}(\omega)$ can be solved from the equation

$$-m\omega^2\vec{r}^{(0)}(\omega) = -m\omega_0^2\vec{r}^{(0)}(\omega) - im\gamma\omega\vec{r}^{(0)}(\omega) - e\vec{E}(\omega). \tag{3.96}$$

It is easy to have

$$\vec{r}^{(0)}(\omega) = \frac{e}{m}\frac{\vec{E}(\omega)}{(\omega^2-\omega_0^2)-i\gamma\omega}. \tag{3.97}$$

The first order perturbation satisfies the equation

$$-m\omega^2\vec{r}^{(1)}(\omega) = -m\omega_0^2\vec{r}^{(1)}(\omega) - im\gamma\omega\vec{r}^{(1)}(\omega) + i\mu_0\chi_{(m)}\omega\frac{e}{c}(\vec{r}^{(0)}(\omega)\times\vec{H}(\omega)). \tag{3.98}$$

It is straightforward to figure out that the solution is

$$\begin{aligned}\vec{r}^{(1)}(\omega) &= -i\mu_0\chi_{(m)}\omega\frac{e}{mc}\frac{\vec{r}^{(0)}(\omega)\times\vec{H}(\omega)}{(\omega^2-\omega_0^2)-i\gamma\omega} \\ &= -i\mu_0\chi_{(m)}\frac{\omega e^2}{m^2c}\frac{\vec{E}(\omega)\times\vec{H}(\omega)}{[(\omega^2-\omega_0^2)-i\gamma\omega]^2}.\end{aligned} \tag{3.99}$$

The polarization of N electrons in a unit volume given by the zeroth order of perturbation is

$$\vec{P}^{(0)}(\omega) = Ne\vec{r}^{(0)}(\omega), \tag{3.100}$$

which is the result that we have seen in Eq.(2.61) of Chapter 2 . We define the electric susceptibility as

$$\chi_{(e)}(\omega) = \frac{Ne^2}{\varepsilon_0 m} \frac{1}{(\omega^2 - \omega_0^2 - i\gamma\omega)} \tag{3.101}$$

The first order of perturbation leads to

$$\begin{aligned} \vec{P}^{(1)}(\omega) &= Ne\vec{r}^{(1)}(\omega) \\ &= -\frac{i\omega}{\mu_0 c^5 Ne} \chi_{(m)} \chi^2_{(e)}(\omega)(\vec{E}(\omega) \times \vec{H}(\omega)) \end{aligned} \tag{3.102}$$

It is seen that in the case of magneto-optic effects, the polarization is modified by the present magnetic field. Generally the magnetic susceptibility $\chi_{(m)}$ is a tensor as well. The microscopic origin of magneto-optic effects is electronic [43, 47]. The interaction between the electron spins and the magnetic field causes the shift of electronic states and consequently changes the dipole moments $\hat{d}_{nm}$ that appear in the expression of susceptibilities. In Chapter 4, we discuss theoretically the Faraday rotation induced by a single electron spin.

4.0 INTRINSIC QUANTUM NOISE IN FARADAY-ROTATION MEASUREMENTS OF A SINGLE-ELECTRON SPIN

Faraday rotation discussed in Chapter 3 is one way to realize quantum non-demolition measurement of electron spin in quantum dots. To describe Faraday rotation, semiclassical models are typically used, based on quantized electron spin states and classical electromagnetic fields. Such treatments neglect the entanglement between electronic and photonic degrees of freedom that produce intrinsic quantum noise, limiting the ultimate sensitivity of this technique. We present a fully quantum-mechanical description of Faraday rotation, and quantify this intrinsic noise. A method for measuring the purity of a given spin state is suggested based on this analysis[1].

4.1 INTRODUCTION

Because of the discovery of long-lived spin coherence in semiconductors such as GaAs[48], the essential requirement of manipulating spins for spintronics and quantum information is now possible. The first quantum computing proposal of Loss and DiVincenzo used electron spin qubits in semiconductor quantum dots (QD)[49] and forecast the importance of measuring single electrons and their spins.

The first step to realizing coherent manipulation of a single electron spin is to orient the spin. Such orientation can be achieved optically (by exciting with circularly polarized light)[50], electrically (by driving the electrons toward a ferromagnetic surface)[51] or thermodynamically (by application of a uniform magnetic field at low temperatures). Photo-

[1]Yanjun Ma and Jeremy Levy, Phys. Rev. A 79, 023830 (2009)

luminescence (PL) allows for measurement of electron spin polarization through the relation between the circular polarization of light and electron spin orientation. However, PL is destructive in that it involves recombination of the electron with a hole. PL measurements are intrinsically limited by the lifetime of the state, and it is not possible to monitor electron spin continuously. Furthermore, unless one uses a technique such as time-resolved upconversion[52, 53, 54] or streak camera measurements, dynamical information is lost.

Time-resolved Faraday and Kerr rotation methods (hereafter referred to as Faraday rotation) have been extensively developed[55, 56, 57], and allow one to probe the spin dynamics of a single electron in a quantum dot. Faraday rotation results from a fundamental interaction between electronic and photonic degrees of freedom. Seigneur et al.[58]have proposed a scheme to implement quantum computation by using the single photon Faraday effect. However, in most semiconductors the Faraday effect is usually quite weak, corresponding to rotation angles $\theta_F \sim 10^{-5}$rad for single electrons. Dynamic information is usually obtained using pump-probe optical techniques: a circularly polarized pump beam creates an initially spin-polarized electron population, and a probe beam subsequently interrogates the spin state at a later time. The experiment is performed repeatedly as a function of the delay to obtain a time-resolved signal with an acceptably high signal-to-noise ratio. In the case of a single electron in a quantum dot, spin coherence can be achieved in the following manner: the quantum dot is configured (either through biasing or doping) to begin in a state that contains a single electron in the conduction band and no holes in the valence band. The quantum dot is excited, promoting a second electron into the conduction band and leaving behind a hole in the valence band. This state is often referred to as a "trion". After one of the electrons recombines with the hole, the remaining electron spin is partially polarized. A linearly polarized probe pulse measures the spin of this electron via the Faraday effect. In most cases, the electron neither begins in a pure state nor remains in one. Hyperfine interactions with nuclear spins quickly produce a mixed state on time scales ˜1-10 ns[59, 60, 61, 62, 63, 64, 65, 66, 67, 68, 69].In this paper, we study the noise introduced by the mixed quantum state of the electron spin analytically and numerically. In this paper, our previous analysis[70] about the noise is extended to a more formal quantum mechanical frame. Since it's from the spin state itself, we call it intrinsic noise.

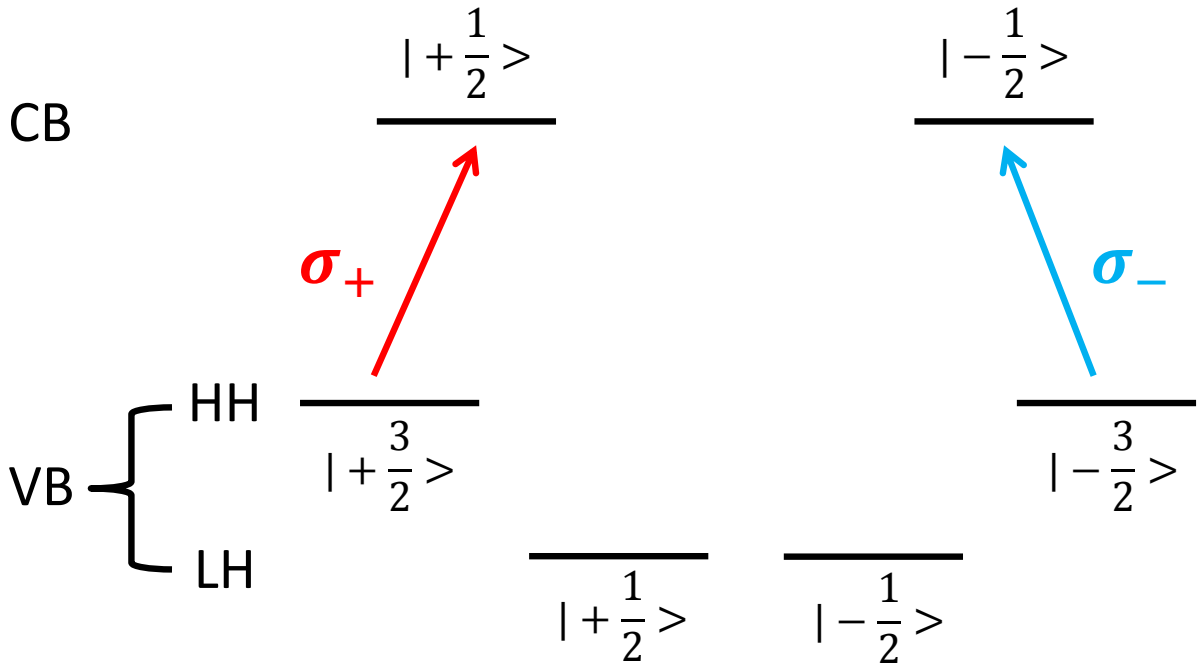

Figure 4.1: (Color online)light induced interband transition.

4.2 THEORETICAL MODEL

Here we discuss in detail the quantum-mechanical source of this noise using a theoretical model that treats both the electron and light field quantum mechanically. We model the interaction between a single electron in a QD and a linearly polarized monochromatic probe laser field. Based on the quantization of the light field that is presented in Chapter 2, we have the Hamiltonian for the photon field written as

$$H_P = \hbar\omega_P(a_L^\dagger a_L + a_R^\dagger a_R), \tag{4.1}$$

where ω_P is the optical frequency of the probe laser, $a_L^\dagger$ and a_L are creation and annihilation operators for left circularly polarized (LCP) photons; $a_R^\dagger$ and a_R are creation and annihilation operators for right circularly polarized (RCP) photons. Due to optical selection rules [50] spin-up (spin-down) electrons interact only with LCP (RCP) photons(See Figure 4.1). The raising and lowering operators satisfy boson commutation relations

$$[a_m, a_n^\dagger] = \delta_{mn}, (m, n = L, R);$$

$$[a_m, a_n] = 0, [a_m^\dagger, a_n^\dagger] = 0.$$

The electron state is quantized as well. We assume that the electron resides in the conduction band quantum-confined ground state in an s-orbital, which means it has total angular momentum $J = \frac{1}{2}$. In the valence band, the electronic ground states are constructed from p-orbital, and hence the total angular momentum is $J = \frac{3}{2}$. Heavy-hole and light-hole intermixing is neglected for simplicity and because it is not expected to affect qualitatively our results. Only the heavy-hole subband is accounted for in our calculation. The Hamiltonian for the electron is given by [71]

$$H_e = \hbar\omega_e(\sigma_{uz} + \sigma_{dz}), \tag{4.2}$$

where

$$\sigma_{uz} = b_{cu}^\dagger b_{cu} - b_{vu}^\dagger b_{vu},$$

$$\sigma_{dz} = b^{\dagger}_{cd} b_{cd} - b^{\dagger}_{vd} b_{vd};$$

subscript "c" and "v" indicate conduction band and valence band respectively; subscripts "u" and "d" refer to spin-up or spin-down states of the electron. The fermion operators satisfy anticommutation relations:

$$\{b_{i\mu}, b^{\dagger}_{j\nu}\} = \delta_{ij}\delta_{\mu\nu},$$

$$\{b_{i\mu}, b_{j\nu}\} = 0, \{b^{\dagger}_{i\mu}, b^{\dagger}_{j\nu}\} = 0,$$

where i and j indicate conduction band or valence band, and μ and ν indicate spin-up or spin-down. A LCP photon couples to a transition between $|+\frac{1}{2}>$ and $|+\frac{3}{2}>$, while a RCP photons couples to a transition between $|-\frac{1}{2}>$ and $|-\frac{3}{2}>$. The interaction Hamiltonian is given by

$$H_I = \lambda_{Lu}(a_L \sigma_{u+} + a^{\dagger}_L \sigma_{u-}) + \lambda_{Rd}(a_R \sigma_{d+} + a^{\dagger}_R \sigma_{d-}), \tag{4.3}$$

where

$$\lambda_{Lu} \propto < +\frac{1}{2}|x + iy| + \frac{3}{2} >,$$

$$\lambda_{Rd} \propto < -\frac{1}{2}|x - iy| - \frac{3}{2} >,$$

$$\sigma_{u+} = b^{\dagger}_{cu} b_{vu}, \sigma_{u-} = \sigma^{\dagger}_{u+},$$

$$\sigma_{d+} = b^{\dagger}_{cd} b_{vd}, \sigma_{d-} = \sigma^{\dagger}_{d+}.$$

The full Hamiltonian of the entire system is given by

$$H = H_P + H_e + H_I$$

By applying the Wigner-Eckart theorem, it can be shown that the two coupling strengths λ_{Lu} and λ_{Rd} must be equal (λ_{Lu}=λ_{Rd}≡λ). Based on the defining anticommutation relations, it can be explicitly shown that $\sigma_{\mu z}$,$\sigma_{\mu+}$ and $\sigma_{\mu-}$ have the following commutation relations:

$$[\sigma_{\mu+}, \sigma_{\nu-}] = \delta_{\mu\nu}\sigma_{\mu z},$$

$$[\sigma_{\mu z}, \sigma_{\nu+}] = 2\delta_{\mu\nu}\sigma_{\mu+},$$

$$[\sigma_{\mu z}, \sigma_{\nu-}] = 2\delta_{\mu\nu}\sigma_{\mu-}.$$

These commutation relations for $\sigma_{\mu z}$,$\sigma_{\mu+}$ and $\sigma_{\mu-}$ are formally identical to those for the Pauli operators, even though they are actually products of fermionic creation and annihilation operators. This feature makes it possible to find an analytic solution within the Heisenberg picture [72]. In the limit $\lambda \ll \mid \omega_P - \omega_e \mid$, the approximate solution for the photon operators is as follows:

$$a_L^\dagger(t) = e^{-it\Omega\sigma_{uz}}a_L^\dagger + g(t)(\sigma_{u+} + \alpha\sigma_{uz}a_L^\dagger), \tag{4.4}$$

$$a_R^\dagger(t) = e^{-it\Omega\sigma_{dz}}a_R^\dagger + g(t)(\sigma_{d+} + \alpha\sigma_{dz}a_R^\dagger), \tag{4.5}$$

where

$$\alpha = \frac{\lambda}{\omega_P - \omega_e},$$

$$\Omega = \lambda\alpha,$$

$$g(t) = \alpha(1 - e^{-i(\omega_P - \omega_e)t}).$$

This approximate solution is correct only when the coupling strength λ is much smaller than ω_e and ω_P. In the section of RESULTS, one can see this criteria is satisfied in the sense that the coupling strength of our sample is on the order of $\sim 10^9$Hz, but the frequency of the laser light and the characteristic frequency of the electron are on the order of $\sim 10^{15}$Hz. This solution, therefore, is a very good approximation and, based on this, one can derive Faraday rotation angle.

Quantum Stokes operators can be used to describe Faraday rotation. They are the quantum-mechanical analogue of classical Stokes parameters. Classical Stokes parameters are defined as the following [33]:

$$S_0 = E_x^* E_x + E_y^* E_y \tag{4.6}$$

$$S_1 = E_x^* E_x - E_y^* E_y \tag{4.7}$$

$$S_2 = E_x^* E_y + E_y^* E_x \tag{4.8}$$

$$S_3 = E_x^* E_y - E_y^* E_x. \tag{4.9}$$

In electrodynamics, the polarization of light can be parameterized by two angles φ and χ in the polarization ellipse. There is a one-to-one correspondence between the polarization-ellipse representation and the Stokes representation (See Figure. 4.2).

Once the light field is known, the Stokes parameters can be computed. The physical interpretation of S_0 is the light intensity; hence, all parameters can be normalized to S_0 (See Figure 4.3).

Quantum Stokes operators are defined in the following way [73, 74]

$$S_0 = a_L^\dagger a_L + a_R^\dagger a_R \tag{4.10}$$

$$S_1 = a_L^\dagger a_R + a_R^\dagger a_L \tag{4.11}$$

$$S_2 = i(a_L^\dagger a_R - a_R^\dagger a_L) \tag{4.12}$$

$$S_3 = a_R^\dagger a_R - a_L^\dagger a_L. \tag{4.13}$$

Information about polarization is obtained by calculating the expectation values of these operators. In a typical Faraday experiment, the probe light is linearly polarized at a 45° angle with respect to a final polarizing beam splitter. After the interaction between the probe light and the electron, the polarization of the transmitted light will be rotated from its initial position by an angle θ_F, known as the Faraday rotation angle. In the Stokes representation, the initial polarization vector lies along the positive S_2 axis. Faraday rotation will result in a rotation of the vector within the $S_1 - S_2$ plane (See Figure 4.4). This vector P is confined

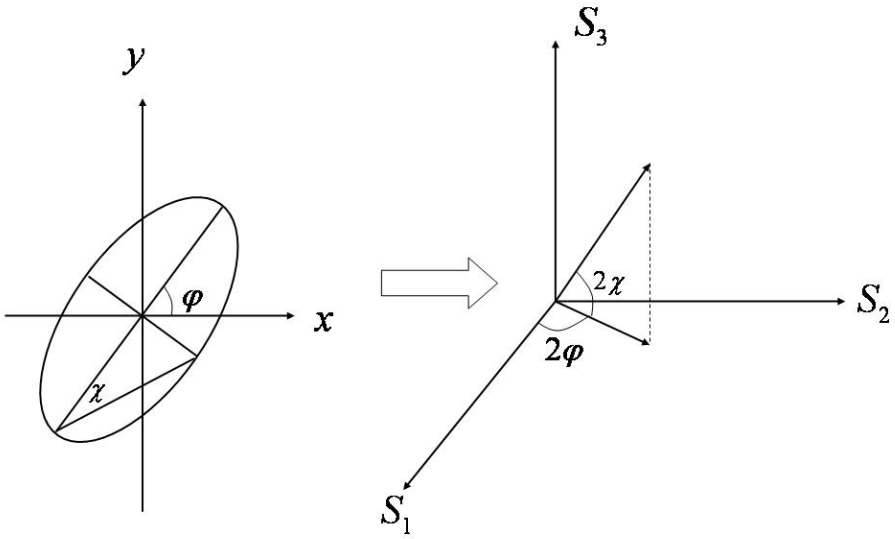

Figure 4.2: The left figure shows the polarization ellipse in real space. The right figure is the Stokes representation of the same polarization.

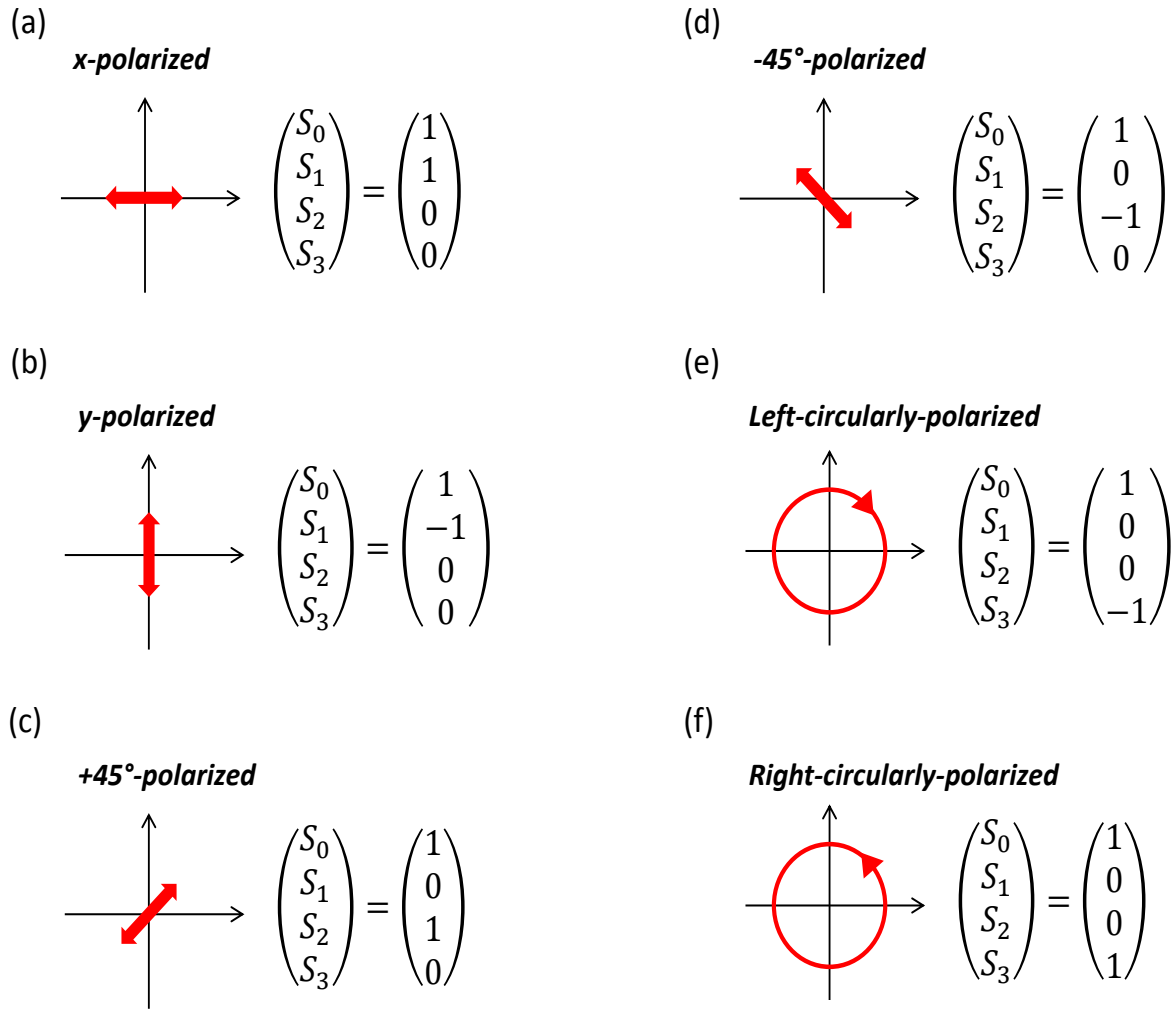

Figure 4.3: (a)-(f)Different polarizations defined in terms of Stokes parameters. S_1, S_2 and S_3 have all been normalized to S_0.

to the plane as long as there is no circular dichroism that can lead to a non-zero expectation value for S_3.

In our calculations, we aim to reproduce the overall magnitude of the rotation angle that has been reported in experimental work [55, 56, 57]. The experimentally observed rotation angle is small: $\theta_F \sim 10^{-5}$rad. Hence, it can be expressed as

$$\theta_F = \frac{1}{2} tan^{-1}(\frac{< S_1 >}{< S_2 >}) \approx \frac{< S_1 >}{2 < S_2 >}. \tag{4.14}$$

4.3 RESULTS

In our calculation, a coherent state $|\nu_L, \nu_R >$ is used for the light field, where $|\nu_L|^2$ and $|\nu_R|^2$ are the average number of left and right circularly polarized photons. These states satisfy the canonical eigenvalue equations for the (non-Hermitian) photon annihilation operators:

$$a_L|\nu_L, \nu_R >= \nu_L|\nu_L, \nu_R >,$$

$$a_R|\nu_L, \nu_R >= \nu_R|\nu_L, \nu_R >,$$

Using the forms $\nu_L = N_L e^{i\theta_L}$ and $\nu_R = N_R e^{i\theta_R}$, the expectation values of Stokes operators for this coherent state can be found

$$\begin{pmatrix} < S_0 > \\ < S_1 > \\ < S_2 > \\ < S_3 > \end{pmatrix} = \begin{pmatrix} N_L^2 + N_R^2 \\ 2N_L N_R cos(\theta_L - \theta_R) \\ 2N_L N_R sin(\theta_L - \theta_R) \\ N_R^2 - N_L^2 \end{pmatrix}. \tag{4.15}$$

In order to start with $+45^\circ$ linearly polarized light, the following condition must be satisfied

$$\begin{cases} N_L^2 = N_R^2 \\ \theta_L - \theta_R = \frac{\pi}{2} \end{cases}$$

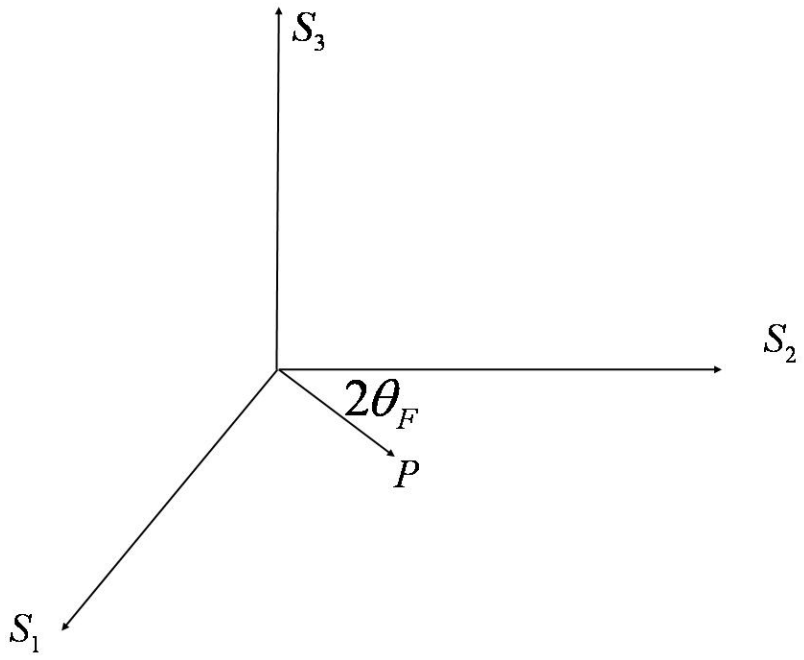

Figure 4.4: Definition of Faraday rotation angle. P indicates the polarization vector of the light field.

To describe the mixed state of an electron, a density matrix formula is employed:

$$\rho_e = \tau|\chi_+ >< \chi_+| + (1-\tau)|\chi_- >< \chi_-|, \tag{4.16}$$

where

$$|\chi_+ >= \cos(\chi)|+\frac{1}{2}> - \sin(\chi)|-\frac{1}{2}>,$$
$$|\chi_- >= \sin(\chi)|+\frac{1}{2}> + \cos(\chi)|-\frac{1}{2}> .$$

Here, τ is a parameter that varies between 0 and 1. Angle χ accounts for the precession of electron spin in the nuclear field. For $\tau = 0$ and $\tau = 1$, one has a pure state, while $\tau = 1/2$ corresponds to a fully mixed (unpolarized) state. Because the electron Hamiltonian is expressed in terms of creation and annihilation operators, caution must be taken when applying those operators onto an electron state. When operators for spin-up electron are applied to the spin-up state, one obtains

$$\sigma_{uz}|+\frac{1}{2}>= |+\frac{1}{2}>,$$
$$\sigma_{uz}|+\frac{3}{2}>= -|+\frac{3}{2}>,$$

and

$$\sigma_{u+}|+\frac{1}{2}>= 0,$$
$$\sigma_{u+}|+\frac{3}{2}>= |+\frac{1}{2}>,$$

and

$$\sigma_{u-}|+\frac{1}{2}>= |+\frac{3}{2}>,$$
$$\sigma_{u-}|+\frac{3}{2}>= 0.$$

Spin-down operators have the same rules when applied to the spin-down state. If a spin-up operator operates on a spin-down state, however, one gets zero. For example,

$$\sigma_{uz}|-\frac{1}{2}>=(b_{cu}^{\dagger}b_{cu}-b_{vu}^{\dagger}b_{vu})|-\frac{1}{2}>=0.$$

The initial state of the whole system is then

$$\rho_0(\tau)=|\nu_L,\nu_R><\nu_L,\nu_R|\otimes\rho_e \tag{4.17}$$

According to the solution Eq.(4.4) and Eq.(4.5), the analytical expression for S_1 and S_2 can be obtained and the expectation values calculated

$$<S_1>=Tr(S_1(t)\rho_0(\tau)),$$

$$<S_2>=Tr(S_1(t)\rho_0(\tau)).$$

The rotation angle is given by

$$\theta_F(t,\tau)=\frac{Tr(S_1(t)\rho_0(\tau))}{2Tr(S_2(t)\rho_0(\tau))}, \tag{4.18}$$

After some algebra, one finds the following expression for the Faraday rotation:

$$\theta_F(t,\tau)=(2\tau-1)(\frac{\lambda^2}{\delta^2}\sin(\delta t)-\sin(\frac{\lambda^2}{\delta}t)), \tag{4.19}$$

where $\delta\equiv\omega_P-\omega_e$. Notice that this equation is only valid for small t. For initial pure spin-up state $\tau=1$, the rotation angle is

$$\theta_+\equiv\theta_F(t,1)=(\frac{\lambda^2}{\delta^2}\sin(\delta t)-\sin(\frac{\lambda^2}{\delta}t)). \tag{4.20}$$

For initial pure spin-down state $\tau=0$, the rotation angle is

$$\theta_-\equiv\theta_F(t,0)=-(\frac{\lambda^2}{\delta^2}\sin(\delta t)-\sin(\frac{\lambda^2}{\delta}t)). \tag{4.21}$$

The fluctuation is given by

$$\Delta\theta_F(t,\tau)=\frac{\sqrt{Tr(S_1^2(t)\rho_0(\tau))-Tr(S_1(t)\rho_0(\tau))^2}}{2Tr(S_2(t)\rho_0(\tau))}. \tag{4.22}$$

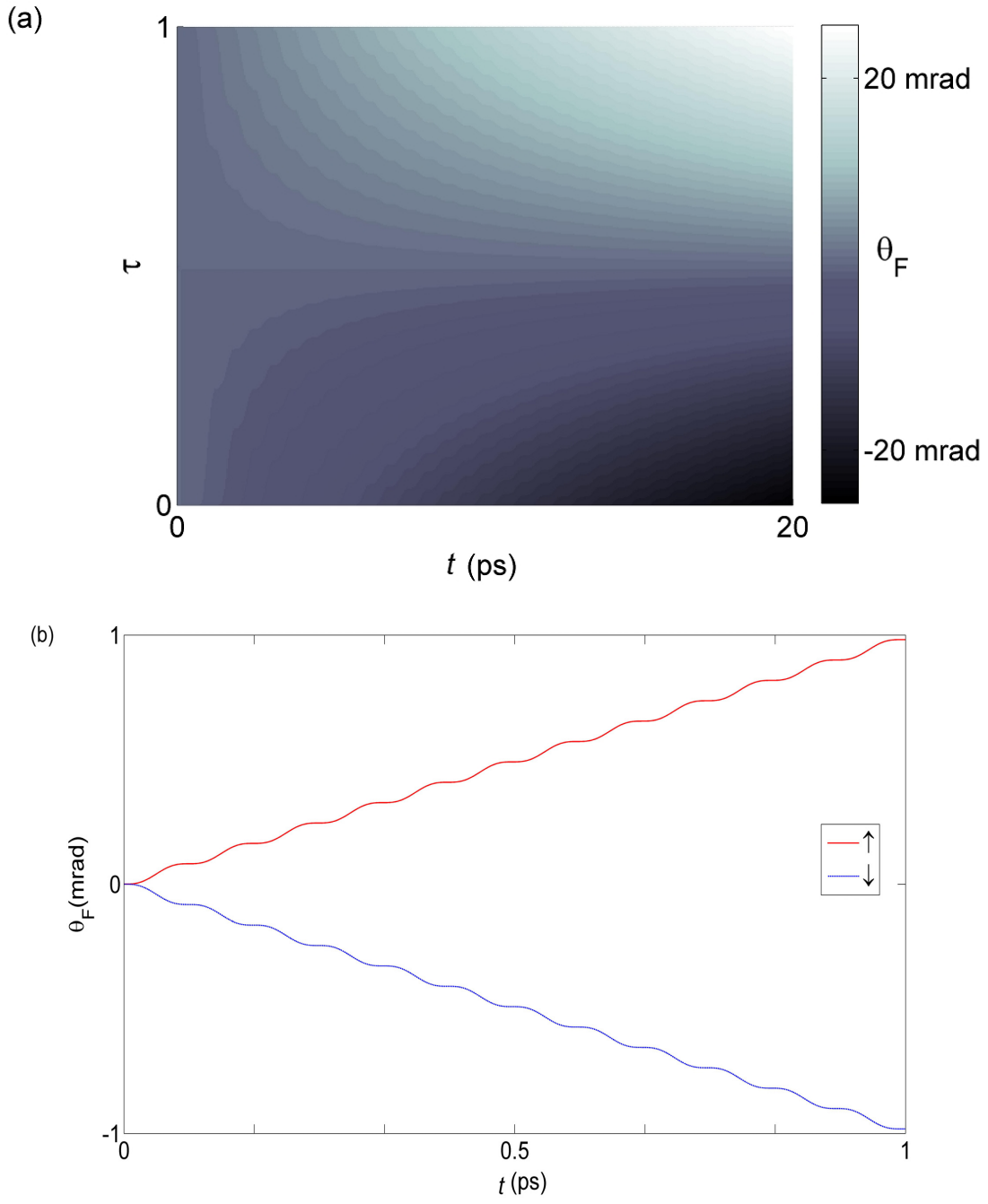

Figure 4.5: (a), Faraday rotation as a function of time and parameter τ. (b), Faraday rotation angle for two pure states. The red solid line corresponds to a spin-up state($\tau = 1$), while the blue line corresponds to a spin-down state($\tau = 0$).

From Eq.(4.19), Eq.(4.20) and Eq.(4.21), the following intuitive result can be proven very easily:

$$\theta_F(t,\tau) = \alpha\theta_+ + (1-\alpha)\theta_-. \tag{4.23}$$

where $\alpha = \sin^2(\chi) + \tau\cos(2\chi)$ and θ_+ (θ_-) is the Faraday rotation angle for an initial state which is a pure spin-up (spin-down) state.

An analytical derivation shows that the fluctuation is a function of both photon number N and the initial electron state.

$$\Delta\theta_F(t,\tau) = \sqrt{\frac{1}{4N} + \alpha(1-\alpha)(\theta_+ - \theta_-)^2}, \tag{4.24}$$

The second term under the square root is the so-called intrinsic noise term.

Numerical simulation is done so that we can compare our analytical calculation to recent Kerr rotation experimental results on single electrons. From Berezosky et al. [55], one finds from a PL plot that the energy for a neutral exciton is about 1.633 eV. That corresponds to the band gap between the top of the valence band and the bottom of the conduction band. From this number, the frequency $\omega_e = \frac{E}{\hbar} = 2.48 \times 10^{15} Hz$. Choosing probe light of wavelength 760nm, which means the frequency is $\omega_P = 2.47 \times 10^{15} Hz$. From [75], one can take the value of the coupling strength to be $\lambda = 98$GHz. In our experiment, the probe power is about 1.57μW: the corresponding photon number is about 5×10^5. In the simulation, the interaction time between the spin and the photon is set to be 20ps. Because the time scale of hyperfine interaction is ˜1-10 ns [59, 60, 61, 62, 63, 64, 65, 66, 67, 68, 69], which is much longer than the simulation time, χ is set to be zero in our numerical analysis. Notice that as expected, if the initial electron state is a pure state, the rotation angle has opposite values for the spin-up state and spin-down state, respectively (See Figure 4.5). For pure spin-up states or spin-down states, the fluctuation (quantum noise) scales with photon number N as $N^{-1/2}$, as expected for shot noise. For mixed states or superposition states, the fluctuation saturates even when the photon number approaches infinity (See Figure 4.6).

One scheme to measure τ is proposed here. Suppose the photon number is so large that the shot noise term in Eq.(4.24) could be neglected. Notice that $\theta_+ = \theta_-$ and when the rotation angle is zero, according to Eq.(4.19) it means τ is $\frac{1}{2}$. If the value $\tau = \frac{1}{2}$ is used in

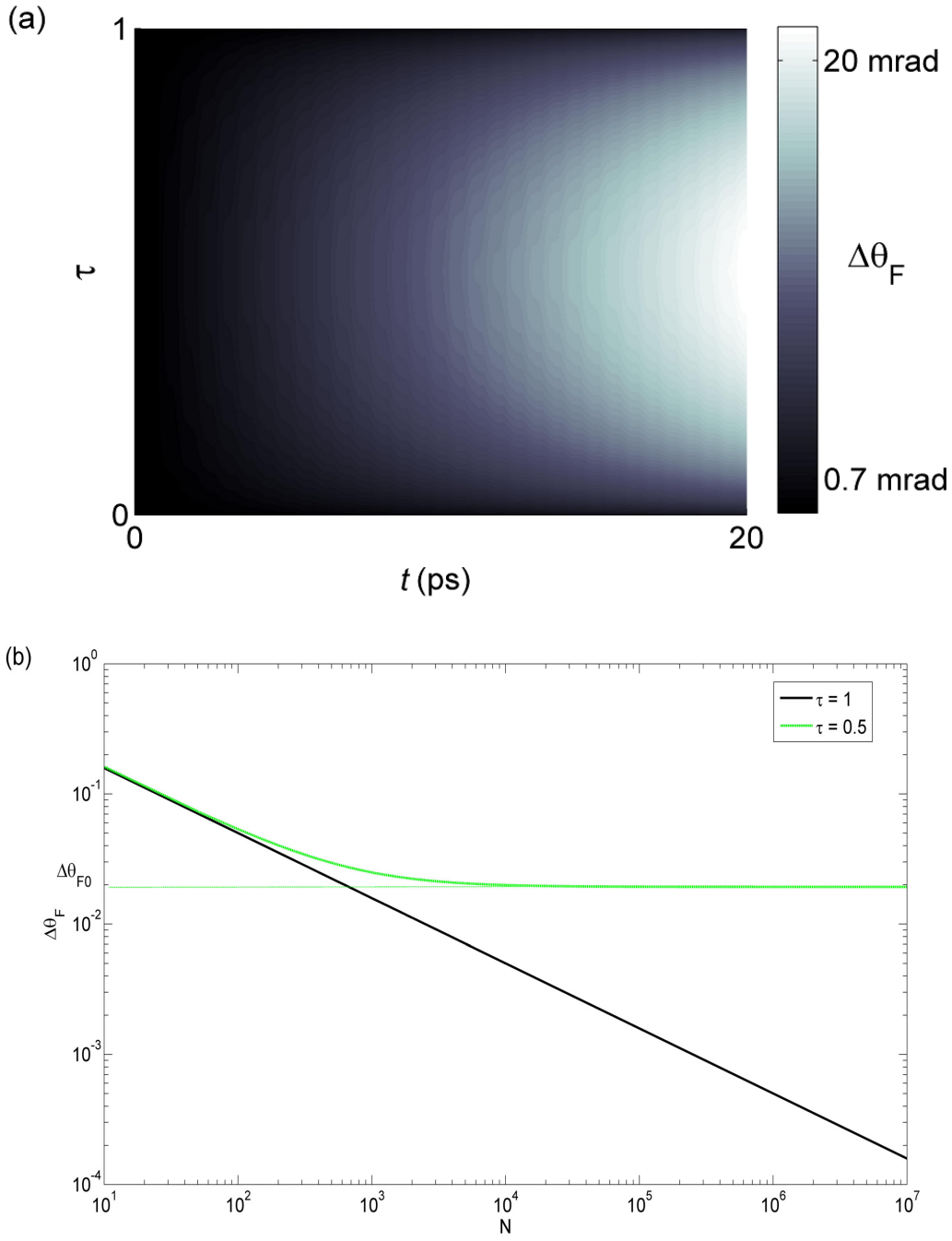

Figure 4.6: (a), Fluctuation of Faraday rotation angle as a function of time and parameter τ. (b), Shot noise and intrinsic noise as a function of photon number N. Shot noise (black line) is from a pure spin-up (spin-down) state, while intrinsic noise (green line) is from a maximally mixed state. In the simulation, the interaction time is chosen to be 20ps in order to make the splitting more obvious, in which case the intrinsic noise saturates at about $\Delta\theta_{F0} = 20mrad$.

Eq.(4.24), one obtains $\Delta\theta_{F0} = \theta_+$. This result implies that one can use the measured values of Faraday angle fluctuation at an extreme value ($\Delta\theta_F$) and at a zero crossing ($\Delta\theta_{F0}$) to measure the purity of the spin state as quantified by τ:

$$\tau = \frac{1}{2}(1 \pm \sqrt{\frac{\Delta\theta_{F0}^2 - \Delta\theta_F^2}{\Delta\theta_{F0}^2 - \frac{1}{4N}}}). \tag{4.25}$$

In the limit of a large number of photons (i.e., where shot noise can be neglected), the above expression simplifies further

$$\tau = \frac{1}{2}(1 \pm \sqrt{1 - \frac{\Delta\theta_F^2}{\Delta\theta_{F0}^2}}). \tag{4.26}$$

The above analysis is based on the assumption that every device in the experiment is perfect, and the noise is only introduced by the quantum state of the electron spin itself. This is, however, not the case in the real experiment. Suppose the overall noise $\Delta\theta_B$ is white noise for the bandwidth in which the experiment is done. It serves as background noise and can be measured by detuning the probe laser, for example. This background contribution can be subtracted from the measured noise $\Delta\theta_M$ and $\Delta\theta_{M0}$, where $\Delta\theta_M$ indicates the measured noise level at extreme points while $\Delta\theta_{M0}$ represents the measured noise at the zero-crossing point. It makes sense to assume the fluctuation due to quantum states is not correlated with the white noise in the device, therefore subtracting the background noise from the measured noise gives the fluctuation due to quantum states

$$\Delta\theta_F^2 = \Delta\theta_M^2 - \Delta\theta_B^2,$$

and

$$\Delta\theta_{F0}^2 = \Delta\theta_{M0}^2 - \Delta\theta_B^2.$$

The Eq.(4.26) therefore becomes

$$\tau = \frac{1}{2}(1 \pm \sqrt{1 - \frac{\Delta\theta_M^2 - \Delta\theta_B^2}{\Delta\theta_{M0}^2 - \Delta\theta_B^2}}). \tag{4.27}$$

Notice that in the above equation, $\Delta\theta_M$ is the *real* noise we see at the extreme points of the rotation angle in the actual experiment. This noise has two sources: external noise, which is $\Delta\theta_B$ and intrinsic noise, which is $\Delta\theta_F$. In the actual experiment, $\Delta\theta_M$ should be larger than $\Delta\theta_B$ due to the fact that the pump for the electron spin is not perfect, therefore the spin that interacts with photons is in a mixed state. However, if $\Delta\theta_M = \Delta\theta_B$, that means the intrinsic noise contribution is zero. From Eq.(4.24), one can see in the limit of large photon number, $\Delta\theta_F = 0$ indicates that τ is either 0 or 1, which is consistent with the result if one plugs $\Delta\theta_M = \Delta\theta_B$ into Eq.(4.27). In other words, if in the real experiment, one observes $\Delta\theta_M = \Delta\theta_B$, then the pumped spin is in either the pure spin-up or spin-down state and one can also pin down the orientation of the spin by looking at the sign of the measured rotation angle.

4.4 CONCLUSION

Using a quantum-mechanical model of Faraday rotation, we find that both the Faraday rotation angle and the fluctuation are functions of the initial electron spin state. If the electron spin is initially in a mixed state, intrinsic noise fluctuations will contain not only shot noise but also intrinsic noise due to weak measurement of the electron's spin state. The reason that this intrinsic noise appears in this scheme is that the measurement done here is non-destructive, and differs from a projective measurement, which causes the collapse of the electron spin wave function to a certain spin direction. Analysis of the noise spectrum should enable quantification of the purity of a given spin state.

5.0 ULTRAFAST LASER CAVITY

As a coherent light source, a laser is the essential part for optical measurements. Generally, the laser systems can be classified into two categories based on the temporal distribution of the output power. If the power is constant in time, the laser is running in a continuous wave mode (Figure 5.1(a)). If the output power is pulsed, the laser is running in a mode-locked mode (Figure 5.1(b)). A mode-locked laser is a laser to which the technique of active or passive mode locking is applied, so that a periodic train of ultrashort pulses is emitted. Mode-locked laser can be applied to a variety of applications such as optical frequency comb [76, 77], pump-probe spectroscopy [78, 79, 80], electro-optical sampling [81, 82, 83, 84] and nonlinear frequency conversion [35, 85, 86].

Mode-locking can be achieved by active modulation of the cavity loss with acoustic-optical modulators or electro-optical modulators [87, 88]. The modulation is performed in such a way that lower laser power experiences more loss than the higher power (Figure 5.2). In this way, a laser pulse with a certain duration can be achieved (usually on the order of a picosecond). Passive mode-locking does not require the presence of an extra modulator inside the cavity, but relies on nonlinear effects such as saturation absorption to realize the modulation of the cavity loss [89, 90]. Since nonlinear effects are typically rapid in time, passive mode-locking can result in much shorter pulse width. In this thesis, we study the passive generation of ultrashort Ti:sapphire laser pulses, in which case the modulation of the cavity loss is realized by the Kerr lensing effect that is produced by the Ti:sapphire crystal [91].

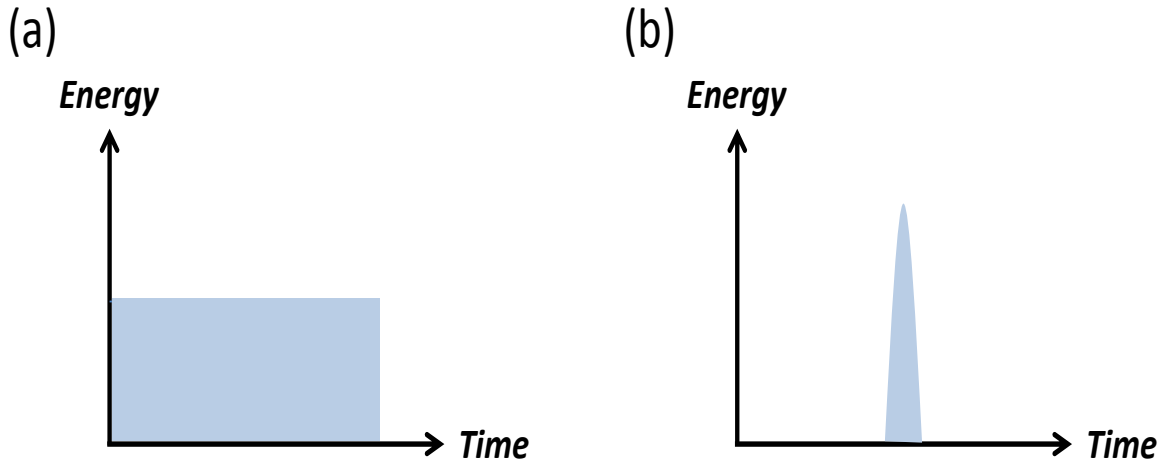

Figure 5.1: Continuous wave mode (a) and mode-locked mode (b) of output laser power.

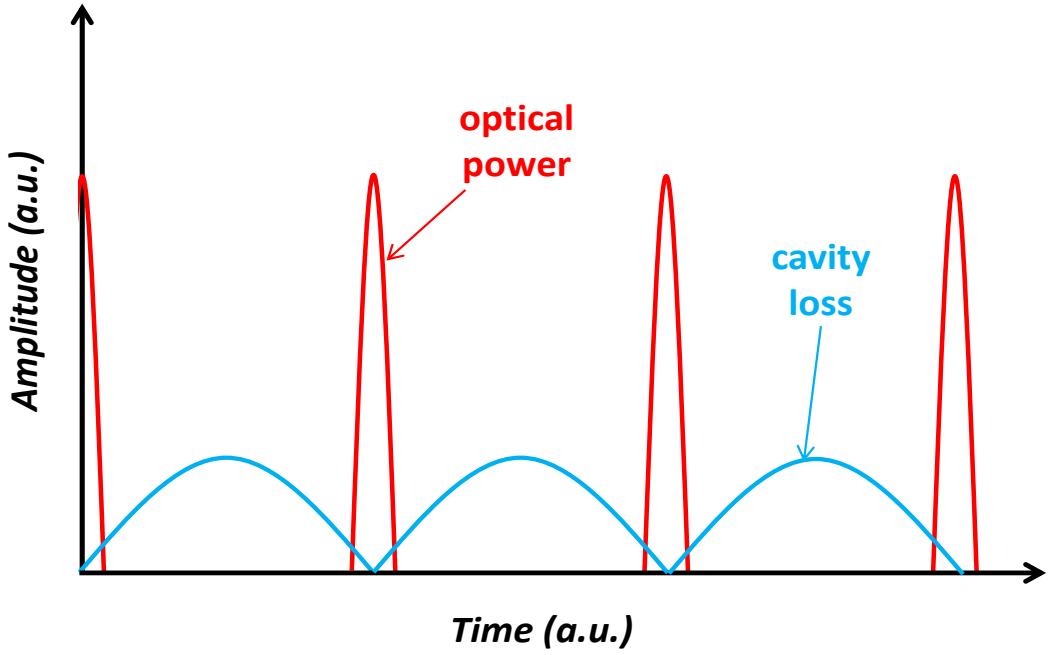

Figure 5.2: Temporal evolution of optical power and losses in an actively mode-locked laser. The modulator causes increased losses for the pulse wings, effectively shortening the pulses.

5.1 MODE-LOCKING

We assume a cavity that can support many frequencies. The central frequency is ω_c, and other frequencies are $\omega_n = \omega_c + n\delta$, where δ is the frequency spacing and $n = -\frac{N-1}{2}, -\frac{N-1}{2} + 1, \cdots, 0, \cdots, \frac{N-1}{2} - 1, \frac{N-1}{2}$. When all the frequency components oscillate in phase, the output field will be a superposition of all fields $E_n = E_0 e^{-i\omega_n t}$. For simplifying the calculation, the amplitude is assumed to be the same and the relative phase is zero.

$$
\begin{aligned}
E(t) &= \sum_{n=-\frac{N-1}{2}}^{\frac{N-1}{2}} E_0 e^{-i\omega_n t} \\
&= E_0 e^{-i\omega_c t} \sum_{n=-\frac{N-1}{2}}^{\frac{N-1}{2}} (cos(n\delta t) + isin(n\delta t)) \\
&= E_0 e^{-i\omega_c t} \sum_{n=-\frac{N-1}{2}}^{\frac{N-1}{2}} cos(n\delta t) \\
&= E_0 e^{-i\omega_c t} (1 + 2\sum_{n=1}^{\frac{N-1}{2}} cos(n\delta t)) \\
&= E_0 e^{-i\omega_c t} \frac{sin(\frac{N}{2}\delta t)}{sin(\frac{\delta t}{2})}.
\end{aligned} \tag{5.1}
$$

This field has its maximum amplitude at $t = \frac{2\pi}{\delta}$. The field amplitude $|E(t)|$ and the width are related to the number of modes that are oscillating in phase: The larger N is, the larger the amplitude $|E(t)|$ is and the smaller the width is (Figure 5.3). Note that the derivation shown here is for a longitudinal mode of the electromagnetic field. Usually for a laser, the transverse mode is desired to be TEM_{00} mode (Gaussian mode). Because in TEM_{00} mode, most of the energy is confined in a single peak, it is the brightest compared to other higher order modes. Secondly, a laser beam in Gaussian mode has the smallest divergence, therefore it is the easiest to be collimated [92]. In the above derivation, the phases of different longitudinal modes are locked, and the laser system in this state is called a mode-locked laser. Theoretical discussion about mode-locking can be found in Ref.**??**.

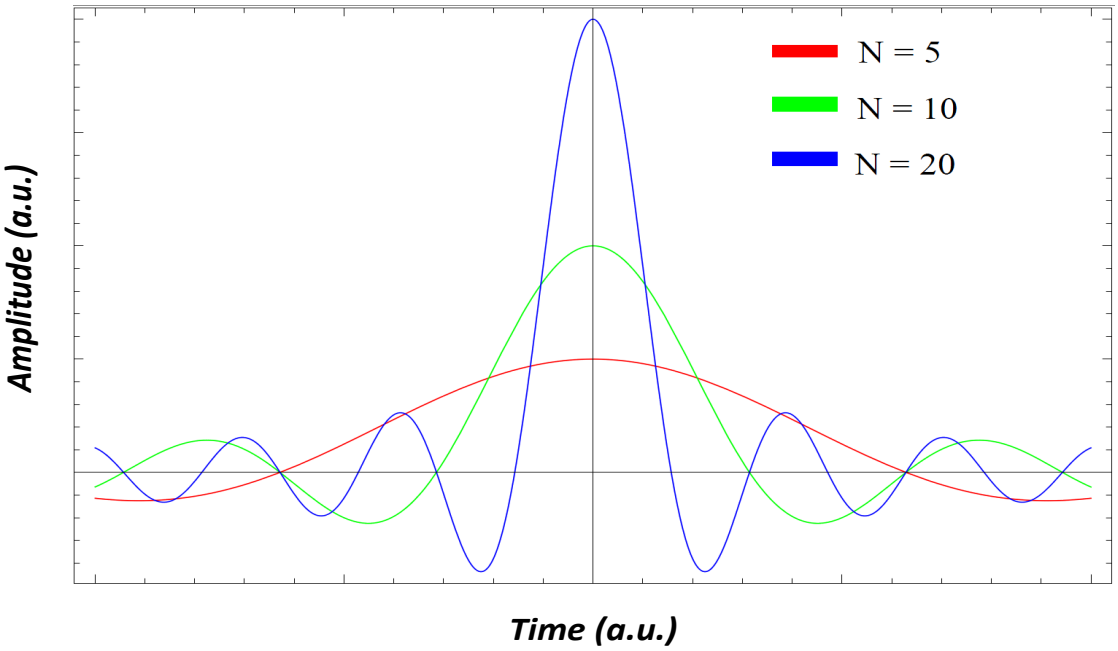

Figure 5.3: Electric field of the mode-locked pulse. The simulation is done for the number of modes N equal to 5, 10 and 20.

The frequency range covered by the N modes is called gain bandwidth, which is determined by the gain medium in the laser. The HeNe laser output wavelength is about 632.8 nm, and the gain bandwidth is around 1.5 GHz, which corresponds to a wavelength range about 0.002 nm. A Ti:Sapphire can have a gain bandwidth about 128 THz, which covers approximately 300 nm wavelength range (See, for example, the website http://micro.magnet.fsu.edu/primer/java/la

Because of its high gain bandwidth, the Ti:Sapphire has been widely used to generate ultrashort laser pulses, ranging from 5 fs to hundreds of fs [38]. In the following, the principle of generating ultrafast pulse is briefly reviewed, based on the nonlinear optics discussed in the previous chapters. A simple mathematical formula is introduced to calculate the cavity stability so that we know how to design and build an ultrafast laser.

The electric field for a laser pulse can be generally expressed as following [36]:

$$E(x,y,z,t) = \frac{1}{2}u(x,y,z)\mathcal{E}(t)e^{i(kz-\omega t)} + c.c. \tag{5.2}$$

where $u(x,y,z)$ and $\mathcal{E}(t)$ describe the spatial and temporal dependence of the electric field respectively. When we want to design a cavity to support ultrashort pulse, we need understand how $u(x,y,z)$ and $\mathcal{E}(t)$ change as the pulse propagates. This problem can be studied by wave propagation equation.

5.2 PULSE SHAPING

In order to achieve certain pulse duration, we need understand the effects that lead to pulse broadening and the ones that shorten the pulse. In both active and passive mode-locking, the most significant factor that limits the pulse width is the chromatic dispersion. To see how dispersion affects the pulse, we can solve the wave equation by treating the nonlinear polarization as a perturbation term. We first focus on the linear polarization $P_L = \varepsilon_0\chi^{(1)}E$. In this case the electric field can be solved analytically. Assuming that the electric field is uniform in both x and y direction, the wave equation is then reduced to

$$\frac{\partial^2}{\partial z^2}E(t,z) = \mu_0\varepsilon_0(1+\chi^{(1)})\frac{\partial^2}{\partial t^2}E(t,z). \tag{5.3}$$

This equation can be solved in the frequency domain by performing Fourier transformation on both sides to obtain

$$\frac{\partial^2}{\partial z^2}E(\omega,z) = -\mu_0\varepsilon_0(1+\chi^{(1)})\omega^2 E(\omega,z). \tag{5.4}$$

It is easy to find the solution for the Fourier component $E(\omega,z)$:

$$E(\omega,z) = E(\omega,0)e^{-ik(\omega)z}, \tag{5.5}$$

where the parameter $k(\omega) = n(\omega)\frac{\omega}{c}$. The function $k(\omega)$ can be expanded as follows:

$$k(\omega) = k(\omega_k) + \frac{dk}{d\omega}(\omega-\omega_k) + \frac{1}{2}\frac{d^2k}{d\omega^2}(\omega-\omega_k)^2 + \cdots$$

The first order derivative $dk/d\omega$ is recognized as $1/v_g$, the inverse of the group velocity. The second order derivative $d^2k/d\omega^2$ is the group velocity dispersion (GVD), and $d^3k/d\omega^3$ is the third order dispersion (TOD), etc.

Sometimes it is useful to express these quantities in terms of refractive index and wavelength. In vacuum, the wavelength $\lambda = \frac{2\pi c}{\omega}$. The derivative

$$d\omega = -\frac{2\pi c}{\lambda^2}d\lambda$$

Therefore we can have

$$\begin{aligned}\frac{dk}{d\omega} &= -\frac{2\pi d(n/\lambda)}{2\pi c/\lambda^2 d\lambda} \\ &= -\frac{\lambda^2}{c}(\frac{1}{\lambda}\frac{dn}{d\lambda} - \frac{n}{\lambda^2}) \\ &= \frac{1}{c}(n - \lambda\frac{dn}{d\lambda})\end{aligned} \tag{5.6}$$

$$\begin{aligned}\frac{d^2k}{d\omega^2} &= -\frac{\lambda^2}{2\pi c^2}\frac{d}{d\lambda}(n-\lambda\frac{dn}{d\lambda}) \\ &= \frac{\lambda^3}{2\pi c^2}\frac{d^2n}{d\lambda^2}\end{aligned} \tag{5.7}$$

The group velocity is then

$$v_g = \frac{c}{n - \lambda \frac{dn}{d\lambda}} \tag{5.8}$$

The GVD is

$$\frac{dv_g}{d\lambda} = \frac{\lambda v_g^2}{c} \frac{d^2 n}{d\lambda^2} \tag{5.9}$$

We assume the temporal dependence of the electric field to be a Gaussian function $E(t) = Ae^{-t^2/\tau^2}$, where the pulse duration is $\tau_p = \sqrt{2ln2}\tau$. Its Fourier transformation is

$$\begin{aligned} E(\omega) &= \frac{A}{\sqrt{2\pi}} \int e^{-t^2/\tau^2} e^{-i\omega t} dt \\ &= \frac{A}{\sqrt{2\pi}} \int e^{-\frac{1}{\tau^2}(t - \frac{i\omega\tau}{2})^2} e^{-\frac{\omega^2\tau^2}{4}} dt \\ &= \frac{A\tau}{2\sqrt{2}} e^{-\frac{\omega^2\tau^2}{4}}. \end{aligned} \tag{5.10}$$

$E(\omega)$ is treated as the initial condition for Eq.5.5. Then the general solution for $E(\omega, z)$ is

$$E(\omega, z) = \frac{A\tau}{2\sqrt{2}} e^{-\frac{\omega^2\tau^2}{4}} e^{-ik(\omega)z}. \tag{5.11}$$

In the time domain the solution is the inverse Fourier transformation

$$E(t, z) = \frac{A\tau}{2\sqrt{2}} \int e^{-\frac{\omega^2\tau^2}{4}} e^{-ik(\omega)z} e^{-i\omega t} d\omega. \tag{5.12}$$

If there is no dispersion, meaning $dn/d\lambda = 0$ (therefore $dk/d\omega = 0$), then Eq.(5.12) simply gives the original pulse function. When there is dispersion but no GVD, which means $dn/d\lambda \neq 0$ and $d^2n/d\lambda^2 = 0$, then Eq.(5.12) is

$$E(t, z) = \frac{A\tau}{2\sqrt{2}} e^{i(\omega_k \frac{z}{v_g} - k(\omega_k)z)} \int e^{-\frac{\omega^2\tau^2}{4}} e^{-i\omega(t - \frac{z}{v_g})} d\omega. \tag{5.13}$$

It is not difficult to see that this integral still preserves the pulse width of the original one. It only shifts the time reference by z/v_g.

However, when the GVD is present, the integral becomes

$$E(t,z) = \frac{A\tau}{2\sqrt{2}} e^{i(\omega_k \frac{z}{v_g} - k(\omega_k)z)} \int e^{-\frac{\omega^2\tau^2}{4}} e^{-i\frac{1}{2}\frac{d^2k}{d\omega^2}(\omega-\omega_k)^2 z} e^{-i\omega(t-\frac{z}{v_g})} d\omega. \tag{5.14}$$

In this case the pulse duration will be [36]

$$\tau' = \tau\sqrt{1 + (\frac{2\frac{d^2k}{d\omega^2}z}{\tau})^2}. \tag{5.15}$$

Eq.(5.15) shows that GVD can lengthen the pulse duration in time.

Another important effect in terms of pulse shaping is self-phase modulation (SPM). As we have seen in Chapter 3, SPM can broaden the spectral width by generating new frequencies. SPM alone cannot alter the pulse duration; however, a shorter pulse can be generated as follows from the Fourier transform of the wider spectral bandwidth. To exploit the broader spectrum for the generation of a shorter pulse, the red and blue components in the temporal wings of the pulse have to be temporarily delayed and advanced, respectively. This means that the group velocity of the red components is slower than the group velocity of the blue components, that is to say, the GVD is negative $dv_g/d\lambda < 0$. Generally, the Ti:sapphire crystal and other materials used for optics have positive GVD (See, for example, Table 7.2 in Ref.[36]). The negative GVD can be introduced by either prism pairs [93] or specially designed mirrors [38, 94, 95]. When the effect of SPM is balanced by the GVD, the pulse duration will be constant in time, which is referred to as a soliton [36, 96]. More advanced techniques such as the spatial light modulator (or pulse shaper) has been invented to provide more sophisticated control of the shape of laser pulses [97].

5.3 GAUSSIAN BEAM AND ABCD MATRIX FORMULA

Now that we have a general propagation equation for electric field, we can plug the field $\mathcal{E}(x,y,z,t)$ into Eq.(1.8). After some algebra[36], we can have a special solution which is the

Gaussian beam[36, 92]

$$E(x,y,z) = \frac{E_0}{\sqrt{1+z^2/\rho_0^2}} e^{-i\Theta(z)} e^{-(x^2+y^2)/w^2(z)} e^{-ik(x^2+y^2)/2R(z)}, \tag{5.16}$$

where

$$\rho_0 = \frac{\pi w_0}{\lambda} \tag{5.17}$$

$$\Theta(z) = arctan(z/\rho_0) \tag{5.18}$$

$$w(z) = w_0\sqrt{1+z^2/\rho_0^2} \tag{5.19}$$

$$R(z) = z + \rho_0^2/z. \tag{5.20}$$

w_0 is the waist of the beam which is defined at $z = 0$ position. The distance $2\rho_0$ is called the Rayleigh range. $R(z)$ is the curvature of the wavefront at position z. When $z = 0$, $R(z)$ goes to infinity which means the wavefront at $z = 0$ is a plane. A single parameter q is defined to characterize the properties of a Gaussian beam

$$\frac{1}{q(z)} = \frac{1}{R(z)} - \frac{i\lambda}{\pi w^2(z)} \tag{5.21}$$

The propagation of a Gaussian beam can be mapped onto the transformation of the parameter $q(z)$ according to the ABCD matrix formalism [36, 98, 92].

In this formalism, the laser beam is modeled as a paraxial ray as shown in the . A paraxial ray is characterized by two parameters: the distance between the ray and the optical axis y and the slope of the ray θ. The optical system can be modeled by its principal planes P_{p1} and P_{p2}. The distances between the principal planes and the input/output planes are x_1 and x_2, respectively.

The parameters of the output ray depend on those of the input ray. This is conveniently written in the matrix form

$$\begin{pmatrix} y_2 \\ \theta_2 \end{pmatrix} = \begin{pmatrix} A & B \\ C & D \end{pmatrix} \begin{pmatrix} y_1 \\ \theta_1 \end{pmatrix} \tag{5.22}$$

The determinant of the transformation matrix is unity:

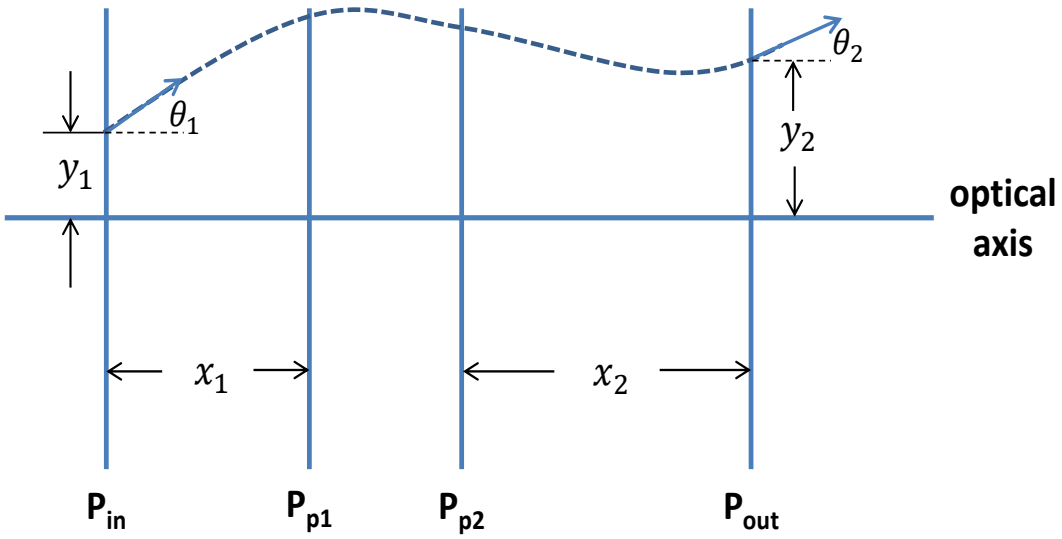

Figure 5.4: Paraxial ray in an optical system

$$AD - BC = 1.$$

The matrix elements are related to the focal length of the optical system and to the position of the principal planes by

$$\begin{aligned} A &= 1 - \frac{x_2}{f} \\ C &= -\frac{1}{f} \\ D &= 1 - \frac{x_1}{f} \end{aligned} \tag{5.23}$$

The ABCD matrix for elemental optical systems are summarized as follows:

By combining the results in Figure 5.5, one can compute the matrix for other optical systems. For example, if a ray travels a distance of d in vacuum before it enters a positive lens with a focal length f, then the output ray from the lens will have the its parameters given by

$$\begin{pmatrix} y_2 \\ \theta_2 \end{pmatrix} = \begin{pmatrix} 1 & 0 \\ -\frac{1}{f} & 1 \end{pmatrix} \begin{pmatrix} 1 & d \\ 0 & 1 \end{pmatrix} \begin{pmatrix} y_1 \\ \theta_1 \end{pmatrix} \tag{5.24}$$

Pay attention to the order of the matrices in above equation. If the initial state of a Gaussian beam is given by q_i, then after the beam passes through an optical system described by a ABCD matrix, the final state q_f will be

$$q_f = \frac{q_i A + B}{q_i C + D}.$$

It should be mentioned that for more careful study of the propagation of laser pulses, a 4×4 matrix is used to include not only the ray properties but also the dispersive effects. Details about the generalized ABCD matrix formalism can be found in [36]. In the study of this thesis, however, we used traditional 2×2 ABCD matrices because those dispersive parameters are difficult to be determined by either experiments or theories. In the following discussion, we will see that the calculation with 2×2 ABCD matrices can provide good enough guidance for designing a cavity.

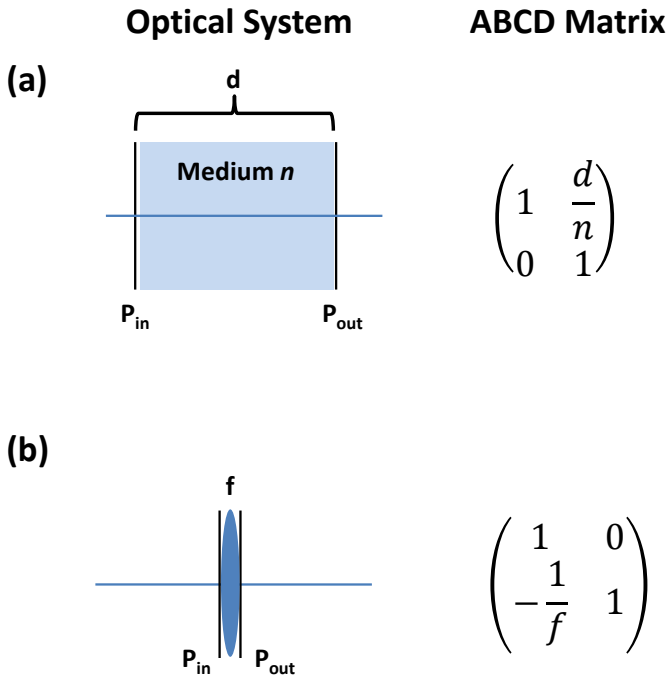

Figure 5.5: ABCD matrix for elemental optical systems. (a), Uniform material with the refractive index n. (b), Convex lens with a focal length f.

5.4 MODELING OF A LASER CAVITY

In order to design a cavity that can be operated in mode-locked mode, ABCD formalism can be exploited to compute the stability of the cavity[1]. Mode-locking can be achieved at the boundary of the stable region. Generally the dynamics of the laser pulse are complicated, and a numerical method is required to solve the equations. A laser cavity can be modeled as the following:

The total cavity length L is determined by the repetition rate f_{rep}.

$$L = \frac{c}{2f_{rep}}. \tag{5.25}$$

The time $t = 2/f_{rep}$ is the time for a pulse to take a round-trip inside the cavity. The total cavity length can be approximately divided into two parts: L_1, which is the length of the path $f_1 - M_2 - M_1$ (See Figure 5.8), and L_2, which is the length of the path $f_2 - M_3 - M_4 - OC$ (See Figure 5.8). The ratio between L_1 and L_2, however, is generally related to the focal length of each focusing mirror [99]

$$\frac{f_1^2}{f_2^2}\frac{L_2 - f_2}{L_1 - f_1} = \gamma. \tag{5.26}$$

In our case, both focusing mirrors have the same focal length, which means $f_1 = f_2$. It is found that when the parameter γ is about $\gamma \approx 1.75$, the cavity favors the mode-locking state to the continuous wave mode [99]. Generally the distance between two focusing mirrors is much smaller than the total length of the cavity. Therefore one approximately has $L \approx L_1 + L_2$. There are two equations for L_1 and L_2

$$\frac{L_2 - f_2}{L_1 - f_1} = 1.75 \tag{5.27}$$

$$L_1 + L_2 = \frac{c}{2f_{rep}} \tag{5.28}$$

From Eq.(5.27)and Eq.(5.28), the length of each arm can be figured out.

[1]The Mathematica codes used for the calculation are listed in Appendix B.

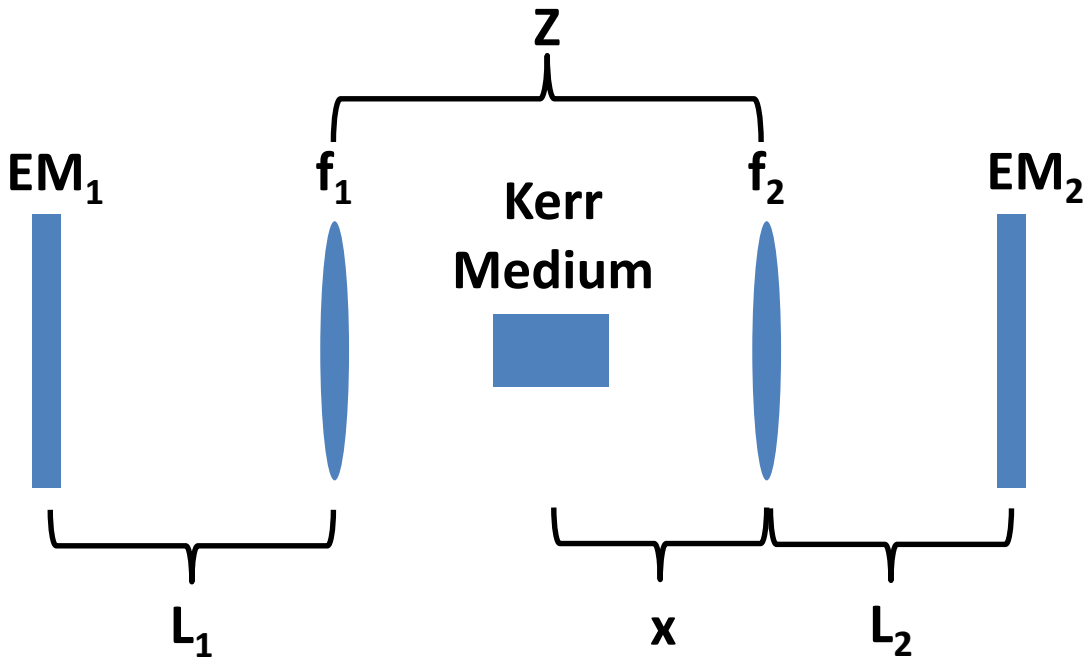

Figure 5.6: Laser cavity model

Astigmatism can cause instable cavity. Because it is the concave mirrors that we use to focus the Ti:sapphire laser, generally when the incident light has a finite angle θ relative to the optical axis of a concave mirror, the concave mirror will focus the light to two different focal points:

$$f_t = \frac{1}{2} R cos(\theta) \tag{5.29}$$

$$f_s = \frac{1}{2} \frac{R}{cos(\theta)}. \tag{5.30}$$

f_t is referred to as the tangential focus while f_s is the sagittal focus. If the angle θ is too large, then these two foci in the Ti:sapphire crystal will be so far away that the pumping efficiency is too low. However, the effective thickness for a Ti:Sapphire crystal with thickness of d in both tangential and sagittal plane is different as well [36].

$$d_t = d \frac{\sqrt{n^2+1}}{n^4} \tag{5.31}$$

$$d_s = d \frac{\sqrt{n^2+1}}{n^2}. \tag{5.32}$$

Therefore under certain conditions, the separation of f_t and f_s can be compensated. The detailed discussion can be found in [100] and [36]. The compensation happens at the incident angle θ

$$\frac{2d}{R} \frac{\sqrt{n^4-1}}{n^4} = \frac{sin^2\theta}{cos\theta}. \tag{5.33}$$

Our simulation can be done in both tangential and sagittal plane, and the details are symmetric except the focus is different. In the following, we will discuss the calculation details for the tangential plane. In order to calculate the conditions for mode-locking to happen, we follow the procedure presented in [101] and [102]. The cavity is divided into two parts: The first part is from the left surface of the Kerr medium, which is Ti:Sapphire in our case, to the end mirror EM_1 then back to the left surface; the second part is from the right surface to the end mirror EM_2 then back to the right surface. We need to compute the ABCD matrix corresponding to these two parts. The first one M_1 is

$$\begin{pmatrix} A_1 & B_1 \\ C_1 & D_1 \end{pmatrix} = \begin{pmatrix} 1 & z-x-d_t \\ 0 & 1 \end{pmatrix} \begin{pmatrix} 1 & 0 \\ -\frac{1}{f_t} & 1 \end{pmatrix} \begin{pmatrix} 1 & L_1 \\ 0 & 1 \end{pmatrix} \begin{pmatrix} 1 & 0 \\ 0 & 1 \end{pmatrix} \begin{pmatrix} 1 & L_1 \\ 0 & 1 \end{pmatrix} \begin{pmatrix} 1 & 0 \\ -\frac{1}{f_t} & 1 \end{pmatrix} \begin{pmatrix} 1 & z-x-d_t \\ 0 & 1 \end{pmatrix} \tag{5.34}$$

The second one M_2 is

$$\begin{pmatrix} A_2 & B_2 \\ C_2 & D_2 \end{pmatrix} = \begin{pmatrix} 1 & x \\ 0 & 1 \end{pmatrix} \begin{pmatrix} 1 & 0 \\ -\frac{1}{f_t} & 1 \end{pmatrix} \begin{pmatrix} 1 & L_2 \\ 0 & 1 \end{pmatrix} \begin{pmatrix} 1 & 0 \\ 0 & 1 \end{pmatrix} \begin{pmatrix} 1 & L_2 \\ 0 & 1 \end{pmatrix} \begin{pmatrix} 1 & 0 \\ -\frac{1}{f_t} & 1 \end{pmatrix} \begin{pmatrix} 1 & x \\ 0 & 1 \end{pmatrix} \tag{5.35}$$

The identity matrix in the middle represents the reflection of a normally incident Gaussian beam. M_1 and M_2 represent the propagation of Ti:sapphire beam outside the crystal. According to the discussion in [101], we must calculate a third matrix M_3 which represent the propagation of the Ti:sapphire beam from EM_1 to EM_2

$$\begin{pmatrix} A_3 & B_3 \\ C_3 & D_3 \end{pmatrix} = \begin{pmatrix} 1 & L_2 \\ 0 & 1 \end{pmatrix} \begin{pmatrix} 1 & 0 \\ -\frac{1}{f_t} & 1 \end{pmatrix} \begin{pmatrix} 1 & x \\ 0 & 1 \end{pmatrix} \begin{pmatrix} 1 & d_t \\ 0 & 1 \end{pmatrix} \begin{pmatrix} 1 & z-x-d_t \\ 0 & 1 \end{pmatrix} \begin{pmatrix} 1 & 0 \\ -\frac{1}{f_t} & 1 \end{pmatrix} \begin{pmatrix} 1 & L_1 \\ 0 & 1 \end{pmatrix} \tag{5.36}$$

Two parameters are introduced to simplify the algebra

$$\alpha_1 = 2\frac{B_1 D_1}{d_t} - \frac{A_1 C_1 d_t}{2} \tag{5.37}$$

$$\alpha_2 = 2\frac{B_2 D_2}{d_t} - \frac{A_2 C_2 d_t}{2} \tag{5.38}$$

The stability of the cavity is described by the function $S = S(x, z)$

$$S(x, z) = A_3 D_3 + B_3 C_3. \tag{5.39}$$

When the value of $S(x,z)$ is in the range $-1 < S(x,z) < 1$, then the cavity can provide output as a stable CW laser [101]. The occurrence of mode-locking is given by the function

$$\delta(x,z) = \frac{1}{w}\frac{dw}{dp},$$

where w is the width of Ti:sapphire laser beam and p is the Ti:sapphire laser power normalized by the critical power P_c which is the power required for self-focusing to happen[103]

$$P_c = \frac{c\varepsilon_0\lambda^2}{2\pi n_2}, \tag{5.40}$$

where λ is the vacuum wavelength of the Ti:sapphire laser and n_2 is the nonlinear refractive index as discussed in the previous chapter. When mode-locking happens, it is required that $\delta(x,z) < 0$ which means that the larger the Ti:sapphire laser power is, the smaller the beam width is, which is exactly the self-focusing effect.

In terms of the ABCD matrix elements, the function δ is written as [101]

$$\delta(x,z) = -\frac{1}{2}\frac{\alpha_1 + \alpha_2 S(x,z)}{\alpha_1^2 + \alpha_2^2 + 2\alpha_1\alpha_2 S(x,z)}. \tag{5.41}$$

By combining the conditions of $-1 < S(x,z) < 1$ and $\delta(x,z) < 0$, we can compute the phase diagram for $S(x,z)$. In Figure 5.7, the two stable regions, where $-1 < S(x,z) < 1$, are separated from each other. Mode-locking can be expected to happen at the boundaries of these two regions [102].

Another question that needs to be addressed is how well the pump laser can spatially overlap with the Ti:sapphire laser. The pumping laser is focused to the Kerr crystal, and its beam waist is assumed to be at the center of the crystal. Ti:sapphire beam is also assumed to have its beam waist at the center of the crystal. From Gaussian optics, we know that at the beam waist, the parameter q should be imaginary [104]

$$q = -\frac{\pi w^2}{i\lambda}, \tag{5.42}$$

where w and λ are the width and the wavelength of the pumping beam respectively. For an optimal mode matching, the beam waist of the pumping laser should be smaller than

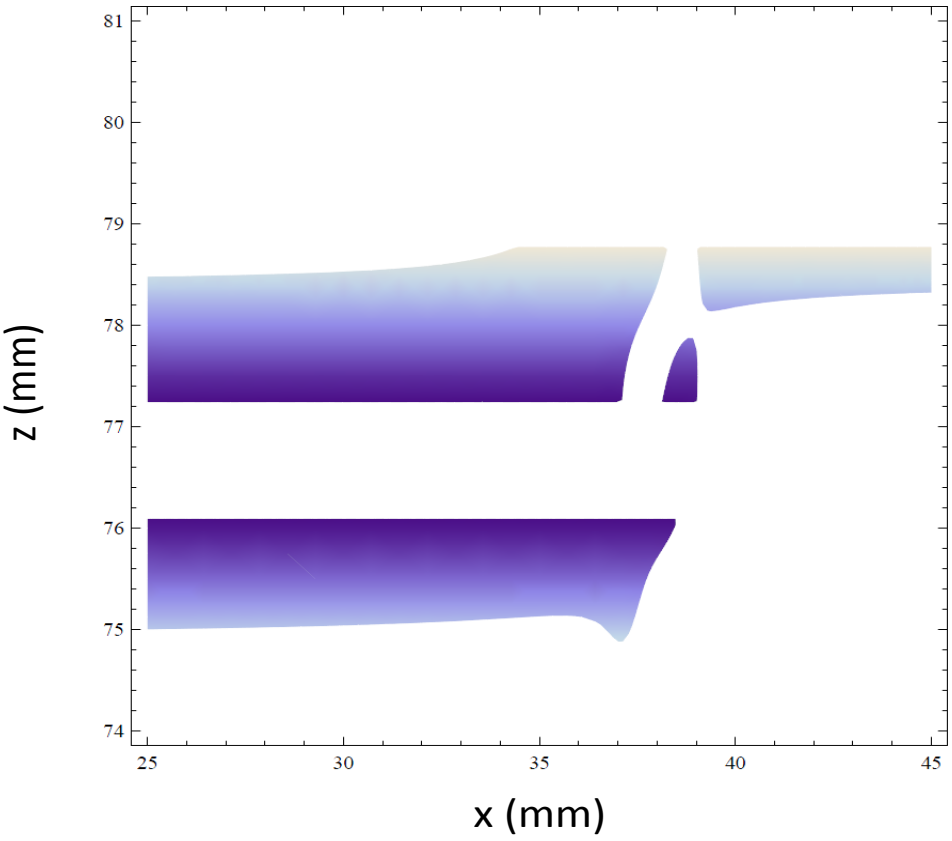

Figure 5.7: Stability of the cavity. The color scale indicates the value of S(x,z).

the beam size of the cavity mode as discussed in [104] and [105]. The q parameter for the pumping beam at the incident plane is

$$q_{p0} = -\frac{\pi w_{p0}^2}{i\lambda_p}, \tag{5.43}$$

where $w_{p0} = 2$ mm is the beam waist at the incident plane, and $\lambda_p = 532$ nm is the pumping wavelength. The ABCD matrix for the pumping beam to go from f lens to the Kerr medium is

$$\begin{pmatrix} A_4 & B_4 \\ C_4 & D_4 \end{pmatrix} = \begin{pmatrix} 1 & x + \frac{d_t}{2} \\ 0 & 1 \end{pmatrix} \begin{pmatrix} 1 & 0 \\ \frac{1}{f_t} & 1 \end{pmatrix} \begin{pmatrix} 1 & y \\ 0 & 1 \end{pmatrix} \begin{pmatrix} 1 & 0 \\ -\frac{1}{f} & 1 \end{pmatrix} \tag{5.44}$$

Note that now the focusing mirror f_2 becomes a negative lens for the pumping light. The q at the waist in the Kerr medium is then given by

$$q_p = \frac{q_{p0} A_4 + B_4}{q_{p0} C_4 + D_4}. \tag{5.45}$$

Since this is the waist of the focused pumping beam, q_p should be imaginary, which requires that

$$\frac{\pi^2 w_p^4}{\lambda_p^2} A_4 C_4 + B_4 D_4 = 0. \tag{5.46}$$

From Eq.(5.46), the relation between the distance y and x can be found, so we can express y as a function $y = y(x)$. This relation can be then plugged into Eq.(5.45) to solve for the beam waist $w_p = w_p(x)$.

On the other hand, the beam waist of the cavity mode in the Kerr medium can be calculated by starting with constructing a ABCD matrix describing a complete cycle of the cavity mode traveling from the center of the Kerr medium, getting reflected at both end mirrors and coming back to the center:

$$\begin{pmatrix} A_5 & B_5 \\ C_5 & D_5 \end{pmatrix} = \begin{pmatrix} 1 & \frac{d_t}{2} \\ 0 & 1 \end{pmatrix} \begin{pmatrix} 1 & x \\ 0 & 1 \end{pmatrix} \begin{pmatrix} 1 & 0 \\ -\frac{1}{f_t} & 1 \end{pmatrix} \begin{pmatrix} 1 & L_2 \\ 0 & 1 \end{pmatrix} \begin{pmatrix} 1 & 0 \\ 0 & 1 \end{pmatrix} \begin{pmatrix} 1 & L_2 \\ 0 & 1 \end{pmatrix} \begin{pmatrix} 1 & 0 \\ -\frac{1}{f_t} & 1 \end{pmatrix} \begin{pmatrix} 1 & x \\ 0 & 1 \end{pmatrix} \begin{pmatrix} 1 & d_t \\ 0 & 1 \end{pmatrix} \begin{pmatrix} 1 & z-x-d_t \\ 0 & 1 \end{pmatrix} \begin{pmatrix} 1 & 0 \\ -\frac{1}{f_t} & 1 \end{pmatrix} \begin{pmatrix} 1 & L_1 \\ 0 & 1 \end{pmatrix} \begin{pmatrix} 1 & 0 \\ 0 & 1 \end{pmatrix} \begin{pmatrix} 1 & L_1 \\ 0 & 1 \end{pmatrix} \begin{pmatrix} 1 & 0 \\ -\frac{1}{f_t} & 1 \end{pmatrix} \begin{pmatrix} 1 & z-x-d_t \\ 0 & 1 \end{pmatrix} \begin{pmatrix} 1 & \frac{d_t}{2} \\ 0 & 1. \end{pmatrix} \tag{5.47}$$

The q paramter for the cavity mode is

$$q_c = \frac{q_c A_5 + B_5}{q_c C_5 + D_5}. \tag{5.48}$$

Again q_c should be imaginary at the waist. Generally, the real part of q_c is a function of x and z. From the phase diagram, we can look for the suitable range of x in the stable region of z by solving the equation

$$Re(q_c(x)) = 0$$

Once we have the range for x, we can solve for the beam waist of the cavity mode

$$w_c(x) = \sqrt{\frac{\lambda_c}{\pi Im(q_c(x))}} \tag{5.49}$$

By comparing $w_c(x)$ with $w_p(x)$, and taking into account the condition $w_p(x) < w_c(x)$ for the optimal mode matching, we can pin down the range of x that leads to the condition for mode-locking to happen with the highest possibility. Once we have the solution for x, we can also solve for y via Eq.(5.46).

In the above discussion, we outline how to calculate the orientation angle for a pair of focusing mirrors in order to compensate the astigmatism. By using ABCD matrix formalism, the distance between the focusing mirrors z, the distance between the Ti:sapphire crystal (Kerr medium) and the focusing mirror x and the distance between the focusing mirror and

the focusing lens for the pumping laser d can all be computed. So far all the calculations are done in the tangential plane. In the sagittal plane, this process can be mirrored. The value of each parameter in both planes shows a slight difference. Nevertheless, calculations discussed here can serve as the guideline for cavity design.

5.5 CAVITY PERFORMANCE

In our customized cavity, the Ti:sapphire crystal is 2 mm thick (CrystalSystem), the focusing mirrors have the radius of 75 mm (Layertec, product number 106234), the repetition rate is designed to be 100 MHz. The cavity folding mirrors are specially designed to compensate the GVD of one another so that each pair has a overall negative GVD (Layertec, product number 102225). In order to have a fine control of the cavity GVD, a pair of fused silica wedges (FemtoLasers, product number OA124) are inserted into the beam path. The transmission of the output coupler (OC) (Layertec, product number 101907) is 5%. The structure of the cavity is shown in Figure 5.8.

Based on the parameters[2] for the intracavity optics shown in Table 5.1, we can calculate the configuration for the cavity (Table 5.2).

The initial configuration (Config. A) can output pulses with about 20 nm FWHM in the spectrum (Figure 8.1(a)). By measuring the pulse duration with a BBO crystal or a GaAsP detector, we find the pulse width is typically about 30 to 40 fs. By replacing folding mirrors (102225 from Layertec) with the ones that have broader bandwidth (103366 from Layertec)(Config. B), the output light can have broader pulse width, which is around 45 nm (Figure 8.1(b)). Calculations based on uncertainty relation shows that the pulse width can be expected to be as short as 15 fs.

[2]The refractive indices are from public resource refractiveindex.info

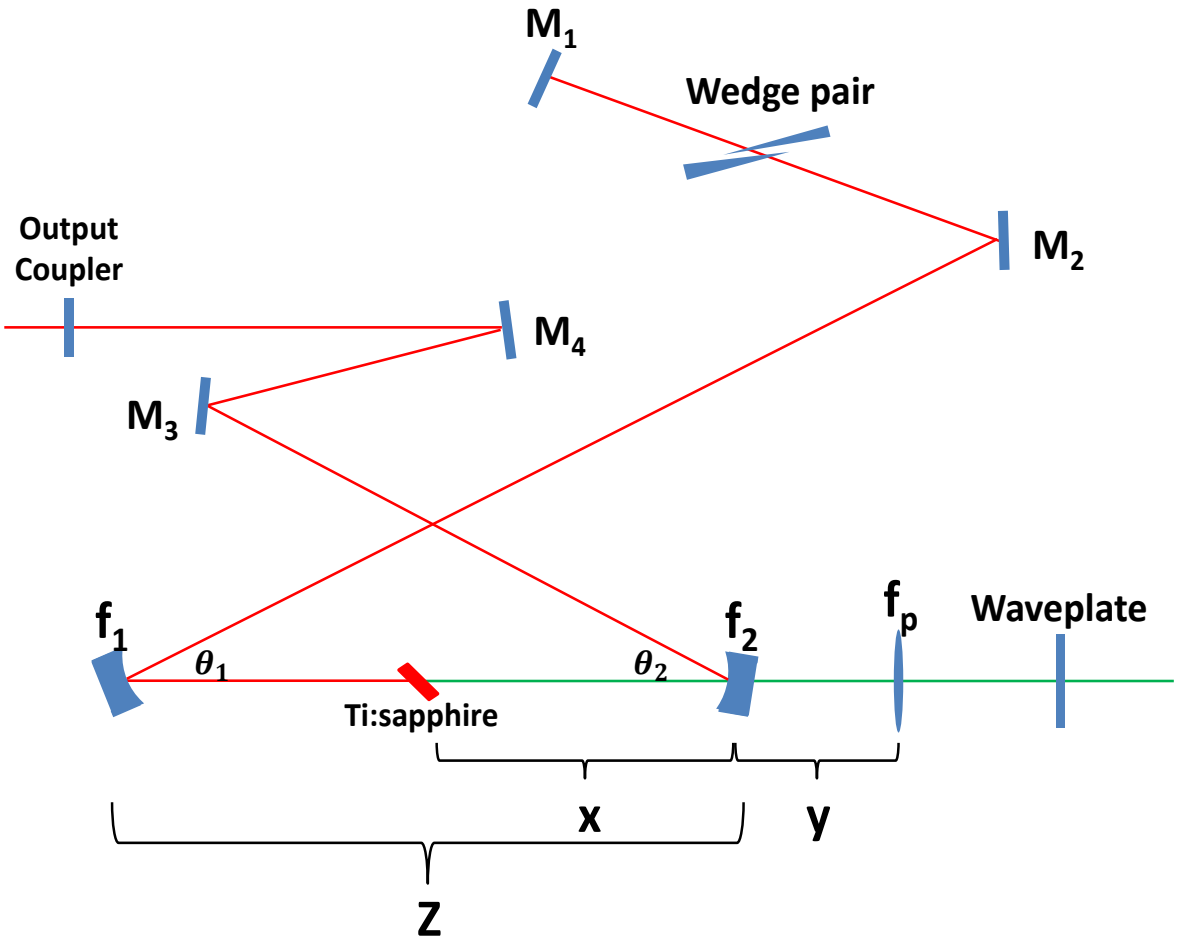

Figure 5.8: Ti:sapphire laser cavity configuration.

Parameter	Value
Crystal thickness	t = 2 mm
Focusing mirror (f_1, f_2) radius	R = 75 mm
Focal length of lens f_p	f_p = 75 mm
Refractive index for Ti:sapphire	n ≈ 1.76 (800 nm)
Refractive index for fused silica	n ≈ 1.45 (800 nm)

Table 5.1: Parameters for intracavity optics.

Parameter	Value
1st Arm length (f_1 to M_1)	$L_1 \approx 944$ mm
2nd Arm length (f_2 to OC)	$L_1 \approx 556$ mm
Folding angle	$\theta_1 = \theta_2 \approx 12°$
Distance x	x $\approx$ 37.5 - 38.3 mm
Distance z	z $\approx$ 77.2 mm
Distance y	y $\approx$ 56 mm
Brewster angle for Ti:sapphire	$\theta_B \approx 60°$
Brewster angle for fused silica	$\theta_B \approx 55°$

Table 5.2: Calculated cavity parameters.

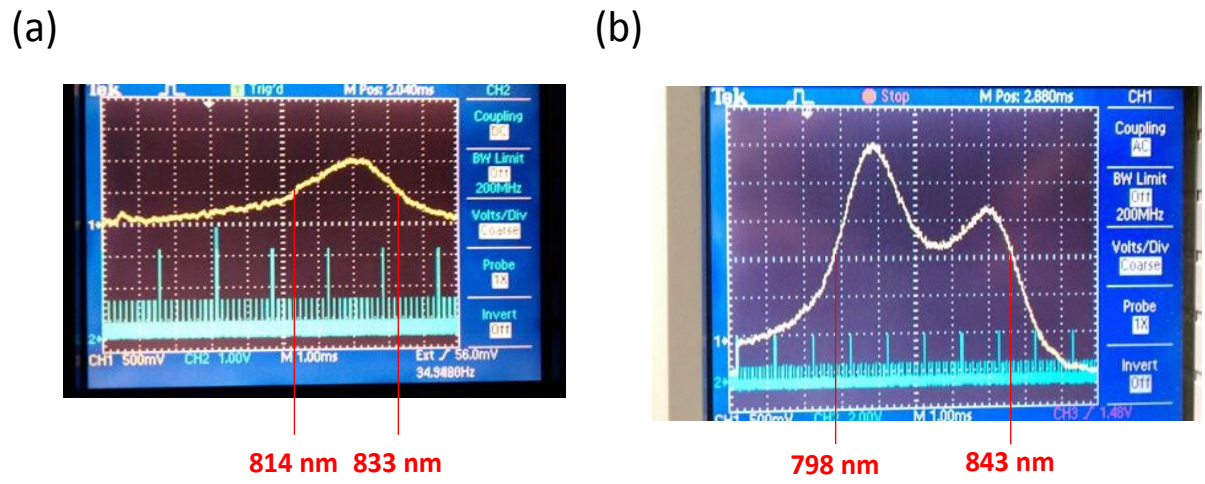

Figure 5.9: The spectrum of the home-built Ti:sapphire laser cavity. (a) The spectrum corresponds to the Configuration A. (b) The spectrum is for Configuration B.

Shape	Intensity Profile $I(t)$	Spectral Profile $S(\Omega)$	τ_p	$\Delta\omega_p$	C_B
Gauss	$e^{-2(t/\tau)^2}$	$e^{-(\Omega\tau/2)^2}$	1.177τ	$2.355/\tau$	0.441
Sech	$sech^2(t/\tau)$	$sech^2(\pi\Omega\tau/2)$	1.763τ	$1.122/\tau$	0.315
Lorentz	$[1+(t/\tau)^2]^{-2}$	$e^{-2\|\Omega\|\tau}$	1.287τ	$0.693/\tau$	0.142
Asym.sech	$[e^{t/\tau}+e^{-3t/\tau}]^{-2}$	$sech(\pi\Omega\tau/2)$	1.043τ	$1.677/\tau$	0.278
Square	1 for $\|t/\tau\| \leq 1$ 0 elsewhere	$sinc^2(\Omega\tau)$	τ	$2.78/\tau$	0.443

Table 5.3: Examples of standard pulse profiles.

5.6 ULTRASHORT PULSE MEASUREMENT

Nowadays, the table-top ultrafast laser can output sub-100 fs pulses. In order to characterize the pulse width, generally, we need something faster in order to sample the pulse. However, this can be challenging practically. A usual way to measure the pulse width is optical autocorrelation. In an autocorrelation measurement, one laser pulse is split into two identical pulses, which interfere with one another in an interferometer. Because the temporal and spectral characteristics of the field are related through Fourier transform, the bandwidth $\Delta\omega_p$ and the measured pulse FWHM τ_p cannot vary independently of each other. There is a minimum bandwidth-duration product (uncertainty relation):

$$\Delta\omega_p\tau_p = 2\pi\Delta f_p\tau_p \geq 2\pi C_B, \tag{5.50}$$

where C_B is a numerical constant on the order of 1, depending on the actual pulse profile (Table 5.3). For example, Figure 5.12 shows the autocorrelation measurement for our customized laser. The measured FWHM is about $\tau_p \approx 53$ fs, and the pulse profile is assumed to be a Sech function. From Table 5.3, the pulse width is $\tau = \tau_p/1.763 \approx 30$ fs.

5.6.1 Field Autocorrelation

The field autocorrelation function is defined as

$$A_f(\tau) = \int E(t)E^*(t-\tau)dt. \tag{5.51}$$

The Fourier transform of $A_f(\tau)$ gives the spectrum of $E(t)$. To see that, we can define the field of light as $E(t) = \mathcal{E}(t)e^{-i\omega t}$, where $\mathcal{E}(t)$ is the field envelop function discussed before. Notice that this envelope function is symmetric in time, namely $\mathcal{E}(t) = \mathcal{E}(-t)$. Therefore

$$E^*(t-\tau) = \mathcal{E}(t-\tau)e^{i\omega(t-\tau)} = \mathcal{E}(\tau-t)e^{-i\omega(\tau-t)} = E(\tau-t)$$

The field autocorrelation function is then

$$A_f(\tau) = \int E(t)E(\tau-t)dt, \tag{5.52}$$

which should be recognized as the convolution of $E(t)$. The Fourier transform of $A_f(\tau)$ is

$$\begin{aligned}
\mathcal{F}(A_f(\tau)) &= \int e^{i\Omega\tau}d\tau \int E(t)E(\tau-t)dt \\
&= \int dtE(t)e^{i\Omega t} \int d\tau E(\tau-t)e^{i\Omega(\tau-t)} \\
&= \int dtE(t)e^{i\Omega t} \int dt' E(t')e^{i\Omega(t')} \\
&= |E(\Omega)|^2
\end{aligned} \tag{5.53}$$

Therefore, field autocorrelation provides information about the spectral amplitude of $E(t)$, while it doesn't capture the information about spectral phase. This forms the basis of Fourier transform spectroscopy [106]. Field autocorrelation can be readily realized in experiments by using a Michelson or Mach-Zehnder interferometer[3] with a linear photodetector which

[3]The difference between Michelson and Mach-Zehnder setup is that a Michelson interferometer uses only one beam splitter to split and recombine pulses while a Mach-Zehnder uses two beam splitters: one for splitting, the other for recombination.

responds to the average intensity of light $I_{ave} = \int dt E(t)E^*(t)$. The measured signal on the detector is then

$$A_f(\tau) = \int (E(t) + E(t-\tau))(E(t) + E(t-\tau))^* dt. \tag{5.54}$$

We can expand this expression

$$\begin{aligned} A_f(\tau) = &\int dt(E(t)E^*(t) + E(t-\tau)E^*(t-\tau)) \\ &+2\int dt(E(t)E^*(t-\tau) \end{aligned} \tag{5.55}$$

When the time delay goes to infinity, we can expect the autocorrelation function to be zero, which means there is no correlation between $E(t)$ and $E(t-\tau)$ if they are separated too far way in time

$$\lim_{\tau\to\infty} A_f(\tau) = 2I_{ave}. \tag{5.56}$$

On the other hand, at zero delay $\tau = 0$, we expect the correlation to be the strongest. The peak value is

$$\lim_{\tau\to 0} A_f(\tau) = 4I_{ave} \tag{5.57}$$

Therefore, we have the ratio

$$\frac{A_f(0)}{A_f(\infty)} = 2:1. \tag{5.58}$$

This result can be seen in Figure 5.10(c). The field autocorrelation is sensitive to the chirp in the pulse: If the instantaneous frequency of a laser pulse depends on time (Figure 5.10(b)) like in the example of self-phase modulation, this effect will be reflected in the field autocorrelation measurement (Figure 5.10(d)).

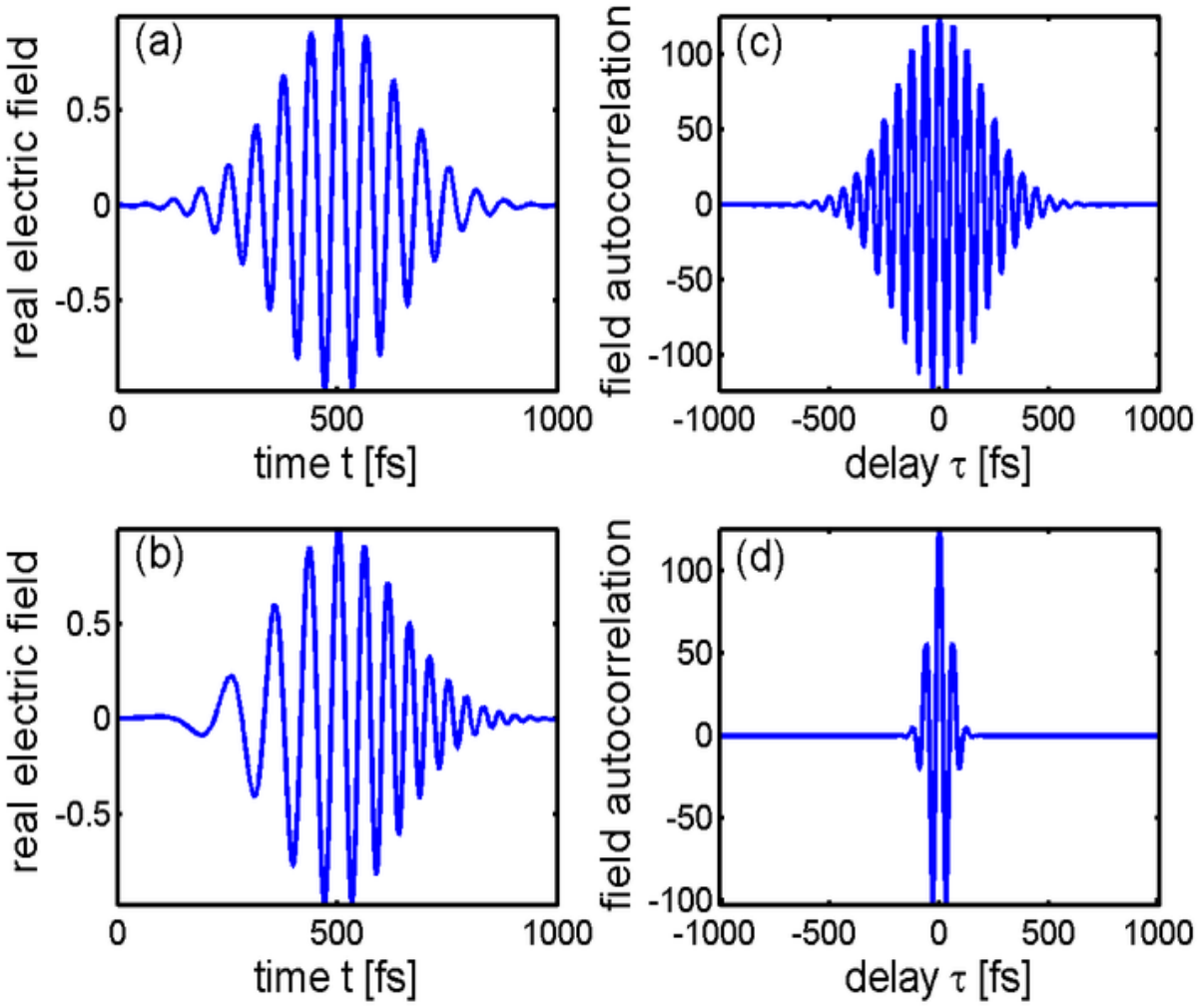

Figure 5.10: Field autocorrelation. (a) The electric field of a laser pulse. (b) The field autocorrelation trace of the pulse in (a). (c) The electric field of a laser pulse of which the instantaneous frequency depends on time. (d) The field autocorrelation trace of the pulse in (c). (*This figure is created by Pgabolde and released on the Wikipedia.)*

5.6.2 Interferometric Autocorrelation

If the photodetector used for an autocorrelation measurement is a nonlinear detector that can respond to I^2_{pulse}, then the interferometric autocorrelation can be carried out. Its functional form is

$$A_i(\tau) = \int ((E(t) + E(t-\tau))(E(t) + E(t-\tau))^*)^2 dt. \tag{5.59}$$

To expand the $A_{int}(\tau)$,

$$\begin{aligned} A_i(\tau) = & \int dt(E^2(t)E^{*2}(t) + E^2(t-\tau)E^{*2}(t-\tau)) \\ & +4\int dtE(t)E^*(t)E(t-\tau)E^*(t-\tau) \\ & + \int dt(E^2(t)E^{*2}(t-\tau) + E^2(t-\tau)E^{*2}(t)) \\ & +2\int dtE(t)E^*(t)(E(t)E^*(t-\tau) + E(t-\tau)E^*(t)) \\ & +2\int dtE(t-\tau)E^*(t-\tau)(E(t)E^*(t-\tau) + E(t-\tau)E^*(t)) \end{aligned} \tag{5.60}$$

By following the same analysis, we can find

$$\frac{A_i(0)}{A_{int}(\infty)} = 8:1. \tag{5.61}$$

In Eq.(5.60), it is not difficult to see there are terms describing fast oscillations: The term $E^2(t)E^{*2}(t-\tau) + E^2(t-\tau)E^{*2}(t)$ is proportional to $cos(2\omega\tau)$; the term $E(t)E^*(t-\tau) + E(t-\tau)E^*(t)$ contains the oscillation $cos(\omega\tau)$. That is the reason that there are oscillation fringes showing up in the interferometric autocorrelation trace (Figure C1(b)). The chirp present in a pulse can also be detected by the interferometric autocorrelation (Figure C1(d)).

Interferometric autocorrelation can be realized by either exploiting the SHG generated by nonlinear optical crystals such as BBO or by measuring the photocurrent produced by two-photon absorption materials such as a GaAsP detector (Hamamatsu, model number G1117). Figure 5.12 shows the interferometric autocorrelation result for the home-built laser. The pulse width is measured as 30 fs.

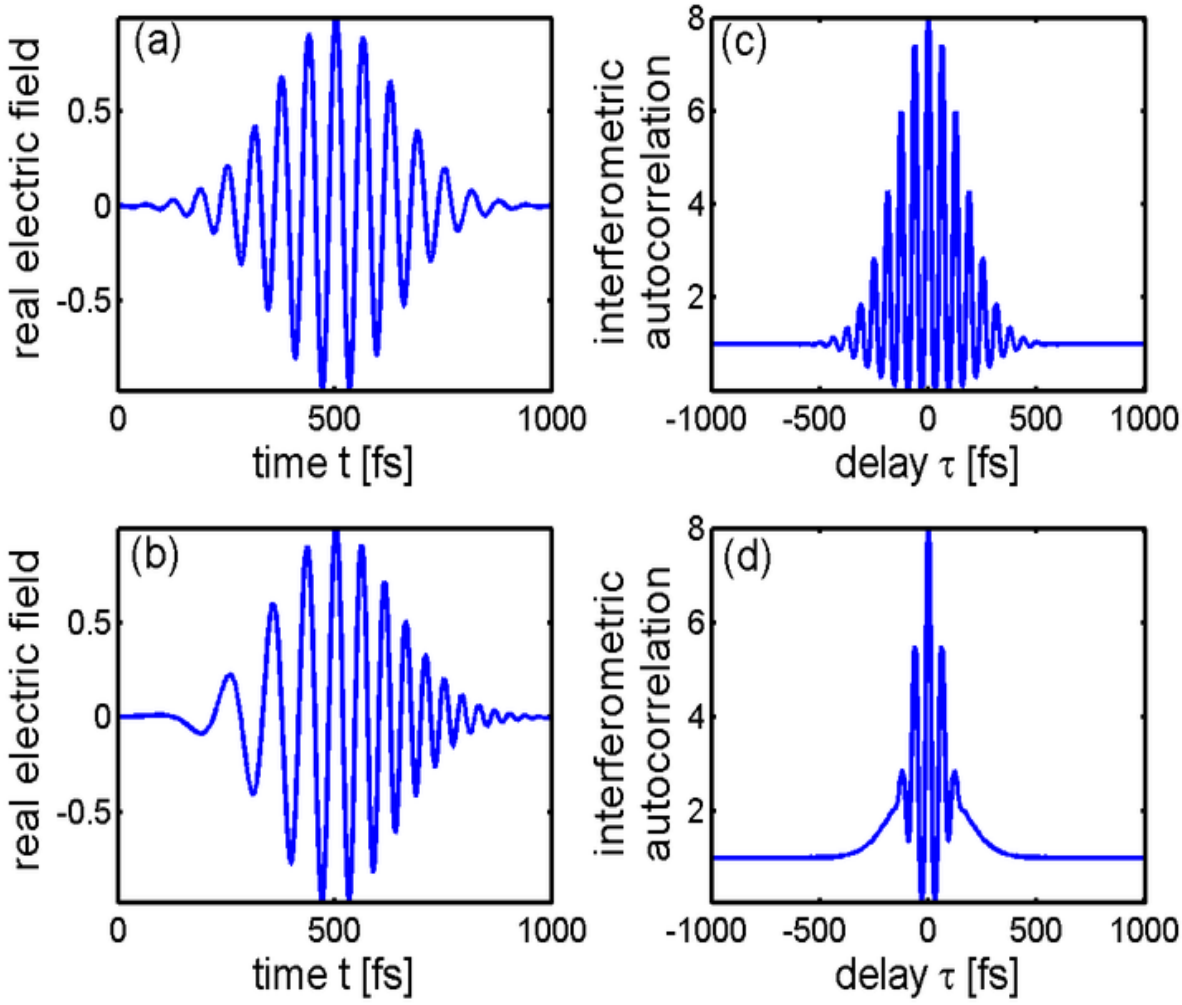

Figure 5.11: Interferometric autocorrelation. (a) The electric field of a laser pulse. (b) The interferometric autocorrelation trace of the pulse in (a). (c) The electric field of a laser pulse in which a certain mount of chirp is present. (d) The interferometric autocorrelation trace of the pulse in (c). (*This figure is created by Pgabolde and released on the Wikipedia.)*

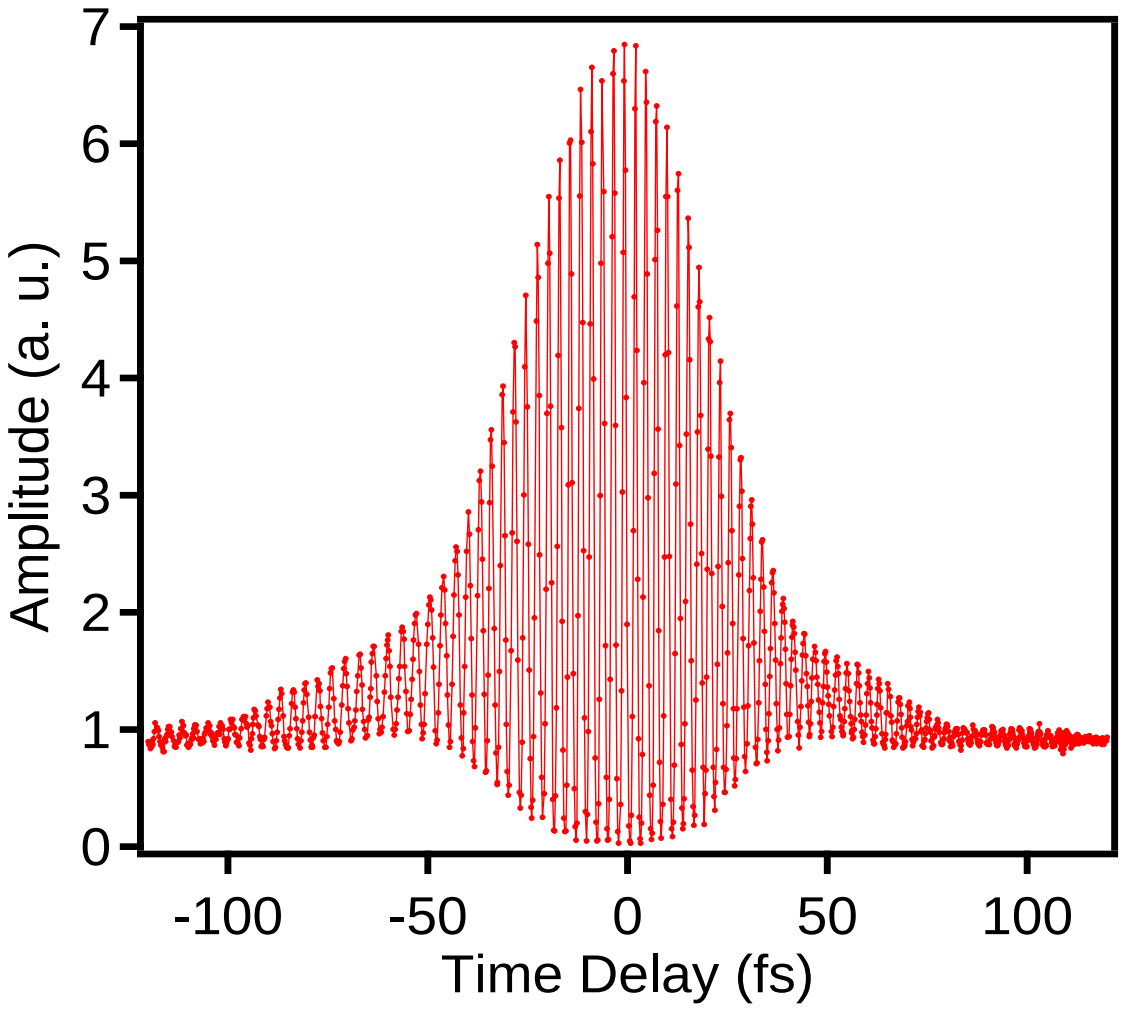

Figure 5.12: Pulse characterization with GaAsP.

5.6.3 Intensity Autocorrelation

If we can somehow remove these oscillating terms in Eq.(C.1), for example, by making two fields have perpendicular polarizations, the resulting autocorrelation function will be

$$\begin{aligned}\bar{A}_I(\tau) = &\int dt(E^2(t)E^{*2}(t) + E^2(t-\tau)E^{*2}(t-\tau)) \\ &+4\int dtE(t)E^*(t)E(t-\tau)E^*(t-\tau)\end{aligned} \tag{5.62}$$

Since it only contains the intensity terms, $\bar{A}_i(\tau)$ is referred to as the intensity autocorrelation function. It is easy to show that

$$\frac{\bar{A}_I(0)}{\bar{A}_I(\infty)} = 3:1. \tag{5.63}$$

Unlike field autocorrelation and interferometric autocorrelation, intensity autocorrelation is not sensitive to the chirp in the pulse (Figure 5.13(d)). Therefore among the three kinds of autocorrelation measurement, interferometric autocorrelation provides the most complete information regarding the characteristics of an optical pulse. In Chapter 7, we will discuss the autocorrelation experiments for the photoconductive nanostructures created at the interface of $LaAlO_3$ and $SrTiO_3$.

Characterization of ultrashort laser pulses is not an easy task. In Appendix C we will discuss some experimental issues about interferometric autocorrelation measurement.

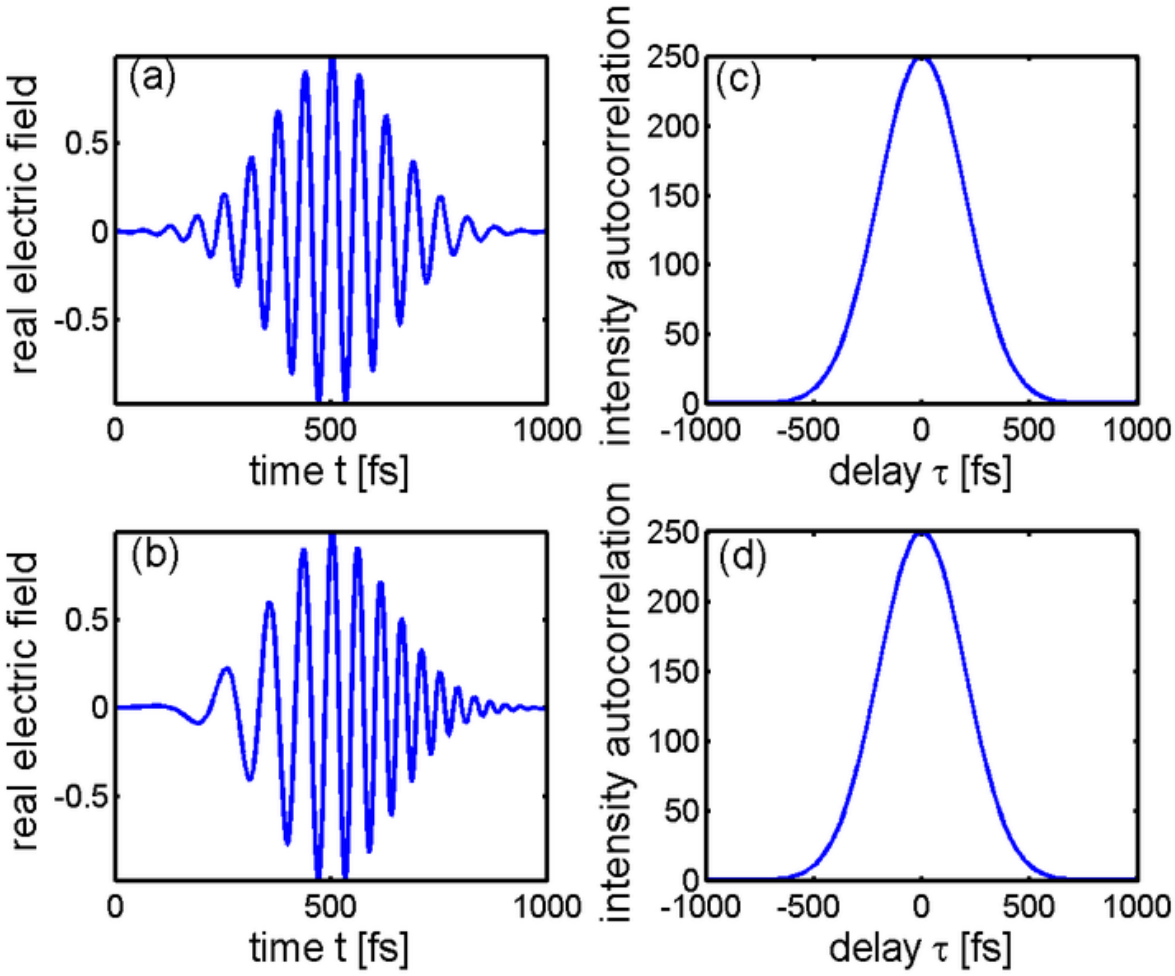

Figure 5.13: Intensity autocorrelation. (a) The electric field of a laser pulse. (b) The intensity autocorrelation trace of the pulse in (a). (c) The electric field of a laser pulse whose instantaneous frequency depends on time. (d) The intensity autocorrelation trace of the pulse in (c). (*This figure is created by Pgabolde and released on the Wikipedia.)*

6.0 INTERFACE PHOTOCONDUCTIVITY

In this chapter, we will discuss the photoconductive nanostructures fabricated at the interface of LAO/STO by c-AFM lithography[1].

Nanophotonic devices are designed to generate, guide or detect light using structures with nanoscale dimensions that are closely tied to their functionality [107, 108, 109, 110]. However, the integration of photonic nanostructures with electronic circuitry [111] remains one of the most challenging aspects of device development. Here we report the development of rewritable nanoscale photodetectors created at the interface between $LaAlO_3$ and $SrTiO_3$. Nanowire junctions with characteristic dimensions of 23 nm are created using a reversible conductive atomic force microscope writing technique [21, 22]. These nanoscale devices exhibit remarkably high gain for their size, in part because of the large electric fields produced in the gap region. The photoconductive response is electric field-tunable and spans the visible to near-infrared regime. The ability to integrate rewritable nanoscale photodetectors with nanowires and transistors in a single material platform foreshadows new families of integrated optoelectronic devices and applications.

6.1 INTRODUCTION

The discovery of a quasi two-dimensional electron gas (q-2DEG) at the interface between insulating oxides [13] has accelerated interest in oxide-based electronics9. The interface between $LaAlO_3$ and $SrTiO_3$ undergoes an abrupt insulator-to-metal transition as a function

[1]P. Irvin, Y. Ma, D. Bogorin, C. Cen, C. W. Bark, C. M. Folkman, C. B. Eom and J. Levy, Nature Photon. 4, 849-852 (2010)

of the number of $LaAlO_3$ layers [15]; for structures at or near the critical thicknesst_c, which is 3 unit cell(u.c.), the conductance becomes highly sensitive to applied electric fields [15]. By applying the electric field locally using a conductive atomic force microscope (c-AFM) probe, one can control this metalinsulator transition with a resolution approaching 1 nm [21, 22]. Devices such as rectifying junctions [23] and transistors [22] can be created, modified and erased with extreme nanoscale precision. Additionally, because $LaAlO_3$ and $SrTiO_3$ are both wide-bandgap insulators, they are essentially transparent at visible wavelengths, making it an interesting material system on which to search for photonic functionality.

6.2 EXPERIMENTAL METHODS

The samples used for experiments are grown by pulsed laser deposition (PLD) at temperature $T = 550\ ^{\circ}C$ and oxygen pressure $P_{O_2} = 10^{-3}$ mbar. In order to probe the interface of $LaAlO_3$ and $SrTiO_3$, low-resistance electrodes are contacted directly to the interfacial quasi-two dimensional electron gas (q-2DEG). Argon ion beam etching is used to mill 25 nm deep into the $SrTiO_3$. Electrodes are then formed by first sputter-depositing a 2 nm Ti adhesion layer followed by 23 nm of Au into the etched region.

Nanostructures are created at the LAO/STO interface by applying positive voltages to the c-AFM tip. Nanoscale insulating gaps are formed by cutting these nanowires with a negatively biased c-AFM tip that passes over the nanowire. Electronic nanostructures can be created with a high degree of precision and, furthermore, are relocatable and reconfigurable. The simplest nanophotonic device consists of a nanowire with a narrow gap or junction. This device was created by first writing the wire with a c-AFM tip bias of $V_{tip} = +10$ V, producing a nanowire with a width of $w_w = 2.5$ nm (Figure 6.1). The junction was created by crossing the wire with $V_{tip} = -10$ V, producing a gap with comparable width $w_w = 2.5$ nm.

In order to locate the working area under an optical microscope, a confocal scanning optical microscope (CSOM) is exploited. The working principle is shown in Figure 6.2.

Ideally, the pinhole passes the light reflected from the focal plane (for example, the plane

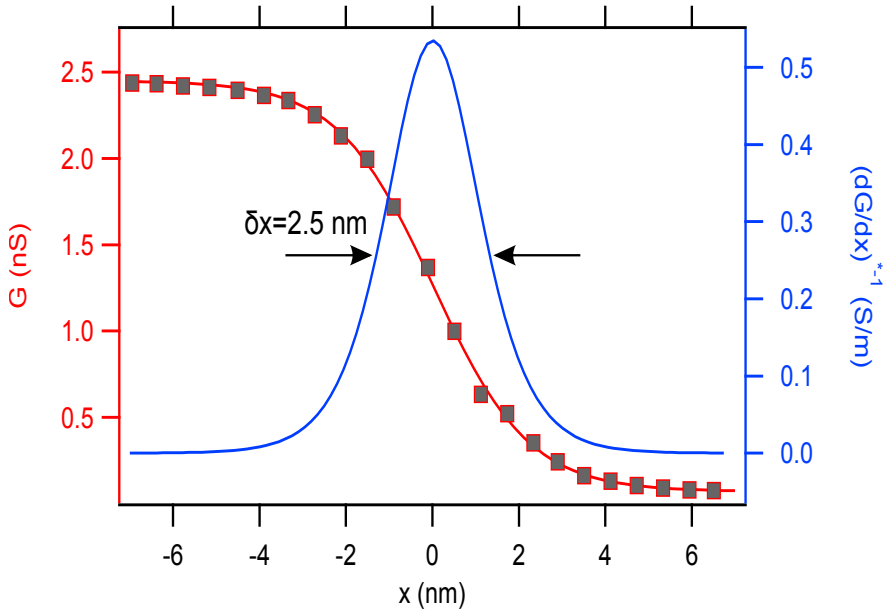

Figure 6.1: Width of wire. Width of wire is determined by moving a reverse-biased tip across the wire while monitoring the conductance G. The change in conductance is fitted to the function $G(x) = G_0 + G_1 tanh(x/h)$. Also plotted is the deconvolved differential conductance (dG/dx), from which we determine the width of the nanowire.

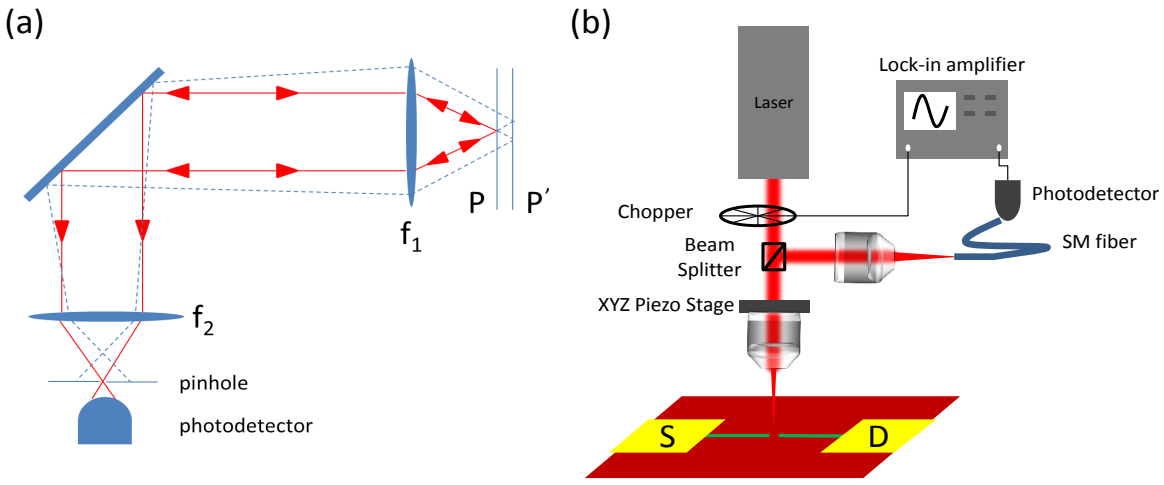

Figure 6.2: Confocal scanning optical microscope (CSOM). (a) The working principle of CSOM. (b) A typical setup of CSOM in experiments.

P in Figure 6.2(a)) but blocks scattering light from any other planes (for example, the plane P' in Figure 6.2(a)). The spatial resolution can be enhanced in this way. Figure 6.2(b) shows a typical setup for CSOM. The reflected light from the sample is collected by the objective, and then coupled into a single mode fiber which has a core size about 8 μm and serves as a pinhole. The light coming out from the fiber is then measured by a Si photodetector. The light is modulated by a chopper and a lock-in amplifier is used to demodulate the output from the Si photodetector. By performing this lock-in measurement, the signal to noise ratio can be enhanced. Figure 6.3 shows a typical reflection image taken by CSOM with a HeNe laser ($\lambda_{HeNe} = 632.5$ nm). The whole scanning area is 30 μm by 30 μm. The surrounding electrodes, which have the width of $4 \sim 5$ μm, can be resolved. Since the gold has much better reflectance than either LAO or STO[2]

Another technique is the scanning photocurrent microscope (SPCM)[112, 113, 114]. In our experiments, the oxide nanostructures are biased with certain voltage. The laser beam is focused onto the sample and raster-scanned over the sample, and the current is measured

[2]Both of them are actually transparent in this wavelength based on their bandgap as we discussed in the Introduction chapter.

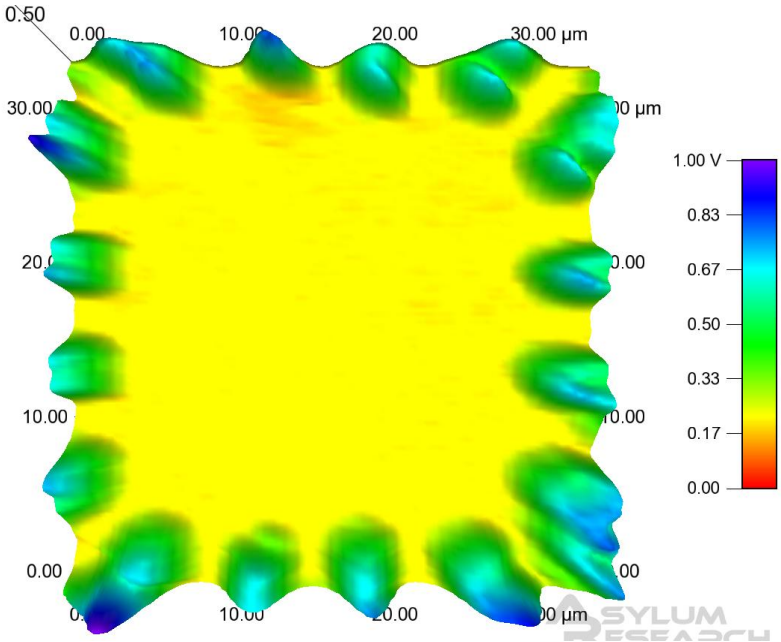

Figure 6.3: Reflection image taken by CSOM with $\lambda = 632.5$ nm. The scanning range is 30 μm by 30 μm. The surrounding gold electrodes, which has a lateral size about 4 to 5 μm are resolved in the image.

as a function of the laser spot position. When the light overlaps with the device a sharp increase in the photocurrent is observed (Figure 6.4). Photocurrent measurements have been performed as long as nine days following c-AFM lithography.

6.3 CHARACTERIZATION OF PHOTOCONDUCTIVITY

The photosensitivity of the devices written at the $LaAlO_3/SrTiO_3$ interface is spatially localized near the gap regions (Figure 6.5). An SPCM image of the photocurrent between two electrodes that do not have a device written between them shows a spatially diffuse photocurrent of less than 2 pA (Figure 6.5(a)). The SPCM image shows a localized photocurrent in the region of the junction (Figure 6.5(b) and (c)). The devices are erasable and reconfigurable. Furthermore, they are not damaged by illumination with I on the order of $KW \cdot cm^{-2}$ intensity. After performing SPCM measurements on the device shown in Figure 6.5(b), the device was erased and a new device created farther from the electrodes (Figure 6.5(c)). The photosensitivity of these devices could be optically modulated at frequencies as high as 3.5 KHz, and the response appeared to be limited by the RC time constant of the device.

The functionality of these devices can be extended by adding an independent gate electrode. Here, we adopt a geometry previously investigated as a nanoscale transistor, a SketchFET[22]. The gate electrode is written perpendicular to the existing sourcedrain nanowire (Figure 6.6).

A gate bias V_{GD} can be used to modify the sourcedrain conductance, enabling conduction between source and drain for positive V_{GD} and inhibiting it for negative V_{GD}. As for the case of the two-terminal wire with junction, photocurrent that is spatially localized near the junction is observed where the device was written (Figure 6.7(a)). A simultaneously acquired laser reflectivity image (Figure 6.7(b)) does not show any observed signature of the nanophotonic detector, such as changes in the absorption or scattering, which is also the case for two-terminal devices.

SPCM images were acquired for an array of source and gate biases. To quantify the

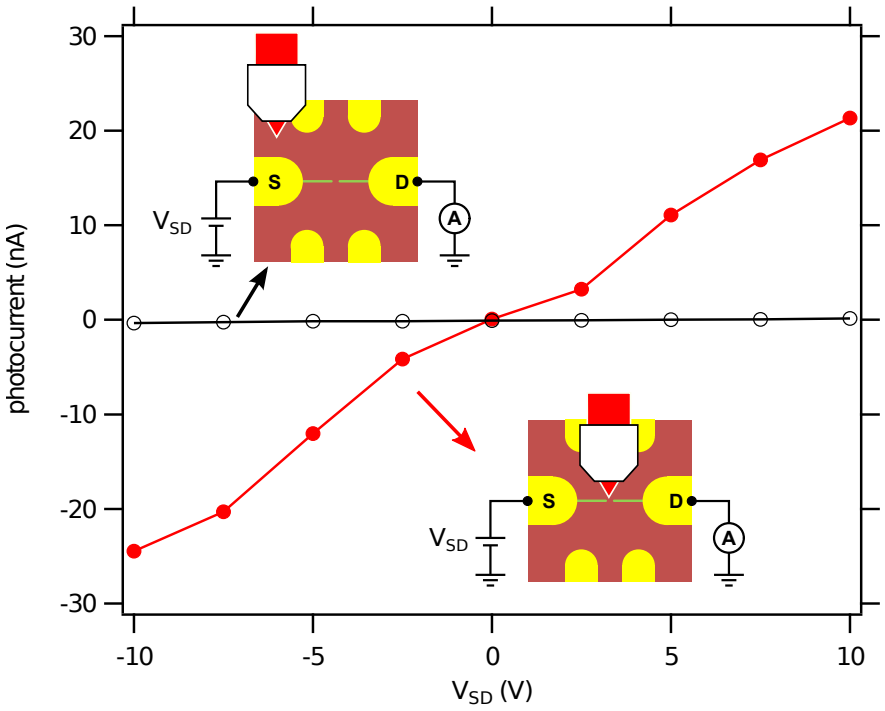

Figure 6.4: Sample photoresponse. Photocurrent collected from a drain electrode (D) versus source bias (V_{SD} applied to a source electrode (S)) when the laser is focused on the photodetector (closed symbols) and 25 mm away (open symbols). Data points are derived from a Gaussian fit to an SPCM image (See the following discussion). (Wavelength,$\lambda = 633$ nm; laser intensity, $I \sim 20\ W \cdot cm^{-2}$ (numerical aperture, NA = 0.73); temperature, T = 80 K.).

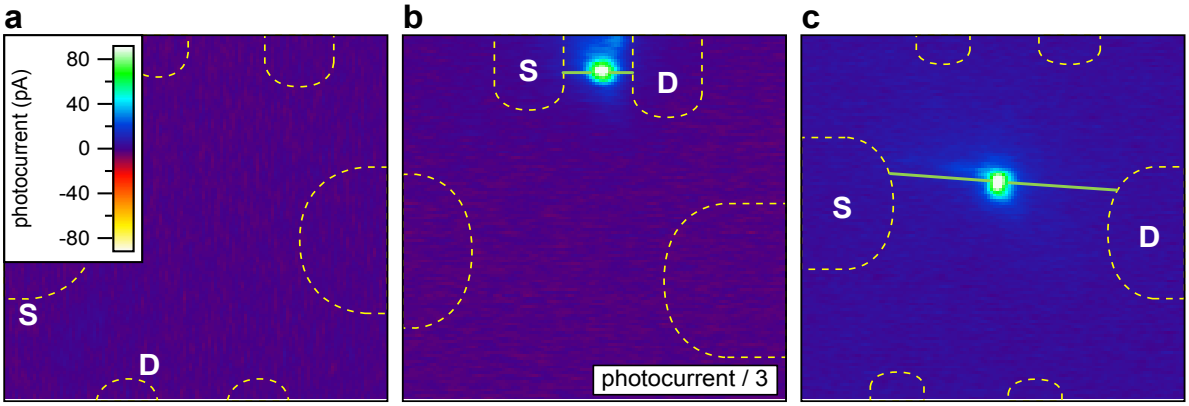

Figure 6.5: Scanning photocurrent microscopy (SPCM) images of various nanostructures written at the $LaAlO_3/SrTiO_3$ interface. Images are 50 $\times$ 50 μm^2. Dashed lines indicate boundaries of areas where electrical contact is made to the $LaAlO_3/SrTiO_3$ interface; solid lines indicate the locations of nanowires. (a) SPCM image of area before any nanostructures are written. (b) SPCM image for a nanowire junction written close to a pair of electrodes. (c) SPCM image formed after erasing the previous nanowire and writing a second nanowire junction in a new location. (d) SPCM image for a set of seven parallel wires with adjacent junctions of width $w_j = 2.5$ nm; the separation between wires is $w_s = 2$ mm. ((a) and (b), $I \sim 20\ KW \cdot cm^{-2}$, $V_{SD} = 0.5$ V; (c) and (d), $I \sim 30\ KW \cdot cm^{-2}$, $V_{SD} = 0.1$ V. All panels: NA = 0.73, T = 300 K.)

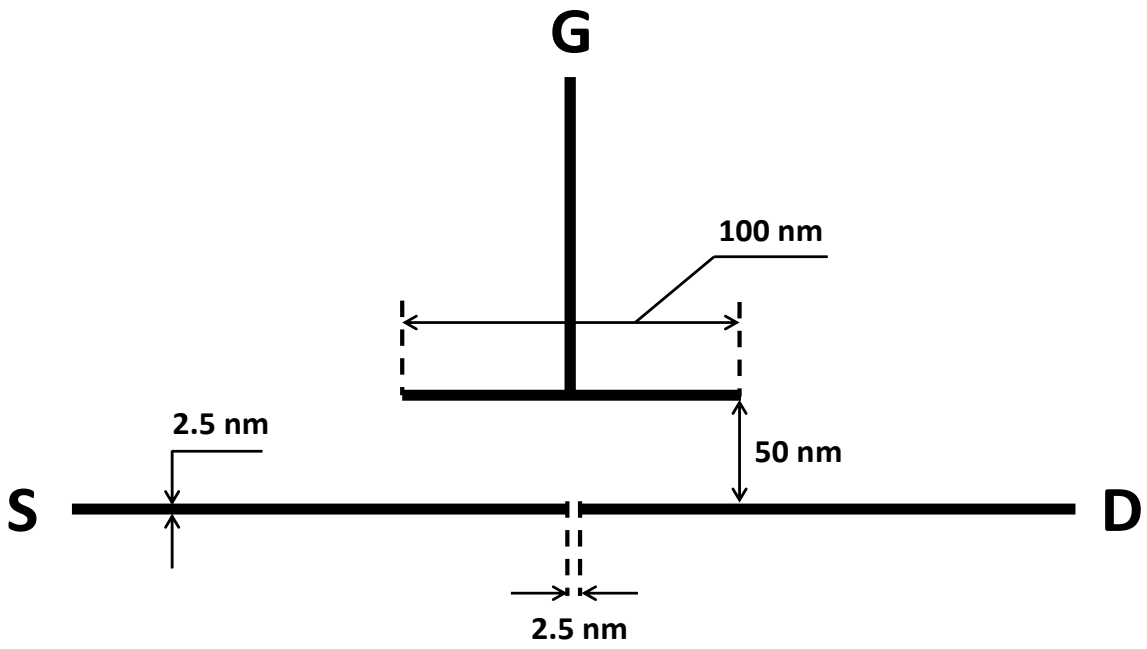

Figure 6.6: Nanophotonic detector geometry. Typical geometry used for three-terminal devices. The source-drain junction width w_j is on the order of the size of the wire width, w_w = 2.5 nm. The gate electrode is positioned 50 nm from the source-drain wire. The T shape helps ensure a uniform electric field from the gate at the site of the junction.

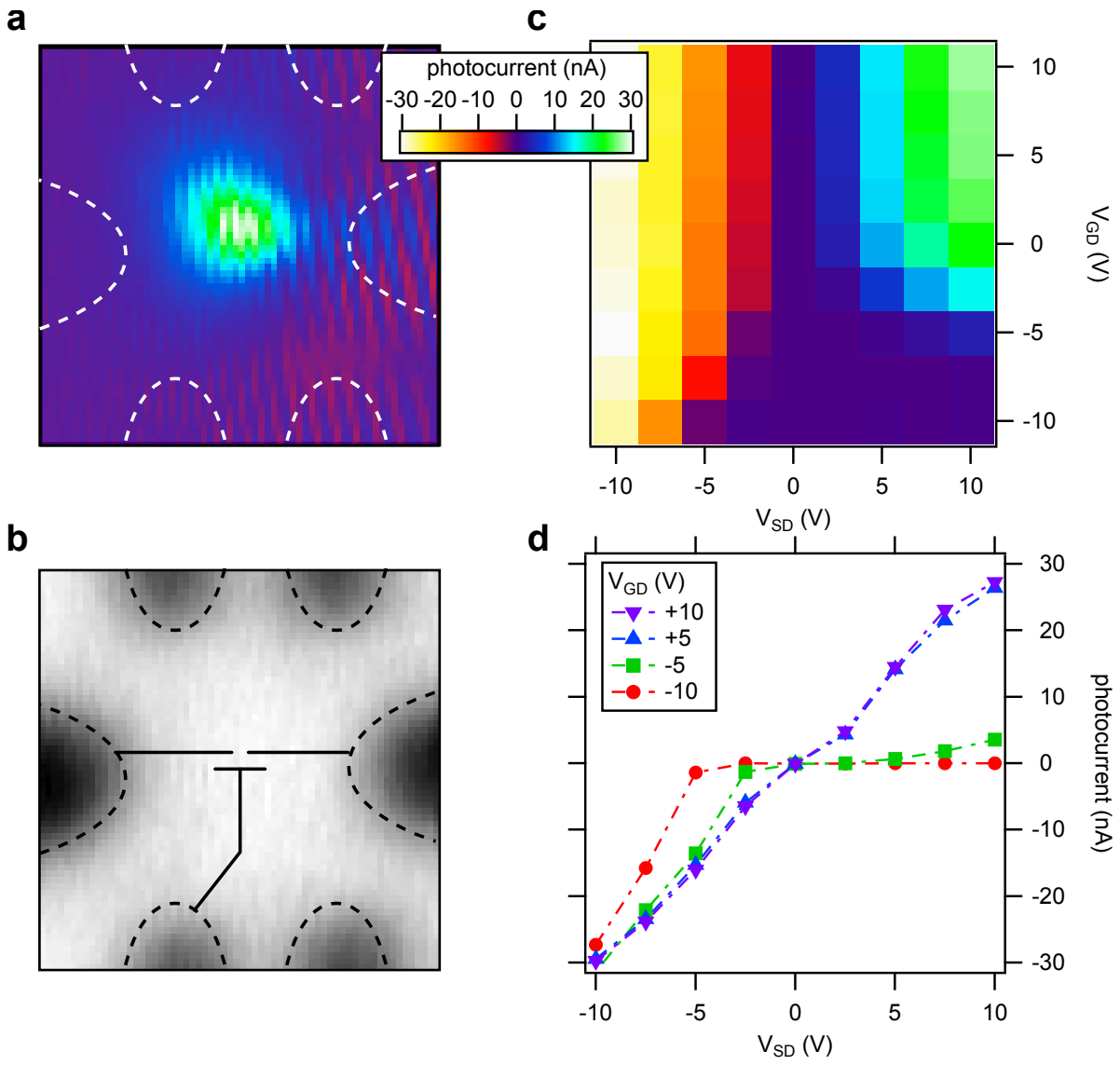

Figure 6.7: Three-terminal, nanoscale, locally gateable photodetector. (a) SPCM image at source and gate biases (V_{SD} and V_{GD}, respectively) of +10 V. (b) Simultaneously acquired reflectivity image. Dashed lines show outlines of electrodes. Solid lines represent nanostructures written with a c-AFM. Both the nanowire widths and gap separations are exaggerated for clarity. Scan size is 50 × 50 μm^2. (c) Photocurrent as a function of V_{SD} and V_{GD}. (d) Photocurrent as a function of V_{SD} plotted for different values of V_{GD}. (I $\sim$ 20 $KW \cdot cm^{-2}$, NA = 0.13, T = 80 K.)

amplitude of the photocurrent response, a two-dimensional Gaussian function is fit to the SPCM images was performed. The image is fit to a two-dimensional Gaussian function

$$f(x,y) = A_0 + A_1 e^{\frac{(x-x_0)^2}{2\sigma_x^2} + \frac{(y-y_0)^2}{2\sigma_y^2}} \tag{6.1}$$

where A_0 is the image offset, A_1 is the amplitude of the 2D peak, x_0 and y_0 are the peak offsets, and σ_x and σ_y are the peak widths. We then define the photocurrent as $i_{PC} = A_1 - A_0$. The amplitude of the Gaussian fitting (photocurrent amplitude) measured as a function of V_{SD} and V_{GD} (Figure 6.7(c)) exhibits a polarity that is always the same sign as V_{SD}, irrespective of V_{GD}, indicating that there is negligible leakage current from the gate to the drain. Furthermore, the photocurrent amplitude is suppressed when V_{SD} is positive while V_{GD} is negative, demonstrating the ability of the gate electrode to tune the photoconductivity in the sourcedrain channel (Figure 6.7(d)).

To investigate the wavelength dependence of these devices, a mode-locked Ti:sapphire laser was focused into a photonic-crystal fibre, which induces very strong self-phase modulation to the laser pulses, to provide tunable laser illumination over the continuous wavelength range $600 - 1000$ nm (ref.[115]). As the white light source power varies with wavelength, the normalized responsivity of the device (i_{pc}/P, where i_{pc} is the photocurrent and P is the laser power) is shown over this wavelength range (Figure 6.8). A reflecting objective (Ealing 25-0506 15X reflecting objective) was used to maintain a constant illumination area versus wavelength. Data points in the vicinity of the pulsed laser source (780 nm) are not shown because of the high peak power and nonlinear effects in the sample (Figure 6.9). A Stark-shifted spectral response is observed with changing V_{GD}. At positive V_{SD}, the photodetector response redshifts as the gate bias is increased. A similar Stark shift is observed when sweeping the source bias(Figure 6.10).

The tuning of the responsivity is enhanced for positive V_{SD}, which is consistent with the behavior demonstrated in Figure 6.7. This evidence of a Stark effect, together with finite-element analysis showing that the electric field is predominantly confined to the gap region (Figure 6.11), indicates that the photo-induced absorption is highly localized.

The intensity dependence of the photocurrent exhibits power-law behavior (Figure 6.9(b)). The photocurrent is assumed to have the intensity dependence as $i_{pc} = AI^m$, where A is a

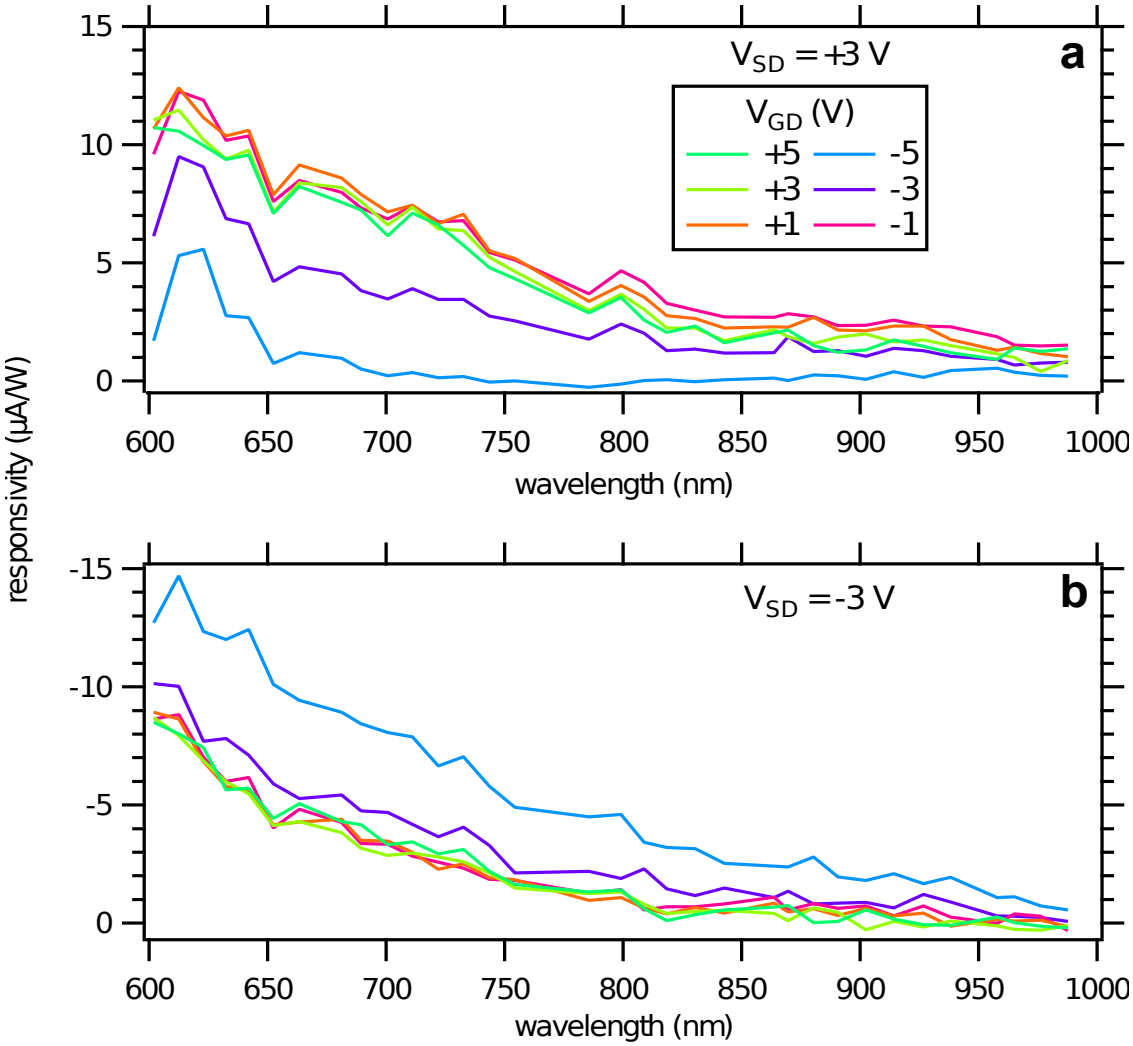

Figure 6.8: Gate-controlled spectral response of photodetector. Fixed position photocurrent as a function of λ and V_{GD} for V_{SD} = +3 V (a) and V_{SD} = -3 V (b). (All panels: NA = 0.28, T = 300 K.)

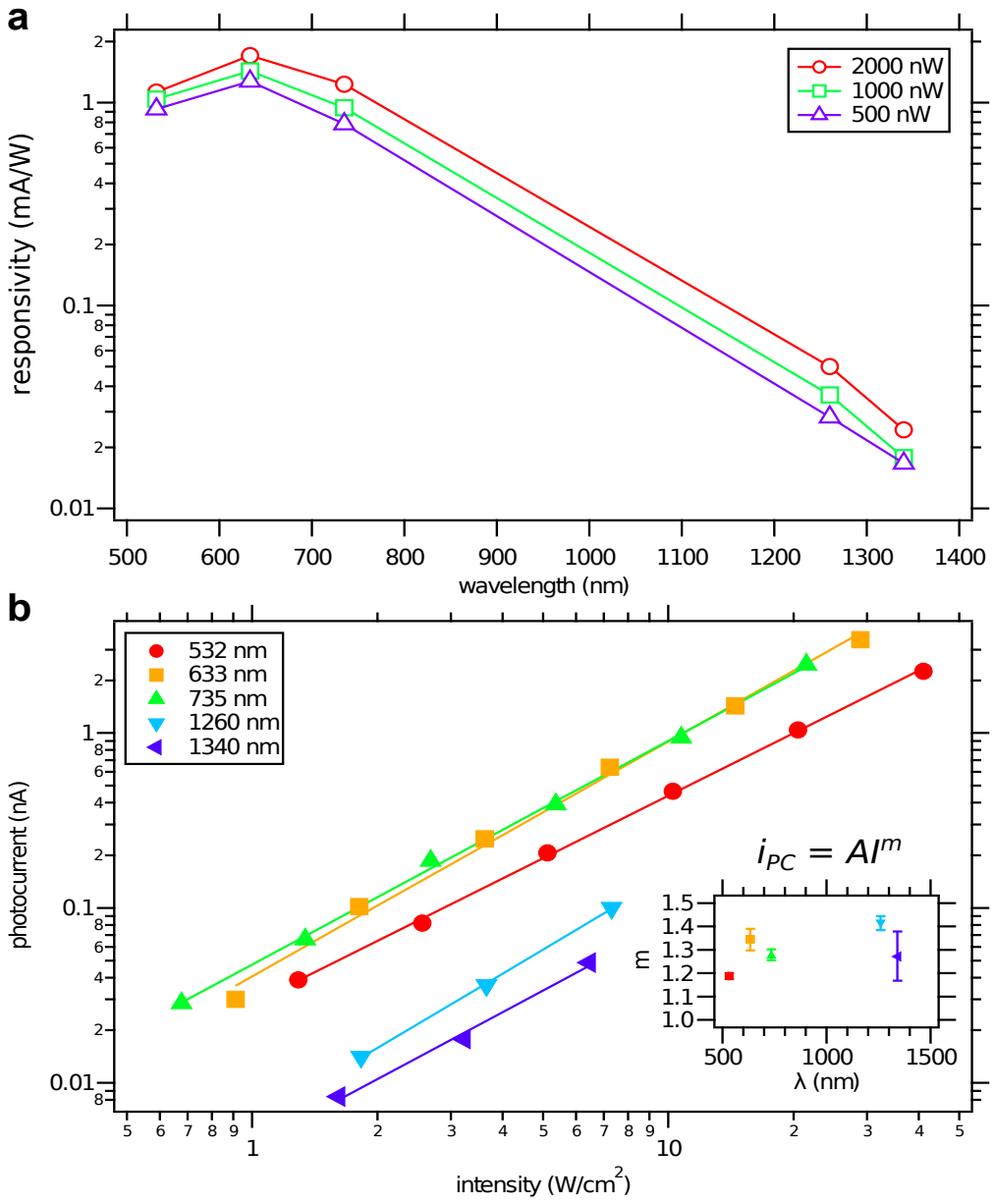

Figure 6.9: Spectral sensitivity and intensity dependence from visible to near-infrared wavelengths. (a) Responsivity of photodetector from 532 nm to 1,340 nm. Symbols are derived from Gaussian fits of SPCM images; lines are guides to the eye. (b) Photocurrent versus optical intensity for different laser wavelengths. Lines are power-law fits. The inset shows the power-law exponent m as a function of wavelength. Error bars represent one standard deviation from the best fit value. (All panels: $V_{SD} = 2$ V, $V_{GD} = 0$ V , NA = 0.13, T = 80 K.)

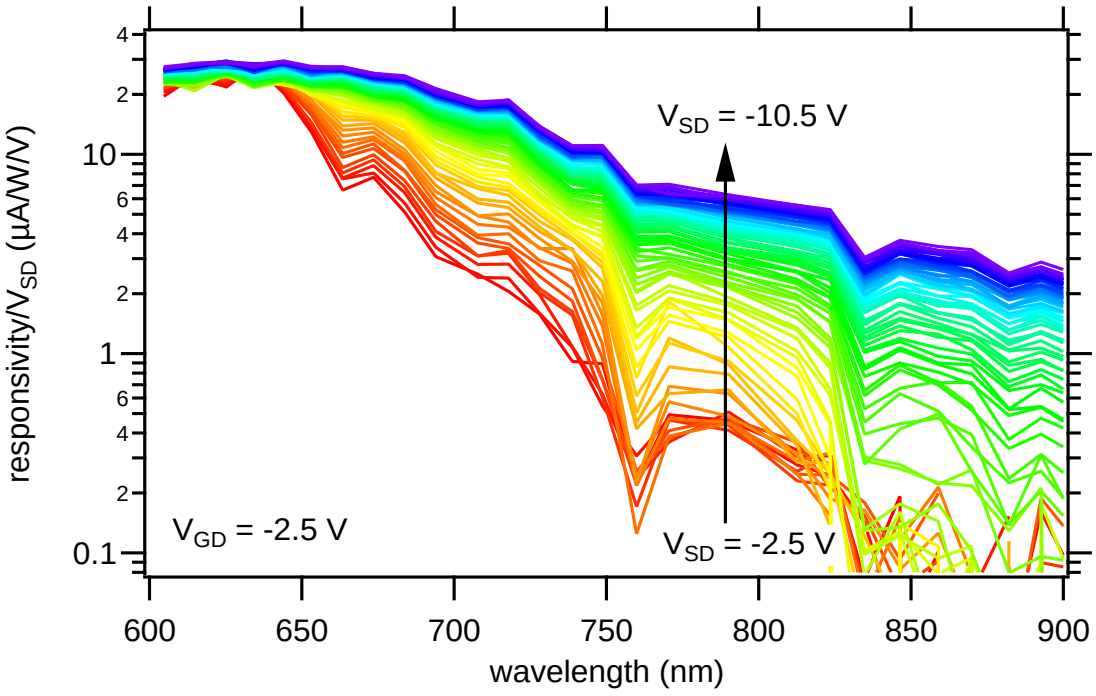

Figure 6.10: Stark Shift with changing source bias. Responsivity, normalized by source voltage (-10.5 V ¡ V_{SD} ¡ -2.5 V), plotted as a function of wavelength. V_{GD} = 2.5 V, NA = 0.28, T = 80 K.

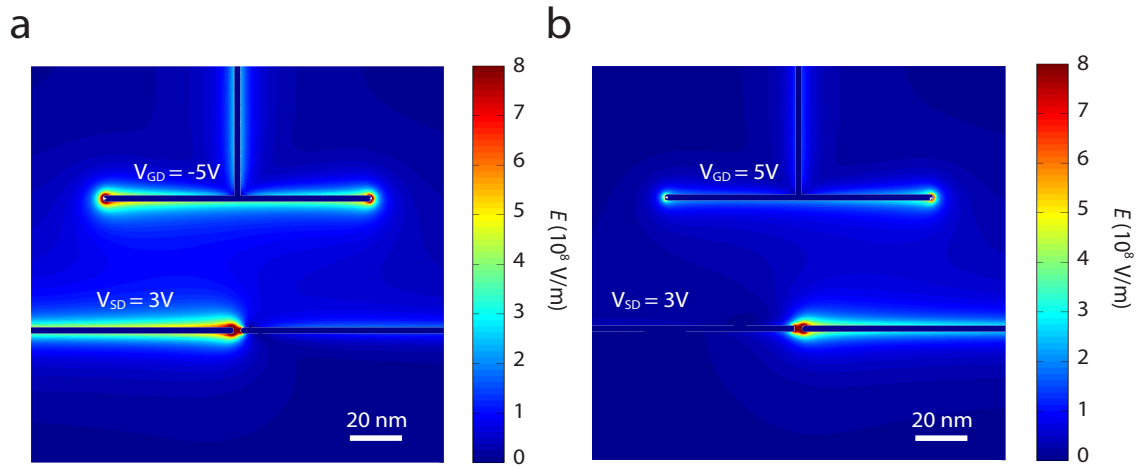

Figure 6.11: Finite element method simulation of electric field E under different bias conditions. (a) V_{SD} = 3 V, V_{GD} = -5 V and (b) V_{SD} = 3 V, V_{GD} = 5 V, assuming dielectric constants ε_{STO} = 300, ε_{LAO} = 24, ε_{air} = 1 and conductive region thickness of 2 nm.

proportionality constant, I is the laser intensity, and $m \sim 1.2$ to 1.4. The super-linear scaling with laser intensity is similar to other systems that are near a metalinsulator transition [116, 117].

There are several possible mechanisms for the photoconductivity. The direct and indirect bandgaps of $SrTiO_3$ (Eg 3.75 eV and 3.25 eV, respectively [19]) are too large to explain the visible to near-infrared photoresponse. Above-band photoexcitation of $SrTiO_3$ can produce excitonic luminescence at visible wavelengths, indicating the existence of mid-gap states [118, 119, 120]. The most readily formed mid-gap states are associated with oxygen vacancies, which are known to form during substrate preparation [121, 122, 123] and growth of LAO/STO heterostructures [124, 125, 126]. Localized states just below the conduction band have been probed via transport in $SrTiO_3$-based field-effect devices [127]. Unintentional doping of $SrTiO_3$ substrates (such as Cr, Fe or Al) can also contribute states within the bandgap [128].

Electrons occupying mid-gap states can be optically excited into the conduction band

using sub-bandgap light. The photoexcited electrons are swept across the junction by the large electric field($E = V_{SD}/w_w \sim 100 \quad MV \cdot cm^{-1}$), resulting in photocurrent. The spectral sensitivity we observe(Figure 6.8 and Figure 6.9) is consistent with previous optical measurements on oxygen vacancy-rich samples [122, 123, 125, 129]. Along the nanowire and sufficiently far from the gap, photo-induced current is negligible because the electric field are screened or otherwise sufficiently small.

6.4 CONCLUSION

The rewritable photodetectors presented here bring new functionality to oxide nanoelectronics. For example, existing nanowire-based molecular sensors [130] rely on the ability to bring an analyte into contact with the sensing area of the detector. Here the roles are reversed: a nanoscale photodetector can be placed in intimate contact with an existing molecule or biological agent. It may be possible to take advantage of the significant Stark-shifted photoresponse to improve the spatial sensitivity well beyond the diffraction limit. The ability to integrate optical and electrical components such as nanowires and transistors may lead to devices that combine, in a single platform, subwavelength optical detection with higher-level electronics-based information processing.

7.0 BROADBAND TERAHERTZ GENERATION AND DETECTION AT TEN NANOMETER SCALE

Terahertz (0.1 THz-30 THz) radiation reveals a wealth of information that is relevant for material, biological, medical and pharmaceutical sciences, with applications that include chemical sensing, homeland security and high-speed electronics. To date, there have been no methods capable of controlling THz radiation at molecular scales. Here we report both generation and detection of broadband terahertz radiation from 10-nm-scale oxide nanojunctions. Frequency components of ultrafast optical radiation are mixed at these junctions, producing broadband THz radiation. These same devices can detect THz radiation with comparable spatial resolution. This unprecedented control, on a scale of four orders of magnitude smaller than the diffraction limit, creates a pathway toward ultra-high-resolution near-field THz imaging, single-molecule fingerprinting, spectroscopic characterization of catalysts, and other applications.

7.1 INTRODUCTION

Terahertz (THz) radiation, with photon energies ranging from a few meV to a hundred meV, is relevant for a wide range of applications and investigations. Examples include chemical sensing[131], far-infrared optical properties of biomolecules like DNA [132], quantification of crystallinity and polymorphism for drugs [133], THz spectroscopy of catalysts [134], and investigations of electron-hole plasmas in III-V semiconductors [135]. A variety of materials have been investigated for generating broadband THz emission, including photoconductive emitters[136, 137, 83, 138], crystals such as ZnTe [139, 82], GaSe [81], GaAs [140, 141, 142],

CdTe[142], $LiNbO_3$[143] and gases [144].

THz detection can be achieved by a complementary set of approaches, including photoconductive dipole antenna fabricated on low-temperature grown GaAs (LT-GaAs) [131, 137, 145], electric-optic (EO) sampling with crystals like ZnTe [81, 82] and $LiTaO_3$ [83, 84], pyroelectric detectors [144], bolometers [146], Schottky barrier diodes [147], superconductor-insulator-superconductor junctions [148], and a single-photon detector [149].

One important application of THz spectroscopy is in the area of high-resolution imaging and sensing. Nanoscale THz sources [150] and submicron detectors [151] have been experimentally realized. Terahertz near-field imaging can achieve sub-wavelength spatial resolution with probes such as apertures [152], metal tips [153, 154] and near-field detectors [155, 156, 157]. However to date, the technology for THz imaging and spectroscopy is unable to provide the spatial resolution necessary for single-molecule studies.

Here we explore the creation of nanoscale THz sources and detectors formed at the $LaAlO_3$ / $SrTiO_3$ (LAO/STO) interface [13, 158]. When the LAO layer is at or close to a critical thickness of 3 unit cells (u.c.), the metal-insulator transition can be locally and reversibly controlled using a conductive atomic force microscope (c-AFM) tip [21, 22]. A variety of nanoscale electronic [22, 23, 24] and photonic [25] devices have already been demonstrated. Compared to many other materials, $SrTiO_3$ has unusually large third-order nonlinear optical susceptibility [37]. Therefore, LAO/STO can be an attractive potential platform for optically generating and detecting THz at nanometer scale.

7.2 SAMPLE GROWTH AND DEVICE FABRICATION

LAO/STO heterostructures are grown by pulsed laser deposition (PLD). The PLD system is equipped with high-pressure RHEED, which is used for precisely monitoring layer-by-layer growth of thin films in-situ. Low miscut ($\sim 0.05^\circ$) (001) $SrTiO_3$ substrates are treated by buffered HF and annealed in oxygen at 1000 C for 2 to 12 hours to produce TiO_2-terminated and atomically smooth surface that has single unit cell height steps. A KrF excimer laser (248 nm) with energy density of $2.0 \sim 2.5$ J/cm^2 and repetition rate of 3 Hz is focused onto

a LaAlO3 single crystal target. Thin layers of $LaAlO_3$ (3.4 u.c.) are deposited on top of TiO_2-terminated $SrTiO_3$ at a temperature of 550 C and oxygen pressure of 10^{-3} mbar. The details of the growth and properties are reported elsewhere [159, 160].

Metallic electrodes are contacted directly with the interface of $LaAlO_3$ and $SrTiO_3$. The deposition process involves two steps. In the first step, Ar^+ milling etches 25 nm deep into the $SrTiO_3$ followed by backfilling of 4 nm Ti adhesion layer and 30 nm Au layer. In the second step, 4 nm Ti layer and 50 nm Au layer is deposited on top of the first Ti-Au layer (Figure 7.1(a)). The first deposition establishes ohmic contact with the interface while the second layer is used for bonding Au wires to make external electric connections. Atomic force microscope (AFM) topography images like Figure 7.1(b) are obtained to identify a clean canvas that has no broken electrodes and regular terraces (Figure 7.1(c)).

Conductive atomic force microscopy (c-AFM) is used for creating the conducting nanostructures. The "writing" and "erasing" processes operate in contact mode. A lock-in amplifier (Signal Recovery 7270) is used to monitor the change of the interface conductance. In Figure 7.2(a) and (b), a sinusoidal excitation voltage (frequency $f_{excit} \sim 26$ Hz and amplitude $V = 100$ mV) is sent to the Source (S) and the current from Drain (D) is detected by a lock-in amplifier at the frequency of f_{excit}. During the device fabrication, AFM is kept in the darkness to suppress any possible photo-doping process and the humidity is maintained at the level of 30% to 35%. Positive voltage (the typical value is 8 V $\sim$ 10 V) is applied to the AFM tip for creating a conducting channel (Figure 7.2(a)) whereas negative bias is used for cutting the channel (Figure 7.2(b)). When a conducting channel is successfully formed between them, the drain current will increase sharply. Four-terminal structures adopted for experiments presented in this letter have typical dimensions as depicted in Figure 7.2(c).

7.3 CHARACTERIZATION OF NONLINEAR PROCESS

Figure 7.3(a) illustrates the basic experimental setup. A nanojunction, consisting of a 10 nm wide nanowire with a 10 nm insulating barrier, is fabricated at the LAO/STO interface with c-AFM lithography. Ultrafast ($\sim$ 30 fs) optical pulses from a Ti: Sapphire laser are

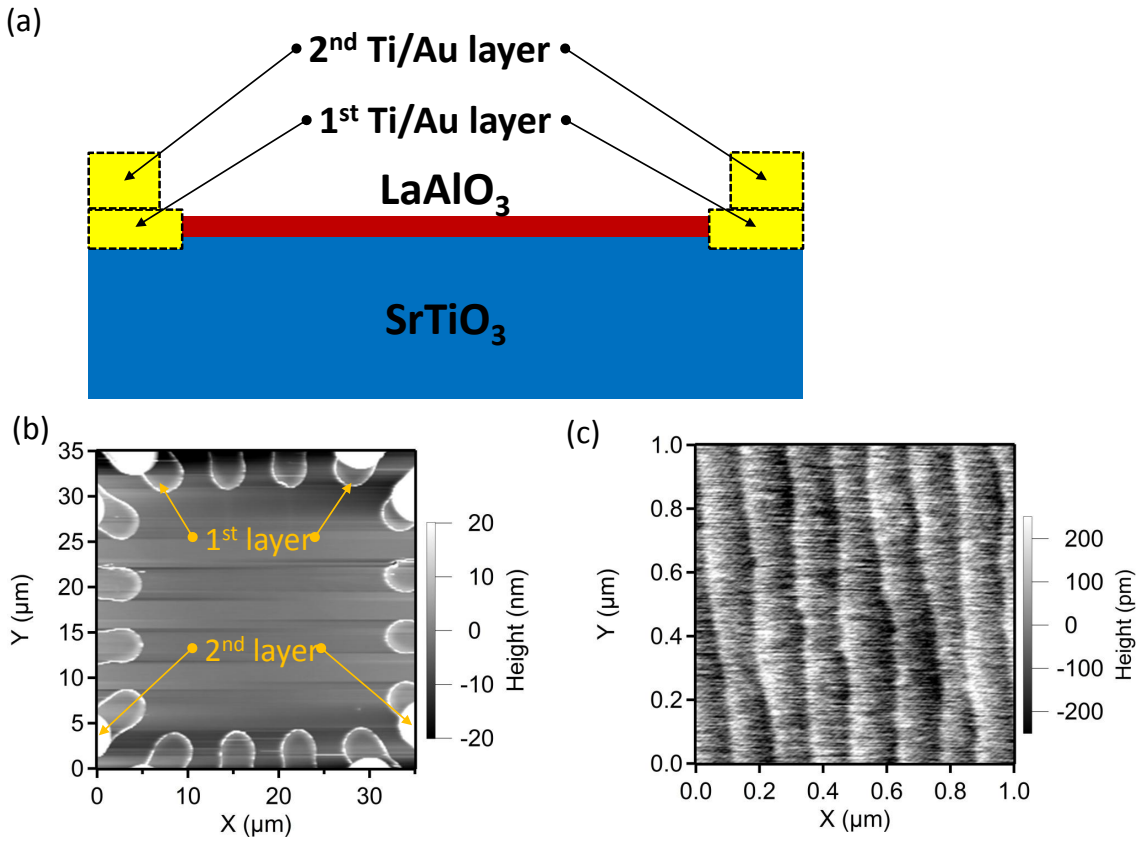

Figure 7.1: Sample structure. (a) Side view of the sample layers. (b) A 35 μm by 35 μm atomic force microscope (AFM) image shows the topography of the sample. The overlap of the first and second Ti/Au layer can be seen in the image. (c) Close-up topography image clearly shows the terraces.

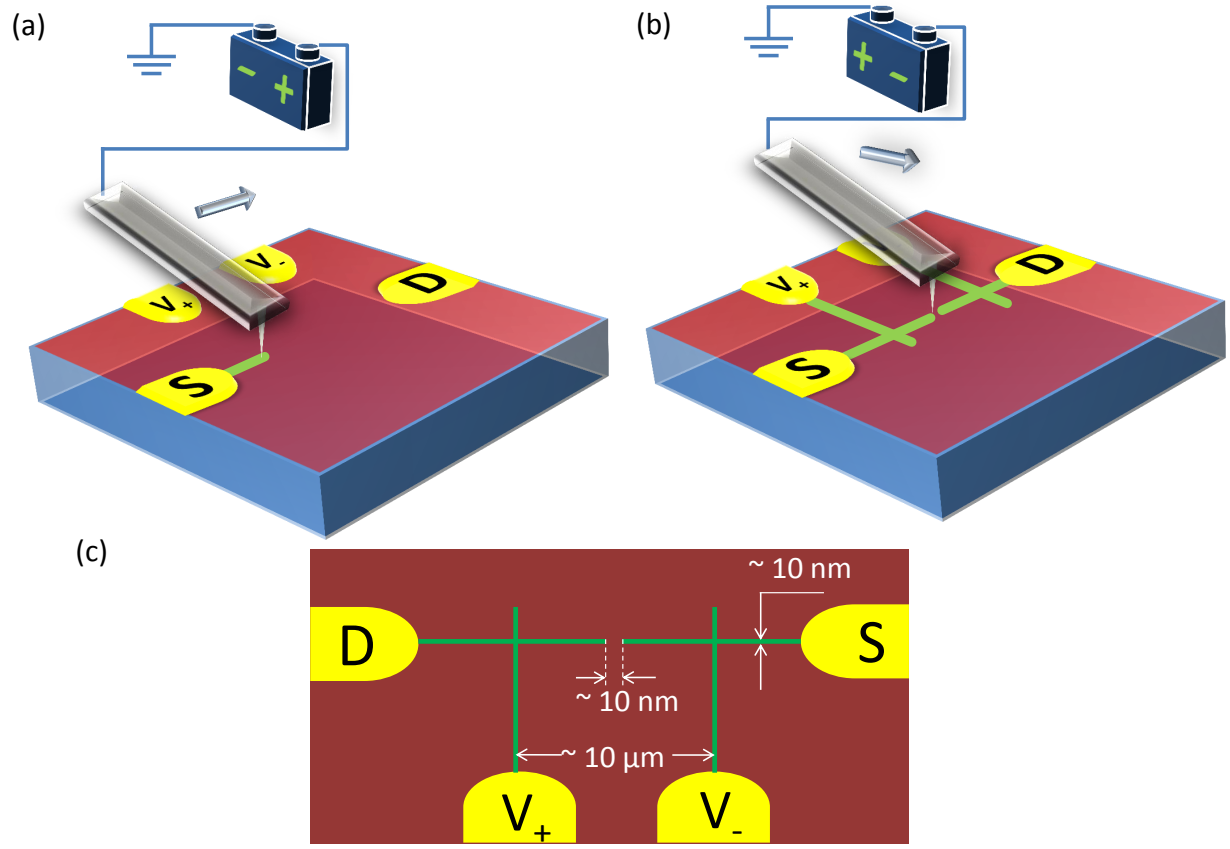

Figure 7.2: Device fabrication and typical dimensions. (a) Conducting channel is written with a positive bias on the c-AFM tip. (b) A negative bias on the tip restores the interface to its initial insulating state and therefore forms a gap in the middle of a conducting channel. (c) The typical dimensions for the devices described in the text.

divided into "pump" and "probe" beams by a Mach-Zehnder interferometer. Photoconductive properties are measured using a four-terminal geometry in which a voltage is applied between source (S) and drain (D) electrodes, and two voltage sensing electrodes, V_+ and V_-, are used to measure the photo-induced differential voltage $\Delta V_{ph} = V_+ - V_-$. All experiments are performed at 80 K except where noted.

By measuring ΔV_{ph} as a function of the (x,y) coordinate of the focused light spot [25, 114], a photoconductive image is generated. In Figure 7.3(b), the diffraction-limited peak shows where the nanojunction was created. By allowing both beams to illuminate the nanojunction and scanning the optical delay line (ODL), dynamical information can be resolved. In Figure 7.3(c), when the chopper is off, interference fringes are observed which is attributed to field autocorrelation. It is noticed that the lower envelope shows larger amplitude than the upper one. By turning the chopper on, lock-in detection can filter away the fast oscillations, leaving only the asymmetric envelope to be detected by averaging over a large number of measurements(Figure 7.3(d)). The response exhibits a full width at half-maximum (FWHM) of 31 fs.

The spatial and temporal response of the device can be measured by repeating the time-resolved measurement at a regular two-dimensional array of locations. After the position of the nanojunction is located by measuring the time-averaged image (Figure 7.3(b)), an array of spatial positions (Figure 7.4) is chosen.

The microscope objective (100X, NA = 0.73) is fixed on a closed-loop 3-axis piezo stage (Piezosystem Jena Tritor T-401-1) which can then be digitally controlled to move the objective and focus the light onto each spot at which the time-resolved measurement could be performed. At each point, the time-resolved signal is measured for V_s set as -1 V, 0 V and +1 V. The time delay is calibrated by measuring the interference of a HeNe laser. By collecting the data for all positions, the serial of time-space images could be formed (See Figure 7.5).

So far time-resolved measurements for the nanojunction have uncovered response which is ultrafast in time, localized in space and tunable by external electric field. Several physical mechanisms are considered to understand the origin of the LAO/STO nanojunction ultrafast response. Processes involving resonant optical absorption and carrier relaxation can be ruled out because the reported lifetime for photo-excited carriers in $SrTiO_3$ is on the order of

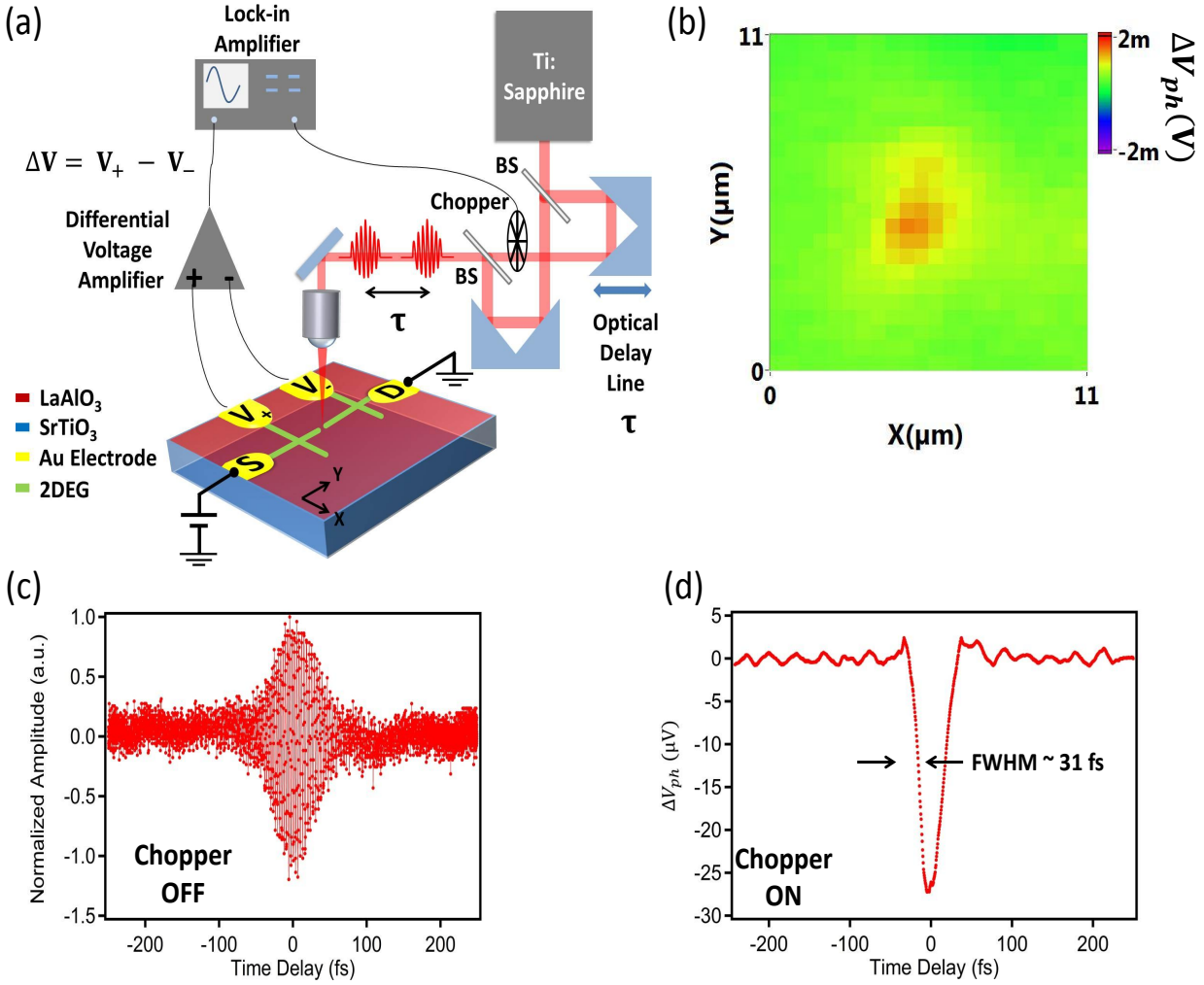

Figure 7.3: Time-resolved photoresponse measurement. (a) Representation of the experimental setup. X and Y indicate the scanning axes. BS: ultrafast beam splitter. (b) ΔV_{ph} image with the color scale showing its amplitude. ($I_{ave} \approx 10$ kW/cm^2 and $V_s = -1$ V.) (c) Time-resolved measurement. Interference fringes are observed when the chopper is turned off. (d) Time-resolved measurement with the chopper on. Offsets have been subtracted. This is the average over 120 measurements. ($I_{ave} \approx 50$ kW/cm^2 and $V_s = -1$ V.)

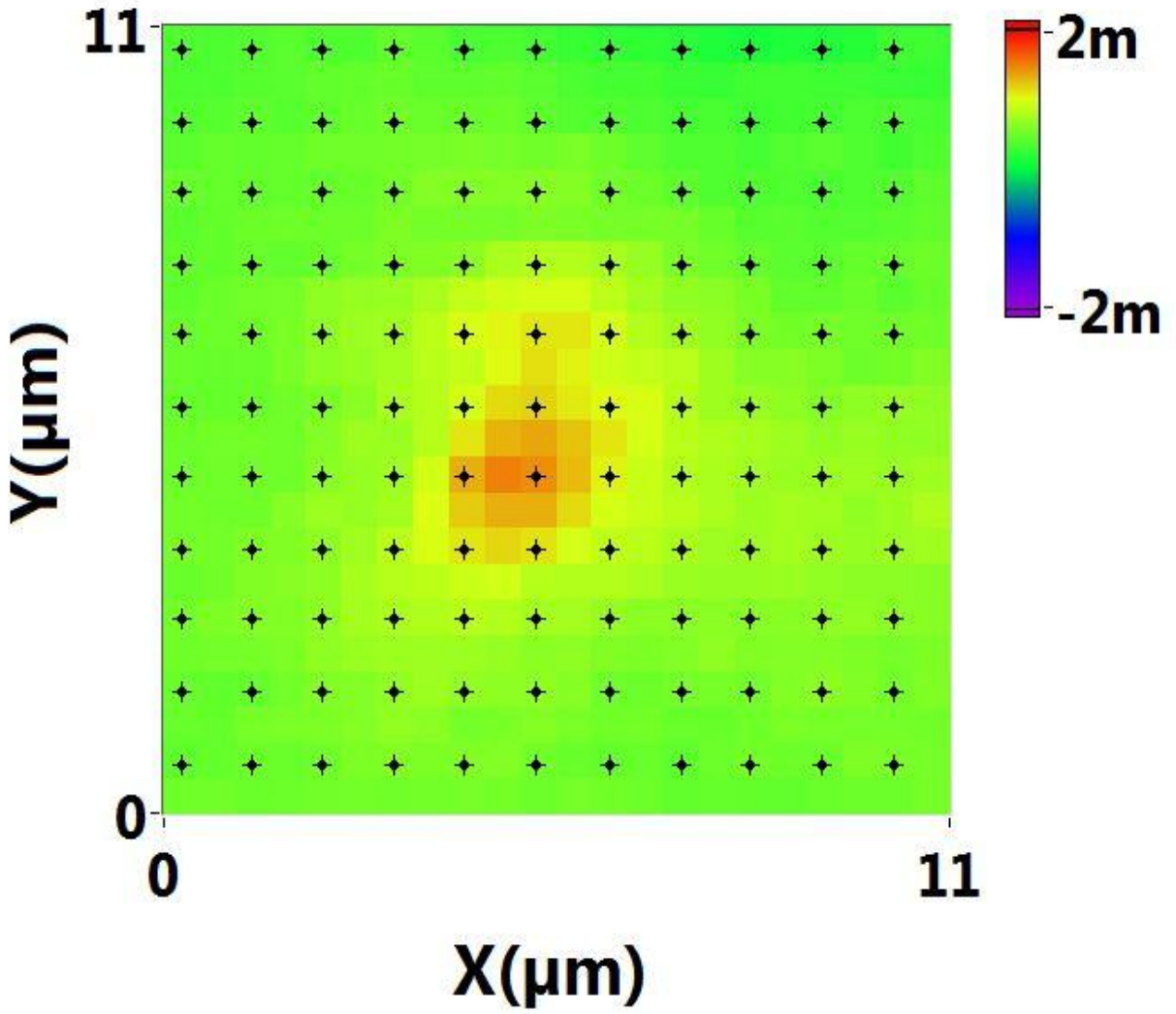

Figure 7.4: Positions chosen for time-resolved measurement. In the time-averaged photo-induced ΔV_{ph} image (the background image), each cross indicates a position at which the time-resolved experiment is carried out. Totally there are 11 by 11 points with 1 μm separation between two adjacent points. The color bar shows the amplitude of ΔV_{ph}.

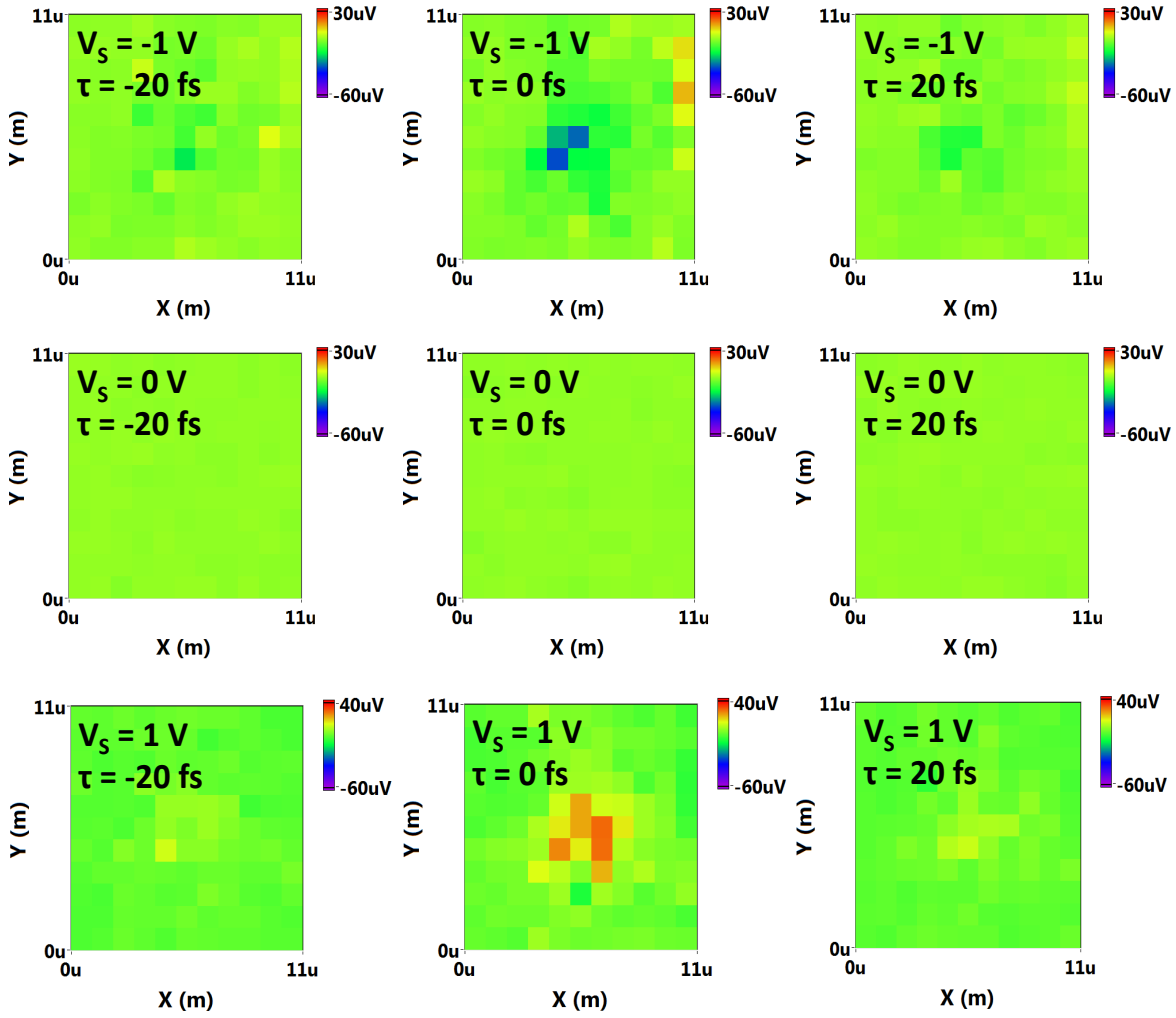

Figure 7.5: Tunable local ultrafast photoresponse. From top to bottom, the three rows represent the measurement for V_s = -1 V, 0 V and +1 V, respectively. From left to right, the three columns correspond to the experiment performed at time delay τ = -20 fs, 0 fs and 20 fs, respectively. (NA = 0.73, $I_{ave} \approx 50$ kW/cm^2 for both pulses.)

nanosecond [119, 161]. Nonlinear $\chi^{(2)}$ or $\chi^{(3)}$ processes, on the other hand, have a much greater inherent bandwidth. $SrTiO_3$ is a centrosymmetric crystal that should not exhibit a bulk second-order nonlinear response. Because inversion symmetry is broken at the interface of LAO/STO, $\chi^{(2)}$ processes can exist [20]. However, the ultrafast response measured here is highly localized at the junction and can be tuned by external electric field; hence, intrinsic $\chi^{(2)}$ processes are unlikely to play an important role. The electric field is strongly confined around the nanojunction [25] and can be on the order of 10^6 V/cm. Therefore, it is believed that the observed ultrafast response results from a $\chi^{(3)}$ process involving one quasi-static local field across the junction and two optical fields:

$$P^i_{NL}(\omega_1 - \omega_2) = \varepsilon_0 \chi^{(3)}_{ijkl}(\omega_1 - \omega_2, 0, \omega_1, -\omega_2) E^j_{bias} E^k_{opt}(\omega_1) E^l_{opt}(-\omega_2), \tag{7.1}$$

where P^i_{NL} is the nonlinear polarization, $\chi^{(3)}_{ijkl}$ is the third-order susceptibility at the nanojunction, E^i_{bias} is the electric field across the nanojunction, and $E^i(\omega)$ is the optical field (i, j, k, l = x, y, z).

The nonlinear polarization P^i_{NL} combines the spatial resolution of the bias field and temporal resolution of the optical field (Figure 7.6). In the experiments described here, the optical fields E^k_{opt} are localized in time ($\sim$ 30 fs duration), and confined to $\sim$ 1 μm in the plane of the junction. The quasistatic field from the junction E^j_{bias} is localized within a volume V $\sim$ (10 nm)^3, defined by the spatial extent of the nanowire which is known from prior investigations [15, 25]. A similarly high spatial and temporal resolution applies for detection, as described in more detail below.

The nonlinear response is analogous to GaAs crystals excited by off-resonance irradiance [140, 141]. For these oxide heterostructures, the incident light has a photon energy $\sim$ 1.48 eV, and $SrTiO_3$ has a direct and indirect band gap of 3.75 eV and 3.25 eV, respectively [19]; hence, the interaction between non-resonant photons and valence electrons in $SrTiO_3$ can be described as a virtual absorption process [162, 163, 164]. Physically, the picture indicates that, when valence electrons interact with non-resonant photons, the electrons remain bound but are shifted from their equilibrium positions by the optical electric field, the result being a transient dipole moment produced via a $\chi^{(3)}$ process that reduces the static external field (Figure 7.7(c)). Because this process involves no real absorption, a FWHM comparable to

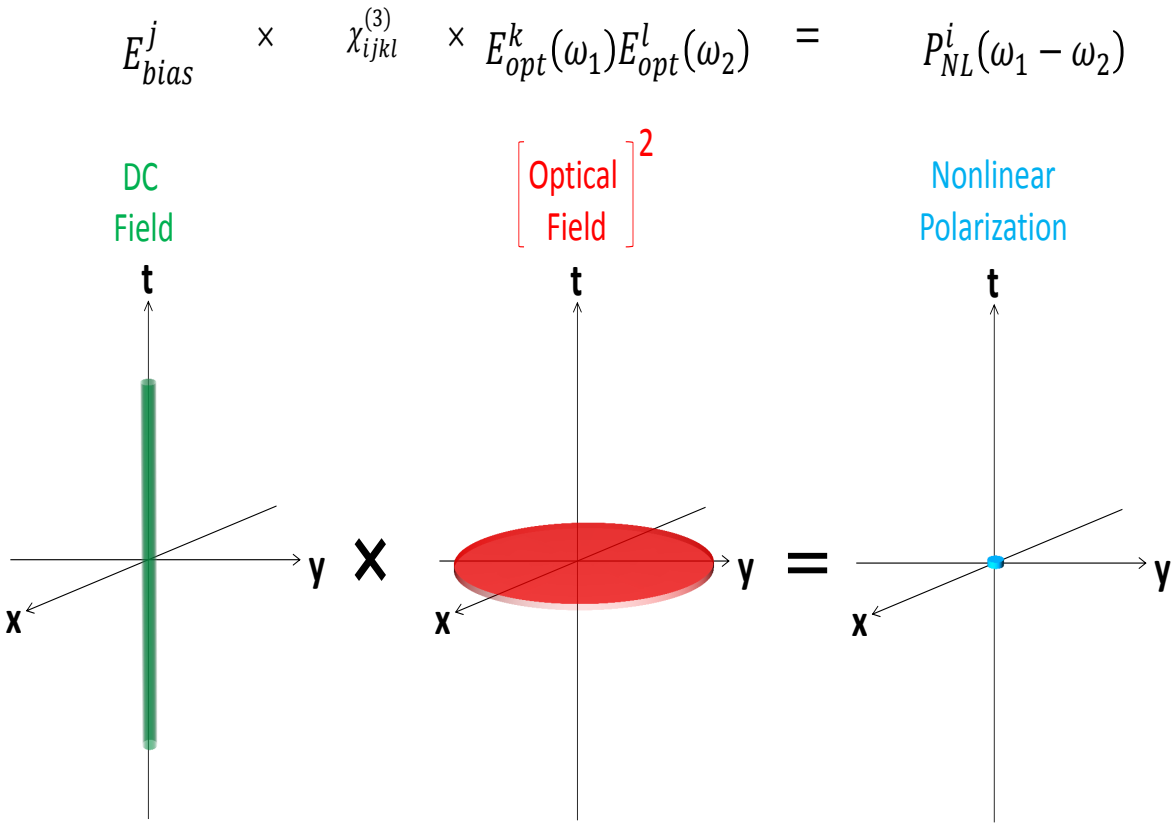

Figure 7.6: Spatiotemporal confinement of the nonlinear polarization. The DC bias field is local in space, while the optical field is local in time. Consequently, the $\chi^{(3)}$ polarization is confined both spatially and temporally.

that of the laser pulse is expected (for example, Figure 7.3(d)).

In order to characterize the $\chi^{(3)}$ process, in all measurements for a single-junction structure, a 2 ps time-delay range is scanned. In addition to the ultrafast response, illumination of these nanojunctions also produces a time-averaged (slow) response manifested as overall offsets in the bias-dependent curves in Figure 7.8. This offset can be attributed to the absorption of photons by electrons occupying the in-gap states in $SrTiO_3$ [120]. Experiments [161, 119, 165]have shown that $SrTiO_3$, especially when subjected to growth of $LaAlO_3$, can form deep traps from either oxygen vacancies [125] or unintentional doping of $SrTiO_3$ substrate [128]. Prior investigations of the wavelength dependence of the photoconductive response and the Stark shifting under electric fields [25] is in agreement with the picture that incoming near-infrared photons can be absorbed by electrons residing in states within the $SrTiO_3$ band gap.

In all characterization measurements, each time-resolved curve is fit to a hyperbolic secant function

$$f(t) = A_0 + A_1 sech^2((t - t_0)/t_w) \tag{7.2}$$

within a time window of 300 fs (black lines in Figure 7.8. Following the fitting process, the amplitude A_1 can be plotted as a function of source bias V_s (Figure 7.9(a)), average intensity I_{ave} (Figure 7.9(b)) and temperature (Figure 7.9(c)), respectively.

The model described above is consistent with the time-resolved signal dependence on the strength of the applied static electric field across the nanojunction. According to Eq. (7.1), the response should depend linearly on $E_{bias} \approx V_s/d$, where d is the size of the gap. In Figure 7.9(a), the amplitude of ultrafast response A_1 is fit to$A_1 \sim V_s^a$, where $a = 0.97$ for $V_s < 0$ and $a = 0.75$ for $V_s > 0$.

The $\chi^{(3)}$ process, described by Eq. (7.1), has a linear dependence on the light intensity $I_{ave} = E(\omega)E(-\omega)$. Fig. 2 (b) shows that in the moderate intensity range, the measured dependence is in good agreement with what is predicted by Eq. (7.1), although certain variation between the two devices is also noticed.

In Figure 7.9(b), for Device #1, measurements in the range $10 \sim 100$ kW/cm^2 (corresponding intensity $I_{ave} \approx 0.1 \sim 1$ mW) show a linear relation with the power law exponent

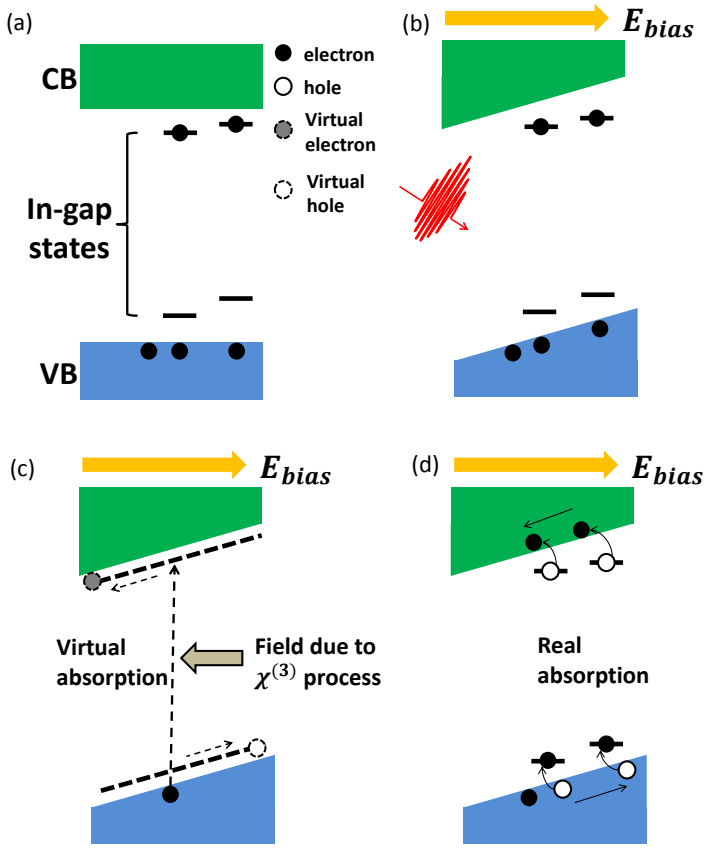

Figure 7.7: Schematic band models for $SrTiO_3$. (a) Energy band diagram showing the in-gap states in $SrTiO_3$. (b) External bias field can bend the bands and incident pulsed laser initiates the interaction between photons and carriers. (c) Virtual absorption. Dashed gray circles and dashed white circles are for virtual electrons and virtual holes respectively. (d) Real absorption results in the photoconductive effect that contributes a finite offset in the signal.

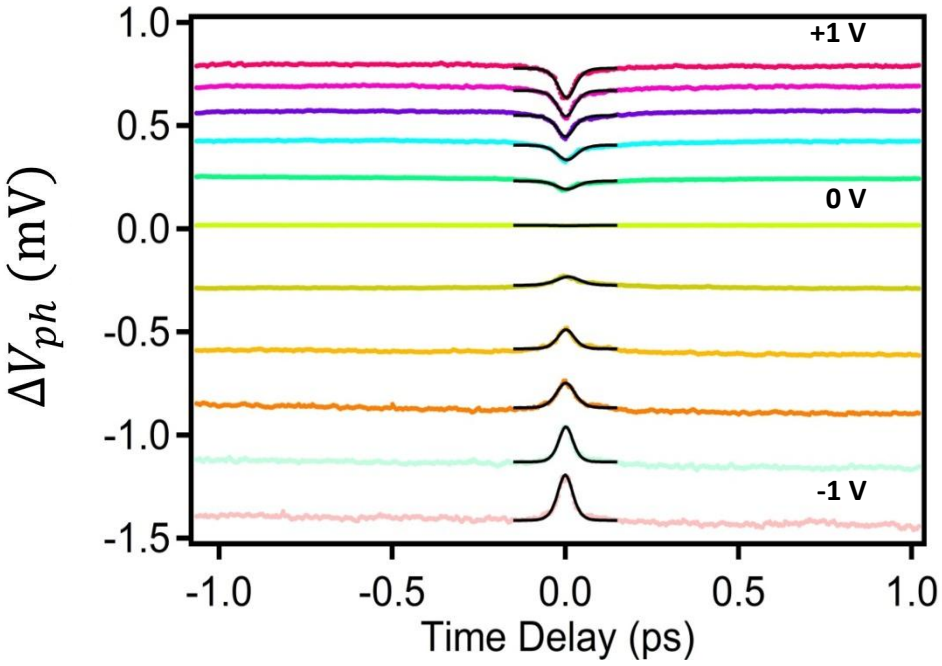

Figure 7.8: Fitting of ultrafast response. Slow offset shows up in the time-resolved measurement. The black curves show the fitting results.

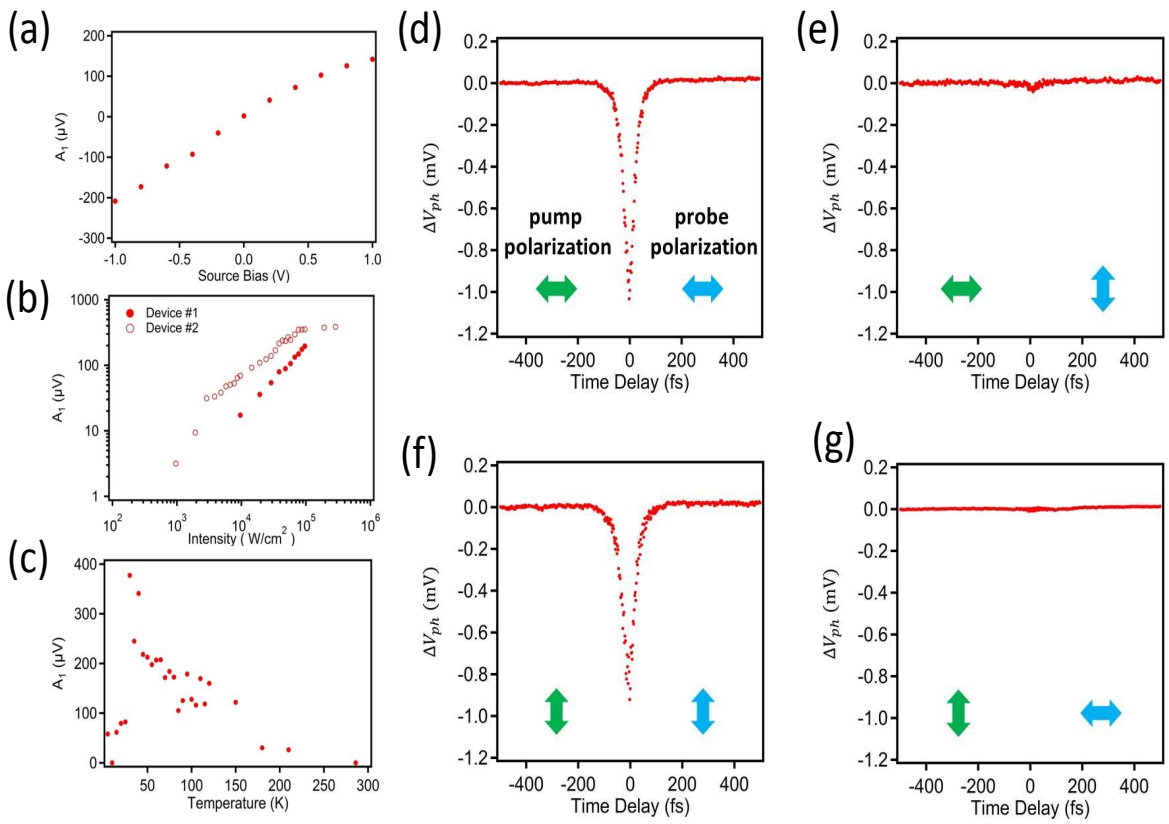

Figure 7.9: (a) Dependence on the strength of the static electric field. ($I_{ave} \approx 50$ kW/cm^2). (b) Intensity dependence. ($V_s =$ -1 V) (c) Temperature dependence. ($V_s =$ -1 V and $I_{ave} \approx 50$ kW/cm^2).(d)-(g), Polarization dependence.

$A_1 \sim I_{ave}^{\beta}$ where $\beta = 1.1$. For Device #2, a wider intensity range is covered (10 μW to 3 mW). When the intensity is low, 960 W/cm^2 $< I_{ave} <$ 3 kW/cm^2, the amplitude increases sharply, with a power law fitting parameter of $\beta = 2.8$. Saturation occurs above $I_{ave} \sim 80$ kW/cm^2. In the moderate intensity range, 3 kW/cm^2 $< I_{ave} <$ 80 kW/cm^2, the power law fitting gives $\beta = 0.8$.

The variation between these two measurements may result from certain unknown factors in the experiment. As argued above, in-gap states are involved in the photoconductivity. However, it is not clear whether or how those states might be modulated during the c-AFM lithography. Another uncertainty is the relative importance of real and virtual absorption processes (Figure 7.7(c) and (d)). It is likely that the number of photons involved in either process has intensity dependence as well. This complexity is not reflected in Eq. (7.1). Other nonlinear processes, such as two-photon absorption, might be initiated in $SrTiO_3$ under certain intensity regimes as well. Nevertheless, based on the measurement in Figure 7.9(b) and taking into account those uncontrollable factors, the dependence of the ultrafast response amplitude on the light intensity is in good agreement with what is predicted by Eq. (7.1).

$SrTiO_3$ undergoes several structural phase transitions [166], which influence the dielectric permittivity and nonlinear optical properties [167, 168]. As the temperature decreased from 290 K to 30 K (Figure 7.9(c)), A_1 is generally increasing. In Ref. [168] a minimum of $\chi^{(3)}$ is found around 30 K, however, this feature is only observed when the electric field across the sample is lower than 1.5 kV/cm [168]. Across the junction, the electric field is several orders of magnitude higher. It is possible that the abrupt change might be related to a local electric-field-induced structural phase transition within the $SrTiO_3$ from tetragonal to orthorhombic [166]. Between 5 K and 20 K the signal decreases before somewhat recovering around 5 K.

The polarization dependence is measured with $V_s = -1$ V and $I_{ave} \approx 50$ kW/cm^2. Vertical polarization of light is defined as the direction along the Y-axis and horizontal direction is along the X-axis, as shown in in Figure 7.3(a). When the polarization of both beams are parallel (Figure 7.9(d) and (f)), a strong time-resolved signal is detected. When their polarizations are mutually perpendicular (Figure 7.9(e) and (g)), the signal is suppressed.

This observation can be explained by the symmetry that $SrTiO_3$ possesses: non-vanishing $\chi^{(3)}$ parameters put constraints on the polarization of light for generating nonzero P_{NL}.

Since $SrTiO_3$ belongs to m3m symmetry group[85], it has the following non-vanishing $\chi^{(3)}$ parameters:

$$\chi^{(3)}_{xxxx} = \chi^{(3)}_{yyyy} = \chi^{(3)}_{zzzz} \tag{7.3}$$

$$\chi^{(3)}_{xxyy} = \chi^{(3)}_{yyxx} = \chi^{(3)}_{xxzz} = \chi^{(3)}_{zzxx} = \chi^{(3)}_{yyzz} = \chi^{(3)}_{zzyy} \tag{7.4}$$

$$\chi^{(3)}_{xyxy} = \chi^{(3)}_{yxyx} = \chi^{(3)}_{xzxz} = \chi^{(3)}_{zxzx} = \chi^{(3)}_{yzyz} = \chi^{(3)}_{zyzy} \tag{7.5}$$

$$\chi^{(3)}_{xyyx} = \chi^{(3)}_{yxxy} = \chi^{(3)}_{xzzx} = \chi^{(3)}_{zxxz} = \chi^{(3)}_{yzzy} = \chi^{(3)}_{zyyz} \tag{7.6}$$

Because the incident light at the junction is normal to the sample, the electric field of the light is transverse. Our samples are grown and processed in such a way that the in-plane principal axes of $SrTiO_3$ are along the X and Y directions in Figure 7.3(a). The polarization dependence found in the experiment can then be explained as follows: The external bias field is applied in the Y direction. The induced field, caused by the separation of virtual holes and virtual electrons(Figure 7.7(c)), then has to be in -Y direction. This means only $\chi^{(3)}_{yyyy}$ and $\chi^{(3)}_{yyxx}$ terms are relevant. However, both of them require the optical fields to be parallel (either in the X or Y direction), otherwise the $\chi^{(3)}$ coefficient will be zero and therefore no virtual absorption can occur:

$$P^{NL}_y \sim \chi^{(3)}_{yyyy}(0,0,\omega,-\omega)E^{bias}_y E_y(\omega)E_y(-\omega) \tag{7.7}$$

$$P^{NL}_y \sim \chi^{(3)}_{yyxx}(0,0,\omega,-\omega)E^{bias}_y E_x(\omega)E_x(-\omega) \tag{7.8}$$

7.4 GENERATION AND DETECTION OF THZ

Motivated by the fact that rectified THz fields can be generated via $\chi^{(3)}$ processes, the experiments that we have shown so far demonstrate the feasibility of generating THz field at 10 nm scale (Figure 7.6). To illustrate the THz field detection mechanism, an experiment

is performed with two nanojunctions, separated by a distance Δx (Figure 7.11(a)). Each nanostructure is illuminated with a focused optical spot. The THz field E_{THz} produced at one junction (source) interacts with the optical field E_{opt} around the other junction (detector). The resulting polarization via the $\chi^{(3)}$ process $P^i \sim E^j_{THz} E^k_{opt} E^l_{opt}$ acts on the detector as a field offsetting the photoconductivity of the nanostructure. The spatial resolution is again determined by the gap [25], while the temporal resolution is determined by the optical pulse duration. Although the two-junction experiment does not directly demonstrate the spatial resolution for THz near-field imaging, based on the above analysis and physical mechanism, it is a reasonable conclusion that the scale of the nanojunction determines the resolution in the near-field region. This field sensing mechanism is analogous to work described in Refs.[155, 157]; however, our detection mechanism is fundamentally different in that the field confinement required by near-field measurement is provided by the spatial confinement of E_{bias} around the nanojunction. The results discussed here are for Δx =12 m; similar measurements with Δx =6 m are shown later. The two junctions are electrically isolated from one another, as confirmed by I-V measurements.

After the nanostructure is written at the interface, the sample is transferred immediately to a cryostat with optical top access (Montana Instruments Cryostation). The chamber is then pumped to vacuum and cooled to the desired operating temperature.

At $T = 80$ K, before the device is exposed to light, electric properties are first characterized. Figure 7.10(b) shows the DC IV measurement for the structure on the left in Figure 7.10(a). The red (green) line is the measurement when DC source bias (V_s) is applied onto Electrode 1 (3) and drain current at Electrode 2 (4) is measured by a preamplifier (Stanford Research Systems SR570). Both devices show ohmic response. The blue curve in Figure 7.10(b) shows the I-V response between Electrodes 1 and 4. Because of the potential barrier at the junction, DC current is prevented from flowing between source to drain. Figure 7.10(c) shows the results for the other device (Electrodes 5-8).

In order to make sure there is no leakage from one device to the other, the conductance between different pairs of electrodes is measured in Figure 7.10(d). In each pair, the source electrode is from the left device while the drain electrode is from the right device. The results indicate there is no DC coupling between two devices.

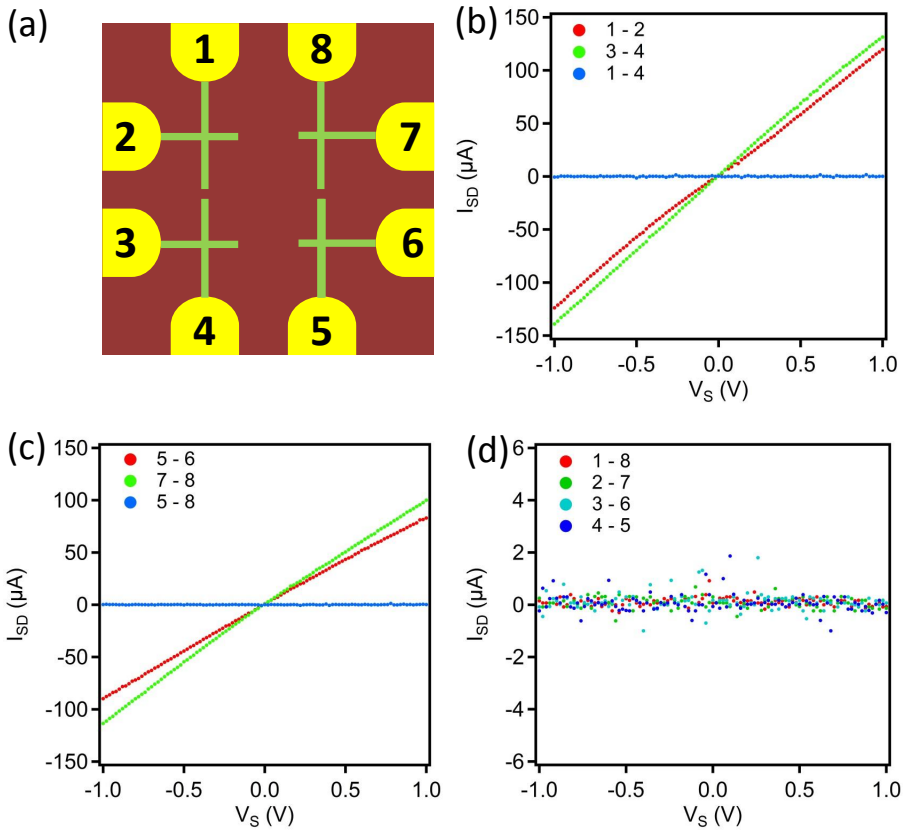

Figure 7.10: (a) Schematic of the nanostructures written at the interface with c-AFM lithography. (b) DC IV measurement for the device on the left in (a). (c) DC IV measurement for the device on the right in (b). (d) DC IV measurement between electrodes from two devices. No DC coupling is detected.

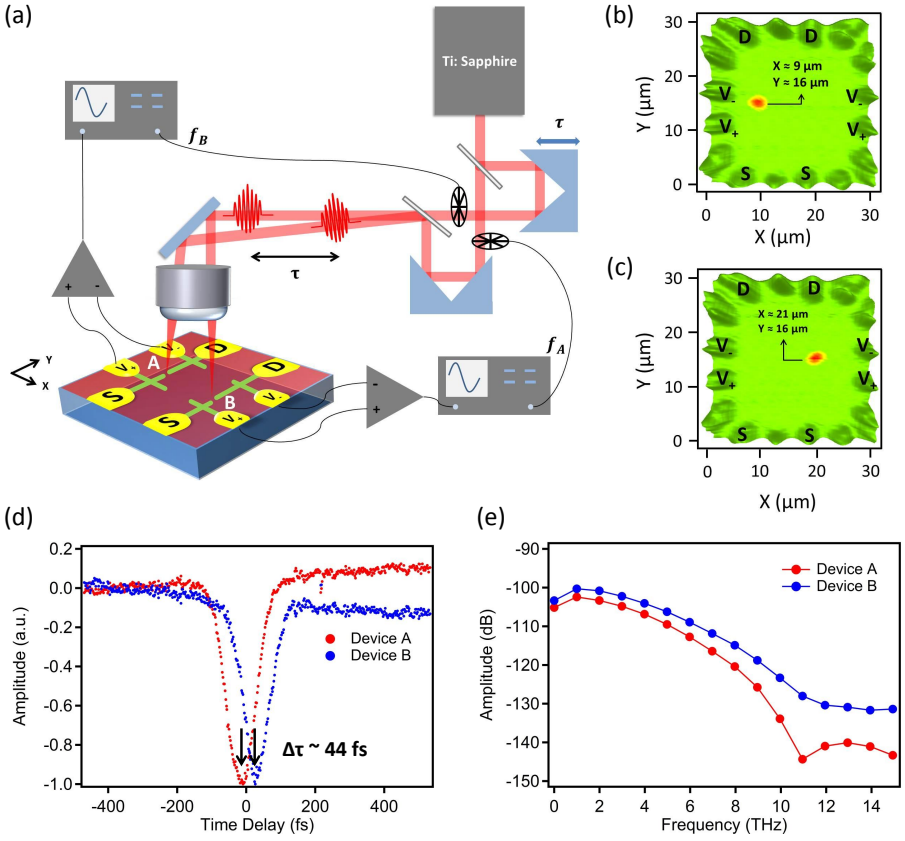

Figure 7.11: (a) Experimental setup for double-junction measurement. The ODL is stepped, and no piezo shaker is used. (b) and (c), The ΔV_{ph} image overlapped with the reflection image. Relevant electrodes are labeled to match (a). The coordinates are extracted from 2D Gaussian function fitting ($I_{ave} \approx 60$ kW/cm^2 and V_s = -1 V on both devices). (d) Time-resolved signal measured from the two devices. Each waveform is an average over 100 measurements ($I_{ave} \approx 70$ kW/cm^2 and V_s = -1 V for both devices). (f) FFT spectra of (d).

The locations of the two junctions are confirmed by overlapping the ΔV_{ph} image with a simultaneously acquired confocal reflectivity image. In Figure 7.11(b) and (c), the surrounding electrodes are imaged via the sample reflectance; the red spot corresponds to the ΔV_{ph} image, indicating the location of the nanojunction. Each beam is focused on one nanojunction. Both are intensity modulated, but at different frequencies: the pump beam, focused on Junction A (the device measured in Figure 7.11(b)), is modulated at frequency $f_A \approx 380$ Hz while the probe beam, focused on Junction B (the device measured in Figure 7.11(c)), is modulated at frequency $f_A \approx 460$ Hz. During the scan of optical delay line, the ΔV_{ph} in Junction A is detected by a lock-in amplifier at frequency f_B. Similarly, the ΔV_{ph} in Junction B is measured by a second lock-in amplifier at frequency f_A. In this configuration, radiation generated by one nanojunction can simultaneously be probed by the other. The ODL is stepped and the piezo shaker used for the single junction characterizations (See the Methods Summary) is turned off for this experiment, making it sensitive to any optical interference effects. A time delay of approximately $\Delta\tau \approx 44$ fs between the two peaks is found in Figure 7.11(d).

The interpretation of this experimental result is as follows: The light pulse focused on one junction produces THz radiation that subsequently propagates to the second junction. The delay corresponds to the propagation time, which is close to that of free space ($t = \Delta x/c = 40$ fs). The negative peaks are ascribed to the near-field component of the rectified THz field.

The spot size of both pump and probe light has been carefully measured to make sure that there is no overlap between them. Behind the focusing objective (20X, NA = 0.53), the size of the laser spot is measured by scanning the laser spot across the edge of a gold electrode while the reflected light is detected in a confocal arrangement. The reflection signal is plotted as a function of the position of laser spot in Figure 7.12. The sharpness of the edge of the gold electrode is confirmed by AFM and assumed to be mathematically represented by a Heaviside step function:

$$H(x) = \begin{cases} 1 & x > 0 \\ \frac{1}{2} & x = 0 \\ 0 & x < 0 \end{cases} \tag{7.9}$$

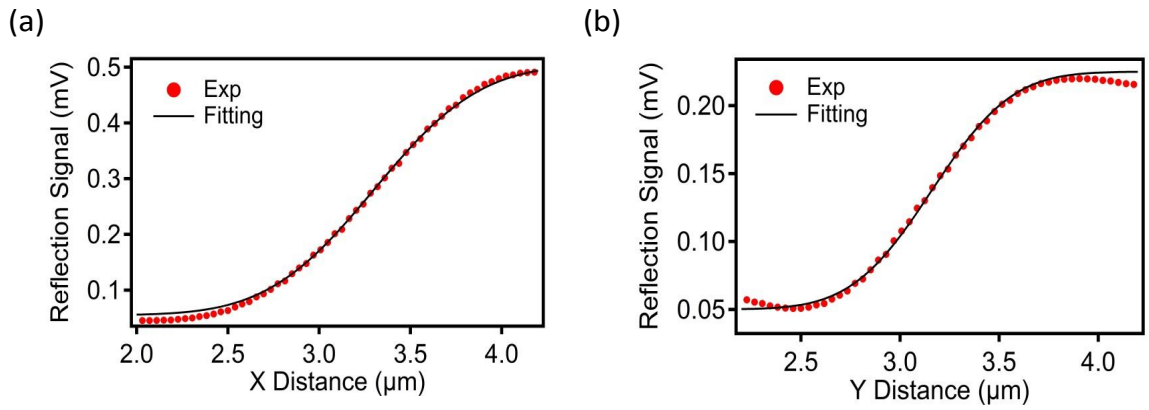

Figure 7.12: Laser spot size measurement behind the focusing objective. (a) The spot size in the X direction. The fitting gives a diameter of 1 μm. (b) The spot size in the Y direction. The fitting gives a diameter of 650 nm.

The laser spot is assumed to have a Gaussian profile. The data are fitted with the following function:

$$R(x) = \frac{a}{2} erfc(\frac{b-x}{c}) + d, \tag{7.10}$$

where a is the magnitude of the step, b is the center location of the step and d is the offset. The function

$$erfc(x) = \frac{2}{\sqrt{\pi}} \int_x^\infty e^{-t^2} dt$$

is called the complementary error function which is a convolution of the Heaviside step function and Gaussian function. The spot size can be estimated from $2\sqrt{ln2} \times c$ where $2\sqrt{ln2}$ is the deconvolution factor.

Depending on in which direction the line-scan is performed, the spot diameter in X and/or Y direction could be measured (X and Y directions are defined in Figure 7.3(a)). From the fitting, it is found that the diameter in the X direction is about 1 μm (uncertainty $\sigma_x \approx 60$ nm) (Figure 7.12(a)) whereas the diameter in the Y direction is about 650 nm

(uncertainty $\sigma_x \approx 70$ nm) (Figure 7.12(b)).

In our experiment, the sample stays in a fixed position while the objective stage is moved to locate the area where nanostructures are present. After the location is found, it is possible that the incident light may not exactly pass through the center of the objective. Therefore the focal plane in the X direction may not spatially overlap with the one in the Y direction. This can cause the slight elliptical shape observed in the measurement. However, from this measurement, one should be able to tell that the laser spot size is by far smaller than the distance between two junctions (either 6 μm or 12 μm).

Because the ΔV_{ph} at Junction B is being measured at frequency f_A (and vice-versa), the detected signal must result from an interaction between the locally generated field and an electric field $E_{emit}(t)$, generated by the other remote junction. The field $E_{emit}(t)$ cannot be an optical field; otherwise one would observe interference fringes as shown in Figure 7.3(c); such interference is not observed (Figure 7.11(d)). Instead, the measured signal should be due to THz emission from one junction that is detected at the other one. A Fourier transform (Figure 7.11(e)) reveals a spectral peak at 1 THz with a 3dB-bandwidth around 3 THz and spectral content extending to 10 THz.

By comparing the measurement for the case of $\Delta x = 12$ μm and $\Delta x = 6$ μm (see the following discussion), one sees that the finite time delay between the measurements for two devices can be tuned by the distance between them. This is a signature of the propagation of the electric field from one device to the other.

The measured rectified field $E_{emit}(t)$ should have its wavelength on the order of ~ 100 μm, which is one order of magnitude larger than the distance between two devices. This implies that it is the near-field component that is measured in Figure 7.11(d). The emitted field can be modeled using a Hertzian dipole radiation expression[137]. A Hertzian dipole model for the radiation field due to a time-varying dipole moment $p(t)$, at a distance r and angle θ relative to the dipole axis, is given as follows:

$$E_{emit}(t) = \frac{1}{4\pi\varepsilon_r\varepsilon_0}\left(\frac{P_{NL}(t)}{r^3} + \frac{n\dot{P}_{NL}(t)}{cr^2} + \frac{n^2\ddot{P}_{NL}(t)}{c^2 r}\right)sin(\theta) \tag{7.11}$$

where ε_r is the relative permittivity, n is the refractive index and c is the speed of light. The first term is the quasi-static field and the second and third term describes the near-field and

far-field contributions.

For the nanostructures at the interface of $LaAlO_3/SrTiO_3$, the dipole moment is proposed to be determined by

$$p(t) = \int_{V_{eff}} d^3x P(\vec{x}, t),$$

where V_{eff}, the effective volume, is defined as the spatial volume in which the electric field is trapped. The V_{eff} is supposed to be centered on the nanojunction around which the electric field is strongly trapped as shown in the previous work (Ref.[25]). $P(\vec{x}, t)$ is the polarization density at the position $\vec{x}$ and time t. By integrating over the whole effective volume, the dipole moment could be calculated.

Due to the small size of the nanojunction (10 nm 10 nm), it is assumed that $P(\vec{x}, t)$ is uniform in V_{eff}. This assumption can simplify the calculation and enable a quick estimation of the contribution from different terms. Now the dipole moment becomes

$$p(t) = V_{eff} P(\vec{x}, t). \tag{7.12}$$

Since it is the nonlinear process that we focus on, only $\chi^{(3)}$ term is included in the expression of polarization density. In frequency domain, it is

$$P_{NL} = \varepsilon_0 \chi^{(3)}(0, 0, \omega, -\omega) E_{bias} E(\omega) E(-\omega). \tag{7.13}$$

In the time domain, it becomes

$$P_{NL} = \varepsilon_0 \int_{t_1}^{t} dt' \int_{t_2}^{t_1} dt'' \chi^{(3)}(t - t', t' - t'') E_{bias} E(t') E^*(t''), \tag{7.14}$$

where $\chi^{(3)}(t - t', t' - t'')$ describes the temporal response of the material to external time-varying electric field. Here we introduce a second assumption: the response of our system is assumed to be instantaneous which results in

$$\chi^{(3)}(t - t', t' - t'') = \chi^{(3)} \delta(t - t') \delta(t' - t''). \tag{7.15}$$

So now

$$P_{NL} = \varepsilon_0 \chi^{(3)} E_{bias} E(t) E^*(t). \tag{7.16}$$

In our experiments, two nanojunctions are aligned along the X direction. The angle θ therefore could be taken as 90°.

Given that nonlinear parameters have been reported in the literature (Ref.[37]) can be estimated as 3×10^{-16} cm^2/V^2($\sim 2 \times 10^{-12}$ esu)[1]. The laser shape is assumed to resemble the square of a hyperbolic secant, and the optical field then becomes

$$E(t) = E_0 sech(\frac{t}{\tau_p}) e^{i\omega t}, \tag{7.17}$$

where E_0 is the amplitude, which is about 440 KV/cm in the experiment. τ_p is the pulse width which is measured to be 30 fs. The nonlinear polarization and its time derivatives are:

$$P_{NL}(t) = \varepsilon_0 \chi^{(3)} E_{bias} E_0^2 sech^2(\frac{t}{\tau_p}), \tag{7.18}$$

$$\dot{P}_{NL}(t) = -\varepsilon_0 \frac{2}{\tau_p} \chi^{(3)} E_{bias} E_0^2 sech^2(\frac{t}{\tau_p}) tanh(\frac{t}{\tau_p}), \tag{7.19}$$

$$\ddot{P}_{NL}(t) = \varepsilon_0 \frac{2}{\tau_p^2} \chi^{(3)} E_{bias} E_0^2 sech^2(\frac{t}{\tau_p})(2 - 3sech^2(\frac{t}{\tau_p})), \tag{7.20}$$

whereE_{bias} is 1 MV/cm for 1 V on the source and 10 nm gap width. By fitting the data in Figure 7.11(d) with the following function:

$$\begin{aligned} f(t) =& a_0 + a_1 t + a_2 sech^2(\frac{t - t_0}{\tau_p}) \\ & [1 + \frac{a_3}{\tau_p} tanh(\frac{t - t_0}{\tau_p}) + \frac{a_4}{\tau_p^2}(2 - 3sech^2(\frac{t - t_0}{\tau_p}))] \end{aligned} \tag{7.21}$$

where

[1]To convert the unit from m^2/V^2 to esu, one can refer to the book[169].

$$a_2 = \frac{\chi^{(3)} E_{bias} E_0^2}{4\pi\varepsilon_r r^3}, \tag{7.22}$$

$$\frac{a_2 a_3}{\tau_p} = -\frac{2n\chi^{(3)} E_{bias} E_0^2}{4\pi\varepsilon_r r^2 c\tau_p}, \tag{7.23}$$

$$\frac{a_2 a_4}{\tau_p^2} = \frac{2n^2\chi^{(3)} E_{bias} E_0^2}{4\pi\varepsilon_r r c^2\tau_p^2}, \tag{7.24}$$

represent the magnitudes of the quasi-static field, near field and far field component respectively.

It is found that in the 12 μm separation case, for the waveform measured by Device A (Figure 7.13(a)), the fitting parameters give the result as

$$\|a_2\| = 27.5 \quad \mu V \cdot cm^{-4}, \tag{7.25}$$

$$\|\frac{a_2 a_3}{\tau_p}\| = 2.4 \quad \mu V \cdot cm^{-4}, \tag{7.26}$$

$$\|\frac{a_2 a_4}{\tau_p^2}\| = 0.14 \quad \mu V \cdot cm^{-4}, \tag{7.27}$$

For Device B (Figure 7.13(b)), they are

$$\|a_2\| = 38.7\mu \quad V \cdot cm^{-4}, \tag{7.28}$$

$$\|\frac{a_2 a_3}{\tau_p}\| = 0.78 \quad \mu V \cdot cm^{-4}, \tag{7.29}$$

$$\|\frac{a_2 a_4}{\tau_p^2}\| = 0.75 \quad \mu V \cdot cm^{-4}, \tag{7.30}$$

This implies that the quasi-static field overwhelms the other two terms and dominates in the observed response.

This THz radiation can propagate from one junction to the other via three different media: vacuum, LAO and STO. Both LAO and STO show strong dispersion and have much larger refractive index for THz frequencies[170, 171]. Therefore, one expects the propagation time for $E_{emit}(t)$ in both oxide layers to be much longer than 40 fs. The dominant response is clearly coming from free-space propagation not strongly coupled to the LAO/STO interface. Much weaker dispersive effects are observed in both the single-junction and double-junction

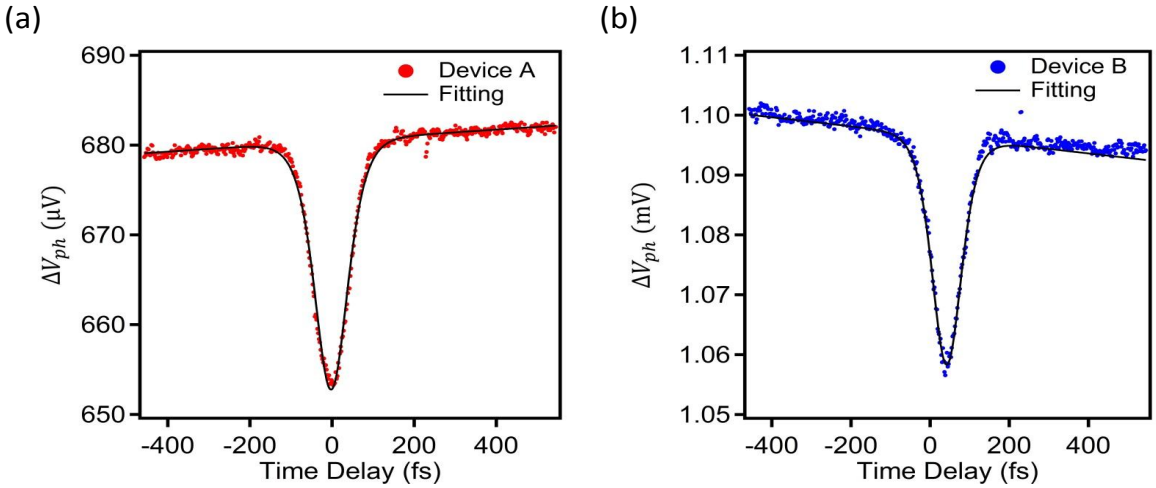

Figure 7.13: Fitting the experimental data with Hertzian dipole model. (a) The measured waveform by Device A that is defined in Figure 7.11 is fitted with Hertzian dipole model to figure out the contribution from different fields. (b) The same analysis as (a) for the data from Device B defined in Figure 7.11.

experiments; an investigation of the self-interaction of THz radiation within the LAO/STO system extends beyond the scope of this paper and will be discussed elsewhere.

The polarization dependence for the two-junction experiment (Figure 7.14) matches that of the single junctions: a time-resolved signal is observed when both polarizations are parallel, and the signal is suppressed when they are perpendicular to each other. The overall similarity between one-junction and two-junction measurements implies that the same physical process is involved in these two different experiments. It is noticed that different polarization configurations lead to slightly different relative time delay (Figure 7.14(a) and (c)).

For the 12 μm separation geometry (Figure 7.11(a)), as discussed above, a cross detection configuration is employed. However, for the 6 μm separation geometry, a different detection scheme is exploited: the pump beam is focused on Device $A^{'}$ (Figure 7.15(a)) and the probe beam is focused on Device $B^{'}$ (Figure 7.15(a)). The pump and probe beam are intensity modulated at frequency $f_{pump} \approx 400$ Hz and $f_{probe} \approx 330$ Hz, respectively. The photo-induced differential voltage ΔV_{ph} in both devices are simultaneously detected by two lock-in amplifiers (Stanford Research System SR830 for Device $A^{'}$ and Signal Recover 7265 for Device $B^{'}$) at frequency $\Delta f = f_{pump} - f_{probe} \approx 70$ Hz.

By fitting the two curves in Figure 7.15(b) with the Hertzian dipole model, one can find that for Device $A^{'}$ (Figure 7.16(a)) there are

$$\|a_2\| = 17.1 \quad \mu V \cdot cm^{-4}, \tag{7.31}$$

$$\|\frac{a_2 a_3}{\tau_p}\| = 6.8 \quad \mu V \cdot cm^{-4}, \tag{7.32}$$

$$\|\frac{a_2 a_4}{\tau_p^2}\| = 4.6 \quad \mu V \cdot cm^{-4}, \tag{7.33}$$

and for Device $B^{'}$ (Figure 7.16(b)) there are

$$\|a_2\| = 17.9 \quad \mu V \cdot cm^{-4}, \tag{7.34}$$

$$\|\frac{a_2 a_3}{\tau_p}\| = 5.7 \quad \mu V \cdot cm^{-4}, \tag{7.35}$$

$$\|\frac{a_2 a_4}{\tau_p^2}\| = 1.4 \quad \mu V \cdot cm^{-4}. \tag{7.36}$$

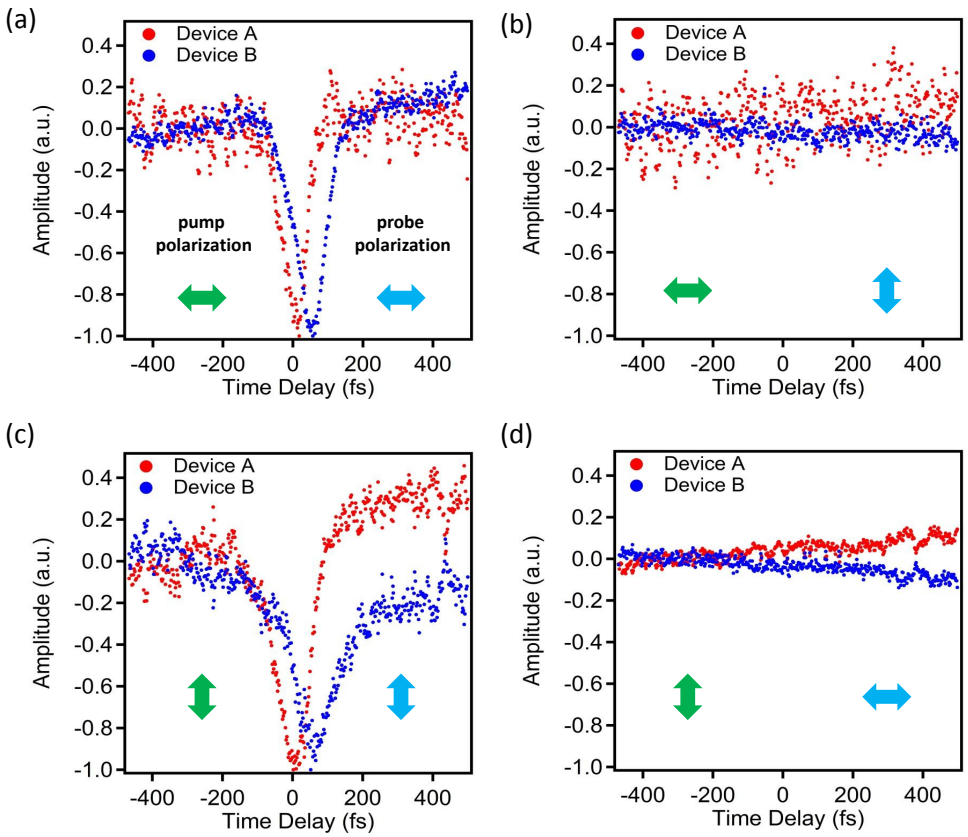

Figure 7.14: (a) The polarization of pump and probe are both in X direction. The relative time delay $\Delta\tau \approx 50$ fs. (b) The polarization of the pump is in the X direction while the polarization of the probe is in the Y direction. (c) Both polarizations are in the Y direction. The relative time delay $\Delta\tau \approx 57$ fs. (d) The polarization of pump is in Y direction while the polarization of probe is in X direction (T = 80 K, NA = 0.53, $I_{ave} \approx 50$ kW/cm^2 and V_s = -1 V on both devices). In (b) and (d), curves are normalized by the values used in (a), respectively. In all figures, each curve is an average over five measurements.

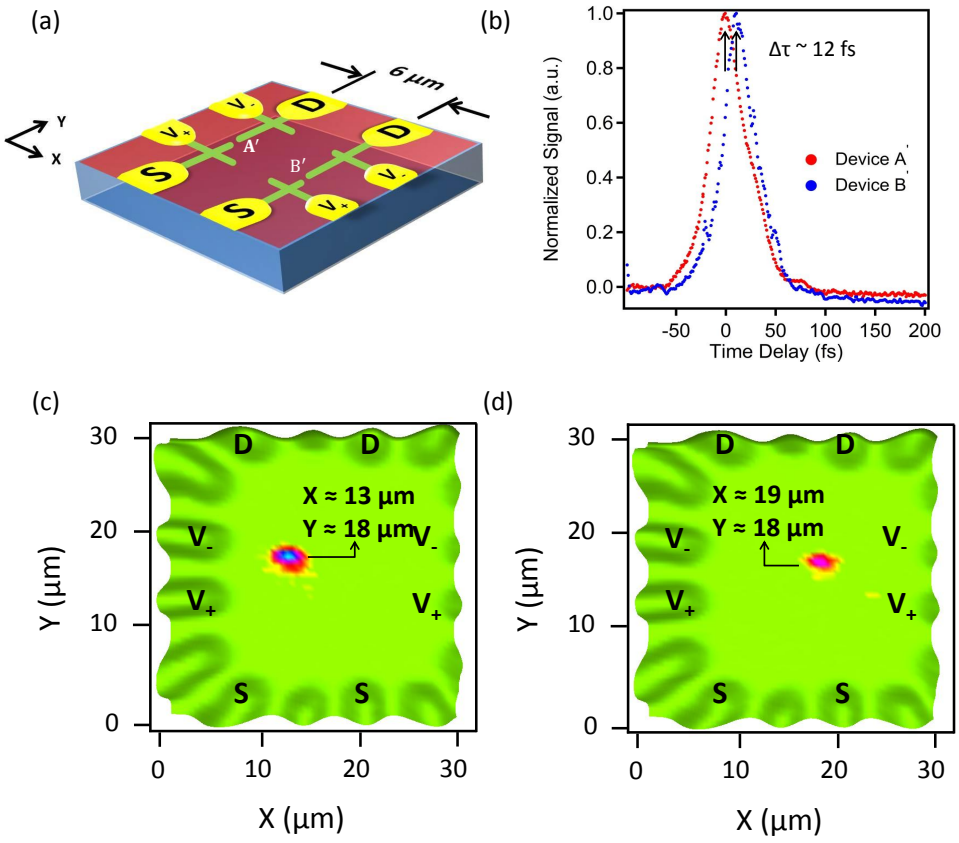

Figure 7.15: (a) Schematic of the double-junction structure. (b) Time-resolved signal from both devices. Each curve is an average of 100 measurements. The time difference between them is about 12 fs (NA = 0.53, $I_{ave} \approx 77$ kW/cm^2 and V_s = - 1 V on both devices). (c) and (d), Time-averaged images overlapped with reflection images show the location of two junctions. Both have the same false color scale and the same scan size of 32 μm by 32 μm. The designed distance between two junctions is 6 μm, which is confirmed by experimental data (NA = 0.53, $I_{ave} \approx 10$ kW/cm^2 , V_s = - 0.1 V for both devices).

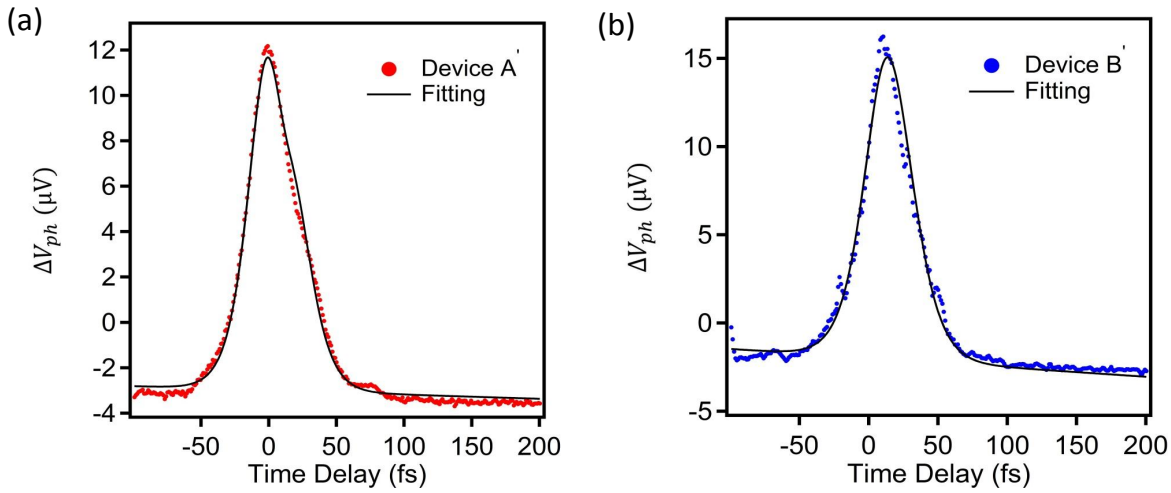

Figure 7.16: Fitting the experimental data with Hertzian dipole model. (a) The measured data for Device $A^{'}$ is fitted with Hertzian dipole model. (b) The fitting analysis for the data from Device $B^{'}$.

The fitting results indicate that in 6 μm case, the measured waveform has almost equal contributions from the quasi-static field, the near-field and the far-field.

7.5 CONCLUSION

The $\chi^{(3)}$ process discovered in the nanostructure at the interface of LAO/STO can give rise to rectified THz fields which provides useful spectral information[131]. As a THz source and sensor, the nanojunction structure offers several advantages: its dimension is comparable to that of a single molecule; it is easy to fabricate, and the THz source and detector can be easily integrated in a micron-scale area. These features allow this platform to be a promising lab-on-chip device for THz near-field imaging of individual molecules.

8.0 OUTLOOK

Chapter 6 and Chapter 7 both show that the oxide nanostructures provide great potential in various photonic applications. The development of a nanoscale THz source and sensor that is close to the size of a single molecule can potentially add new families of THz devices to THz spectroscopy research [172].

When light interacts with nanostructures, it can couple to free-electron excitations at the surface. The electromagnetic resonances associated with the surface plasmons form quasi-particles called surface plasmon polaritons (SPP). They have become the focus of intense research owing to their subwavelength confinement and potential ability to perform ultrasensitive optical measurements [173, 174, 175]. In optical pump-probe experiments on the nanodevices at the interface of $LaAlO_3/SrTiO_3$, strong oscillations are observed. One possible origin is the excitation of SPP in the oxide heterostructure.

8.1 THZ SPECTROSCOPY FOR A SINGLE MOLECULE

At the time when this thesis is synthesized, THz spectroscopy has not been applied to a single molecule yet because of the lack of enough sensitivity and sufficiently high spatial resolution. One strength of the c-AFM lithography method is that it can fabricate devices that can be as small as 2 nm. This dimension approaches the size of a single molecule. One possible way to realize the imaging for a single molecule is to integrate our nanoscale THz emitter and detector platform with an atomic force microscope (AFM). The AFM can be exploited to locate the target of imaging. Afterwards, the same AFM can be used to create both the emitter and detector in close proximity to the target (Figure 8.1). Another approach involves

electrostatic trapping of single particles [176]. Polar particles can be attracted by the electric field confined in the nanojunction. By measuring the transport properties, one can determine whether the particle is trapped or not, and subsequently perform THz spectroscopy with and without the particle or molecule.

8.2 NANOSCALE SURFACE PLASMON POLARITON

The oxide photonic nanostructures may also provide opportunities to explore surface plasmon polaritons (SPP) in oxide heterostructures. A SPP is usually excited at the interface between metal and dielectrics, and its basic properties can be understood by solving the Maxwell equation.

$$\begin{aligned} \nabla \cdot \vec{D} &= \rho_f \\ \nabla \times \vec{E} &= -\frac{\partial \vec{B}}{\partial t} \\ \nabla \cdot \vec{B} &= 0 \\ \nabla \times \vec{H} &= \vec{J}_f + \frac{\partial \vec{D}}{\partial t} \end{aligned} \tag{8.1}$$

8.2.1 Surface Plasmon Polariton

Because there are usually no free charges or currents in either metal or dielectrics, we can set $\rho_f = 0$ and $\vec{J}_f = 0$. Therefore, the Maxwell equations become:

$$\begin{aligned} \nabla \cdot \vec{D} &= 0 \\ \nabla \times \vec{E} &= -\frac{\partial \vec{B}}{\partial t} \\ \nabla \cdot \vec{B} &= 0 \\ \nabla \times \vec{H} &= \frac{\partial \vec{D}}{\partial t} \end{aligned} \tag{8.2}$$

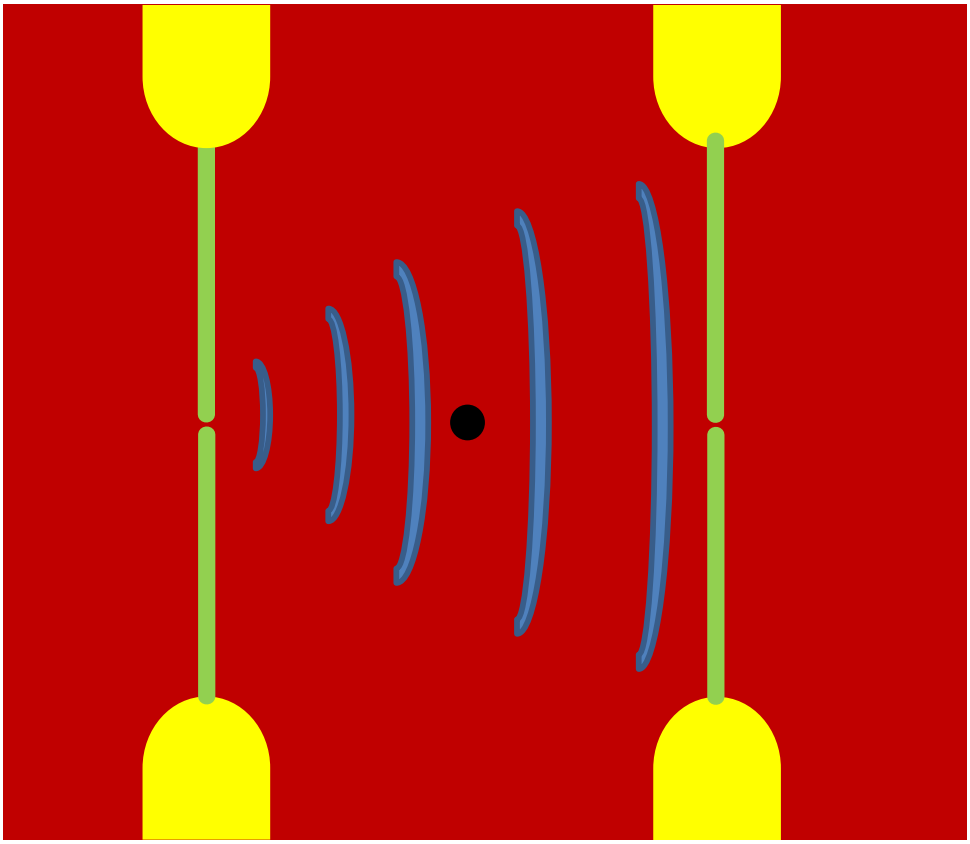

Figure 8.1: Device geometry for THz spectroscopy for a single molecule.

Suppose the incident electromagnetic wave is p-polarized (Figure 8.2), which means the magnetic field $\vec{H}$ is in the y direction while the electric field $\vec{E}$ has both x and z component. The fields in the metal are

$$\vec{E}_m = (E_{mx}, 0, E_{mz})e^{i(k_{mx}x - k_{mz}z)}e^{-i\omega t} \tag{8.3}$$

$$\vec{H}_m = (0, H_{my}, 0)e^{i(k_{mx}x - k_{mz}z)}e^{-i\omega t} \tag{8.4}$$

The fields in the dielectrics are

$$\vec{E}_d = (E_{dx}, 0, E_{dz})e^{i(k_{dx}x + k_{dz}z)}e^{-i\omega t} \tag{8.5}$$

$$\vec{H}_d = (0, H_{dy}, 0)e^{i(k_{dx}x + k_{dz}z)}e^{-i\omega t} \tag{8.6}$$

At the boundary, the normal components of $\vec{D}$ and $\vec{B}$ must be continuous and the tangential components of $\vec{E}$ and $\vec{H}$ must be continuous. Since we have

$$\vec{D} = \varepsilon_0 \varepsilon_r \vec{E}$$

$$\vec{B} = \mu_0 \mu_r \vec{H}$$

and we can assume that $\mu_r \approx 1$. The boundary conditions are

$$\varepsilon_{rm} E_{mz} = \varepsilon_{rd} E_{dz} \tag{8.7}$$

$$E_{mx} = E_{dx} \tag{8.8}$$

$$H_{my} = H_{dy} \tag{8.9}$$

In the metal, the relation between $\vec{H}$ field and $\vec{E}$ field is

$$-\frac{\partial H_{my}}{\partial z} = \varepsilon_0 \varepsilon_{rm} \frac{\partial E_{mx}}{\partial t} \tag{8.10}$$

$$\frac{\partial H_{my}}{\partial x} = \varepsilon_0 \varepsilon_{rm} \frac{\partial E_{mz}}{\partial t} \tag{8.11}$$

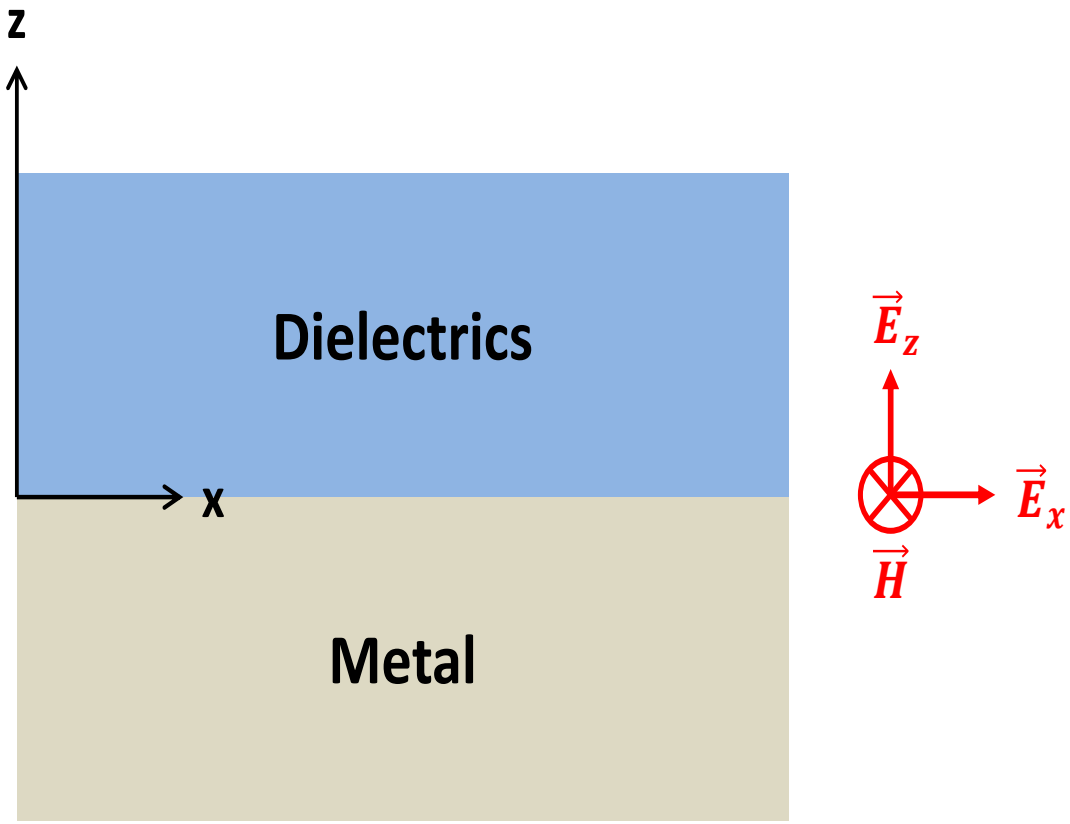

Figure 8.2: Surface plasmon polaritons at the metal-dielectrics interface.

which leads to

$$k_{mz}H_{my} = -\varepsilon_0\varepsilon_{rm}\omega E_{mx} \tag{8.12}$$

$$k_{mx}H_{my} = -\varepsilon_0\varepsilon_{rm}\omega E_{mz} \tag{8.13}$$

Similarly, in the dielectric we have

$$k_{dz}H_{dy} = \varepsilon_0\varepsilon_{rd}\omega E_{dx} \tag{8.14}$$

$$k_{dx}H_{dy} = -\varepsilon_0\varepsilon_{rd}\omega E_{dz} \tag{8.15}$$

From Eq.(8.13) and Eq.(8.15), we can derive that

$$k_{mx} = k_{dx}. \tag{8.16}$$

From Eq.(8.12) and Eq.(8.14), we have

$$\frac{k_{mz}}{k_{dz}} = -\frac{\varepsilon_{rm}}{\varepsilon_{rd}}. \tag{8.17}$$

From the wave equation in metal and dielectrics, we can have

$$k_{mx}^2 + k_{mz}^2 = \frac{\varepsilon_{rm}}{c^2}\omega^2 \tag{8.18}$$

$$k_{dx}^2 + k_{dz}^2 = \frac{\varepsilon_{rd}}{c^2}\omega^2 \tag{8.19}$$

Since $k_{mx} = k_{dx}$, it is readily to have

$$k_{mz}^2 - k_{dz}^2 = \frac{\varepsilon_{rm} - \varepsilon_{rd}}{c^2}\omega^2 \tag{8.20}$$

From Eq.(8.17) and Eq.(8.20), we can solve for k_{mz} and k_{dz}

$$k_{mz}^2 = \frac{\omega^2}{c^2}\frac{\varepsilon_{rm}^2}{\varepsilon_{rm} + \varepsilon_{rd}} \tag{8.21}$$

$$k_{dz}^2 = \frac{\omega^2}{c^2}\frac{\varepsilon_{rd}^2}{\varepsilon_{rm} + \varepsilon_{rd}} \tag{8.22}$$

and k_{mx} (or k_{dx}) is found to be

$$k_{mx}^2 = k_{dx}^2 = \frac{\omega^2}{c^2}\frac{\varepsilon_{rm}\varepsilon_{rd}}{\varepsilon_{rm}+\varepsilon_{rd}} \tag{8.23}$$

For k_{mx} (and k_{dx}) to be real, we must have $Re(\varepsilon_{rm}) < 0$ and $|\varepsilon_{rm}| > \varepsilon_{rd}$. Under this condition, both k_{mz} and k_{dz} are imaginary. This solution describes a situation that the electromagnetic field can propagate alone the x direction at the interface between metal and dielectric, but the field decays inside both metal and dielectrics.

We assume that the incident wave is s-polarized, which means the electric field is in the y direction while the magnetic field has both x and z components. In metal, the fields are

$$\vec{E}_m = (0, E_{my}, 0)e^{i(k_{mx}x - k_{mz}z)}e^{-i\omega t} \tag{8.24}$$

$$\vec{H}_m = (H_{mx}, 0, H_{mz})e^{i(k_{mx}x - k_{mz}z)}e^{-i\omega t} \tag{8.25}$$

In the dielectrics, the fields are

$$\vec{E}_d = (0, E_{dy}, 0)e^{i(k_{dx}x + k_{dz}z)}e^{-i\omega t} \tag{8.26}$$

$$\vec{H}_d = (H_{dx}, 0, H_{dz})e^{i(k_{dx}x + k_{dz}z)}e^{-i\omega t} \tag{8.27}$$

The boundary conditions now are

$$H_{mz} = H_{dz} \tag{8.28}$$

$$E_{my} = E_{dy} \tag{8.29}$$

$$H_{mx} = H_{dx} \tag{8.30}$$

In the metal, the relation between the $\vec{H}$ field and $\vec{E}$ field can be found to be

$$-\frac{\partial E_{my}}{\partial z} = \mu_0\frac{\partial H_{mx}}{\partial t} \tag{8.31}$$

$$\frac{\partial E_{my}}{\partial x} = \mu_0\frac{\partial H_{mz}}{\partial t} \tag{8.32}$$

which leads to

$$k_{mz}E_{my} = -\mu_0\omega H_{mx} \tag{8.33}$$

$$k_{mx}E_{my} = -\mu_0\omega H_{mz} \tag{8.34}$$

Similarly in dielectrics we have

$$k_{dz}E_{dy} = \mu_0\omega H_{dx} \tag{8.35}$$

$$k_{dx}E_{dy} = -\mu_0\omega H_{dz} \tag{8.36}$$

From Eq.(8.33) and Eq.(8.35), we have

$$(k_{mz} + k_{dz})E_{my} = 0. \tag{8.37}$$

If $E_{my} \neq 0$, then we have

$$k_{mz} = -k_{dz}. \tag{8.38}$$

From Eq.(8.34) and Eq.(8.36) we also have

$$k_{mx} = k_{dx}. \tag{8.39}$$

Then from the dispersion relation, we can reach the result that $k_{mx}^2 + k_{mz}^2 = k_{dx}^2 + k_{dz}^2$ which means

$$\varepsilon_{rm} = \varepsilon_{rd} \tag{8.40}$$

which is not possible. Therefore we have to require that $E_{my} = 0$. Therefore s-polarized surface plasmon cannot exist.

Different schemes that are used to excite the surface plasmon polariton (SPP) are summarized in Figure 8.3.

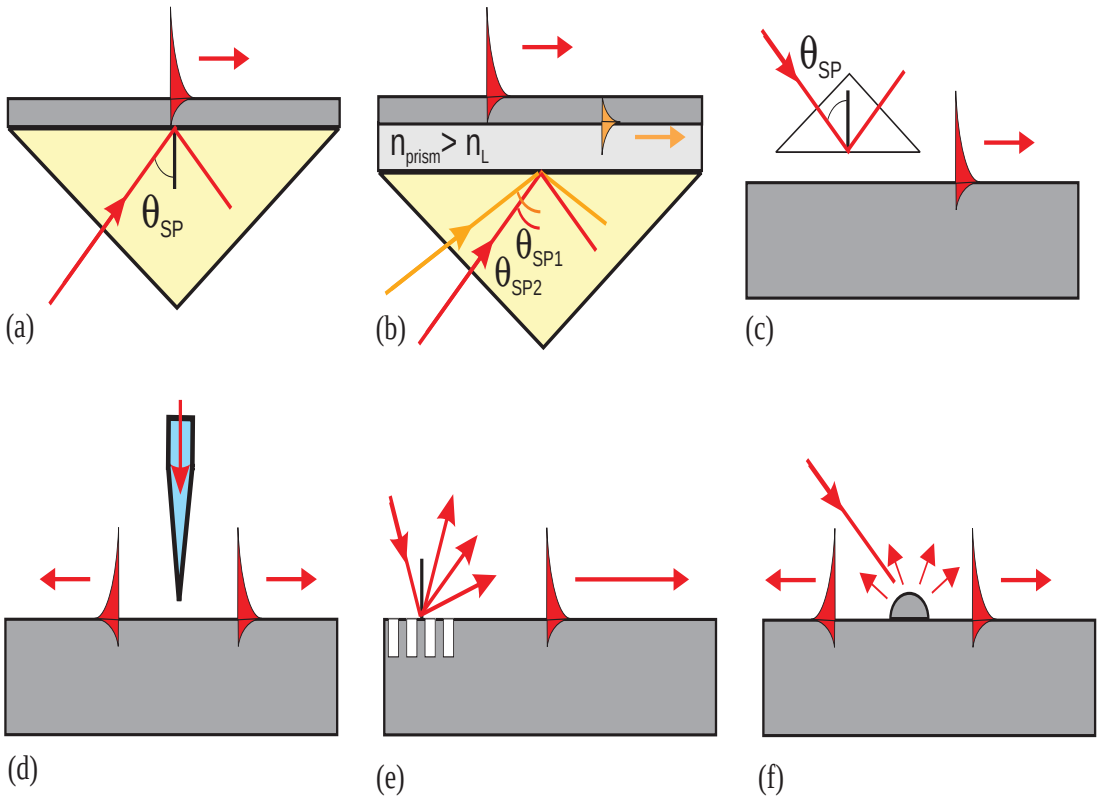

Figure 8.3: SPP excitation configuration. (a) Kretschmann geometry. (b) Two-layer Kretschmann geometry. (c) Otto geometry. (d) Excitation with a scanning near-field optical microscope probe. (e) Diffraction on a grating. (f) Diffraction on surface features.(This figure is from Ref. [177].)

8.2.2 Preliminary Results

For the sketched nanostructures at the interface of LAO/STO, we also observe strong oscillations in the time-resolved experiments. The nanostructure has the configuration shown in Figure 8.4.

The setup of the time-resolved experiments is basically the same as shown in Chapter 7. When both pump and probe are focused onto the junction, the ultrafast response discussed in Chapter 7 is discovered. However, at certain spots other than the nanojunction, we observe fast oscillations (Figure 8.5(e) and (f)) with frequencies about 78 THz(Figure 8.6(a) and (b)), although the physical origin of these strong oscillations requires further study.

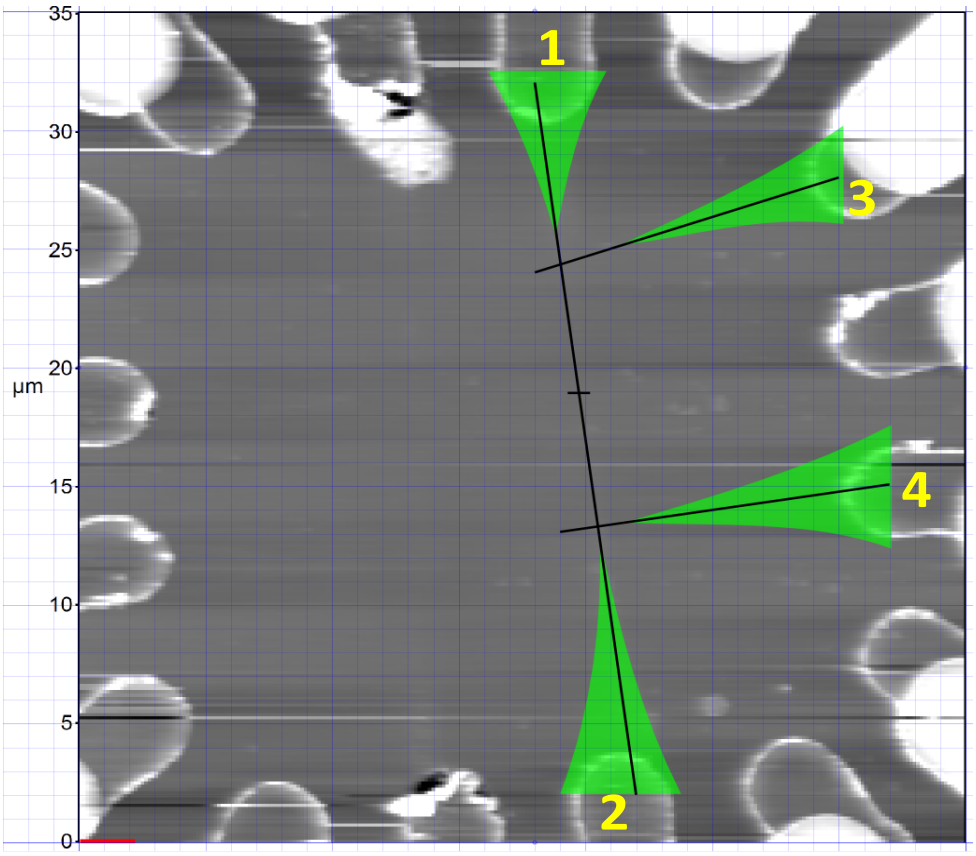

Figure 8.4: The configuration of the nanodevice. The backgroud is the topography image obtained by AFM. The green funnels indicate the area where the scanning is performed with positive voltages on the AFM tip. The black lines indicate the positions of nanowires created by applying positive voltages onto the tip. The short horizontal line that crosses the nanowire between Electrode 1 and 2 indicate the trajectory scanned with negative voltage on the AFM probe. Electrode 1 and 2 are used as source and drain. Electrode 3 and 4 are for sensing the voltage cross the junction.

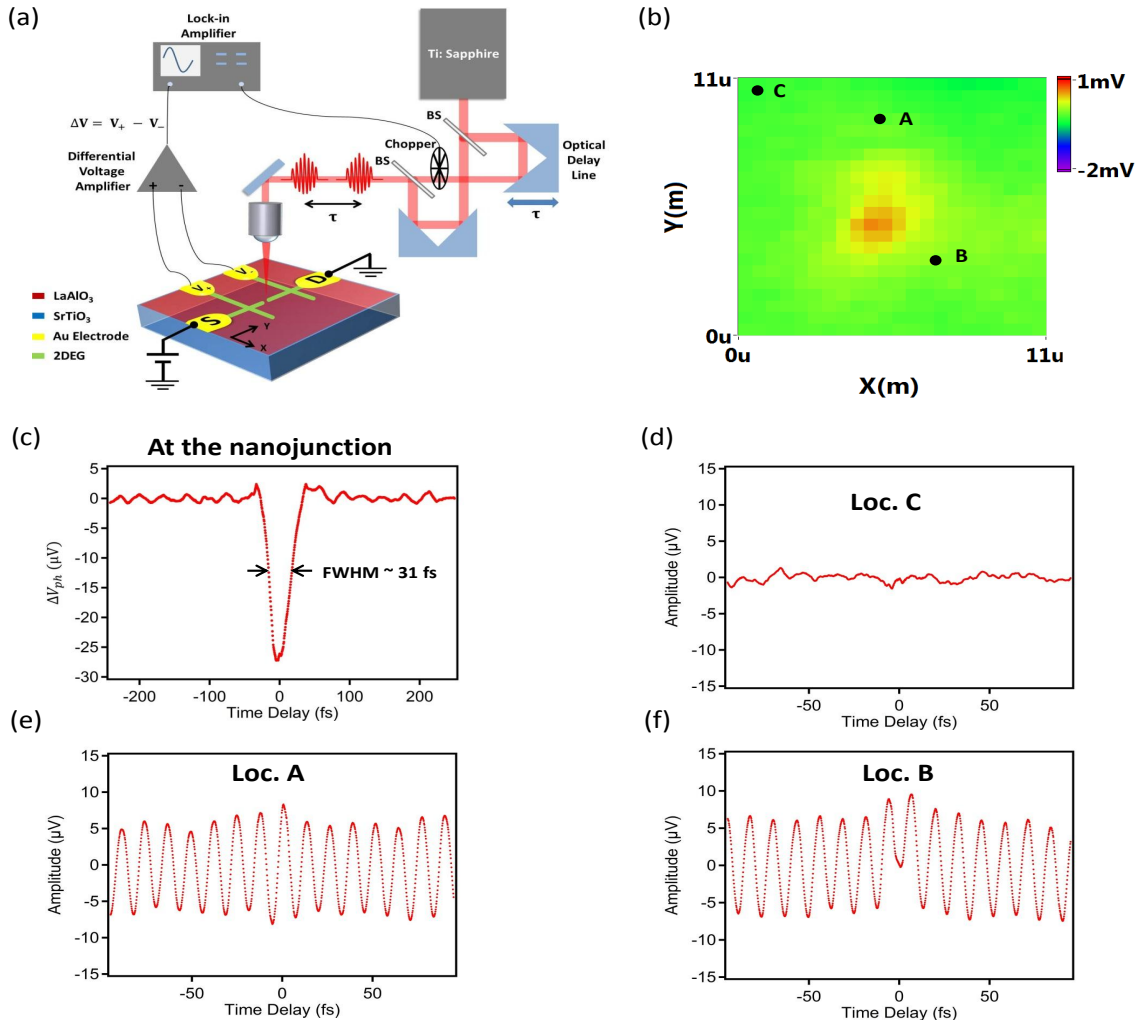

Figure 8.5: Possible plasmonic effect observed in the oxide nanostructures at the interface of $LaAlO_3/SrTiO_3$. (a) Experimental setup for time-resolved measurements. S and D stand for the source and drain terminal. V_+ and V_- are sensing the voltage ΔV cross the gap. X and Y indicate the scanning directions. (b) Scanning photoconductivity image. The color scale shows the magnitude of ΔV. The diffraction-limited peak shows the location of the nanojunction. Location A and B indicate the positions at which the oscillations are observed. Location C is a reference point at which no oscillation is observed. ($NA = 0.73$, $I_{ave} = 10$ kW/cm^2, V_s = -1 V) (c) Temporal response when both pump and probe are focused onto the nanojunction. ($NA = 0.73$, $I_{ave} = 50$ kW/cm^2.) (d-f), Temporal response when both beams are focused onto Location C (d), A (e) and B (f), respectively. Each waveform is an average of 120 measurements. ($NA = 0.73$, $I_{ave} = 50$ kW/cm^2.)

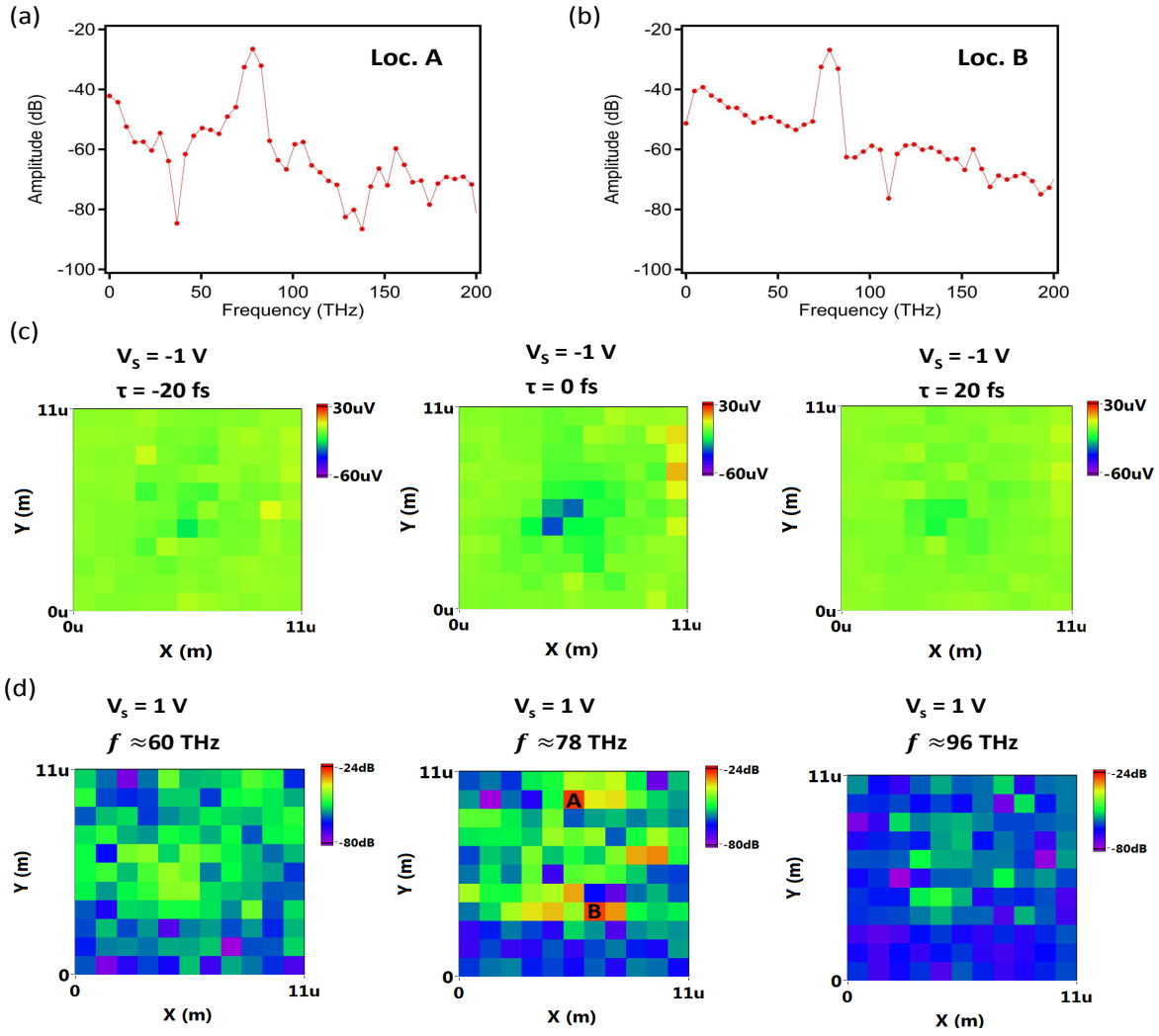

Figure 8.6: Temporal-spatial and frequency-spatial images. (a) Fourier transform of the temporal response in Figure 8.5(e). (b) Fourier transform of the temporal response in Figure 8.5(f). (c), Temporal-spatial images show that the ultrafast response is localized around the nanojunction. ($NA = 0.73$, $I_{ave} = 50$ kW/cm^2.) (d), Frequency-spatial images show that the 78 THz oscillation is near the conductive nanowires. ($NA = 0.73$, $I_{ave} = 50$ kW/cm^2.)

APPENDIX A

DOUBLE-PULSE PHENOMENON

During the characterization of our customized Ti:sapphire laser, we notice sometimes that the spectrum shows oscillation patterns like in Figure A1. This is the signature of double pulses[1].

One way to detect double pulses is to use a fast photodetector and an oscilloscope. Figure A2 shows such a measurement. In Figure A2(a), no double pulses occur. However, in Figure A2(b), when an oscillation pattern shows up in the spectrum, two pulses close to each other are detected.

The reason for the occurrence of the double pulsing phenomenon is believed to have to do with both the pumping power and the intracavity dispersion [99]. In practice, it is found that an easy way to solve the problem is to decrease the pumping power until the oscillation patterns in the spectrum go away. However, this method is not always applicable because the pumping power cannot be decreased below the threshold value required for mode-locking to occur. Therefore, the fused silica wedge pair in the cavity should be adjusted to change the intracavity dispersion. Double pulsing may be eliminated under certain dispersion condition. For our home-built Ti:sapphire laser, the pumping power is usually set at $4 \sim 4.2$ W. The output power of the mode-locking mode is about 170 mW. Higher output power may result in double pulses.

[1] An online article describing double pulses can be found here.

(a)

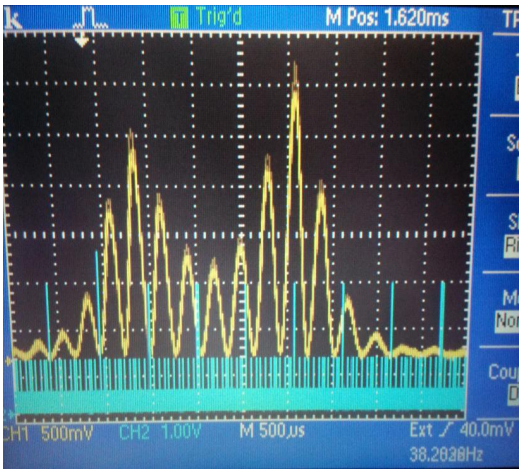

(b)

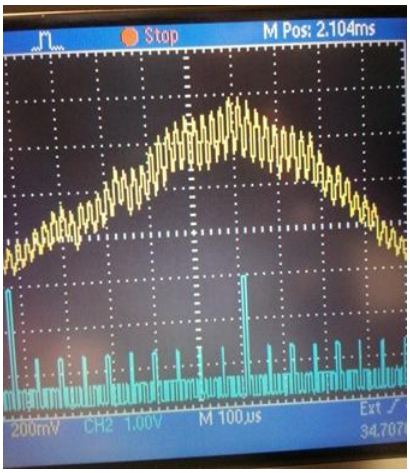

Figure A1: The spectrum of the mode-locked laser shows oscillations when double pulsing occurs.

(a)

(b)

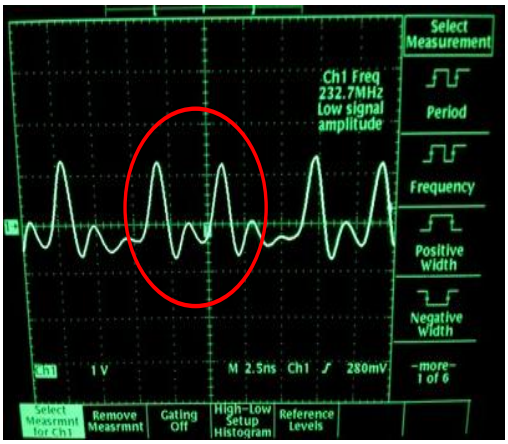

Figure A2: (a) The normal mode-locking mode outputs pulses with designed repetition rate. (b) When double pulsing occurs, the laser can output two pulses that are close to one another like the ones in the red circle. They are seperated by ≈ 2.5 ns. The measured repetition rate is roughly doubled as well.

APPENDIX B

MATHEMATICA CODE FOR CALCULATION OF A LASER CAVITY

In this chapter, the Mathematica code for calculating the mode-locking conditions for our customized Ti:sapphire laser is presented with comments explaining what each command does.

All quantities are expressed in the unit of millimeters(mm). The following codes are used in Mathematica 7. First of all, we need to define several parameters:

$$\mathrm{d} = 2 \quad * \text{ The thickness of the crystal. } *$$

$$\mathrm{R} = 75 \quad * \text{ The radius of the focusing mirror. } *$$

$$\mathrm{n} = 1.76 \quad * \text{ The refractive index of the crystal at 800 nm. } *$$

$$\mathrm{f} = 75 \quad * \text{ The focal length of the convex lens for the pumping light. } *$$

We then solve for the folding angle of two focusing mirrors

$$\mathrm{sol} = \mathrm{Solve}[\frac{\mathrm{Sin[x]Sin[x]}}{\mathrm{Cos[x]}} == \frac{\mathrm{d}}{\mathrm{R}}\frac{\sqrt{\mathrm{n}^4-1}\sqrt{\mathrm{n}^2-1}}{\mathrm{n}^4}, \mathrm{x}]$$

$$\mathrm{theta} = \mathrm{x/.sol[[2]]}$$

$$\mathrm{foldingangle} = 2 * \mathrm{theta} * 180/\pi$$

The focus and effective thickness in the tangential plane are defined as

$$\text{fa} = \text{RCos[theta]}/2$$
$$\text{dea} = \frac{\text{d}\sqrt{\text{n}^2+1}}{\text{n}^4}$$

The focus and effective thickness in the sagittal plane are

$$\text{fb} = \text{R}/2\text{Cos[theta]}$$
$$\text{deb} = \frac{\text{d}\sqrt{\text{n}^2+1}}{\text{n}^2}$$

From now on, the following codes are written for the tangential plane. Calculations in the sagittal plane can be done by replacing the quantity fa and dea with fb and deb, respectively.

Now we can calculate the length of two arms L_1 and L_2

$$\text{arm} = \text{Solve}[\{\text{d1} + \text{d2} == 1500, \frac{\text{d2} - \text{fa}}{\text{d1} - \text{fa}} == 1.75\}, \text{d1}, \text{d2}]$$
$$\text{L1} = \text{d1}/.\text{arm}[[1]][[1]]$$
$$\text{L2} = \text{d2}/.\text{arm}[[1]][[2]]$$

Before we can calculate the function $S(x, z)$ and $\delta(x, z)$, we need compute several matrices as described in Chapter 5

$$\text{Aa} = \begin{pmatrix} 1 & \text{z-x-dea} \\ 0 & 1 \end{pmatrix} \cdot \begin{pmatrix} 1 & 0 \\ -\frac{1}{\text{fa}} & 1 \end{pmatrix} \cdot \begin{pmatrix} 1 & \text{L1} \\ 0 & 1 \end{pmatrix} \cdot \begin{pmatrix} 1 & 0 \\ 0 & 1 \end{pmatrix} \cdot \begin{pmatrix} 1 & \text{L1} \\ 0 & 1 \end{pmatrix} \cdot \begin{pmatrix} 1 & 0 \\ -\frac{1}{\text{fa}} & 1 \end{pmatrix} \cdot \begin{pmatrix} 1 & \text{z-x-dea} \\ 0 & 1 \end{pmatrix}$$

$$\text{Ba} = \begin{pmatrix} 1 & \text{x} \\ 0 & 1 \end{pmatrix} \cdot \begin{pmatrix} 1 & 0 \\ -\frac{1}{\text{fa}} & 1 \end{pmatrix} \cdot \begin{pmatrix} 1 & \text{L2} \\ 0 & 1 \end{pmatrix} \cdot \begin{pmatrix} 1 & 0 \\ 0 & 1 \end{pmatrix} \cdot \begin{pmatrix} 1 & \text{L2} \\ 0 & 1 \end{pmatrix} \cdot \begin{pmatrix} 1 & 0 \\ -\frac{1}{\text{fa}} & 1 \end{pmatrix} \cdot \begin{pmatrix} 1 & \text{x} \\ 0 & 1 \end{pmatrix}$$

$$\text{Ma} = \begin{pmatrix} 1 & \text{L2} \\ 0 & 1 \end{pmatrix} \cdot \begin{pmatrix} 1 & 0 \\ -\frac{1}{\text{fa}} & 1 \end{pmatrix} \cdot \begin{pmatrix} 1 & \text{x} \\ 0 & 1 \end{pmatrix} \cdot \begin{pmatrix} 1 & \text{dea} \\ 0 & 1 \end{pmatrix} \cdot \begin{pmatrix} 1 & \text{z-x-dea} \\ 0 & 1 \end{pmatrix} \cdot \begin{pmatrix} 1 & 0 \\ -\frac{1}{\text{fa}} & 1 \end{pmatrix} \cdot \begin{pmatrix} 1 & \text{L1} \\ 0 & 1 \end{pmatrix}$$

Two functions can be defined in Mathematica

$$\text{a1a[x\_,z\_]} := \frac{2\text{Aa[[1]][[2]]Aa[[2]][[2]]}}{\text{dea}} - \frac{\text{Aa[[1]][[1]]Aa[[2]][[1]]dea}}{2}$$
$$\text{a2a[x\_,z\_]} := \frac{2\text{Ba[[1]][[2]]Ba[[2]][[2]]}}{\text{dea}} - \frac{\text{Ba[[1]][[1]]Ba[[2]][[1]]dea}}{2}$$

The stability function $S(x, z)$ is given by

$$\text{Sa[x\_,z\_]} := \text{Ma[[1]][[1]]Ma[[2]][[2]] + Ma[[1]][[2]]Ma[[2]][[1]]}$$

The function $\delta(x, z)$ is

$$\text{deltaa[x\_,z\_]} := \frac{\text{a1a[x,z] + a2a[x,z]Sa[x,z]}}{2(a1a[x,z]^2 + a2a[x,z]^2 + 2a1a[x,z]a2a[x,z]Sa[x,z])}$$

We can plot $S(x, z)$ out

$$\text{Plot3D[Sa[x,z], \{x, 25, 45\}, \{z, 74, 81\},}$$
$$\text{RegionFunction} \to \text{Function[\{x, z, y\}, } -1 < \text{Sa[x,z]} < 1]]$$

The parameter range for mode-locking to occur can be computed by calculating $S(x, z)$ under the condition of $\delta(x, z) < 0$

$$\text{DensityPlot[Sa[x,z], \{x, 25, 45\}, \{z, 74, 81\},}$$
$$\text{RegionFunction} \to \text{Function[\{x, z, y\}, } -1 < \text{Sa[x,z]} < 1\&\&\text{deltaa[x,z]} < 0]]$$

The following codes describe the calculation for mode matching. We first compute the following matrix

$$\text{Matrixa} = \begin{pmatrix} 1 & \frac{\text{dea}}{2} \\ 0 & 1 \end{pmatrix} \cdot \begin{pmatrix} 1 & \text{x} \\ 0 & 1 \end{pmatrix} \cdot \begin{pmatrix} 1 & 0 \\ -\frac{1}{\text{fa}} & 1 \end{pmatrix} \cdot \begin{pmatrix} 1 & \text{L2} \\ 0 & 1 \end{pmatrix} \cdot \begin{pmatrix} 1 & 0 \\ 0 & 1 \end{pmatrix} \cdot \begin{pmatrix} 1 & \text{L2} \\ 0 & 1 \end{pmatrix} \cdot \begin{pmatrix} 1 & 0 \\ -\frac{1}{\text{fa}} & 1 \end{pmatrix}$$
$$\cdot \begin{pmatrix} 1 & \text{x} \\ 0 & 1 \end{pmatrix} \cdot \begin{pmatrix} 1 & \text{dea} \\ 0 & 1 \end{pmatrix} \cdot \begin{pmatrix} 1 & \text{z-x-dea} \\ 0 & 1 \end{pmatrix} \cdot \begin{pmatrix} 1 & 0 \\ -\frac{1}{\text{fa}} & 1 \end{pmatrix} \cdot \begin{pmatrix} 1 & \text{L1} \\ 0 & 1 \end{pmatrix} \cdot \begin{pmatrix} 1 & 0 \\ 0 & 1 \end{pmatrix}$$
$$\cdot \begin{pmatrix} 1 & \text{L1} \\ 0 & 1 \end{pmatrix} \cdot \begin{pmatrix} 1 & 0 \\ -\frac{1}{\text{fa}} & 1 \end{pmatrix} \cdot \begin{pmatrix} 1 & \text{z-x-dea} \\ 0 & 1 \end{pmatrix} \begin{pmatrix} 1 & \frac{\text{dea}}{2} \\ 0 & 1 \end{pmatrix}$$

Then we can solve for the beam waist of the cavity mode at the center of Ti:sapphire crystal by calculating the q parameter

$$\text{qsolution} = \text{Solve}[\text{q} == \frac{\text{qMatrixa}[[1]][[1]] + \text{Matrixa}[[1]][[2]]}{\text{qMatrixa}[[2]][[1]] + \text{Matrixa}[[2]][[2]]}, \text{q}]$$

The first element in the solution list given by the above calculation can be defined as a function qfunctiona[x_,z_]. The center wavelength of the cavity mode is

$$\text{Lambdac} = 830 * 10^{-6}$$

The beam waist function is

$$\text{wca}[\text{x\_},\text{z\_}] := \sqrt{\frac{\text{Lambdac}}{\pi \text{Im}[\frac{1}{\text{qfunctiona}[\text{x\_},\text{z\_}]}]}}$$

The beam waist as a function of x can be plotted out by running the following Mathematica commands

$$\text{array3a} = \{\};$$

$$\text{Do}[\text{a} = \{\text{x}/.\text{FindRoot}[\text{Re}[\frac{1}{\text{qfunctiona}[\text{x,z}]}], \text{x}, 25, 45],$$
$$\text{wca}[\text{x,z}]/.\text{FindRoot}[\text{Re}[\frac{1}{\text{qfunctiona}[\text{x,z}]}], \text{x}, 25, 45]\};$$
$$\text{AppendTo}[\text{array3a,a}],\text{z}, 77.3, 78.8, 0.1];$$

We also need compute the beam waist of the pumping light at the center of the crystal. In order to do that, we calculate the following matrix first

$$\text{M1a} = \begin{pmatrix} 1 & \text{x} + \frac{\text{dea}}{2} \\ 0 & 1 \end{pmatrix} \cdot \begin{pmatrix} 1 & 0 \\ -\frac{1}{\text{fa}} & 1 \end{pmatrix} \cdot \begin{pmatrix} 1 & \text{d2} \\ 0 & 1 \end{pmatrix} \cdot \begin{pmatrix} 1 & 0 \\ -\frac{1}{\text{f}} & 1 \end{pmatrix}$$

where d2 is the distance between the focusing lens for the pumping light and the focusing mirror for the cavity mode. The parameters for the pumping light are

$\text{wp} = 2$ * input beam radius. *

$\text{Lambdap} = 533 * 10^{-6}$ * pumping wavelength *

$\text{c} = 3.14^2 * \text{wp}^4/\text{Lambdap}^2$ * a constant *

$\text{q1} = \dfrac{\pi wp^2}{\text{iLambdap}}$ * The initial q parameter for the pumping light *

The q parameter of the pumping light at the center of the crystal is found by the following computation

$$\text{q2solution} = \text{Solve}[\text{q2} == \frac{\text{q1M1a}[[1]][[1]] + \text{M1a}[[1]][[2]]}{\text{q1M1a}[[2]][[1]] + \text{M1a}[[2]][[2]]}, \text{q2}]$$

The first element of the solution array is defined as a function q2functiona[x_]. The beam waist is

$$\text{wpa}[\text{x\_}] := \sqrt{\frac{\text{Lambdap}}{\pi \text{Im}[\frac{1}{\text{q2functiona}[\text{x\_}]}]}}$$

We can make a plot of wpa[x]

$$\text{d2solutiona} = \text{Solve}[\text{cM1a}[[1]][[1]]\text{M1a}[[2]][[1]] + \text{M1a}[[1]][[2]]\text{M1a}[[2]][[2]] == 0, \text{d2}]$$

$$\text{array5a} = \{\};$$

Do[m = {x, wpa[x]/.d2solutiona[[2]]; AppendTo[array5a,m],x, 37.1521, 38.6278, 0.1];

By comparing array3a with array5a, the suitable values of x can be located at where the beam waist of the cavity mode is greater than the one of the pumping mode. The distance d2 can also be plotted as a function of x

array6a ={};

Do[m = {x, d2/.d2solutiona[[2]]; AppendTo[array6a,m],x, 37.1521, 38.6278, 0.1];

Once the x is found, d2 can be fixed. The identical calculation can be repeated for the sagittal plane with fa and dea replaced with fb and deb, respectively. The results from both planes do not show much discrepancy.

APPENDIX C

INTERFEROMETRIC AUTOCORRELATION

Although sophisticated methods, such as FROG [178] and SPIDER [179], have been developed for characterizing the qualities of ultrashort pulses simultaneously, they are not straightforward to use, given that they are heavily equipment- or software-oriented. As a consequence, interferometric autocorrelation (IA) is the most widely used technique due to its effectiveness and accessibility, because only a nonlinear crystal, some mirrors and a photodetector are required . A two-photon absorption detector, like GaAsP in our case, can simplify the setup even further.

The specific measured waveform in an IA experiment is sensitive to the spectral phase of a pulse, the pulse shape and intensity ratio between two interfered pulses [180, 181, 182]. Systematic errors like too low sampling rate can distort the final measurement as well [183]. The purpose of this appendix is to summarize various situations in interferometric autocorrelation measurement that have been or possibly will come across during experiments so that one can avoid some of the errors or at least be cautious of them.

C.1 TWO-PHOTON ABSORPTION DETECTOR

GaAsP[1] is a two-photon absorption (TPA) detector used for IA measurements. There is discussion about the competition between TPA and SHG in GaAsP [184]. These two processes

[1]This item is from Hamamatsu, model number G1117.

may lead to different waveforms in IA measurements. In our experiments, we also notice that GaAsP will be overloaded if the input power is too high. The signature of overloading in GaAsP is that the envelope of the IA waveform is up-side down, meaning that the lower envelope shows larger amplitude than the upper envelope. To avoid this error, an iris can be put in front of the GaAsP detector. By adjusting the size of the opening, one can control how much power is incident onto the detector. The GaAsP detector should be placed at the focus of the focusing element, either a lens or an objective. We usually use the same objectives for the GaAsP detector as for the samples so that the pulse which hits the GaAsP travels through the same optics as the one which hits the sample. By monitoring the pulse quality with GaAsP, we can determine how well the pulse is preserved before it hits the sample.

Another important factor is the orientation of the GaAsP relative to the incident beam. The angle should be adjusted in order to have an optimal signal. If the detector is off too much, then waveforms shown in Figure C6 may possibly show up.

C.2 PULSE SHAPE

The shape of the laser pulse intensity is a dominant factor in determining the shape of the IA waveform, which is closely related to the spectrum by the Fourier transform. For example, the spectrum shown in Figure 8.1(a) gives a $sech^2$ intensity profile; while the spectrum shown in the case of 8.1(b), the intensity is assumed to have the functional form of $(\frac{sin(x)}{x})^2$ [185, 186].

Figure C1, from Ref. [186], summarizes the simulated possible IA results for various pulse shapes. The left column gives the IA measurement with insets showing the intensity $I(t)$, spectral phase $\Phi(t)$ and instantaneous frequency $\omega(t)$ as a function of time t respectively. The right column gives the spectrum (or power spectral distribution (PSD)) of the corresponding pulse. Different situations included in Figure C1 are:

(a) Bandwidth-limited Gaussian laser pulse of 10 fs duration.

(b) Bandwidth-limited Gaussian laser pulse of 10 fs duration shifted in time to -20 fs.

(c) Symmetrical broadened Gaussian laser pulse due to 200 fs^2 GVD.

(d) Gaussian laser pulse with the third order dispersion is 1000 fs^3.

(e) Combined action of all spectral phase coefficients from (a) to (d).

(f) π step at the central frequency.

(g) π step displaced from the central frequency.

(h) Sine modulation at central frequency with $\Pi(\omega) = sin(20fs(\omega - \omega_0))$.

(i) Cosine modulation at central frequency with $\Pi(\omega) = cos(20fs(\omega - \omega_0))$.

(j) Sine modulation at central frequency with $\Pi(\omega) = sin(30fs(\omega - \omega_0))$.

(k) Symmetrical clipping of spectrum.

(l) Blocking of central frequency components.

(m) Off center absorption.

(n) Self-phase modulation. Note the spectral broadening.

(o) Double pulses (See Appendix A) with pulse-to-pulse delay of 60 fs.

The pulse shape is determined by the spectrum. Generally it can not be varied by simply tuning the mirrors. It has to do with the quality of intracavity optics. When the pulse width τ is in the range of 20 fs $< \tau <$ 100 fs, the pulse shape is typically assumed to be $sech^2$ function. When the pulse is sub-20 fs, the typical pulse shape is typically sin(x)/x [180]. By comparing our results (See Figure C2) with the ones listed in Figure C1 and the characterization in Ref. [185], we believe that our home-built laser generates pulses in the shape of sin(x)/x.

C.3 FINITE CHIRP

In Chapter 3, we see SPM can introduce chirp into the laser pulses. In Chapter 5 we know that in order to get transform-limited pulse width, the chirp present in the pulse must be balanced. Unbalanced chirp can be reflected in the IA measurement (Figure C3(b)). The dependence of the IA waveform on various chirp values is shown in Figure C3.The detail calculation can be found in Ref. [36].

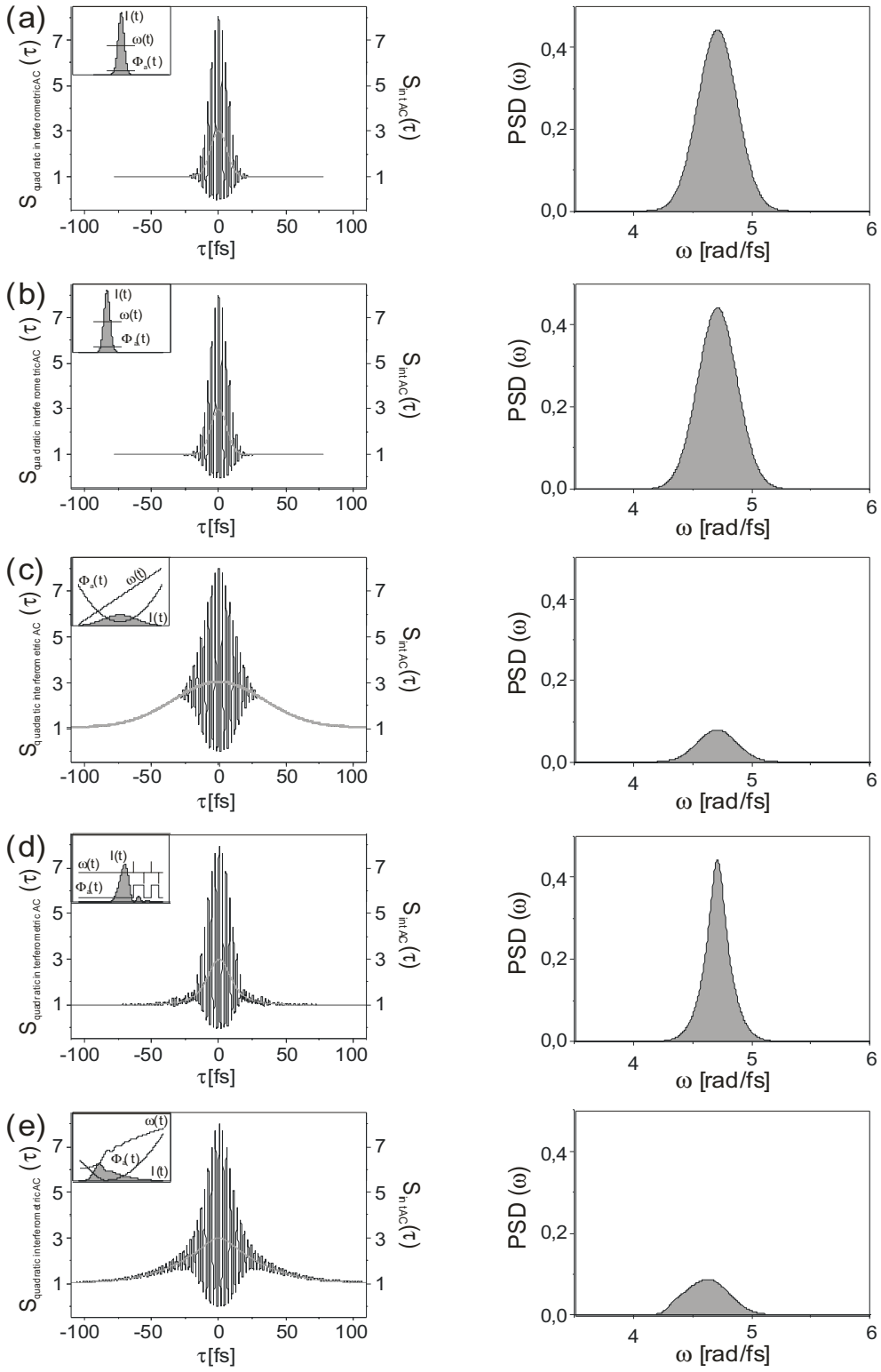
(a)
(b)
(c)
(d)
(e)
I(t)
ω(t)
τ[fs]
ω [rad/fs]
PSD (ω)

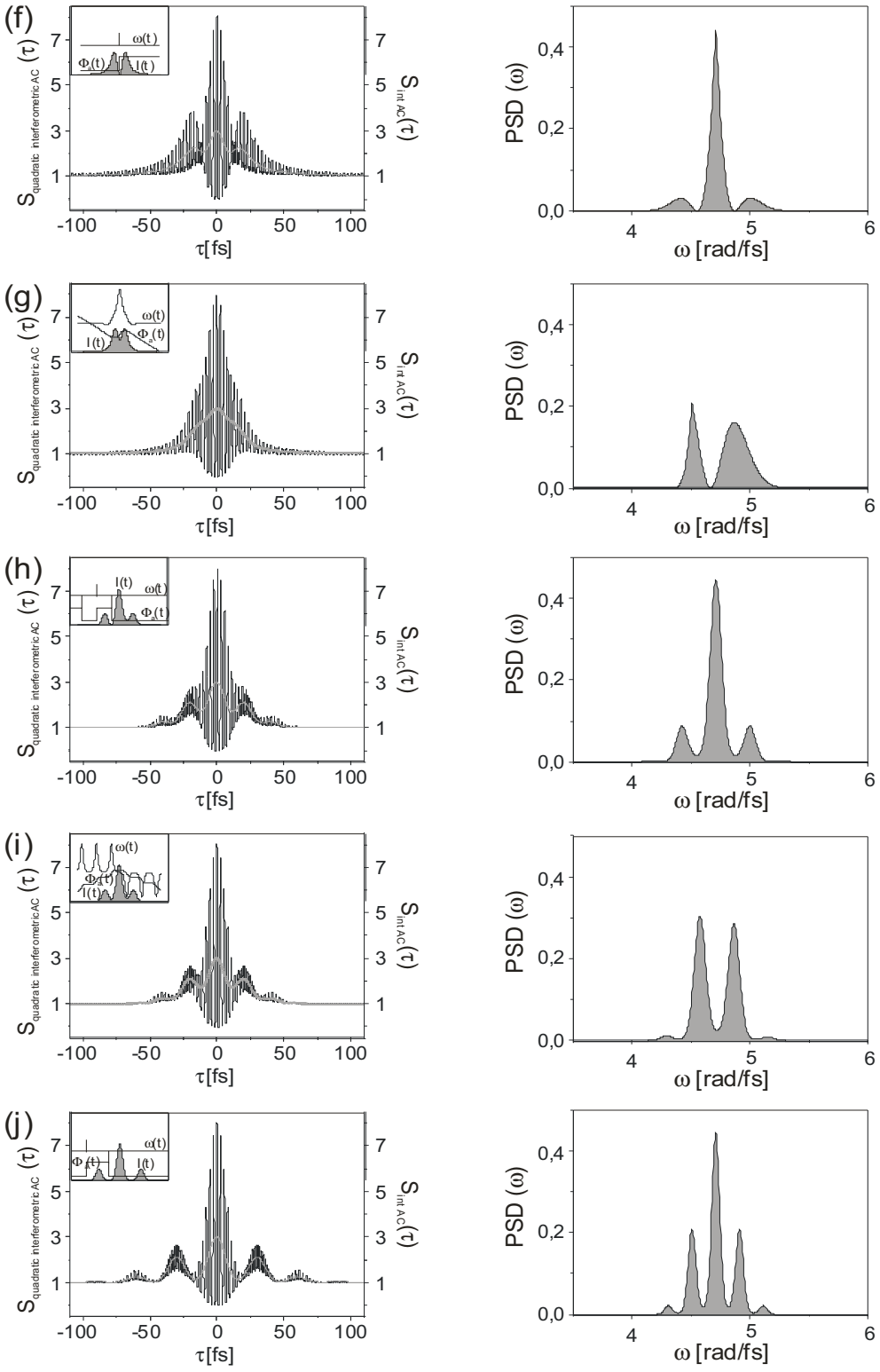
(f)
(g)
(h)
(i)
(j)
ω(t)
Φ(t)
I(t)
S quadratic interferometric AC (τ)
S int AC (τ)
τ[fs]
PSD (ω)
ω [rad/fs]

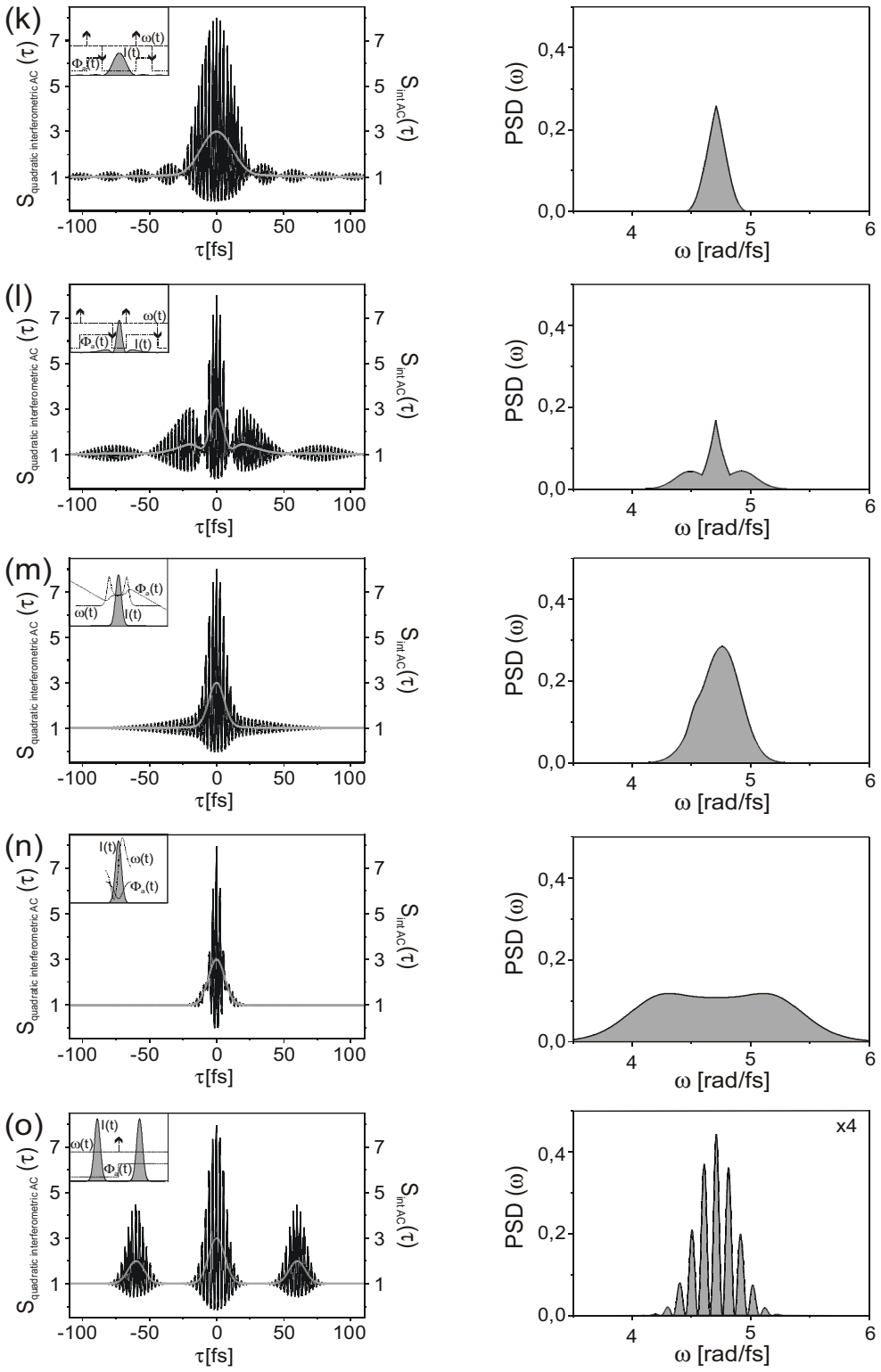

Figure C1: Interferometric autocorrelation for various pulse shapes (See Ref. [186]).

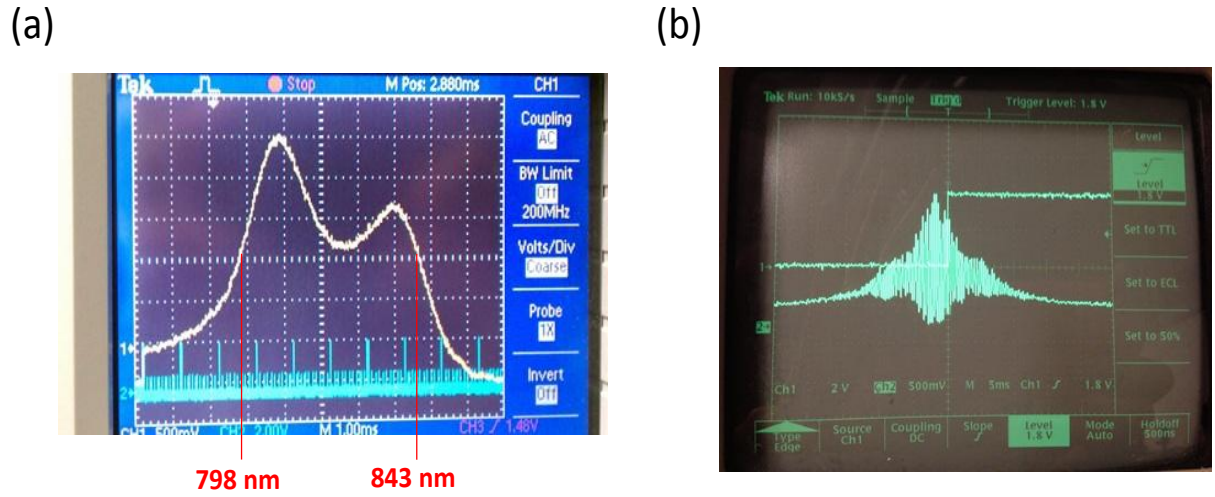

Figure C2: (a) The spectrum of the laser pulse. (b) The IA measurement for the pulse.

There are several optics that can be adjusted to balance the chirp in the pulse. The first one is the compression mirror pair at the output of the laser cavity. By changing the number of times that the laser beam bounces back and forth on the pair of mirrors, one can control how much negative GVD is introduced to the pulse. This should coarsely compensate the positive GVD introduced by all the following optics. After this mirror pair is set, one can adjust the extracavity fused silica wedge pair[2], which provides finer control of the amount of negative GVD in the pulse. If no improvement is achieved by adjusting the extracavity pair, then one can turn to the intracavity pair. However, be cautious about the intracavity one because when the intracavity wedge pair is being tuned, it is possible that one can lose the mode-lock at a certain point.

[2]If one wants to shorten the pulse duration, CaF_2 wedge pairs could be tried. They are available from Venteon.

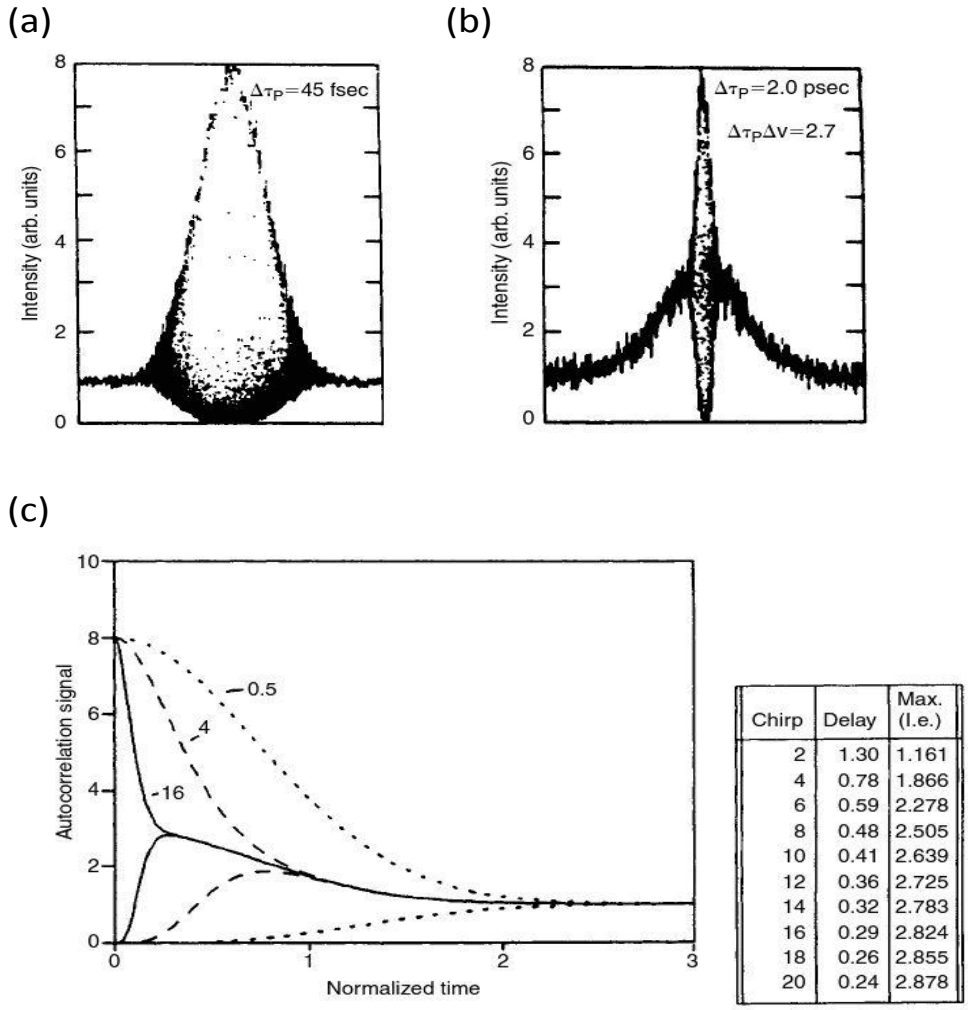

Chirp	Delay	Max. (I.e.)
2	1.30	1.161
4	0.78	1.866
6	0.59	2.278
8	0.48	2.505
10	0.41	2.639
12	0.36	2.725
14	0.32	2.783
16	0.29	2.824
18	0.26	2.855
20	0.24	2.878

Figure C3: Interferometric autocorrelation for the laser pulse from the same laser with the chirp (a) balanced and (b) unbalanced. (c) Interferometric autocorrelation for various chirp values.(This figure is from Ref. [36].)

C.4 UNEVEN INTERFERENCE ARMS

If the intensities of two interfered pulses are not exactly identical, then the ratio 8:1 in the IA measurement may not be reached. To see that, we can do a simple calculation by defining $E_1(t) = aE_2(t)$, where the proportional factor a is in the range $0 \leq a \leq 1$. The IA function becomes

$$\begin{aligned} A_i(\tau) = &\int dt(E^2(t)E^{*2}(t) + a^2E^2(t-\tau)E^{*2}(t-\tau)) \\ &+4a^2 \int dtE(t)E^*(t)E(t-\tau)E^*(t-\tau) \\ &+a^2 \int dt(E^2(t)E^{*2}(t-\tau) + E^2(t-\tau)E^{*2}(t)) \\ &+2a \int dtE(t)E^*(t)(E(t)E^*(t-\tau) + E(t-\tau)E^*(t)) \\ &+2a^2 \int dtE(t-\tau)E^*(t-\tau)(E(t)E^*(t-\tau) + E(t-\tau)E^*(t)) \end{aligned} \tag{C.1}$$

Then the ratio between $A_i(0)$ and $A_i(\infty)$ is

$$\frac{A_i(0)}{A_i(\infty)} = \frac{1+4a+7a^2+4a^3}{1+a}. \tag{C.2}$$

Therefore in the experiment, if these two pulses are not exactly identical, one may not be able to see the ratio of 8:1 (Figure C4). Other factors like the pulse front tilt can also result in a ratio less than 8:1 [182].

Once the optics is set up, the ratio of the powers for the two arms is fixed. During the experiment, we do see that they are not exactly identical. However, as long as we use a 50% ultrafast beam splitter[3], the ratio is very close to 1.

[3]This item is from Layertec, model number 104040.

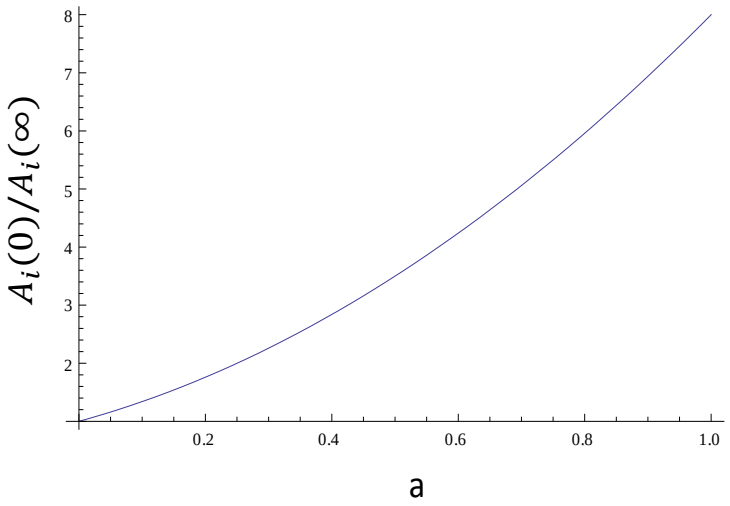

Figure C4: The ratio between $A_i(0)$ and $A_i(\infty)$ as a function of the relative amplitude of two pulses.

C.5 ASYMMETRIC IA MEASUREMENT

Sometimes, the waveform from an IA measurement can be asymmetric in time (See Figure C5). This could result from either (1) asymmetric motion of the optical delay line (ODL). When the ODL is moved back and forth, its trajectory of motion in one direction does not overlap with the one in the other direction or (2) the pulse is made asymmetric for one beam but not the other. For example, if the dispersion conditions in both beam paths are different, then the pulse in one beam may be stretched or compressed while the pulse in the other is unchanged.

C.6 RANDOM PHASE NOISE

Air turbulence and mechanical instability can introduce fluctuation in the optical path length, which manifests itself as phase noise in the laser pulse [183]. This random phase

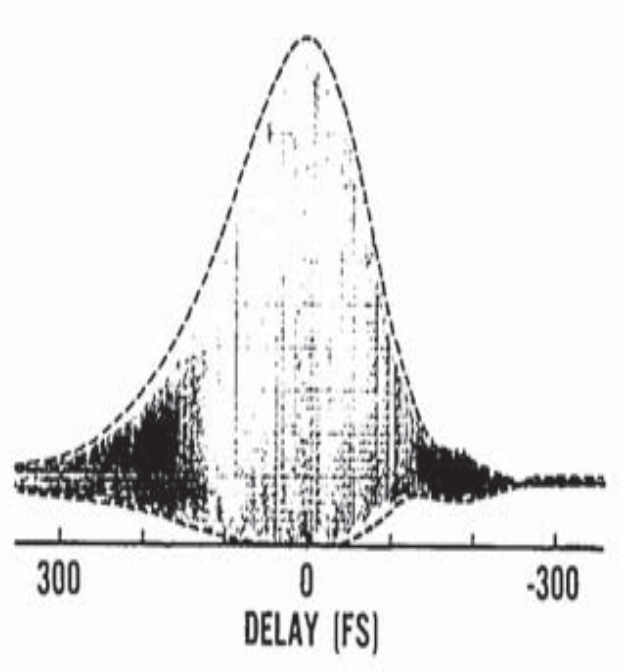

Figure C5: Asymmetric interferometric autocorrelation (Ref. [36]).

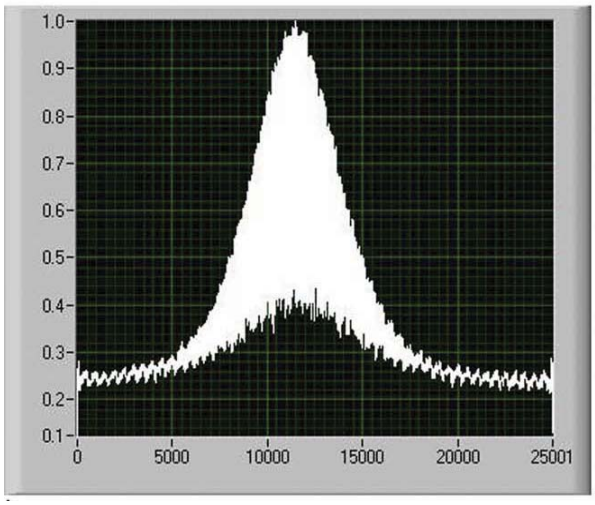

Figure C6: Random phase noise in interferometric autocorrelation measurement.(This figure is from Ref. [183].)

noise can lead to the IA measurement shown in Figure C6.

What we found in the experiments is that when waveforms like the one in Figure C6 is observed, one should check the optics for both arms to make sure that the spatial overlap between the two beams is as good as possible. As mentioned above, the orientation and the position of GaAsP detector can also be adjusted. The third factor is the ODL. One can try different waveforms used to drive the motion of the ODL, such as sine and triangular wave.

C.7 SUMMARY

Since the IA is sensitive to various parameters, measuring the pulse duration based on IA can be tricky. One example is that in IA measurement, one always assume that the pulse shape is already known, which enables the extraction of the pulse width from experimental results. However, different pulse shapes correspond to different deconvolution factors. In most cases, a $sech^{(2)}$ profile is assumed. In certain cases, this assumption must be modified

[180]. A better way to make use of IA is to combine the spectral and temporal measurement. As described in Ref. [187], one can measure the power spectrum $S(\omega)$ of a laser pulse. The pulse intensity is fount to be $I(t) = \mathcal{F}^2(\sqrt{S(\omega)})$, where $\mathcal{F}$ denotes the Fourier transform. Once the intensity $I(t)$ is known, the IA function can be theoretically derived or numerically calculated, which acts as a reference in comparison with the experimentally measured IA trace.

APPENDIX D

CAVITY ALIGNMENT

In this appendix, we will discuss how to align the intracavity optics in order to achieve the optimal mode-locking state. First of all, the height of the Ti:Sapphire crystal determines the height of all optics in the cavity. In order to measure the height of both the cavity mode and pump mode beam, we can set up an iris for which the height is set to be the same as the Ti:Sapphire crystal. The output power of the pump laser can be set to be as low as 10 mW for aligning the cavity.

1. Before we insert the waveplate and focusing lens for the pump beam, we should check its height by placing the iris at Position 1, which is close to the cavity input, and Position 2, which is close to the focusing mirror f_2 (See Figure D1). Once the height of the pump beam is correctly set, it should pass the center of f_1 and f_2. Green light can transmit the focusing mirror, therefore one should see some residual pump light after f_1. The incident angle of the pump beam on the Ti:Sapphire crystal should be the Brewster angle. The angle of the two focusing mirrors, f_1 and f_2, and the distance between them, should be close to the calculated values discussed in Chapter 5.
2. Next we can insert the waveplate and focusing lens f_p. Make sure the pump beam passes through the center of both of them. One should see divergent green light coming out from f_1. A laser blocker can be set after f_1 to stop it. The waveplate should be set so that the transmitted green light is horizontally polarized. Once the polarization of the pump beam is rotated to be horizontal, the reflected green light from the crystal, which

Figure D1: Pump beam alignment.

can be stopped with a laser blocker, should have the minimal intensity. The distance between f_p and f_2 should be about the same as calculated in Chapter 5.

3. Now we can move on to set up the mirror M_1 and M_2. Make sure the length of the path $f_1 - M_2 - M_1$ is close to the calculated value (L_1) in Chapter 5. The same iris should be used to check the height of the beam between $f_1 - M_2$ and $M_2 - M_1$. The reflected green light from f_1 should be strong enough to be seen by eyes; however, the luminescence from the Ti:Sapphire crystal, which looks red, is very dim. The trick to adjust the height is to use the green light as the guidance. One should make sure that the green beam passes through the center of the iris for all the positions shown in Figure D2. One now may notice the appearance of a second green beam after f_1. That is the reflected light from M_1.
4. Next we can set up the other path $f_2 - M_3 - M_4 - OC$. We need make sure that the path length is about the value of L_2 given in Chapter 5. The alignment for this path is a little tricky since this path is shorter and optics are placed in a more compact configuration, there is no room for the iris to be inserted. First of all, we must adjust the mirrors to land the cavity mode at the center of M_3, M_4 and OC (See Figure D3). This may be difficult since the reflected green light from f_2 is too weak to be seen. Therefore, one can only rely on the luminescence from the Ti:Sapphire crystal. To see the luminescence, one can wear laser goggles or use an infrared viewer.
5. Now we need to make sure that the cavity mode in both paths L_1 and L_2 overlaps. We can insert a laser blocker between M_1 and M_2 to block the reflected beam from the

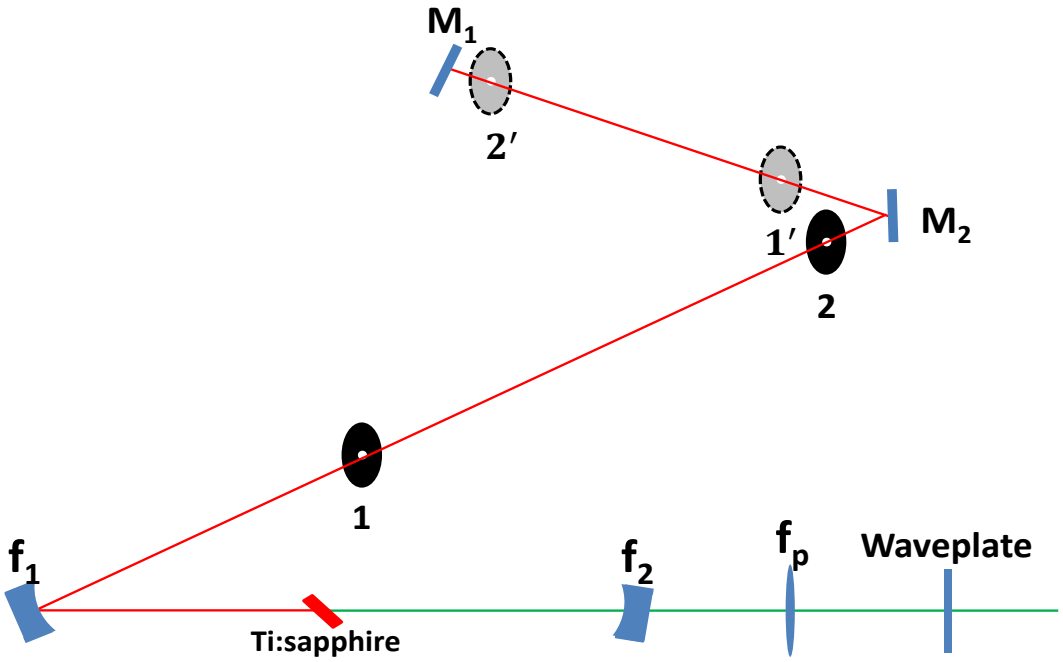

Figure D2: Cavity mode alignment (Part I).

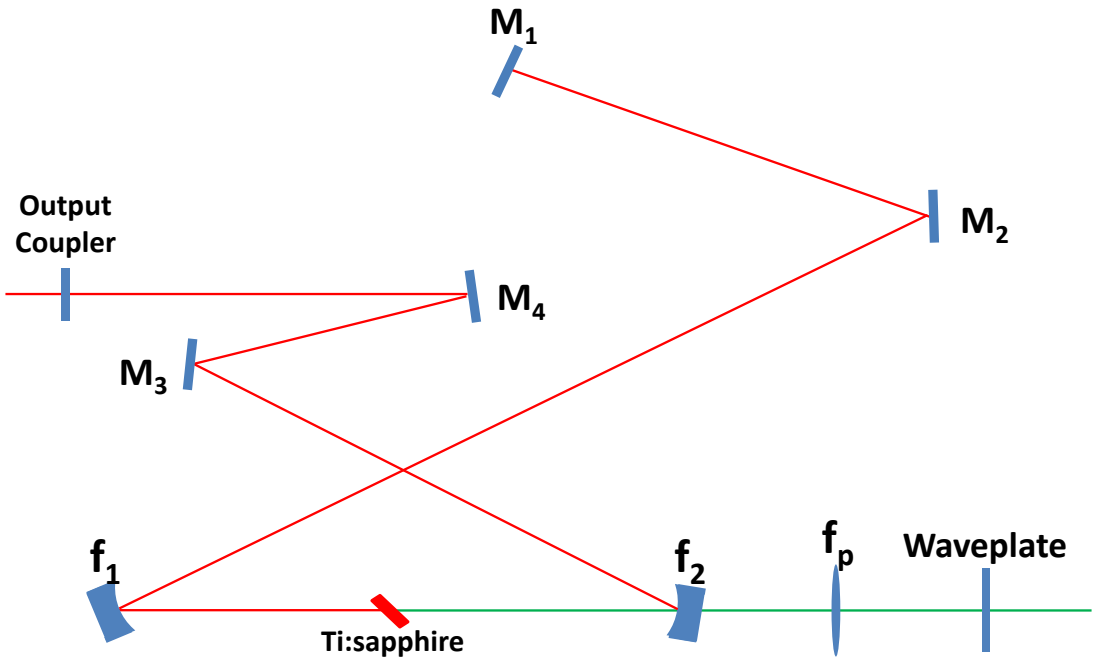

Figure D3: Cavity mode alignment (Part II).

ending mirror M_1 (See Figure D4). Now the luminescence we observe at Position 1 and 2 includes two parts (1) the luminescence reflected by f_1 (2) the light reflected by the output coupler and passing through M_4, M_3, f_2, Ti:Sapphire and f_1, successively. As long as we can overlap the light from these two paths at both Position 1 and 2, we can be sure that the cavity mode in path L_1 and L_2 overlaps with each other. To do that, we can adjust the OC to overlap the beams at Position 1 and M_3 at Position 2. Keep adjusting these two until the light overlaps well at both positions.

6. Now we are ready to try to get the cavity to lase. We can increase the pump power to 5 W (The maximum power of the Verdi-V5.). If the cavity starts to lase, one should see a bright spot after the output coupler. If the cavity does not lase, then one can try the beam walking by adjusting the ending mirror M_1 and OC. Before walking the beam, a power meter can be used to collect the output light from the cavity. To walk the beam, one can start with the X axis of M_1 by slowly turning the knob counterclockwise (or clockwise) a little bit. Then the X axis knob of OC should be adjusted slowly. If the output power increases, one can go to M_1 and keep turning the X knob in the same counterclockwise direction (or clockwise), then go back to adjust the X knob of OC. If the output power decreases, one should go to M_1 and turn the X knob in an opposite way such as clockwise (or counterclockwise), then adjust OC to see if the power can be increased. This adjustment should be repeated until the power is maximized. After the X axis is done, one should go through the same process for the Y axis. One ought to repeat the iterative alignment for both directions to optimize the output power. If one has trouble in getting the cavity to lase by adjusting the output coupler and M_1, one should try to move f_1 a little.
7. After the cavity starts to lase, the fused silica wedge pair can be installed. The angle should be the Brewster angle.
8. After the installation of the wedge pair, the cavity may stop lasing. One need to do beam walking to bring the cavity back to the lasing state. The power is not the only parameter one should optimize for CW mode. The output laser mode and the spectral line width are important as well. The mode should be Gaussian. The narrower the spectral line width is, the better. By combining the beam walking process with M_1 and the output

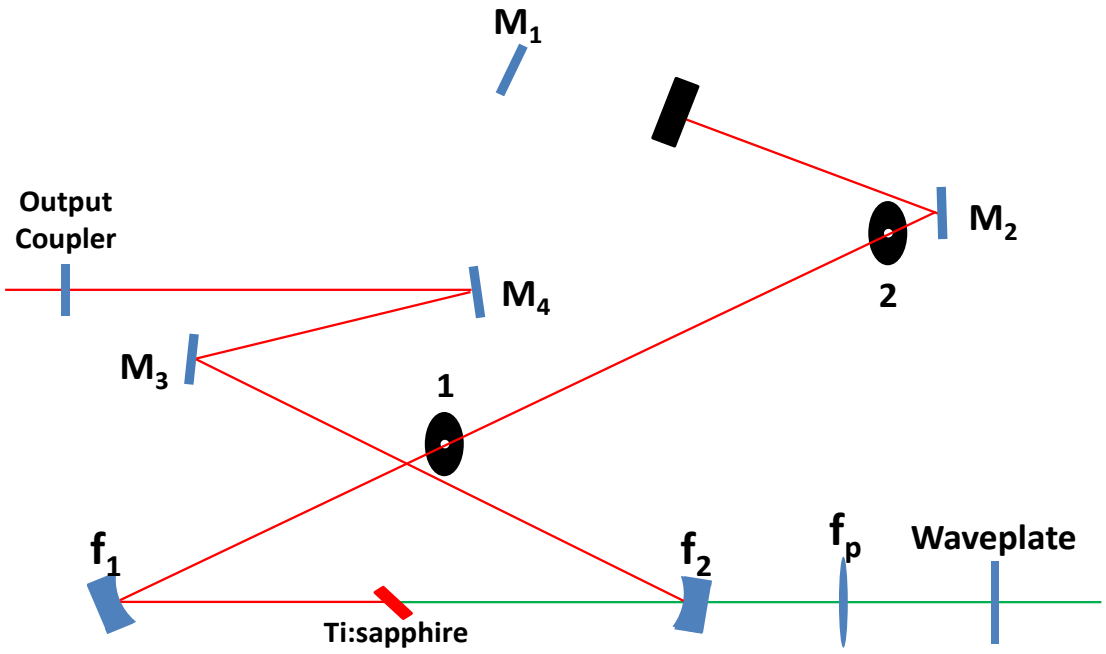

Figure D4: Overlap of the cavity mode in the two arms.

coupler with the adjustment of f_1, one should achieve a state in which all parameters are optimized.

9. Once the CW mode is optimal, we can try mode-locking. In order to initiate the mode-locking, the cavity must be disturbed. One can do that by pushing f_1 a little then release it. It can take some time to tune the alignment so that the mode-locking can occur. One can start with f_1 by moving it a little bit then shake it. If mode-locking does not occur, keep moving f_1. Both our experience and theories indicate that mode-locking is more sensitive to the position of f_2 than the position of f_1. Therefore, if one has trouble in getting laser mode-locked by adjusting f_1, one can try to move f_2.
10. Once the mode-locking is achieved, one can play with the wedge pair to optimize the intracavity GVD conditions so that the output laser pulse has the minimal duration.
11. In order to measure the pulse width with autocorrelation, one may need to adjust the extracavity GVD control optics as well. That includes a pair of compression mirrors which has negative GVD and a pair of fused silica wedge pair.

BIBLIOGRAPHY

[1] R. J. Silbey, R. A. Alberty, and M. G. Bawendi, *Physical Chemistry, 4th ed.* (John Wiley and Sons, 2005).

[2] A. P. Alivisatos, *Semiconductor Clusters, Nanocrystals, and Quantum Dots*, Science **271**(5251), 933 (1996).

[3] A. Cho, *Advances in molecular beam epitaxy (MBE)*, Journal of Crystal Growth **111**(14), 1 (1991).

[4] K. FURUYA and Y. MIYAMOTO, *GaInAsP/InP ORGANOMETALLIC VAPOR PHASE EPITAXY FOR RESEARCH AND FABRICATION OF DEVICES*, International Journal of High Speed Electronics and Systems **01**(03n04), 347 (1990).

[5] K. L. P., A. D. G., and T. S., *Few-electron quantum dots*, Reports on Progress in Physics **64**(6), 701 (2001).

[6] J. M. Elzerman, R. Hanson, L. H. Willems van Beveren, B. Witkamp, L. M. K. Vandersypen, and L. P. Kouwenhoven, *Single-Shot Read-Out of an Individual Electron Spin in a Quantum Dot*, Nature **430**(6998), 431 (2004).

[7] Y. Narukawa, Y. Kawakami, M. Funato, S. Fujita, S. Fujita, and S. Nakamura, *Role of self-formed InGaN quantum dots for exciton localization in the purple laser diode emitting at 420 nm*, Applied Physics Letters **70**(8), 981 (1997).

[8] V. I. Klimov, A. A. Mikhailovsky, S. Xu, A. Malko, J. A. Hollingsworth, C. A. Leatherdale, H.-J. Eisler, and M. G. Bawendi, *Optical Gain and Stimulated Emission in Nanocrystal Quantum Dots*, Science **290**(5490), 314 (2000).

[9] P. Michler, A. Kiraz, C. Becher, W. V. Schoenfeld, P. M. Petroff, L. Zhang, E. Hu, and A. Imamoglu, *A Quantum Dot Single-Photon Turnstile Device*, Science **290**(5500), 2282 (2000).

[10] A. Lu, D. D. Awschalom, G. Burkard, D. P. DiVincenzo, D. Loss, M. Sherwin, and A. Small, *Quantum Information Processing Using Quantum Dot Spins and Cavity QED*, Phys. Rev. Lett. **83**, 4204 (1999).

[11] R. D. Parks, *Superconductivity* (CRC Press, 1969).

[12] K. A. Müller and H. Burkard, *$SrTi_3$: An intrinsic quantum paraelectric below 4 K*, Phys. Rev. B **19**, 3593 (1979).

[13] A. Ohtomo and H. Y. Hwang, *A High-Mobility Electron Gas at the $LaAlO_3/SrTiO_3$ Heterointerface*, Nature **427**(6973), 423 (2004).

[14] N. Nakagawa, H. Y. Hwang, and D. A. Muller, *Why Some Interfaces Cannot Be Sharp*, Nature Mater. **5**(3), 204 (2006).

[15] S. Thiel, G. Hammerl, A. Schmehl, C. W. Schneider, and J. Mannhart, *Tunable Quasi-Two-Dimensional Electron Gases in Oxide Heterostructures*, Science **313**(5795), 1942 (2006).

[16] Z. S. Popović, S. Satpathy, and R. M. Martin, *Origin of the Two-Dimensional Electron Gas Carrier Density at the $LaAlO_3$ on $SrTiO_3$ Interface*, Phys. Rev. Lett. **101**, 256801 (2008).

[17] J. Lee and A. A. Demkov, *Charge origin and localization at the n-type $SrTiO_3/LaAlO_3$ interface*, Phys. Rev. B **78**, 193104 (2008).

[18] G. Murtaza and I. Ahmad, *Shift of indirect to direct bandgap and optical response of LaAlO[sub 3] under pressure*, Journal of Applied Physics **111**(12), 123116 (2012).

[19] K. van Benthem, C. Elsässer, and R. H. French, *Bulk Electronic Structure of $SrTiO_3$: Experiment and Theory*, Journal of Applied Physics **90**(12), 6156 (2001).

[20] A. Savoia, D. Paparo, P. Perna, Z. Ristic, M. Salluzzo, F. Miletto Granozio, U. Scotti di Uccio, C. Richter, S. Thiel, J. Mannhart, and L. Marrucci, *Polar Catastrophe and Electronic Reconstructions at the $LaAlO_3/SrTiO_3$ Interface: Evidence from Optical Second Harmonic Generation*, Phys. Rev. B **80**, 075110 (2009).

[21] C. Cen, S. Thiel, G. Hammerl, C. W. Schneider, K. E. Andersen, C. S. Hellberg, J. Mannhart, and J. Levy, *Nanoscale Control of an Interfacial Metal-Insulator Transition at Room Temperature*, Nature Mater. **7**(4), 298 (2008).

[22] C. Cen, S. Thiel, J. Mannhart, and J. Levy, *Oxide Nanoelectronics on Demand*, Science **323**(5917), 1026 (2009).

[23] D. F. Bogorin, C. W. Bark, H. W. Jang, C. Cen, C. M. Folkman, C.-B. Eom, and J. Levy, *Nanoscale rectification at the LaAlO[sub 3]/SrTiO[sub 3] interface*, Applied Physics Letters **97**(1), 013102 (2010).

[24] G. Cheng, P. F. Siles, F. Bi, C. Cen, D. F. Bogorin, C. W. Bark, C. M. Folkman, J. W. Park, C. B. Eom, G. Medeiros-Ribeiro, and J. Levy, *Sketched Oxide Single-Electron Transistor*, Nature Nanotech. **6**(6), 343 (2011).

[25] P. Irvin, Y. Ma, D. F. Bogorin, C. Cen, C. W. Bark, C. M. Folkman, C. B. Eom, and J. Levy, *Rewritable Nanoscale Oxide Photodetector*, Nature Mater. **4**(12), 849 (2010).

[26] N. Reyren, S. Thiel, A. D. Caviglia, L. F. Kourkoutis, G. Hammerl, C. Richter, C. W. Schneider, T. Kopp, A.-S. Retschi, D. Jaccard, M. Gabay, D. A. Muller, *et al.*, *Superconducting Interfaces Between Insulating Oxides*, Science **317**(5842), 1196 (2007).

[27] A. D. Caviglia, S. Gariglio, N. Reyren, D. Jaccard, T. Schneider, M. Gabay, S. Thiel, G. Hammerl, J. Mannhart, and J. M. Triscone, *Electric Field Control of the $LaAlO_3/SrTiO_3$ Interface Ground State*, Nature **456**(7222), 624 (2008).

[28] A. Brinkman, M. Huijben, M. V. Zalk, J. Huijben, U. Zeitler, J. C. Maan, W. G. V. Der Wiel, G. Rijnders, D. H. A. Blank, and H. Hilgenkamp, *Magnetic Effects at the Interface Between Non-magnetic Oxides*, Nature Mater. **6**(7), 493 (2007).

[29] Ariando, X. Wang, G. Baskaran, Z. Q. Liu, J. Huijben, J. B. Yi, A. Annadi, A. Roy Barman, A. Rusydi, S. Dhar, Y. P. Feng, J. Ding, *et al.*, *Electronic Phase Separation at the $LaAlO_3/SrTiO_3$ Interface*, Nature Commun. **2**, 188 (2007).

[30] D. A. Dikin, M. Mehta, C. W. Bark, C. M. Folkman, C. B. Eom, and V. Chandrasekhar, *Coexistence of Superconductivity and Ferromagnetism in Two Dimensions*, Phys. Rev. Lett. **107**, 056802 (2011).

[31] J. A. Bert, B. Kalisky, C. Bell, M. Kim, Y. Hikita, H. Y. Hwang, and K. A. Moler, *Direct Imaging of the Coexistence of Ferromagnetism and Superconductivity at the $LaAlO_3/SrTiO_3$ Interface*, Nature Phys. **7**(10), 767 (2011).

[32] J. D. Jackson, *Classical Electrodynamics* (John Wiley and Sons, 1999).

[33] L. Mandel and E. Wolf, *Optical Coherence and Quantum Optics* (Cambridge University Press, 1995).

[34] E. Jaynes and F. Cummings, *Comparison of quantum and semiclassical radiation theories with application to the beam maser*, Proceedings of the IEEE **51**(1), 89 (1963).

[35] R. W. Boyd, *Nonlinear Optics* (Academic Press, 2008).

[36] J.-C. Diels and W. Rudolph, *Ultrafast Laser Pulse Phenomena* (Academic Press, 2006).

[37] R. Nakamura and Y. Kanematsu, *Femtosecond Spectral Snapshots Based on Electronic Optical Kerr Effect*, Review of Scientific Instruments **75**(3), 636 (2004).

[38] G. Steinmeyer, D. H. Sutter, L. Gallmann, N. Matuschek, and U. Keller, *Frontiers in Ultrashort Pulse Generation: Pushing the Limits in Linear and Nonlinear Optics*, Science **286**(5444), 1507 (1999).

[39] M. H. Frosz and P. E. Andersen, *Supercontinuum Generation: Can Pulse Broadening Be Stopped?*, Nature Photon. **1**(11), 611 (2007).

[40] A. P. Godse and U. A. Bakshi, *Semiconductor Devices and Circuits* (Technical Publications Pune, 2008).

[41] A. Onton and L. M. Foster, *Indirect, Γ_{8v}-X_{1c}, band gap in $GaAs_{1-x}P_x$*, Journal of Applied Physics **43**(12), 5084 (1972).

[42] J. K. Ranka, A. L. Gaeta, A. Baltuska, M. S. Pshenichnikov, and D. A. Wiersma, *Autocorrelation Measurement of 6-fs Pulses Based on the Two-Photon-Induced Photocurrent in a GaAsP Photodiode*, Opt. Lett. **22**(17), 1344 (1997).

[43] D. Budker, W. Gawlik, D. F. Kimball, S. M. Rochester, V. V. Yashchuk, and A. Weis, *Resonant nonlinear magneto-optical effects in atoms*, Rev. Mod. Phys. **74**, 1153 (2002).

[44] P. A. Schulz, *Wavelength independent Faraday isolator*, Appl. Opt. **28**(20), 4458 (1989).

[45] L. Sun, S. Jiang, J. D. Zuegel, and J. R. Marciante, *All-fiber optical isolator based on Faraday rotation in highly terbium-doped fiber*, Opt. Lett. **35**(5), 706 (2010).

[46] M. I. Dyakonov, *Spin Physics in Semiconductors* (Springer, 2008).

[47] P. S. Pershan, *Magneto-Optical Effects*, Journal of Applied Physics **38**(3), 1482 (1967).

[48] J. M. Kikkawa and D. D. Awschalom, *Resonant Spin Amplification in n-Type GaAs*, Phys. Rev. Lett. **80**, 4313 (1998).

[49] D. Loss and D. P. DiVincenzo, *Quantum computation with quantum dots*, Phys. Rev. A **57**, 120 (1998).

[50] F. Meier and B. P. Zakharchenya, *Optical Orientation* (Elsevier Science Publishers, 1964).

[51] R. J. Epstein, I. Malajovich, R. K. Kawakami, Y. Chye, M. Hanson, P. M. Petroff, A. C. Gossard, and D. D. Awschalom, *Spontaneous spin coherence in n -GaAs produced by ferromagnetic proximity polarization*, Phys. Rev. B **65**, 121202 (2002).

[52] J. F. Smyth, D. A. Tulchinsky, D. D. Awschalom, N. Samarth, H. Luo, and J. K. Furdyna, *Femtosecond scattering dynamics in magnetic semiconductor spin superlattices*, Phys. Rev. Lett. **71**, 601 (1993).

[53] M. P. Hehlen, G. Frei, and H. U. Güdel, *Dynamics of infrared-to-visible upconversion in $Cs_3Lu_2Br_9$:1Er^{3+}*, Phys. Rev. B **50**, 16264 (1994).

[54] R. Kumar, A. S. Vengurlekar, S. S. Prabhu, J. Shah, and L. N. Pfeiffer, *Picosecond time evolution of free electron-hole pairs into excitons in GaAs quantum wells*, Phys. Rev. B **54**, 4891 (1996).

[55] J. Berezovsky, M. H. Mikkelsen, O. Gywat, N. G. Stoltz, L. A. Coldren, and D. D. Awschalom, *Nondestructive Optical Measurements of a Single Electron Spin in a Quantum Dot*, Science **314**(5807), 1916 (2006).

[56] M. Atature, J. Dreiser, A. Badolato, and A. Imamoglu, *Observation of Faraday rotation from a single confined spin*, Nature Phys. **3**(2), 101 (2007).

[57] M. H. Mikkelsen, J. Berezovsky, N. G. Stoltz, L. A. Coldren, and D. D. Awschalom, *Optically detected coherent spin dynamics of a single electron in a quantum dot*, Nature Phys. **3**(11), 770 (2007).

[58] H. P. Seigneur, M. N. Leuenberger, and W. V. Schoenfeld, *Single-photon Mach–Zehnder interferometer for quantum networks based on the single-photon Faraday effect*, Journal of Applied Physics **104**(1), 014307 (2008).

[59] I. A. Merkulov, A. L. Efros, and M. Rosen, *Electron spin relaxation by nuclei in semiconductor quantum dots*, Phys. Rev. B **65**, 205309 (2002).

[60] A. V. Khaetskii, D. Loss, and L. Glazman, *Electron Spin Decoherence in Quantum Dots due to Interaction with Nuclei*, Phys. Rev. Lett. **88**, 186802 (2002).

[61] A. C. Johnson, J. R. Petta, J. M. Taylor, A. Yacoby, M. D. Lukin, C. M. Marcus, M. P. Hanson, and A. C. Gossard, *Triplet-singlet spin relaxation via nuclei in a double quantum dot*, Nature **435**(7044), 925 (2005).

[62] A. S. Bracker, E. A. Stinaff, D. Gammon, M. E. Ware, J. G. Tischler, A. Shabaev, A. L. Efros, D. Park, D. Gershoni, V. L. Korenev, and I. A. Merkulov, *Optical Pumping of the Electronic and Nuclear Spin of Single Charge-Tunable Quantum Dots*, Phys. Rev. Lett. **94**, 047402 (2005).

[63] P.-F. Braun, X. Marie, L. Lombez, B. Urbaszek, T. Amand, P. Renucci, V. K. Kalevich, K. V. Kavokin, O. Krebs, P. Voisin, and Y. Masumoto, *Direct Observation of the Electron Spin Relaxation Induced by Nuclei in Quantum Dots*, Phys. Rev. Lett. **94**, 116601 (2005).

[64] F. H. L. Koppens, J. A. Folk, J. M. Elzerman, R. Hanson, L. H. W. van Beveren, I. T. Vink, H. P. Tranitz, W. Wegscheider, L. P. Kouwenhoven, and L. M. K. Vandersypen, *Control and Detection of Singlet-Triplet Mixing in a Random Nuclear Field*, Science **309**(5739), 1346 (2005).

[65] J. R. Petta, A. C. Johnson, J. M. Taylor, E. A. Laird, A. Yacoby, M. D. Lukin, C. M. Marcus, M. P. Hanson, and A. C. Gossard, *Coherent Manipulation of Coupled Electron Spins in Semiconductor Quantum Dots*, Science **309**(5744), 2180 (2005).

[66] J. Schliemann, A. V. Khaetskii, and D. Loss, *Spin decay and quantum parallelism*, Phys. Rev. B **66**, 245303 (2002).

[67] A. Khaetskii, D. Loss, and L. Glazman, *Electron spin evolution induced by interaction with nuclei in a quantum dot*, Phys. Rev. B **67**, 195329 (2003).

[68] W. A. Coish and D. Loss, *Hyperfine interaction in a quantum dot: Non-Markovian electron spin dynamics*, Phys. Rev. B **70**, 195340 (2004).

[69] W. Zhang, V. V. Dobrovitski, K. A. Al-Hassanieh, E. Dagotto, and B. N. Harmon, *Hyperfine interaction induced decoherence of electron spins in quantum dots*, Phys. Rev. B **74**, 205313 (2006).

[70] P. Irvin, P. S. Fodor, and J. Levy, *Gigahertz optical spin transceiver*, Opt. Express **15**(18), 11756 (2007).

[71] M. Sugita, S. Machida, and Y. Yamamoto, *Quantum nondemolition measurement of a single electron spin in a quantum dot*, arXiv:quant-ph/0301064 (2003).

[72] J. R. Ackerhalt and K. Rzążewski, *Heisenberg-picture operator perturbation theory*, Phys. Rev. A **12**, 2549 (1975).

[73] N. Korolkova, G. Leuchs, R. Loudon, T. C. Ralph, and C. Silberhorn, *Polarization squeezing and continuous-variable polarization entanglement*, Phys. Rev. A **65**, 052306 (2002).

[74] Y. Takahashi, K. Honda, N. Tanaka, K. Toyoda, K. Ishikawa, and T. Yabuzaki, *Quantum nondemolition measurement of spin via the paramagnetic Faraday rotation*, Phys. Rev. A **60**, 4974 (1999).

[75] G. Khitrova, H. M. Gibbs, M. Kira, S. W. Koch, and A. Scherer, *Vacuum Rabi Splitting in Semiconductors*, Nature Phys. **2**(2), 81 (2006).

[76] L. Matos, D. Kleppner, O. Kuzucu, T. R. Schibli, J. Kim, E. P. Ippen, and F. X. Kaertner, *Direct frequency comb generation from an octave-spanning, prismlessTi:sapphire laser*, Opt. Lett. **29**(14), 1683 (2004).

[77] R. J. Jones, K. D. Moll, M. J. Thorpe, and J. Ye, *Phase-Coherent Frequency Combs in the Vacuum Ultraviolet via High-Harmonic Generation inside a Femtosecond Enhancement Cavity*, Phys. Rev. Lett. **94**, 193201 (2005).

[78] S. Woutersen, U. Emmerichs, and H. J. Bakker, *Femtosecond Mid-IR Pump-Probe Spectroscopy of Liquid Water: Evidence for a Two-Component Structure*, Science **278**(5338), 658 (1997).

[79] A. Gloskovskii, D. A. Valdaitsev, M. Cinchetti, S. A. Nepijko, J. Lange, M. Aeschlimann, M. Bauer, M. Klimenkov, L. V. Viduta, P. M. Tomchuk, and G. Schönhense, *Electron emission from films of Ag and Au nanoparticles excited by a femtosecond pump-probe laser*, Phys. Rev. B **77**, 195427 (2008).

[80] A. Ueda, K. Matsuda, T. Tayagaki, and Y. Kanemitsu, *Carrier multiplication in carbon nanotubes studied by femtosecond pump-probe spectroscopy*, Applied Physics Letters **92**(23), 233105 (2008).

[81] R. Huber, A. Brodschelm, F. Tauser, and A. Leitenstorfer, *Generation and field-resolved detection of femtosecond electromagnetic pulses tunable up to 41 THz*, Applied Physics Letters **76**(22), 3191 (2000).

[82] A. Nahata, A. S. Weling, and T. F. Heinz, *A wideband coherent terahertz spectroscopy system using optical rectification and electro-optic sampling*, Applied Physics Letters **69**(16), 2321 (1996).

[83] X. Zheng, Y. Xu, R. Sobolewski, R. Adam, M. Mikulics, M. Siegel, and P. Kordoš, *Femtosecond Response of a Free-standing LT-GaAs Photoconductive Switch*, Appl. Opt. **42**(9), 1726 (2003).

[84] U. Keil and D. Dykaar, *Ultrafast pulse generation in photoconductive switches*, Quantum Electronics, IEEE Journal of **32**(9), 1664 (1996).

[85] R. L. Sutherland, D. G. McLean, and K. S., *Handbook of Nonlinear Optics* (Marcel Dekker, 2003).

[86] G. D. Boyd and D. A. Kleinman, *Parametric Interaction of Focused Gaussian Light Beams*, Journal of Applied Physics **39**(8), 3597 (1968).

[87] L. E. Hargrove, R. L. Fork, and M. A. Pollack, *LOCKING OF He[Single Bond]Ne LASER MODES INDUCED BY SYNCHRONOUS INTRACAVITY MODULATION*, Applied Physics Letters **5**(1), 4 (1964).

[88] D. Kuizenga and A. Siegman, *FM and AM mode locking of the homogeneous laser - Part I: Theory*, Quantum Electronics, IEEE Journal of **6**(11), 694 (1970).

[89] H. W. Mocker and R. J. Collins, *MODE COMPETITION AND SELF-LOCKING EFFECTS IN A Q-SWITCHED RUBY LASER*, Applied Physics Letters **7**(10), 270 (1965).

[90] E. Ippen, *Principles of passive mode locking*, Applied Physics B **58**, 159 (1994).

[91] T. Brabec, C. Spielmann, P. F. Curley, and F. Krausz, *Kerr lens mode locking*, Opt. Lett. **17**(18), 1292 (1992).

[92] A. E. Siegman, *Lasers* (University Science Books, 1986).

[93] R. L. Fork, O. E. Martinez, and J. P. Gordon, *Negative dispersion using pairs of prisms*, Opt. Lett. **9**(5), 150 (1984).

[94] A. Stingl, M. Lenzner, C. Spielmann, F. Krausz, and R. Szipöcs, *Sub-10-fs mirror-dispersion-controlled Ti:sapphire laser*, Opt. Lett. **20**(6), 602 (1995).

[95] A. Stingl, C. Spielmann, F. Krausz, and R. Szipöcs, *Generation of 11-fs pulses from a Ti:sapphire laser without the use of prisms*, Opt. Lett. **19**(3), 204 (1994).

[96] O. E. Martinez, R. L. Fork, and J. P. Gordon, *Theory of passively mode-locked lasers including self-phase modulation and group-velocity dispersion*, Opt. Lett. **9**(5), 156 (1984).

[97] A. M. Weiner, *Femtosecond pulse shaping using spatial light modulators*, Review of Scientific Instruments **71**(5), 1929 (2000).

[98] H. Kogelnik and T. Li, *Laser Beams and Resonators*, Appl. Opt. **5**(10), 1550 (1966).

[99] C. Spielmann, P. Curley, T. Brabec, and F. Krausz, *Ultrabroadband Femtosecond Lasers*, Quantum Electronics, IEEE Journal of **30**(4), 1100 (1994).

[100] D. Kane, *Astigmatism Compensation in Off-Axis Laser Resonators with Two or More Coupled Foci*, Optics Communications **71**(34), 113 (1989).

[101] V. Magni, G. Cerullo, and S. D. Silvestri, *Closed form Gaussian Beam Analysis of Resonators Containing a Kerr Medium for Femtosecond Lasers*, Optics Communications **101**(56), 365 (1993).

[102] G. Cerullo, S. D. Silvestri, V. Magni, and L. Pallaro, *Resonators for Kerr-lens mode-locked femtosecond Ti:sapphire lasers*, Opt. Lett. **19**(11), 807 (1994).

[103] V. Magni, G. Cerullo, and S. D. Silvestri, *ABCD Matrix Analysis of Propagation of Gaussian Beams through Kerr Media*, Optics Communications **96**(46), 348 (1993).

[104] D. M. Kane, *Ti:sapphire laser cavity mode and pump-laser mode calculations*, Appl. Opt. **33**(18), 3849 (1994).

[105] A. Alfrey, *Modeling of longitudinally pumped CW Ti:sapphire laser oscillators*, Quantum Electronics, IEEE Journal of **25**(4), 760 (1989).

[106] P. R. Griffiths and J. A. de Haseth, *Fourier Transform Infrared Spectrometry* (Wiley-Blackwell, 2007).

[107] J. Wang, M. S. Gudiksen, X. Duan, Y. Cui, and C. M. Lieber, *Highly Polarized Photoluminescence and Photodetection from Single Indium Phosphide Nanowires*, Science **293**(5534), 1455 (2001).

[108] D. J. Sirbuly, M. Law, H. Yan, and P. Yang, *Semiconductor Nanowires for Subwavelength Photonics Integration*, The Journal of Physical Chemistry B **109**(32), 15190 (2005).

[109] R. Agarwal and C. Lieber, *Semiconductor nanowires: optics and optoelectronics*, Applied Physics A **85**, 209 (2006).

[110] B. Tian, X. Zheng, T. Kempa, Y. Fang, N. Yu, G. Yu, J. Huang, and C. M. Lieber, *Coaxial silicon nanowires as solar cells and nanoelectronic power sources*, Nature **449**(7164), 885 (2007).

[111] Z. Fan, J. C. Ho, Z. A. Jacobson, H. Razavi, and A. Javey, *Large-scale, heterogeneous integration of nanowire arrays for image sensor circuitry*, Proceedings of the National Academy of Sciences **105**(32), 11066 (2008).

[112] K. Balasubramanian, M. Burghard, K. Kern, M. Scolari, and A. Mews, *Photocurrent Imaging of Charge Transport Barriers in Carbon Nanotube Devices*, Nano Letters **5**(3), 507 (2005).

[113] F. Xia, T. Mueller, R. Golizadeh-Mojarad, M. Freitag, Y.-m. Lin, J. Tsang, V. Perebeinos, and P. Avouris, *Photocurrent Imaging and Efficient Photon Detection in a Graphene Transistor*, Nano Letters **9**(3), 1039 (2009).

[114] Y. Ahn, J. Dunning, and J. Park, *Scanning Photocurrent Imaging and Electronic Band Studies in Silicon Nanowire Field Effect Transistors*, Nano Letters **5**(7), 1367 (2005).

[115] J. M. Dudley, G. Genty, and S. Coen, *Supercontinuum generation in photonic crystal fiber*, Rev. Mod. Phys. **78**, 1135 (2006).

[116] F. Stckmann, *Superlinear Photoconductivity*, physica status solidi (b) **34**(2), 751 (1969).

[117] S. Prezioso, S. M. Hossain, A. Anopchenko, L. Pavesi, M. Wang, G. Pucker, and P. Bellutti, *Superlinear photovoltaic effect in Si nanocrystals based metal-insulator-semiconductor devices*, Applied Physics Letters **94**(6), 062108 (2009).

[118] L. Grabner, *Photoluminescence in $SrTiO_3$*, Phys. Rev. **177**, 1315 (1969).

[119] R. Leonelli and J. L. Brebner, *Time-resolved spectroscopy of the visible emission band in strontium titanate*, Phys. Rev. B **33**, 8649 (1986).

[120] H. Okamura, M. Matsubara, K. Tanaka, K. Fukui, M. Terakami, H. Nakagawa, Y. Ikemoto, T. Moriwaki, H. Kimura, and T. Nanba, *Photogenerated Carriers in $SrTiO_3$ Probed by Mid-Infrared Absorption*, Journal of the Physical Society of Japan **75**(2), 023703 (2006).

[121] M. Kawasaki, K. Takahashi, T. Maeda, R. Tsuchiya, and M. Shinohara, *Atomic Control of the $SrTiO_3$ Crystal Surface*, Science **266**(5190), 1540 (1994).

[122] M. Kareev, S. Prosandeev, J. Liu, C. Gan, A. Kareev, J. W. Freeland, M. Xiao, and J. Chakhalian, *Atomic control and characterization of surface defect states of TiO[sub 2] terminated SrTiO[sub 3] single crystals*, Applied Physics Letters **93**(6), 061909 (2008).

[123] J. Zhang, S. Walsh, C. Brooks, D. G. Schlom, and L. J. Brillson, *Depth-resolved cathodoluminescence spectroscopy study of defects in $SrTiO_3$* (AVS, 2008), vol. 26, pp. 1466–1471.

[124] G. Herranz, M. Basletić, M. Bibes, C. Carrétéro, E. Tafra, E. Jacquet, K. Bouzehouane, C. Deranlot, A. Hamzić, J.-M. Broto, A. Barthélémy, and A. Fert, *High Mobility in $LaAlO_3/SrTiO_3$ Heterostructures: Origin, Dimensionality, and Perspectives*, Phys. Rev. Lett. **98**, 216803 (2007).

[125] A. Kalabukhov, R. Gunnarsson, J. Börjesson, E. Olsson, T. Claeson, and D. Winkler, *Effect of oxygen vacancies in the $SrTiO_3$ substrate on the electrical properties of the $LaAlO_3/SrTiO_3$ interface*, Phys. Rev. B **75**, 121404 (2007).

[126] M. Basletic, J. L. Maurice, C. Carretero, G. Herranz, O. Copie, M. Bibes, E. Jacquet, K. Bouzehouane, S. Fusil, and A. Barthelemy, *Mapping the spatial distribution of charge carriers in LaAlO3/SrTiO3 heterostructures*, Nature Mater. **7**(8), 621 (2008).

[127] K. Shibuya, T. Ohnishi, T. Sato, and M. Lippmaa, *Metal-insulator transition in SrTiO[sub 3] induced by field effect*, Journal of Applied Physics **102**(8), 083713 (2007).

[128] T. Feng, *Anomalous photoelectronic processes in $SrTiO_3$*, Phys. Rev. B **25**, 627 (1982).

[129] S. S. A. Seo, Z. Marton, W. S. Choi, G. W. J. Hassink, D. H. A. Blank, H. Y. Hwang, T. W. Noh, T. Egami, and H. N. Lee, *Multiple conducting carriers generated in LaAlO[sub 3]/SrTiO[sub 3] heterostructures*, Applied Physics Letters **95**(8), 082107 (2009).

[130] Y. Cui, Q. Wei, H. Park, and C. M. Lieber, *Nanowire Nanosensors for Highly Sensitive and Selective Detection of Biological and Chemical Species*, Science **293**(5533), 1289 (2001).

[131] M. Walther, B. M. Fischer, A. Ortner, A. Bitzer, A. Thoman, and H. Helm, *Chemical Sensing and Imaging with Pulsed Terahertz Radiation*, Anal. Bioanal. Chem. **397**, 1009 (2010).

[132] A. Markelz, A. Roitberg, and E. Heilweil, *Pulsed terahertz spectroscopy of DNA, bovine serum albumin and collagen between 0.1 and 2.0 THz*, Chemical Physics Letters **320**(1), 42 (2000).

[133] C. J. Strachan, P. F. Taday, D. A. Newnham, K. C. Gordon, J. A. Zeitler, M. Pepper, and T. Rades, *Using terahertz pulsed spectroscopy to quantify pharmaceutical polymorphism and crystallinity*, Journal of Pharmaceutical Sciences **94**(4), 837 (2005).

[134] E. P. J. Parrott, J. A. Zeitler, J. McGregor, S.-P. Oei, H. E. Unalan, S.-C. Tan, W. I. Milne, J.-P. Tessonnier, R. Schlogl, and L. F. Gladden, *Understanding the Dielectric Properties of Heat-Treated Carbon Nanofibers at Terahertz Frequencies: a New Perspective on the Catalytic Activity of Structured Carbonaceous Materials*, The Journal of Physical Chemistry C **113**(24), 10554 (2009).

[135] R. Huber, F. Tauser, A. Brodschelm, M. Bichler, G. Abstreiter, and A. Leitenstorfer, *How many-particle interactions develop after ultrafast excitation of an electron-hole plasma*, Nature **414**(6861), 286 (2001).

[136] J. Shan and T. Heinz, *Terahertz Radiation from Semiconductors*, in *Ultrafast Dynamical Processes in Semiconductors*, edited by K.-T. Tsen (Springer Berlin Heidelberg, 2004), vol. 92 of *Topics in Applied Physics*, pp. 1–56.

[137] D. H. Auston, K. P. Cheung, and P. R. Smith, *Picosecond photoconducting Hertzian dipoles*, Applied Physics Letters **45**(3), 284 (1984).

[138] K. Sakai, *Terahertz Optoelectronics* (Spring, 2005).

[139] G. L. Dakovski, B. Kubera, and J. Shan, *Localized terahertz generation via optical rectification in ZnTe*, J. Opt. Soc. Am. B **22**(8), 1667 (2005).

[140] B. B. Hu, X.-C. Zhang, and D. H. Auston, *Terahertz radiation induced by subband-gap femtosecond optical excitation of GaAs*, Phys. Rev. Lett. **67**, 2709 (1991).

[141] B. B. Hu, A. S. Weling, D. H. Auston, A. V. Kuznetsov, and C. J. Stanton, *dc-electric-field dependence of THz radiation induced by femtosecond optical excitation of bulk GaAs*, Phys. Rev. B **49**, 2234 (1994).

[142] A. Rice, Y. Jin, X. F. Ma, X.-C. Zhang, D. Bliss, J. Larkin, and M. Alexander, *Terahertz optical rectification from ¡110¿ zinc-blende crystals*, Applied Physics Letters **64**(11), 1324 (1994).

[143] J. A. Fülöp, L. Pálfalvi, S. Klingebiel, G. Almási, F. Krausz, S. Karsch, and J. Hebling, *Generation of sub-mJ terahertz pulses by optical rectification*, Opt. Lett. **37**(4), 557 (2012).

[144] K. Y. Kim, A. J. Taylor, J. H. Glownia, and G. Rodriguez, *Coherent control of terahertz supercontinuum generation in ultrafast laser-gas interactions*, Nature Photon. **2**(10), 605 (2008).

[145] K. Reimann, *Table-top sources of ultrashort THz pulses*, Reports on Progress in Physics **70**(10), 1597 (2007).

[146] M. Kroug, S. Cherednichenko, H. Merkel, E. Kollberg, B. Voronov, G. Gol'tsman, H. Huebers, and H. Richter, *NbN hot electron bolometric mixers for terahertz receivers*, Applied Superconductivity, IEEE Transactions on **11**(1), 962 (2001).

[147] T. Yasui, A. Nishimura, T. Suzuki, K. Nakayama, and S. Okajima, *Detection system operating at up to 7 THz using quasioptics and Schottky barrier diodes*, Review of Scientific Instruments **77**(6), 066102 (2006).

[148] S. Ariyoshi, C. Otani, A. Dobroiu, H. Sato, K. Kawase, H. M. Shimizu, T. Taino, and H. Matsuo, *Terahertz imaging with a direct detector based on superconducting tunnel junctions*, Applied Physics Letters **88**(20), 203503 (2006).

[149] S. Komiyama, O. Astafiev, V. Antonov, T. Kutsuwa, and H. Hirai, *A single-photon detector in the far-infrared range*, Nature **403**(6768), 405 (2000).

[150] W. Knap, J. Lusakowski, T. Parenty, S. Bollaert, A. Cappy, V. V. Popov, and M. S. Shur, *Terahertz emission by plasma waves in 60 nm gate high electron mobility transistors*, Applied Physics Letters **84**(13), 2331 (2004).

[151] W. Knap, Y. Deng, S. Rumyantsev, and M. S. Shur, *Resonant detection of subterahertz and terahertz radiation by plasma waves in submicron field-effect transistors*, Applied Physics Letters **81**(24), 4637 (2002).

[152] S. Hunsche, M. Koch, I. Brener, and M. Nuss, *THz near-field imaging*, Optics Communications **150**(1), 22 (1998).

[153] A. J. Huber, F. Keilmann, J. Wittborn, J. Aizpurua, and R. Hillenbrand, *Terahertz Near-Field Nanoscopy of Mobile Carriers in Single Semiconductor Nanodevices*, Nano Letters **8**(11), 3766 (2008), pMID: 18837565.

[154] H.-T. Chen, R. Kersting, and G. C. Cho, *Terahertz imaging with nanometer resolution*, Applied Physics Letters **83**(15), 3009 (2003).

[155] A. Bitzer, A. Ortner, and M. Walther, *Terahertz near-field microscopy with subwavelength spatial resolution based on photoconductive antennas*, Appl. Opt. **49**(19), E1 (2010).

[156] Y. Kawano, *Highly Sensitive Detector for On-Chip Near-Field THz Imaging*, Selected Topics in Quantum Electronics, IEEE Journal of **17**(1), 67 (2011).

[157] Y. Kawano and K. Ishibashi, *An On-Chip Near-Field Terahertz Probe and Detector*, Nature Photon. **2**(10), 618 (2008).

[158] J. Mannhart and D. G. Schlom, *Oxide InterfacesAn Opportunity for Electronics*, Science **327**(5973), 1607 (2010).

[159] C. W. Bark, D. A. Felker, Y. Wang, Y. Zhang, H. W. Jang, C. M. Folkman, J. W. Park, S. H. Baek, H. Zhou, D. D. Fong, X. Q. Pan, E. Y. Tsymbal, *et al.*, *Tailoring a two-dimensional electron gas at the LaAlO3/SrTiO3 (001) interface by epitaxial strain*, Proceedings of the National Academy of Sciences **108**(12), 4720 (2011).

[160] J. W. Park, D. F. Bogorin, C. Cen, D. A. Felker, Y. Zhang, C. T. Nelson, C. W. Bark, C. M. Folkman, X. Q. Pan, M. S. Rzchowski, J. Levy, and C. B. Eom, *Creation of a two-dimensional electron gas at an oxide interface on silicon*, Nature Commun. **1**, 94 (2010).

[161] Y. Kanemitsu and Y. Yamada, *Light emission from SrTiO3*, physica status solidi (b) **248**(2), 416 (2011).

[162] E. Yablonovitch, J. P. Heritage, D. E. Aspnes, and Y. Yafet, *Virtual photoconductivity*, Phys. Rev. Lett. **63**, 976 (1989).

[163] Y. Yafet and E. Yablonovitch, *Virtual photoconductivity due to intense optical radiation transmitted through a semiconductor*, Phys. Rev. B **43**, 12480 (1991).

[164] M. Yamanishi, *Field-induced optical nonlinearity due to virtual transitions in semiconductor quantum well structures*, Phys. Rev. Lett. **59**, 1014 (1987).

[165] Z. Ristic, R. Di Capua, F. Chiarella, G. M. De Luca, I. Maggio-Aprile, M. Radovic, and M. Salluzzo, *Photodoping and in-gap interface states across the metal-insulator transition in $LaAlO_3/SrTiO_3$ heterostructures*, Phys. Rev. B **86**, 045127 (2012).

[166] F. W. Lytle, *X-Ray Diffractometry of Low-Temperature Phase Transformations in Strontium Titanate*, Journal of Applied Physics **35**(7), 2212 (1964).

[167] R. C. Neville, B. Hoeneisen, and C. A. Mead, *Permittivity of Strontium Titanate*, Journal of Applied Physics **43**(5), 2124 (1972).

[168] J. Hemberger, P. Lunkenheimer, R. Viana, R. Böhmer, and A. Loidl, *Electric-field-dependent dielectric constant and nonlinear susceptibility in* $SrTiO_3$, Phys. Rev. B **52**, 13159 (1995).

[169] T. Schneider, *Nonlinear Optics in Telecommunications* (Springer, 2004).

[170] D. Grischkowsky and S. ren Keiding, *THz time-domain spectroscopy of high T[sub c] substrates*, Applied Physics Letters **57**(10), 1055 (1990).

[171] J. Han, F. Wan, Z. Zhu, and W. Zhang, *Dielectric response of soft mode in ferroelectric SrTiO[sub 3]*, Applied Physics Letters **90**(3), 031104 (2007).

[172] S. L. Dexheimer, *Terahertz Spectroscopy* (CRC Press, 2008).

[173] V. V. Temnov, *Ultrafast Acousto-Magneto-Plasmonics*, Nature Photon. **6**(11), 728 (2012).

[174] M. Kauranen and A. V. Zayats, *Nonlinear Plasmonics*, Nature Photon. **6**(11), 737 (2012).

[175] A. N. Grigorenko, M. Polini, and K. S. Novoselov, *Graphene Plasmonics*, Nature Photon. **6**(11), 749 (2012).

[176] A. Bezryadin, C. Dekker, and G. Schmid, *Electrostatic trapping of single conducting nanoparticles between nanoelectrodes*, Applied Physics Letters **71**(9), 1273 (1997).

[177] A. V. Zayats, I. I. Smolyaninov, and A. A. Maradudin, *Nano-optics of surface plasmon polaritons*, Physics Reports **408**(3), 131 (2005).

[178] R. Trebino, K. W. DeLong, D. N. Fittinghoff, J. N. Sweetser, M. A. Krumbügel, B. A. Richman, and D. J. Kane, *Measuring ultrashort laser pulses in the time-frequency domain using frequency-resolved optical gating*, Review of Scientific Instruments **68**(9), 3277 (1997).

[179] L. Gallmann, D. H. Sutter, N. Matuschek, G. Steinmeyer, U. Keller, C. Iaconis, and I. A. Walmsley, *Characterization of sub-6-fs optical pulses with spectral phase interferometry for direct electric-field reconstruction*, Opt. Lett. **24**(18), 1314 (1999).

[180] F. Hache, T. J. Driscoll, M. Cavallari, and G. M. Gale, *Measurement of ultrashort pulse-durations by interferometricautocorrelation: influence of various parameters*, Appl. Opt. **35**(18), 3230 (1996).

[181] J.-C. M. Diels, J. J. Fontaine, I. C. McMichael, and F. Simoni, *Control and measurement of ultrashort pulse shapes (in amplitude and phase) with femtosecond accuracy*, Appl. Opt. **24**(9), 1270 (1985).

[182] N. Gorunski, N. Dimitrov, A. Dreischuh, and G. G. Paulus, *Pulse-front tilt created in misaligned dispersionless optical systems and correct interferometric autocorrelation*, Optics Communications **283**(24), 5192 (2010).

[183] A. Sharma, P. Naik, and P. Gupta, *The effect of errors and detector noise on sensitive detection of chirp and pulse asymmetry of ultrashort laser pulses from interferometric autocorrelation signals*, Optics Communications **259**(1), 350 (2006).

[184] S. Santran, M. Martinez-Rosas, L. Canioni, and L. Sarger, *Characterization of optical nonlinearity in semiconductor photodiodes using cross-polarized autocorrelation*, Quantum Electronics, IEEE Journal of **40**(12), 1687 (2004).

[185] K. Gabel, P. Rubbuldt, R. Lebert, and A. Valster, *Diode pumped Cr3+:LiCAF fs-laser*, Optics Communications **157**(16), 327 (1998).

[186] M. Wollenhaupt, A. Assion, and T. Baumert, *Femtosecond Laser Pulses: Linear Properties, Manipulation, Generation and Measurement*, in *Springer Handbook of Lasers and Optics*, edited by F. Trger (Springer New York, 2007), pp. 937–983.

[187] B. E. Lemoff and C. P. J. Barty, *Generation of high-peak-power 20-fs pulses from a regeneratively initiated, self-mode-locked Ti:sapphire laser*, Opt. Lett. **17**(19), 1367 (1992).